



HAL
open science

Techniques d'estimation du déplacement d'un véhicule sans GPS et autres exemples de conception de systèmes de navigation MEMS

Pierre-Jean Bristeau

► **To cite this version:**

Pierre-Jean Bristeau. Techniques d'estimation du déplacement d'un véhicule sans GPS et autres exemples de conception de systèmes de navigation MEMS. Automatique / Robotique. École Nationale Supérieure des Mines de Paris, 2011. Français. NNT: . pastel-00755348

HAL Id: pastel-00755348

<https://pastel.hal.science/pastel-00755348>

Submitted on 21 Nov 2012

HAL is a multi-disciplinary open access archive for the deposit and dissemination of scientific research documents, whether they are published or not. The documents may come from teaching and research institutions in France or abroad, or from public or private research centers.

L'archive ouverte pluridisciplinaire **HAL**, est destinée au dépôt et à la diffusion de documents scientifiques de niveau recherche, publiés ou non, émanant des établissements d'enseignement et de recherche français ou étrangers, des laboratoires publics ou privés.

École doctorale n°432: Sciences des Métiers de l'Ingénieur (SMI)

Doctorat ParisTech

T H È S E

pour obtenir le grade de docteur délivré par

l'École Nationale Supérieure des Mines de Paris

Spécialité « Mathématique et Automatique »

présentée et soutenue publiquement par

Pierre-Jean BRISTEAU

le 6 décembre 2011

**Techniques d'estimation du déplacement
d'un véhicule sans GPS
et autres exemples de conception
de systèmes de navigation MEMS**

Directeur de thèse: **Nicolas PETIT**

Jury

M. Tarek HAMEL, Professeur, I3S, Université de Nice-Sophia-Antipolis
M. Lorenzo MARCONI, Professeur, LAR-DEIS, Université de Bologne
M. Knut GRAICHEN, Professeur, IMRM, Université d'Ulm
M. Vincent ANDRIEU, Chargé de recherche, LAGEP, CNRS
M. Philippe MOUYON, Docteur, DCSD, ONERA
M. Nicolas PETIT, Professeur, CAS, MINES ParisTech
M. Xavier MICHÉ, Ingénieur, ST(SI)²
M. David VISSIÈRE, Docteur, SYSNAV

Rapporteur
Rapporteur
Examinateur
Examinateur
Examinateur
Examinateur
Invité
Invité

Graduate School n°432: Sciences des Métiers de l'Ingénieur (SMI)

ParisTech

PHD THESIS

To obtain the Doctor's degree from

École Nationale Supérieure des Mines de Paris

Speciality « Mathématique et Automatique »

defended in public by

Pierre-Jean BRISTEAU

on December 6th, 2011

**Motion estimation techniques
for GPS-free vehicle
and other examples
of MEMS navigation systems design**

Thesis advisor: **Nicolas PETIT**

Committee

M. Tarek HAMEL, Professor, I3S, University of Nice-Sophia-Antipolis
M. Lorenzo MARCONI, Professor, LAR-DEIS, University of Bologna
M. Knut GRAICHEN, Professor, IMRM, University of Ulm
M. Vincent ANDRIEU, Chargé de recherche, LAGEP, CNRS
M. Philippe MOUYON, Doctor, DCSD, ONERA
M. Nicolas PETIT, Professor, CAS, MINES ParisTech
M. Xavier MICHÉ, Engineer, ST(SI)²
M. David VISSIÈRE, Doctor, SYSNAV

Reviewer
Reviewer
Examiner
Examiner
Examiner
Examiner
Invited
Invited

**T
H
È
S
E**

PIERRE-JEAN BRISTEAU

Centre Automatique et Systèmes
Unité Mathématiques et Systèmes
MINES ParisTech
60 boulevard St Michel 75272 Paris Cedex
France.

E-mail: pierre-jean.bristeau@mines-paris.org

Key words. - GPS-free navigation systems, MEMS sensors, embedded systems, observability, Kalman filtering, interconnected observers, temporally interconnected observers, automotive vehicle, micro-UAV, mini-rocket

Mots clés. - systèmes de navigation sans GPS, capteurs MEMS, systèmes embarqués, observabilité, filtrage de Kalman, observateurs interconnectés, observateurs temporellement interconnectés, véhicule automobile, micro-drone, mini-fusée

La recherche doit avant tout être un jeu et un plaisir.

PIERRE JOLIOT, *La recherche passionnément*, Ed. Odile Jacob.

L'esprit qui invente est toujours mécontent de ses progrès, parce qu'il voit au-delà.

JEAN LE ROND D'ALEMBERT, *Encyclopédie*, Briasson, David, Le Breton & Durand.

REMERCIEMENTS

Je remercie, en premier lieu, mon directeur de thèse, Nicolas Petit, qui m'a guidé et appuyé dans mes recherches, en me laissant à la fois une grande autonomie et en me proposant une grande diversité de sujets et d'activités.

Je remercie également David Vissière pour l'opportunité qu'il m'a donnée de travailler sur ce sujet aussi captivant que l'avait été un précédent stage à ses côtés, pour sa confiance et son soutien.

Je les remercie tous les deux de m'avoir associé à leur projet SYSNAV au sein duquel j'espère pouvoir continuer à travailler de manière fructueuse à leurs côtés.

Je suis reconnaissant envers messieurs Hamel et Marconi pour l'honneur qu'ils m'ont fait en acceptant d'être rapporteurs de cette thèse. Mes remerciements vont de même à messieurs Graichen, Andrieu et Mouyon pour leur présence dans mon jury.

Je remercie tout particulièrement Xavier Miché pour son accompagnement et son implication au cours de ma thèse et sa présence à ma soutenance.

J'adresse aussi mes remerciements à Philippe Martin pour ses discussions toujours animées et à Laurent Praly pour son aide précieuse.

Je ne saurais oublier mes " collègues " doctorants, en particulier, Erwan, Eric et Caroline ainsi que ceux que j'ai côtoyés lors de mes trois années au CAS, Mathieu, Thomas, Florent, Zakhi, Paul, Delphine, Hadis et Nadège. Je pense bien sûr également aux stagiaires que j'ai eu plaisir à encadrer.

Je remercie également mes " collègues de la première heure " Alain, Quentin et Yohann pour leur soutien technique toujours enthousiaste. Mes remerciements vont aussi à Manu, Nicolas et Lionel qui ont partagé avec moi quelques problématiques scientifiques.

Pour boucler la boucle, je remercie sincèrement Gaël Désilles qui m'a mis le pied à l'étrier dans ce milieu passionnant que forment la navigation et les personnes qui le constituent.

Bien sûr, je tiens à remercier ma famille et mes amis, souvent intéressés, parfois intrigués mais toujours présents à mes côtés.

Enfin, je tiens à remercier, sur un plan plus personnel, Nicolas pour ces années passées à ses côtés, depuis un entretien (en béquilles) pour un stage jusqu'à l'obtention de cette thèse. M'investir dans cette thèse fut un plaisir et cela tient pour beaucoup à son humanité et à sa façon d'animer le CAS, parfaitement illustrée par les citations en page précédente.

Motion estimation techniques
for GPS-free vehicle
and other examples
of MEMS navigation systems design

RÉSUMÉ

Dans cette thèse, on explique la conception et la mise au point d'un système de navigation sans GPS pour un véhicule automobile. Ce système exploite des mesures de champs magnétiques réalisées à bord du véhicule en mouvement, combinées à des mesures inertielles réalisées à partir de capteurs MEMS bas coût. Il permet de reconstituer, à partir d'une condition initiale, la trajectoire du véhicule en temps réel. Un prototype fonctionnel complet est présenté ainsi que des résultats expérimentaux. La conception de ce système repose sur une analyse de l'observabilité d'un modèle classique du véhicule, qui permet d'établir comment les différents biais et défauts des capteurs peuvent être estimés grâce à des filtres de Kalman agencés suivant deux schémas d'interconnexion: par partition des variables d'états et par séquençement. Une analyse de convergence des schémas d'estimation est étudiée. En dernière partie du manuscrit, deux autres exemples de systèmes de navigation à base de capteurs MEMS sont décrits, celui du quadricoptère Parrot AR.Drone et celui de fusées expérimentales à propulsion hybride, pour lesquels les mêmes principes de conception sont appliqués.

ABSTRACT

In this thesis, we explain the design and development of a GPS-free navigation system for automotive vehicles. This system uses magnetic field measurements performed onboard the vehicle in motion, and combines them with inertial measurements from other low costs MEMS sensors. It allows one to reconstruct the path of the vehicle from the initial condition in real time. A complete prototype is presented along with experimental results. The design of this system is based on an analysis of the observability of a classical model of the vehicle. This serves to establish how the various biases and shortcomings of the sensors can be estimated through Kalman filters arranged in two interconnection schemes: a partition of the state variables and a temporal interconnection. An analysis of convergence of the estimates is performed. In the final part of the manuscript, two other examples of MEMS-based navigation systems are described, including the AR.Drone quadrotor and experimental hybrid rockets for which the same design principles are applied.

Contents

Introduction	1
1 Notations	3
1.1 Frames of reference and parametrization of orientation	3
1.2 Euler angles	4
1.3 Quaternions	4
1.4 States, dynamics and measurement	6
Acronyms	9
I Kalman filtering and observability	11
2 A quick tour of Kalman filtering	15
2.1 Kalman-Bucy filter	15
2.2 Extended Kalman filter	19
2.3 Discrete-time Kalman filter	20
2.3.1 Sampled Linear-Time-Invariant system	21
2.3.2 Mixed continuous-discrete-time filtering	22
2.3.3 Multi-rates Kalman filter	23
2.3.4 Remarks on the units	24
2.4 Computational burden and numerical accuracy	24
2.4.1 Sequential processing	24
2.4.2 Joseph form	25
2.4.3 Information filter	25
2.4.4 Square-root filter	26
3 Observability properties and their roles in the convergence of Kalman filters	27
3.1 Uniform and Complete Observability	27
3.2 Differential Observability	28
3.3 Existence and convergence of the Kalman filter	32
3.3.1 Lower bound on the solution of the covariance equation from boundedness of the system	33

3.3.2	Upper bound stemming from the Uniform and Complete Observability property	34
3.3.3	Convergence of the Kalman filter	36
3.3.4	Estimation of the convergence rate	37
3.4	Conclusion and main result	38
II	GPS-free automotive relative navigation system	39
4	Exploitation of magnetic measurements onboard a vehicle	43
4.1	Magnetic velocimeter	44
4.1.1	Frequency detection	45
4.1.2	Stops detection	47
4.1.3	Phase detection	48
4.2	Magnetic heading determination	49
4.2.1	Hard iron / soft iron distortions	50
4.2.2	Ellipse detection	51
4.2.3	Complementary filter	54
5	Description of the relative navigation problem	55
5.1	Vehicle model under consideration	55
5.2	Embedded sensors	57
5.3	A view of practical issues	58
6	Design of the navigation system	61
6.1	Observer design	61
6.1.1	Interconnected subsystems	61
6.1.2	Decomposition into Temporally Interconnected Observers	65
6.2	Observability for the models used in the Temporally Interconnected Observers	68
6.2.1	Uniform and Complete Observability of the straight-line motion model	68
6.2.2	Differential Observability of the curve motion model	68
6.3	Convergence of the Temporally Interconnected Observers structure	73
7	Practical implementation and experimental results	79
7.1	Implementation of Kalman filtering	79
7.2	On-line alignment procedure	81
7.3	Numerical rate of convergence estimates	83
7.4	Fault detection strategy	83
7.5	Optimal smoothing for multi-rates filtering and a posteriori trajectory smoothing	85
7.6	Results	87
7.6.1	Simulation illustrating biases estimation properties	87
7.6.2	Short range experimental real-time reconstruction	90
7.6.3	Long range trajectory real-time reconstruction	91

III	Other examples of navigation system design	95
8	The navigation problem aboard the AR.Drone	97
8.1	Navigation problem	99
8.2	Aerodynamics modeling	100
8.2.1	Method to calculate aerodynamics effects	101
8.2.2	Dynamic coupling between the vehicle and the rotors	104
8.3	Observer design and presentation of results	107
9	A navigation problem for an experimental mini-rocket	115
9.1	The rocket under consideration	116
9.1.1	Model	116
9.1.2	Onboard instrumentation	118
9.2	Trajectory estimation	118
9.2.1	A typical trajectory	118
9.2.2	Estimation technique	119
9.2.3	Results exploiting in-flight measurements	120
9.3	Estimation of propulsion parameters	122
9.3.1	Combustion system measurements	123
9.3.2	Thrust model of hybrid engine	123
9.3.3	Results exploiting in-flight measurements	124
9.4	Conclusion	126
	Conclusion	129
	Appendix	133
A	Discussion on the smoothing technique: a comparison with back-and-forth filtering on simple examples	135
A.1	Cramér-Rao bound for a biased estimator	136
A.2	Identification of a constant	138
A.2.1	Back-and-Forth Nudging	139
A.2.2	Back-and-Forth Kalman filtering	141
A.2.3	Mean estimator	142
A.3	Estimation of a first-order dynamics	145
A.3.1	Back-and-Forth Nudging	145
A.3.2	Back-and-Forth Kalman Filtering	146
B	The role of the location of the center of gravity in quadrotor stability	151

Bibliography

157

Introduction

In this thesis, we expose the principles of a navigation system that we have created for automotive applications. It consists of embedded Micro-Electro-Mechanical Systems (MEMS) sensors and allows one to estimate the position and the orientation, relative to initial conditions, of an automotive vehicle. The major feature of this system is that it does not use any Global Positioning System (GPS) receiver.

This thesis describes the scientific steps that have been necessary to design a functional prototype. This design relies on the observability properties of the vehicle dynamics model when it is equipped with a particular set of sensors. The fundamental principles employed to estimate the vehicle motion stem from the theory of inertial navigation. Classically, when high quality (tactical grade) inertial sensors (accelerometers and gyrometers) are used, their signals can be integrated once then twice to obtain, sequentially, attitudes, velocities and position estimates. In this thesis, we consider low-cost MEMS sensors. Their numerous defects, among which are non negligible biases, discard the classic technique previously mentioned. In particular, the biases generate overwhelming drift in the integrations producing the estimates. Other solutions must be found.

Onboard the vehicle, we embed MEMS accelerometers, gyrometers along with magnetometers and a barometric altitude sensor. A particularity of our approach is that the magnetometers are used to measure the ground velocity and the heading of the vehicle. The relative redundancy of the sensors measurements is analyzed through careful investigations on observability. In details, it is shown that all the variables needed to estimate the relative motion of the vehicle can be reconstructed. The model under consideration is a simple six degrees of freedom (6-DOF) rigid body dynamics, in constant contact with the road, without slip. The sensors are modeled according to classic error models incorporating biases. A main contribution of the thesis is to show the reconstructibility of the dynamics state vector in this context. We now explain how this study is organized.

Usually, reconstructibility can be conveniently established by invoking a classic Kalman filter (as recalled in Chapter 2) which asymptotic convergence is guaranteed under the Uniform and Complete Observability (UCO) property (recalled in Section 3.1). This point is exposed in details in Section 3.3. Formally, the UCO property is difficult to establish. Much more conveniently, we propose to relate it to an easily checkable rank test of Differential Observability (DO) as is exposed in Section 3.2. A result of Chapter 3 is that DO implies UCO which, in turn, implies convergence of Kalman filtering. This result guides us in the design of the navigation system.

The use of magnetic measurements onboard an automotive vehicle is detailed in Chapter 4. The relative redundancy previously mentioned is in fact difficult to use as ambiguities in the sensors data come into play in a way depending on the (a priori unknown) nature of the vehicle trajectory. In details, the malicious effects of vehicle braking on the magnetometer information, and the interaction of rotations, translations, and slopes on gyrometric data are detailed in Chapter 5. In the navigation filter, we split the state variables into subsets. This allows us to isolate the effects of each sensor bias. During favorable sequences, the bias are estimated. Then, the estimates can be used to handle the discussed malicious effects. Bias estimation is relatively straightforward for accelerometers but the situation is much more involved for gyrometers. The natural couplings of axes due to the Euler angles parametrization (recalled in Section 1.2) suggest to isolate the yaw angle and the corresponding bias. On the other hand, the roll and pitch angles and the corresponding gyrometers biases must be estimated jointly. All these considerations yield us to introduce a structure of interconnected observers detailed in Section 6.1.1. At the center of the interconnection is the roll-pitch subdynamics. It is the subject of Chapter 6.1.2. Globally, this sub-dynamics is not observable. The variables can not be simultaneously observed, but the observability deficiency corresponds to a different variable depending on the nature of the trajectory currently followed by the vehicle. For this reason, the roll-pitch dynamics is observed using three Temporally Interconnected Observers (TIO). The introduction of this class of observers is also a contribution of the thesis. At each instant, only one of the TIO is processing measurements, the others being updated (propagated) in open loop. The TIO constitute a set of separately contracting then propagating dynamics. In the case under consideration, convergence of the TIO scheme is proved. This is the contribution of Section 6.3.

Numerous field experiments have been conducted and a selection of them, along with details of implementation, are reported in Chapter 7. It appears that, in urban or countryside experiments, over periods ranging from several hours to days, for traveled distances of 1 km to 600 km, the actual motion of the vehicle can be reconstructed relatively accurately. The error between the position reconstructed from perfect initial conditions and the actual position of the vehicle is below 10% of the traveled distance, more often that not below 5%.

The rest of the manuscript is dedicated to other examples of navigation filter design. Chapter 8 describes the attitude and velocity data fusion algorithms embedded in the AR.Drone (Parrot©). As is exposed, it relies on a tight coupling of inertial sensors and camera streams. This navigation system is the heart of this popular autonomous Unmanned Aerial Vehicle (UAV). Chapter 9 reports trajectory estimation results for experimental mini-rockets operated by *Centre National d'Etudes Spatiales*, National Center for Space Research (CNES). Off-line processing of embedded sensors serve to quantify the engine efficiency. In both cases, the employed navigation techniques are discussed at the light of the observability-based design advocated in this thesis.

Chapter 1

Notations

Notations

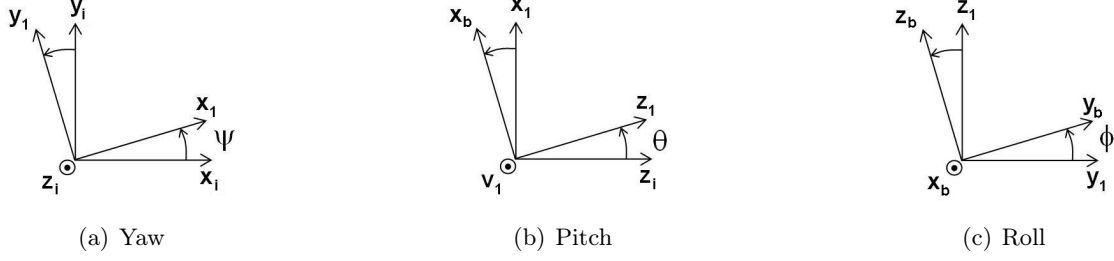
Ce chapitre introduit les notations générales utilisées ultérieurement dans cette thèse. Les repères de référence y sont détaillés ainsi que deux façons de déterminer leurs orientations respectives. Les variables dynamiques sont présentées sous leur forme vectorielle et en composantes scalaires.

1.1 Frames of reference and parametrization of orientation

For each application considered in this thesis, a Galilean frame of reference is considered. This (local) inertial frame is noted $R_i = (\mathbf{x}_i, \mathbf{y}_i, \mathbf{z}_i)$ and is oriented using the North-East-Down formalism, the \mathbf{z}_i axis being aligned with the gravity direction, the \mathbf{x}_i axis with the local meridian and the \mathbf{y}_i axis with the local parallel, respectively. Its origin is O_i . Earth rotation, Earth curvature and local variations of gravity are neglected.

A body frame $R_b = (\mathbf{x}_b, \mathbf{y}_b, \mathbf{z}_b)$ is associated to the vehicle under consideration. Its origin O_b is the center of gravity of the vehicle. The \mathbf{x}_b axis is taken aligned with the longitudinal axis of the vehicle, the \mathbf{z}_b is directed downward such that the plane $(\mathbf{x}_b, \mathbf{z}_b)$ is a symmetry plane for the vehicle, and, finally, the \mathbf{y}_b axis completes the direct frame. The orientation of the body frame compared to the inertial frame is given by three successive rotations described in Fig. 1.1. From the inertial frame, the first rotation, of angle ψ , is around the \mathbf{z}_i axis, the second rotation, of angle θ , is around the intermediate \mathbf{y}_1 axis and finally the third rotation, of angle ϕ , is around the \mathbf{x}_b axis.

This choice of rotations is one possibility among various Euler angles combinations (here a ZYX combination). It corresponds to angles used in aeronautics [Titterton and Weston, 2004], where the ψ -angle is named *yaw* angle (or heading angle), the θ -angle is the *pitch* angle and the ϕ -angle is the *roll* angle.


 Figure 1.1: Orientation of the R_b frame with respect to the R_i frame.

The change of coordinates from R_i to R_b can be expressed in terms of the Euler angles under the form of the following matrix

$$P_{R_i \rightarrow R_b} = \begin{pmatrix} c_\theta c_\psi & c_\theta s_\psi & -s_\theta \\ s_\phi s_\theta c_\psi - c_\phi s_\psi & s_\phi s_\theta s_\psi + c_\phi c_\psi & s_\phi c_\theta \\ c_\phi s_\theta c_\psi + s_\phi s_\psi & c_\phi s_\theta s_\psi - s_\phi c_\psi & c_\phi c_\theta \end{pmatrix} \quad (1.1)$$

where $c_\theta = \cos \theta$ and $s_\psi = \sin \psi$, e.g.

1.2 Euler angles

The rotation of R_b with respect to R_i is described by the rotation vector $\boldsymbol{\Omega}$ whose components, when expressed in the body frame are the *roll rate* p , the *pitch rate* q and the *yaw rate* r . In vector notations, one has

$$\begin{aligned} \boldsymbol{\Omega} &= p \mathbf{x}_b + q \mathbf{y}_b + r \mathbf{z}_b \\ &= \dot{\psi} \mathbf{z}_i + \dot{\theta} \mathbf{y}_1 + \dot{\phi} \mathbf{x}_b \\ &= (\dot{\phi} - \dot{\psi} s_\theta) \mathbf{x}_b + (\dot{\theta} c_\phi + \dot{\psi} s_\phi c_\theta) \mathbf{y}_b + (\dot{\psi} c_\phi c_\theta - \dot{\theta} s_\phi) \mathbf{z}_b \end{aligned} \quad (1.2)$$

The sequence of rotations pictured in Fig. 1.1 introduces coupling between the angles dynamics. The rotation components in the body frame, (p, q, r) are different from the angles derivatives $(\dot{\phi}, \dot{\theta}, \dot{\psi})$. One-to-one correspondence relations are given below

$$\begin{cases} p = \dot{\phi} - \dot{\psi} s_\theta \\ q = \dot{\theta} c_\phi + \dot{\psi} s_\phi c_\theta \\ r = \dot{\psi} c_\phi c_\theta - \dot{\theta} s_\phi \end{cases} \quad \begin{cases} \dot{\psi} = \frac{s_\phi q + c_\phi r}{c_\theta} \\ \dot{\theta} = c_\phi q - s_\phi r \\ \dot{\phi} = p + (s_\phi q + c_\phi r) \frac{s_\theta}{c_\theta} \end{cases}$$

1.3 Quaternions

Depending on the considered application, the singularity encountered by the Euler angles around $\theta = \pm\pi/2$ can reveal more or less troublesome. Simply, quaternions can be introduced

to circumvent it. The quaternion describes the orientation of R_b with respect to R_i by a three-dimensional vector and a rotation around this vector. Naturally, this leads a four parameters representation. To obtain uniqueness of the description, the quaternion is normalized.

In summary, a quaternion \mathcal{Q} is a quadruplet (q_0, q_1, q_2, q_3) constrained by $q_0^2 + q_1^2 + q_2^2 + q_3^2 = 1$

$$\mathcal{Q} = \begin{bmatrix} q_0 \\ q_1 \\ q_2 \\ q_3 \end{bmatrix} \triangleq \begin{bmatrix} \cos \mu/2 \\ \mu_x/\mu \sin \mu/2 \\ \mu_y/\mu \sin \mu/2 \\ \mu_z/\mu \sin \mu/2 \end{bmatrix}$$

where μ_x, μ_y, μ_z can be interpreted as the components of the mentioned vector and μ defines the rotation angle.

The time derivative of the quaternion is bilinear and can be written under either of the following two convenient forms

$$\dot{\mathcal{Q}} = \frac{1}{2} \begin{pmatrix} 0 & -p & -q & -r \\ p & 0 & r & -q \\ q & -r & 0 & p \\ r & q & -p & 0 \end{pmatrix} \mathcal{Q} = \frac{1}{2} \begin{pmatrix} q_0 & -q_1 & -q_2 & -q_3 \\ q_1 & q_0 & -q_3 & -q_2 \\ q_2 & q_3 & q_0 & -q_1 \\ q_3 & -q_2 & q_1 & q_0 \end{pmatrix} \begin{bmatrix} 0 \\ p \\ q \\ r \end{bmatrix}$$

In application, it is often necessary to implement the discrete-time version of the preceding differential equation. In a numerical scheme, additive integration scheme presented below in Eq. (1.3) preserves the norm. But, the usually considered normalization step can introduce significant errors when the discretization step is too large compared to the bandwidth of the dynamics of (p, q, r) .

$$\begin{cases} \tilde{\mathcal{Q}}(t) = \mathcal{Q}(t) + \dot{\mathcal{Q}}(t)\Delta t \\ \mathcal{Q}(t + \Delta t) = \tilde{\mathcal{Q}}(t) / \|\tilde{\mathcal{Q}}(t)\| \end{cases} \quad (1.3)$$

In such cases, multiplicative integration can be preferred despite its increased computational burden. It takes the form, which will be used in Chapter 9,

$$\begin{cases} \alpha(t) = \Delta t \|\boldsymbol{\Omega}(t)\|, & \mathbf{n}(t) = \begin{bmatrix} p \\ q \\ r \end{bmatrix} / \|\boldsymbol{\Omega}(t)\|, & \tilde{\mathcal{Q}}(t) = \begin{bmatrix} \cos \alpha(t)/2 \\ \mathbf{n}(t) \sin \alpha(t)/2 \end{bmatrix} \\ \mathcal{Q}(t + \Delta t) = \begin{pmatrix} q_0 & -q_1 & -q_2 & -q_3 \\ q_1 & q_0 & q_3 & -q_2 \\ q_2 & -q_3 & q_0 & q_1 \\ q_3 & q_2 & -q_1 & q_0 \end{pmatrix} (t) \tilde{\mathcal{Q}}(t) \end{cases}$$

Finally, the one-to-one correspondence between Euler angles and quaternions is given below.

$$\begin{cases} q_0 = \cos \frac{\phi}{2} \cos \frac{\theta}{2} \cos \frac{\psi}{2} + \sin \frac{\phi}{2} \sin \frac{\theta}{2} \sin \frac{\psi}{2} \\ q_1 = \sin \frac{\phi}{2} \cos \frac{\theta}{2} \cos \frac{\psi}{2} - \cos \frac{\phi}{2} \sin \frac{\theta}{2} \sin \frac{\psi}{2} \\ q_2 = \cos \frac{\phi}{2} \sin \frac{\theta}{2} \cos \frac{\psi}{2} + \sin \frac{\phi}{2} \cos \frac{\theta}{2} \sin \frac{\psi}{2} \\ q_3 = -\cos \frac{\phi}{2} \cos \frac{\theta}{2} \sin \frac{\psi}{2} + \sin \frac{\phi}{2} \sin \frac{\theta}{2} \cos \frac{\psi}{2} \end{cases} \begin{cases} \phi = \arctan \frac{2(q_2 q_3 + q_0 q_1)}{q_0^2 - q_1^2 - q_2^2 + q_3^2} \\ \theta = \arcsin -2(q_1 q_3 - q_0 q_2) \\ \psi = \arctan \frac{2(q_1 q_2 + q_0 q_3)}{q_0^2 + q_1^2 - q_2^2 - q_3^2} \end{cases}$$

The change of coordinates matrix (1.1) can also be expressed in terms of quaternion.

$$P_{R_i \rightarrow R_b} = \begin{pmatrix} q_0^2 + q_1^2 - q_2^2 - q_3^2 & 2(q_1 q_2 + q_0 q_3) & 2(q_1 q_3 - q_0 q_2) \\ 2(q_1 q_2 - q_0 q_3) & q_0^2 + q_2^2 - q_1^2 - q_3^2 & 2(q_2 q_3 + q_0 q_1) \\ 2(q_1 q_3 + q_0 q_2) & 2(q_2 q_3 - q_0 q_1) & q_0^2 + q_3^2 - q_1^2 - q_2^2 \end{pmatrix}$$

1.4 States, dynamics and measurement

From the preceding, orientation of the body frame is given by the triplet (ϕ, θ, ψ) or equivalently by the (normalized) quaternion (q_0, q_1, q_2, q_3) . The components of the rotation vector $\boldsymbol{\Omega}$ of the body frame R_b with respect to the inertial frame R_i , expressed in the body frame R_b , are denoted by (p, q, r) . The change of coordinates matrix, from the inertial frame to the body frame, noted $P_{R_i \rightarrow R_b}$, satisfies

$$\frac{d}{dt} P_{R_i \rightarrow R_b} = -\boldsymbol{\Omega} \wedge P_{R_i \rightarrow R_b}$$

The position of the rigid body defined by the position of its center of mass O_b with respect to the origin O_i of the reference frame R_i expressed in the inertial frame is given by (x, y, z) . The velocity \mathbf{V} relative to the inertial frame is expressed by (u, v, w) in R_b coordinates and by (v_x, v_y, v_z) in R_i coordinates, it satisfies the vector definition

$$\left. \frac{d\mathbf{O}_i \mathbf{O}_b}{dt} \right|_{R_i} = \mathbf{V}$$

which, once projected onto R_b , gives

$$\frac{d}{dt} \begin{bmatrix} x \\ y \\ z \end{bmatrix} = \begin{bmatrix} v_x \\ v_y \\ v_z \end{bmatrix} = P_{R_b \rightarrow R_i} \begin{bmatrix} u \\ v \\ w \end{bmatrix}$$

The acceleration $\boldsymbol{\Gamma}$ of the rigid body relative to the inertial frame expressed in the body frame is $(\Gamma_x, \Gamma_y, \Gamma_z)$. One has

$$\left. \frac{d\mathbf{V}}{dt} \right|_{R_b} = \left. \frac{d\mathbf{V}}{dt} \right|_{R_i} - \boldsymbol{\Omega} \wedge \mathbf{V} = \boldsymbol{\Gamma} - \boldsymbol{\Omega} \wedge \mathbf{V}$$

which, once projected onto R_b , gives

$$\frac{d}{dt} \begin{bmatrix} u \\ v \\ w \end{bmatrix} = \begin{bmatrix} \Gamma_x \\ \Gamma_y \\ \Gamma_z \end{bmatrix} - \begin{bmatrix} p \\ q \\ r \end{bmatrix} \wedge \begin{bmatrix} u \\ v \\ w \end{bmatrix}$$

Unless otherwise specified, the sensor frame is the same as the body frame and the measurements inherit the subscript m . For example, the gyrometers give the measurement vector $\boldsymbol{\Omega}_m = [p_m \ q_m \ r_m]^T$ and the accelerometers give the measured specific acceleration

$\mathbf{\Gamma}_m = [a_{xm} \ a_{ym} \ a_{zm}]^T$ which are the measurements of $[a_x \ a_y \ a_z]^T$. In case perfect sensors are considered (noise and biases being neglected), it yields

$$\mathbf{\Omega}_m = \mathbf{\Omega}, \quad \mathbf{\Gamma}_m = \mathbf{\Gamma} - P_{R_i \rightarrow R_b} \begin{bmatrix} 0 \\ 0 \\ g \end{bmatrix}$$

$$\frac{d}{dt} \begin{bmatrix} u \\ v \\ w \end{bmatrix} = \begin{bmatrix} a_{xm} \\ a_{ym} \\ a_{zm} \end{bmatrix} + g \begin{bmatrix} -s\theta \\ s_\phi c\theta \\ c_\phi c\theta \end{bmatrix} - \begin{bmatrix} p_m \\ q_m \\ r_m \end{bmatrix} \wedge \begin{bmatrix} u \\ v \\ w \end{bmatrix}$$

where g stands for the gravity and equals 9.81 m.s^{-2} .

Depending on the application under consideration, position, velocity, angles and angular rates are gathered in the vector \mathbf{X} with potentially other interesting states, for example, aerodynamics states or biases. In the case when (known) controls appear in the dynamics, they are represented by the vector \mathbf{U} . All the measurements are assembled in the vector \mathbf{Y} . The dimension of the state \mathbf{X} (respectively the measurement \mathbf{Y}) is noted n (resp. m). The time-varying dynamics are written in state-space form as

$$\begin{cases} \dot{\mathbf{X}} = f(\mathbf{X}, \mathbf{U}, t) \\ \mathbf{Y} = g(\mathbf{X}, \mathbf{U}, t) \end{cases} \quad (1.4)$$

Acronyms

6-DOF six degrees of freedom.

AEKF Adaptive High Gain Extended Kalman Filter.

BFN Back-and-Forth Nudging.

CNES *Centre National d'Etudes Spatiales*, National Center for Space Research.

CO Complete Observability.

DKF Distributed Kalman Filter.

DO Differential Observability.

EKF Extended Kalman Filter.

FFT Fast Fourier Transform.

GPS Global Positioning System.

HEKF Hybrid Extended Kalman Filter.

HGEKF High Gain Extended Kalman Filter.

IEKF Invariant Extended Kalman Filter.

IEKF Iterated Extended Kalman Filter.

IF Information Filter.

IGRF International Geomagnetic Reference Field.

IMU Inertial Measurement Unit.

ISA International Standard Atmosphere.

LCD Light Crystal Display.

LTI Linear-Time-Invariant.

LTV Linear-Time-Varying.

MEMS Micro-Electro-Mechanical Systems.

ONERA *Office National d'Etudes et de Recherches Aérospatiales*, French Aerospace Lab.

PDA Pitch Determination Algorithm.

PERSEUS project *Projet Etudiant de Recherche Spatiale Européen Universitaire et Scientifique*, European Student Project on Academic and Scientific Space Research.

PKF Pseudo Kalman Filter.

PSD Power Spectral Density.

SR-IF Square-Root Information Filter.

SR-UKF Square-Root Unscented Kalman Filter.

TIO Temporally Interconnected Observers.

UAV Unmanned Aerial Vehicle.

UCE Uniform and Complete Estimatability.

UCO Uniform and Complete Observability.

UKF Unscented Kalman Filter.

UO Uniform Observability.

ZUPT Zero velocity Update.

Part I

Kalman filtering and observability

Filtrage de Kalman et observabilité

Introduction

This part of the thesis contains a short exposition of Kalman filtering theory and related discussions on observability properties. The subject is well-established. In 1974, T. Kailath already proposed “a view of three decades of linear filtering theory” in a celebrated article [Kailath, 1974]. Thirty-seven years later, we propose a shortened view which clearly does not claim to be as exhaustive as the cited survey work, but simply aims only at highlighting key elements used in this thesis by situating the Kalman filter in the filtering theory. We gather here some well-known results on filtering, along with implementation considerations.

Optimal estimation problem treated from a stochastic point of view can be traced back to the pioneering works of Kolmogorov and Wiener. In the 1940s, Kolmogorov [Kolmogorov, 1941] and Wiener [Wiener, 1942] worked simultaneously on the question of a posteriori optimal estimation, which concerned the combination of knowledges on statistics in time series with needs at that time in communication engineering. Their seminal works announced the numerous future research efforts to find optimal filter in the sense of minimization of the stochastic parameters of error estimation. At this early time, the Wiener filter was dealing only with stationary processes. Estimation was realized a posteriori considering knowledge of all past values of the signal, with a filter design aiming at finding the filter impulse response minimizing the root mean square error covariance. We now sketch the philosophy of the method. The interested reader will find all the necessary details in [Van Trees, 1968].

Consider a signal $a(t)$ of covariance function $\kappa_a(t, u)$, corrupted by a noise $n(t)$ with covariance $\kappa_n(t, u)$. The objective is to find the filter impulse response $t \mapsto h(t)$ which provides the “best” estimate $\hat{a}(t)$ from the measurement $r(t) = a(t) + n(t)$ having the covariance function $\kappa_r(t, u) = \kappa_a(t, u) + \kappa_n(t, u) + 2\kappa_{an}(t, u)$. Optimality is formulated as the minimization problem

$$\min_h E \left[\frac{1}{T} \int_0^T (a(t) - \hat{a}(t))^2 dt \right]$$

with

$$\hat{a}(t) = \int_0^t h(t, u)r(u)du$$

The corresponding necessary and sufficient condition for optimality is the following

$$\kappa_{ar}(t, u) = \int_0^T h(t, v)\kappa_r(u, v)dv, \quad 0 \leq t \leq T, \quad 0 < u < T$$

where $\kappa_{ar}(t, u)$ is the cross-covariance function between the signal to estimate, $a(t)$ and the measurement $r(t)$ (equal to $\kappa_a(t)$ if the signal and the noise are uncorrelated)

Wiener filtering treats stationary processes with knowledge of infinite past. Then, the optimal filter satisfies the following equation known as the Wiener-Hopf equation

$$\kappa_{ar}(\tau) = \int_0^\infty h(\nu)\kappa_r(\tau - \nu)d\nu, \quad 0 < \tau < \infty$$

Continuous and discrete solutions of this equation are presented in [Levinson, 1947, Wiener, 1949, Van Trees, 1968]. Early in the works of Wiener, it became evident that the

assumption of stationarity and knowledge of the entire past were incompatible with the majority of practical problems (as noted in [Bucy and Joseph, 1968]). Soon, these assumptions were relaxed to form another problem. For non-stationary problems, assuming that observations were known only over a finite time interval in the past, a theory emerged under the well known name of Kalman-Bucy filtering or Kalman filtering [Kalman, 1960b, Kalman and Bucy, 1961].

In the applications treated in this thesis, the Kalman filtering will be our main tool for embedded data fusion. In Chapter 2, we expose this technique. In Chapter 3, we make a connection with the observability properties and establish a result guaranteeing the convergence of Kalman filter using an easy to check differential observability condition (Theorem 10). These are the main contributions of this part.

Chapter 2 focuses on the Kalman filter and its different forms and implementations. The condition of convergence being well known for Linear-Time-Invariant (LTI) dynamics, Chapter 3 is dedicated to the observability property sufficient for exponential convergence of Kalman filter for Linear-Time-Varying (LTV) dynamics.

Chapter 2

A quick tour of Kalman filtering

Un rapide panorama sur le filtrage de Kalman

Ce chapitre rappelle les éléments-clefs du filtre de Kalman. La version continue de Kalman-Bucy est utilisée afin de mettre en évidence les grandes lignes pour établir l'optimalité du filtre de Kalman. Outre la version étendue du filtre, la version discrète est également détaillée avec les différentes problématiques de discrétisation et de multi-échantillonnage afférentes. Enfin, plusieurs développements visant à réduire d'une part la charge de calcul et, d'autre part, à améliorer la précision numérique sont présentés.

2.1 Kalman-Bucy filter

In the 1960s, Kalman [Kalman, 1960b] and Bucy [Kalman and Bucy, 1961] worked, first separately and then together, to derive a filter which is optimal in the sense of minimization of the covariance of the error estimation. It has the advantage of offering the possibility to deal with many more types of processes than the Wiener filter thanks to the introduction of a dynamic process model and, very importantly, it can be implemented in real time as data are treated as they become available. Historically, the continuous-time formulation of the Kalman filter is not the first which has emerged but, compared to the discrete-time version, it is relatively simpler to understand, and, interestingly, easier and shorter to derive. This is why the discrete-time Kalman filter is only presented later in this chapter, along with its different implementations.

The Kalman filter is an adaptive optimal filter for a LTV system described by a dynamic process model involving dynamics noise (or disturbance input) and an observation equation corrupted with noise. In the following, the matrices $A(t)$, $B(t)$, $C(t)$ are analytic.

$$\begin{cases} \dot{\mathbf{X}}(t) = A(t)\mathbf{X}(t) + B(t)\mathbf{U}(t) + \mathbf{w}(t) \\ \mathbf{Y}(t) = C(t)\mathbf{X}(t) + \mathbf{v}(t) \end{cases} \quad (2.1)$$

The dynamics noise $\mathbf{w}(t)$ is a white, zero-mean Gaussian continuous random process¹ of Power Spectral Density (PSD) matrix $Q(t)$ which is symmetric definite positive

$$\begin{cases} E[\mathbf{w}(t)] = 0 \\ E[\mathbf{w}(t)\mathbf{w}^T(\tau)] = Q(t)\delta(t - \tau) \end{cases} \quad (2.2)$$

where $\delta(t - \tau)$ is the Dirac function.

The measurement noise $\mathbf{v}(t)$ is a white, zero-mean Gaussian continuous random process of PSD matrix $R(t)$ which is symmetric definite positive.

$$\begin{cases} E[\mathbf{v}(t)] = 0 \\ E[\mathbf{v}(t)\mathbf{v}^T(\tau)] = R(t)\delta(t - \tau) \end{cases} \quad (2.3)$$

The PSD matrix $R(t)$ is taken definite positive even if singularity can be handled, see [Faurre, 1971, Gelb, 1974]. The noises are assumed white and zero-mean without loss of generality since biases and Markovian representation of coloration can be added to the state. Dynamics noises and measurement noises are assumed uncorrelated (their correlation is addressed in [Van Trees, 1968, Faurre, 1971, Gelb, 1974]).

$$E[\mathbf{w}(t)\mathbf{v}^T(\tau)] = 0 \quad (2.4)$$

The expected value and the covariance of the initial state are used to initialize the observer.

$$\begin{cases} \hat{\mathbf{X}}_0 \triangleq E[\mathbf{X}(0)] \\ P_0 \triangleq E[(\mathbf{X}(0) - \hat{\mathbf{X}}_0)(\mathbf{X}(0) - \hat{\mathbf{X}}_0)^T] \end{cases} \quad (2.5)$$

Theorem 1 (Kalman filter). *The unbiased optimal filter of system (2.1) in the sense of minimum covariance matrix P is given by the observer $\hat{\mathbf{X}}$, a.k.a. Kalman filter, computed with the Kalman gain $K(t)$, obtained from the covariance equation (or differential Riccati equation), initialized using Eq. (2.5).*

$$\begin{cases} \dot{\hat{\mathbf{X}}}(t) = A(t)\hat{\mathbf{X}}(t) + B(t)\mathbf{U}(t) + K(t)(\mathbf{Y}(t) - C(t)\hat{\mathbf{X}}(t)) \\ K(t) = P(t)C^T(t)R^{-1}(t) \\ \dot{P}(t) = A(t)P(t) + P(t)A^T(t) + Q(t) - P(t)C^T(t)R^{-1}(t)C(t)P(t) \end{cases} \quad (2.6)$$

The first equation can be interpreted as a combination of *propagation*, from the term found in the right-hand-side of (2.1)

$$A(t)\hat{\mathbf{X}}(t) + B(t)\mathbf{U}(t)$$

1. A white continuous random process is a mathematical object without physical realization since its energy is infinite. It can only be considered through a filter which limits the bandwidth of the process. The dynamic process model is a stochastic differential equation and should be formally considered by the yardstick of Itô integral or Stratonovich integral (see [Jazwinski, 1970]).

and *update* (or *correction*), using the difference between the measurements and the predicted value of the measurements (called innovation)

$$+K(t)(\mathbf{Y}(t) - C(t)\hat{\mathbf{X}}(t))$$

Similarly, the third equation combines the propagation of the covariance due to the dynamics and the modeling uncertainties²

$$A(t)P(t) + P(t)A^T(t) + Q(t)$$

with the correction supplied by the measurement,

$$-P(t)C^T(t)R^{-1}(t)C(t)P(t)$$

Proof of existence of such an observer (in the sense of definition of \hat{X} and P for all times) will be detailed in Chapter 3.3. For simplicity, the spirit of the proof of optimality [Alazard, 2006] is given here in the time-invariant case, that is to say the matrices A, B, C, M, Q and R are constant. Time-varying proofs are given in [Van Trees, 1968, Bucy and Joseph, 1968, Jazwinski, 1970, Gelb, 1974, Stengel, 1994].

Proof. The linear time-invariant system is

$$\begin{cases} \dot{\mathbf{X}}(t) = A\mathbf{X}(t) + B\mathbf{U}(t) + \mathbf{w}(t) \\ \mathbf{Y}(t) = C\mathbf{X}(t) + \mathbf{v}(t) \end{cases}$$

The filter is of the following form

$$\dot{\hat{\mathbf{X}}}(t) = A_f(t)\hat{\mathbf{X}}(t) + B_f(t)\mathbf{U}(t) + K_f(t)\mathbf{Y}(t)$$

Note $\tilde{\mathbf{X}}(t)$ the estimation error, $\tilde{\mathbf{X}}(t) = \mathbf{X}(t) - \hat{\mathbf{X}}(t)$

$$\begin{aligned} \dot{\tilde{\mathbf{X}}}(t) &= A\mathbf{X}(t) + B\mathbf{U}(t) + \mathbf{w}(t) - A_f(t)\hat{\mathbf{X}}(t) - B_f(t)\mathbf{U}(t) - K_f(t)(C\mathbf{X}(t) + \mathbf{v}(t)) \\ &= (A - K_f(t)C)\mathbf{X}(t) - A_f(t)\hat{\mathbf{X}}(t) + (B - B_f(t))\mathbf{U}(t) + \mathbf{w}(t) - K_f(t)\mathbf{v}(t) \\ &= \begin{cases} (A - K_f(t)C)\tilde{\mathbf{X}}(t) + (A - K_f(t)C - A_f(t))\hat{\mathbf{X}}(t) \\ +(B - B_f(t))\mathbf{U}(t) + \mathbf{w}(t) - K_f(t)\mathbf{v}(t) \end{cases} \end{aligned} \quad (2.7)$$

The input \mathbf{U} being deterministic and the measurement \mathbf{Y} being Gaussian, the observer $\hat{\mathbf{X}}$ is a Gaussian random variable (such as the state \mathbf{X}). The Kalman filter has to be unbiased and shall provide minimal variance. The expected value of the error estimation is

$$\frac{d}{dt}(E(\tilde{\mathbf{X}})(t)) = E(\dot{\tilde{\mathbf{X}}}(t)) = \begin{cases} (A - K_f(t)C)E(\tilde{\mathbf{X}}(t)) + (A - K_f(t)C - A_f(t))E(\hat{\mathbf{X}}(t)) \\ +(B - B_f(t))\mathbf{U}(t) \end{cases}$$

2. If \mathbf{U} contains an additive noise characterized by the PSD matrix Q_u , one has to add the term $B(t)Q_u(t)B^T(t)$ to take into account uncertainties brought by the input.

It appears that this expected value tends to 0, for all $U(t)$ and for all $E(\hat{\mathbf{X}}(t))$ if and only if

$$\begin{cases} A_f(t) = A - K_f(t)C \\ B_f(t) = B \\ A - K_f(t)C \text{ yields an asymptotically stable LTV dynamics} \end{cases} \quad (2.8)$$

The observer takes the following form

$$\dot{\hat{\mathbf{X}}}(t) = A\hat{\mathbf{X}}(t) + BU(t) + K_f(t)(Y(t) - C\hat{\mathbf{X}}(t))$$

The optimal minimum variance filter is obtained for the gain which minimizes the error estimation variance. The criterion $J(t)$ to be minimized is as follows

$$J(t) = \sum E(\tilde{\mathbf{X}}_i^2(t)) = E(\tilde{\mathbf{X}}^T(t)\tilde{\mathbf{X}}(t)) = \text{trace}(E(\tilde{\mathbf{X}}(t)\tilde{\mathbf{X}}^T(t)))$$

Note $P(t) = E(\tilde{\mathbf{X}}(t)\tilde{\mathbf{X}}^T(t))$ the error estimation covariance matrix. Combining Eq. (2.8) with Eq. (2.7), one gets

$$\dot{\tilde{\mathbf{X}}}(t) = (A - K_f(t)C)\tilde{\mathbf{X}}(t) + \mathbf{w}(t) - K_f(t)\mathbf{v}(t) \quad (2.9)$$

Consider the transition matrix $\Phi_K(t, s)$ of the LTV dynamics $\dot{\tilde{\mathbf{X}}}(t) = (A - K_f(t)C)\tilde{\mathbf{X}}(t)$

$$\frac{\partial \Phi_K}{\partial t}(t, s) = (A - K_f(t)C)\Phi_K(t, s), \quad \Phi_K(t, t) = I \quad (2.10)$$

The solution $\tilde{\mathbf{X}}(t)$ can be derived

$$\begin{aligned} \tilde{\mathbf{X}}(t) &= \Phi_K(0, t)\tilde{\mathbf{X}}_0 + \int_0^t \Phi_K(\tau, t)(\mathbf{w}(\tau) - K_f(\tau)\mathbf{v}(\tau))d\tau \\ &= \Phi_K(0, t) \left(\tilde{\mathbf{X}}_0 + \int_0^t \Phi_K(\tau, 0)(\mathbf{w}(\tau) - K_f(\tau)\mathbf{v}(\tau))d\tau \right) \end{aligned}$$

Then the covariance matrix can be derived,

$$\begin{aligned} P(t) &= E \left(\begin{array}{c} \Phi_K(0, t) \left(\tilde{\mathbf{X}}_0 + \int_0^t \Phi_K(\tau, 0)(\mathbf{w}(\tau) - K_f(\tau)\mathbf{v}(\tau))d\tau \right) \\ \left(\tilde{\mathbf{X}}_0^T + \int_0^t (\mathbf{w}^T(\tau) - \mathbf{v}^T(\tau)K_f^T(\tau))\Phi_K^T(\tau, 0)d\tau \right) \Phi_K^T(0, t) \end{array} \right) \\ &= \Phi_K(0, t)E \left(\begin{array}{c} \tilde{\mathbf{X}}_0\tilde{\mathbf{X}}_0^T \\ + \iint_0^t \Phi_K(\tau, 0) \left(\begin{array}{c} (\mathbf{w}(\tau) - K_f(\tau)\mathbf{v}(\tau)) \\ (\mathbf{w}^T(s) - \mathbf{v}^T(s)K_f^T(s)) \end{array} \right) \Phi_K^T(s, 0)d\tau ds \end{array} \right) \Phi_K^T(0, t) \end{aligned}$$

From Eq. (2.2-2.5), the cross-products vanish. One then gets

$$P(t) = \Phi_K(0, t) \left(P_0 + \int_0^t \Phi_K(\tau, 0)(Q + K_f(\tau)RK_f^T(\tau))\Phi_K^T(\tau, 0)d\tau \right) \Phi_K^T(0, t)$$

Finally, the derivative can be obtained

$$\begin{aligned}
 \dot{P}(t) &= \begin{vmatrix} (A - K_f(t)C)P(t) + P(t)(A - K_f(t)C)^T \\ + \Phi_K(0, t)\Phi_K(t, 0)(Q + K_f(t)RK_f^T(t))\Phi_K^T(t, 0)\Phi_K^T(0, t) \end{vmatrix} \\
 &= (A - K_f(t)C)P(t) + P(t)(A - K_f(t)C)^T + Q + K_f(t)RK_f^T(t) \\
 &= \begin{vmatrix} AP(t) + P(t)A^T + Q - P(t)C^T R^{-1}CP(t) \\ + (K_f(t) - P(t)C^T R^{-1})R(K_f(t) - P(t)C^T R^{-1})^T \end{vmatrix}
 \end{aligned}$$

To minimize the covariance matrix over time, it is sufficient to minimize the derivative above. Since the term with $K_f(t)$ is quadratic, the best choice is the following gain, the Kalman gain

$$K_f(t) = P(t)C^T R^{-1}$$

□

2.2 Extended Kalman filter

A classical extension of the Kalman filter technique is known as the Extended Kalman Filter (EKF). Consider the following nonlinear system

$$\begin{cases} \dot{\mathbf{X}}(t) = f(\mathbf{X}(t), \mathbf{U}(t), \mathbf{w}(t), t) \\ \mathbf{Y}(t) = h(\mathbf{X}(t), t) + \mathbf{v}(t) \end{cases} \quad (2.11)$$

The Kalman-Bucy filter equations have been adapted to handle nonlinear dynamics (see [Gelb, 1974, Stengel, 1994]): state propagation and measurement remain nonlinear, but update and covariance propagation are realized with linearization around the actual estimate, dropping out the higher terms of Taylor series. This simply gives the EKF.

$$\begin{cases} \dot{\hat{\mathbf{X}}}(t) = f(\hat{\mathbf{X}}(t), \mathbf{U}(t), t) + K(t)(\mathbf{Y}(t) - h(\hat{\mathbf{X}}(t), t)) \\ K(t) = P(t)C^T(t)R^{-1}(t) \\ \dot{P}(t) = A(t)P(t) + P(t)A^T(t) + M(t)Q(t)M^T(t) - P(t)C^T(t)R^{-1}(t)C(t)P(t) \end{cases}$$

with

$$\begin{cases} A(t) = \frac{\partial f}{\partial \mathbf{X}}(\hat{\mathbf{X}}(t), \mathbf{U}(t), t) \\ C(t) = \frac{\partial h}{\partial \mathbf{X}}(\hat{\mathbf{X}}(t), t) \\ M(t) = \frac{\partial f}{\partial \mathbf{w}}(\hat{\mathbf{X}}(t), \mathbf{U}(t), t) \end{cases}$$

Other extensions have been considered, e.g. the Iterated Extended Kalman Filter (IEKF) [Denham and Pines, 1966], the High Gain Extended Kalman Filter (HGEKF) [Deza, 1991, Deza et al., 1992], the Pseudo Kalman Filter (PKF) [Viéville and Sander, 1992], the Unscented Kalman Filter (UKF) [Julier and Uhlmann, 1997, Wan and Van Der Merwe, 2000], or, recently, the Invariant Extended Kalman Filter (IEKF) [Bonnabel et al., 2008], the Adaptive High Gain Extended Kalman Filter (AEKF) [Boizot, 2010].

2.3 Discrete-time Kalman filter

We now turn to the discrete-time version of the Kalman filter. This is mostly useful in view of implementation. Consider the following discrete-time system

$$\begin{cases} \mathbf{X}(k) = F(k-1)\mathbf{X}(k-1) + G(k-1)\mathbf{U}(k-1) + \mathbf{w}(k-1) \\ \mathbf{Y}(k) = H(k)\mathbf{X}(k) + \mathbf{v}(k) \end{cases} \quad (2.12)$$

The dynamics noise $\mathbf{w}(k)$ is a white, zero-mean Gaussian discrete random process of covariance matrix $W(k)$ which is symmetric definite positive.

$$\begin{cases} E[\mathbf{w}(k)] = 0 \\ E[\mathbf{w}(k)\mathbf{w}^T(k')] = W(k)\delta_{k,k'} \end{cases} \quad (2.13)$$

where $\delta_{k,k'}$ is the Kronecker delta function.

The measurement noise $\mathbf{v}(k)$ is a white, zero-mean Gaussian discrete random process of covariance matrix $V(k)$ which is symmetric definite positive.

$$\begin{cases} E[\mathbf{v}(k)] = 0 \\ E[\mathbf{v}(k)\mathbf{v}^T(k')] = V(k)\delta_{k,k'} \end{cases} \quad (2.14)$$

The dynamics noise and the measurement noise are assumed to be uncorrelated.

$$E[\mathbf{w}(k)\mathbf{v}^T(k')] = 0$$

The expected value and the covariance of the initial state are used to initialize the observer

$$\begin{cases} E[\mathbf{X}(0)] \triangleq \hat{\mathbf{X}}_0 \\ E[(\mathbf{X}(0) - \hat{\mathbf{X}}_0)(\mathbf{X}(0) - \hat{\mathbf{X}}_0)^T] \triangleq P_0 \end{cases}$$

Theorem 2 (Discrete Kalman filter). *The unbiased optimal filter of system (2.12) in the sense of minimum variance is given by the observer $\hat{\mathbf{X}}$ computed with the Kalman gain $K(k)$. This observer can be decomposed in two steps. The first one, indicated by the subscript p , is called propagation or extrapolation, it relies on the known dynamics of the system. The second one, indicated by the subscript u , is called update or correction and uses the measurement³.*

$$\text{Propagation} \begin{cases} \mathbf{X}_p(k) = F(k-1)\mathbf{X}_u(k-1) + G(k-1)\mathbf{U}(k-1) \\ P_p(k) = F(k-1)P_u(k-1)F^T(k-1) + W(k-1) \end{cases} \quad (2.15)$$

$$\text{Update} \begin{cases} K(k) = P_p(k)H^T(k)(H(k)P_p(k)H^T(k) + V(k))^{-1} \\ \mathbf{X}_u(k) = \mathbf{X}_p(k) + K(k)(\mathbf{Y}(k) - H(k)\mathbf{X}_p(k)) \\ P_u(k) = (P_p^{-1}(k) + H^T(k)V^{-1}(k)H(k))^{-1} \end{cases} \quad (2.16)$$

The complete derivation of the discrete Kalman filter as the optimal minimum covariance filter is based on the same arguments as the continuous Kalman filter and can be found in [Stengel, 1994]. Further developments presented in the following parts can be found in [Jazwinski, 1970, Stengel, 1994].

3. Hat superscript is omitted when subscript is present to simplify the reading.

2.3.1 Sampled Linear-Time-Invariant system

We briefly recall here the sampling step allowing to turn a continuous-time LTI dynamics into a discrete-time system. Consider a sampled LTI system whose dynamics is given by Eq. (2.1). The sampling period of the measurement \mathbf{Y} is noted Δt and zero-order hold is applied on deterministic signal \mathbf{U} . To the continuous time $k\Delta t$, corresponds the discrete index k .

The general solution of the continuous system allows to write the propagation during the sampling period

$$\begin{aligned}\mathbf{X}(k\Delta t) &= e^{A\Delta t}\mathbf{X}((k-1)\Delta t) + \left(\int_{(k-1)\Delta t}^{k\Delta t} e^{A(k\Delta t-\tau)}(B\mathbf{U}(k-1) + \mathbf{w}(\tau))d\tau \right) \\ &= e^{A\Delta t}\mathbf{X}((k-1)\Delta t) + \int_0^{\Delta t} e^{A\tau}Bd\tau\mathbf{U}(k-1) + \int_0^{\Delta t} e^{A\tau}\mathbf{w}(k\Delta t-\tau)d\tau\end{aligned}$$

The measurement equation is as follows

$$\mathbf{Y}(k\Delta t) = C\mathbf{X}(k\Delta t) + \mathbf{v}(k\Delta t)$$

The terms of Eq. (2.12) can be identified as

$$F = e^{A\Delta t}, \quad G = \int_0^{\Delta t} e^{A\tau}Bd\tau, \quad H = C$$

The measurement noise equivalence relies on $\mathbf{v}(k\Delta t) = \mathbf{v}(k)$. As a consequence of the sampling, the PSD matrix of the continuous process is related to the covariance of the discrete process by the following equation ⁴

$$V = R/\Delta t$$

Concerning the dynamics noise, the equivalence is more straightforward since the continuous random process is filtered by the dynamics equation.

$$\begin{aligned}W &= E(\mathbf{w}(k-1)\mathbf{w}^T(k-1)) \\ &= E\left(\int_0^{\Delta t} e^{A\tau}\mathbf{w}(k\Delta t-\tau)d\tau \left(\int_0^{\Delta t} e^{A\tau}\mathbf{w}(k\Delta t-\tau)d\tau \right)^T \right) \\ &= E\left(\int_0^{\Delta t} \int_0^{\Delta t} e^{A\tau}\mathbf{w}(k\Delta t-\tau)\mathbf{w}^T(k\Delta t-s)e^{A^T s}d\tau ds \right) \\ &= \int_0^{\Delta t} \int_0^{\Delta t} e^{A\tau}E(\mathbf{w}(k\Delta t-\tau)\mathbf{w}^T(k\Delta t-s))e^{A^T s}d\tau ds \\ &= \int_0^{\Delta t} \int_0^{\Delta t} e^{A\tau}Q\delta(\tau-s)M^T e^{A^T s}d\tau ds \\ &= \int_0^{\Delta t} e^{A\tau}Qe^{A^T \tau}d\tau\end{aligned}$$

4. For further explanation on the meaning of a continuous white random process and equivalence with discrete random process, see [Jazwinski, 1970, Gelb, 1974].

If the sampling period is sufficiently short compared to the time constant of the considered system, the following approximation can be used

$$W = Q\Delta t$$

Sampled LTI system is presented here to simplify the writing but the same derivation can be realized for a LTV system. In particular, previous correspondences can also be used to formulate an EKF.

$$\begin{aligned} F(k-1) &= \exp\left(\frac{\partial f}{\partial \mathbf{X}}(\mathbf{X}_e(k-1), \mathbf{U}(k-1), (k-1)\Delta t)\Delta t\right) \\ G(k-1) &= \left| \int_0^{\Delta t} \exp\left(\frac{\partial f}{\partial \mathbf{X}}(\mathbf{X}_e(k-1), \mathbf{U}(k-1), (k-1)\Delta t)\tau\right) d\tau \right. \\ &\quad \left. \times \frac{\partial f}{\partial \mathbf{U}}(\mathbf{X}_e(k-1), \mathbf{U}(k-1), (k-1)\Delta t) \right. \\ H(k) &= \frac{\partial h}{\partial \mathbf{X}}(\mathbf{X}_p(k), k\Delta t) \end{aligned}$$

2.3.2 Mixed continuous-discrete-time filtering

The combination of continuous Kalman filter and discrete Kalman filter is possible and can be used when the dynamical system is described by a continuous equation and the measurement occurs as discrete events.

$$\begin{cases} \dot{\mathbf{X}}(t) = A(t)\mathbf{X}(t) + B(t)\mathbf{U}(t) + \mathbf{w}(t) \\ \mathbf{Y}(k) = H(k)\mathbf{X}(k) + \mathbf{v}(k) \end{cases}$$

Both noises remain uncorrelated and defined by Eq. (2.2,2.14).

In this case, one has to consider continuous propagation of the estimate and of the covariance between two discrete updates.

$$\begin{cases} \dot{\hat{\mathbf{X}}}(t) = A(t)\hat{\mathbf{X}}(t) + B(t)\mathbf{U}(t) \\ \dot{P}(t) = A(t)P(t) + P(t)A^T(t) + Q(t) & \text{for } (k-1)\Delta t \leq t < k\Delta t \\ K(k) = P_p(k)H^T(k) (H(k)P_p(k)H^T(k) + V(k))^{-1} \\ \mathbf{X}_u(k) = \mathbf{X}_p(k) + K(k) (\mathbf{Y}(k) - H(k)\mathbf{X}_p(k)) \\ P_u(k) = (P_p^{-1}(k) + H^T(k)V^{-1}(k)H(k))^{-1} \end{cases}$$

with continuation guaranteed by

$$\begin{aligned} \hat{\mathbf{X}}((k-1)\Delta t) &= \mathbf{X}_u(k-1), & P((k-1)\Delta t) &= P_u(k-1) \\ \mathbf{X}_p(k) &= \hat{\mathbf{X}}(k\Delta t), & P_p(k) &= P(k\Delta t) \end{aligned}$$

The merits of the continuous propagation, which is actually computed using a discretization scheme, remains in the chosen algorithm: the propagation step can be realized with a shorter fixed-step (shorter than the sampling period of the measurement) or with an adaptive step such

as in a Runge-Kutta algorithm, which is beneficial if the time elapsed between two measurements is large compared to the characteristic time of the dynamics.

The main difference with the discrete-time propagation lies in the order of the operations : continuous propagation is a discretized exact equation (high order terms in Δt are simplified in the last operation) although discrete propagation is an exact equation applied to a discretized system (high order terms in Δt are simplified in the calculus of the transition matrix)⁵.

In particular, the continuous-discrete formulation can reveal handy in the case of non-linear dynamics (it is named Hybrid Extended Kalman Filter (HEKF) [Stengel, 1994]). State propagation is realized from the non-linear dynamics, integrated with an adapted scheme

$$\begin{aligned}\hat{\mathbf{X}}(t) &= \mathbf{X}_u(k-1) + \int_{(k-1)\Delta t}^t f(\hat{\mathbf{X}}(\tau), \mathbf{U}(\tau), \tau) d\tau \\ \mathbf{X}_p(k) &= \hat{\mathbf{X}}(k\Delta t)\end{aligned}$$

The covariance propagation is computed with the system linearized on each value of the interval of propagation

$$\begin{aligned}P(t) &= P_u(k-1) + \int_{(k-1)\Delta t}^t A(\tau)P(\tau) + P(\tau)A^T(\tau) + M(\tau)Q(\tau)M^T(\tau) d\tau \\ \text{with } A(\tau) &= \frac{\partial f}{\partial \mathbf{X}}(\hat{\mathbf{X}}(\tau), \mathbf{U}(\tau), \tau) \text{ and } M(\tau) = \frac{\partial f}{\partial \mathbf{w}}(\hat{\mathbf{X}}(\tau), \mathbf{U}(\tau), \tau) \\ P_p(k) &= P(k\Delta t)\end{aligned}$$

The discrete update step remains unchanged, as presented previously.

2.3.3 Multi-rates Kalman filter

The multi-rates Kalman filter is used in the case of flow of measurements are produced at different rates or if the dynamics is strongly non-linear and its characteristic time is shorter than the measurement period. The propagation is computed using the shortest period (i.e. a sampling rate high enough) and the update occurs only when a new measurement occurs. For example, consider the attitude estimation of a rigid body in rotation, equipped with gyrometers at 100 Hz and accelerometers at 10 Hz. The main clock of the filter shall be set at 100 Hz. At each step, propagation is realized. One time out of ten, update is computed from both measurements, otherwise only gyrometers are used⁶.

In case of multi-rates Kalman filter, one should pay close attention to the value of covariance matrices, depending on whether they have been found in a sensor data sheet or stem from experimental evaluations. Further details can be found in [Gelb, 1974].

5. This remark only apply to systems with continuous dynamics.

6. Omit the fast measurement and consider only the slow one when it occurs can be a way to reduce the computational burden, according to the sequential processing methodology presented in Section 2.4.1

2.3.4 Remarks on the units

In discrete-time descriptions, W and V are covariance matrices. In continuous-time descriptions, Q is a PSD matrix of a noise homogeneous to the derivative of the state whereas R is a spectral density matrix of a noise homogeneous to the measurement. In both cases, P is a covariance matrix. The units of the matrices are as follows

$$\begin{aligned} [W] &= [\mathbf{X}]^2 & [V] &= [\mathbf{Y}]^2 \\ [Q] &= ([\mathbf{X}].s^{-1})^2.s = [\mathbf{X}]^2.s^{-1} & [R] &= [\mathbf{Y}]^2.s \\ [P] &= [\mathbf{X}]^2 \end{aligned}$$

2.4 Computational burden and numerical accuracy

For mathematical consistency and numerical stability, it is of paramount importance that the error estimation covariance matrix P remains definite positive. Several methods [Kaminski et al., 1971, Anderson and Moore, 1979, Rao and Durrant-Whyte, 1991, Stengel, 1994, Olfati-Saber, 2005] to propagate and update the matrix P have been developed to improve the numerical accuracy while keeping the computational burden low. In particular, efforts have been focused on the matrix inversions in the update step (2.16) which is the most time-consuming operation of the filter.

As can be shown in [Stengel, 1994], by manipulation of the update equations in Eq. (2.16) and thanks to the matrix inversion lemma, also known as Sherman-Morrison-Woodbury formula [Nocedal and Wright, 1999], the following form of the update of the covariance matrix can be found

$$P_u(k) = (\mathbb{1}_n - K(k)H(k))P_p(k)$$

The two embedded inversions of matrices of size n have vanished and have been favorably replaced with products.

2.4.1 Sequential processing

The Kalman gain equation is essentially based on a matrix inversion of size m . The equations in Eq. (2.16) realize a simultaneous processing of the measurements. By contrast, if the measurement noise matrix V can be decomposed under a block-diagonal form, sequential processing of the measurements can be considered⁷. Consider the matrix V as follows

$$V = \left[\begin{array}{c|c|c|c|c} V_1 & & & & \\ \hline & V_2 & & & \\ \hline & & \ddots & & \\ \hline & & & V_{l-1} & \\ \hline & & & & V_l \end{array} \right]$$

7. Sequential processing is also adapted to multi-rates measurements since each block can be computed according to the occurrence of new measurements.

Each measurement block, indexed by $i \in [1..l]$, can be computed separately in a loop, with H_i the corresponding rows of H . For each i ,

$$\begin{aligned} K_i(k) &= P_{i-1}(k)H_i^T(k) \left(H_i(k)P_{i-1}(k)H_i^T(k) + V_i(k) \right)^{-1} \\ P_i(k) &= (\mathbf{1}_n - K_i(k)H_i(k))P_{i-1}(k) \end{aligned}$$

The loop is initialized with $P_0(k) = P_p(k)$ and the result is $P_u(k) = P_l(k)$. The state update can be computed outside the loop with the following equation, with the block-inversion of V ,

$$\mathbf{X}_u(k) = \mathbf{X}_p(k) + P_u(k)H^T(k)V^{-1}(k) (\mathbf{Y}(k) - H(k)\mathbf{X}_p(k))$$

The main interest of the sequential processing is to replace a matrix inversion of size m by l matrix inversions of lower size, possibly by m scalar inversions if the matrix V is diagonal. This can reveal important since the inversion of a $m \times m$ matrix requires $O(m^3)$ operations.

2.4.2 Joseph form

In spite of a larger computational burden, the Joseph form can be used to preserve positive-definiteness and symmetry of the covariance matrix.

$$P_u(k) = (\mathbf{1}_n - K(k)H(k))P_p(k)(\mathbf{1}_n - K(k)H(k))^T + K(k)V(k)K^T(k)$$

2.4.3 Information filter

The conventional Kalman filter is based on the propagation and update of the covariance matrix (size n) thanks to Kalman gain computed from matrix inversion of size m . It appears that the previously discussed sequential processing is an efficient solution if the noise covariance matrix can be block-diagonalized. Yet, an alternative form can be useful when the state size n is small compared to the measurement size m , for example, in case of networked (possibly redundant) sensors [Rao and Durrant-Whyte, 1991, Murray et al., 2002, Olfati-Saber, 2005].

This alternative form is called Information Filter (IF) because, instead of the covariance matrix, it is the information matrix (inverse of the covariance matrix) which is updated and propagated.

$$I_p(k) = P_p^{-1}(k) \quad \text{and} \quad I_u(k) = P_u^{-1}(k)$$

Note $\Lambda(k) = (F(k)P_u(k)F^T(k))^{-1}$ and apply the matrix inversion lemma to Eq. (2.15) to obtain

$$I_p(k) = (\mathbf{1}_n - \Lambda(k)(\Lambda(k) + W^{-1}(k))^{-1}) \Lambda(k) \tag{2.17}$$

From Eq. (2.16),

$$I_u(k) = I_p(k) + H^T(k)V^{-1}(k)H(k) \tag{2.18}$$

To obtain equations more adapted to distributed filtering, instead of propagating the state, the following quantities are considered

$$\mathbf{X}_p(k) = I_p(k)\mathbf{X}_p(k) \quad \text{and} \quad \mathbf{X}_u(k) = I_u(k)\mathbf{X}_u(k)$$

From the propagation and update state equations,

$$\mathbf{X}_p(k) = (\mathbf{1}_n - \Lambda(k)(\Lambda(k) + W^{-1}(k))^{-1}) F^{-T}(k) \mathbf{X}_u(k-1) + I_p(k) G(k) \mathbf{U}(k) \quad (2.19)$$

$$\mathbf{X}_u(k) = \mathbf{X}_p(k) + H^T(k) V^{-1}(k) \mathbf{Y}(k) \quad (2.20)$$

The information filter consists in Eq. (2.17-2.18,2.19-2.20) without need to explicitly compute the Kalman gains. The propagation step uses two matrix inversions of size n although the update step needs only one matrix inversion of size m (which can be outside the loop if the noise is stationary). The additive form of the “state” update in Eq. (2.20) is well suited to networked sensors since each sensor can send its part of information without needs of knowing the measurements of the other sensors. This particular form of the IF is named Decentralized or Distributed Kalman Filter (DKF). One counterpart of the information form is that it can not be initialized with a perfect knowledge of the state (comparatively, the conventional Kalman filter can not be initialized with infinite uncertainty).

2.4.4 Square-root filter

The square-root form of the Kalman filter was developed to manage ill-conditioned estimation problems, that is to say when the dynamics process contains both slow and fast modes, or when the noise covariance matrices are themselves ill-conditioned (very accurate measurements mixed with very noisy ones). The ability to deal with high condition number for covariance matrix is limited by the number of significant digits of the processor in charge of the computation of the algorithm. Interestingly, to a double precision symmetric positive definite matrix, corresponds a single precision square-root matrix. Reformulating the Kalman filter in terms of square roots allows one to improve the accuracy or equivalently to reduce the number of bits to be handled by the processor. Moreover, using square-root formulations also guarantees that the covariance matrix is numerically symmetric and positive-semidefinite.

Several forms of square-root filters exist, such as Potter, Schmidt or Kaminski formulations. The interested reader could refer to [Kaminski et al., 1971, Morf and Kailath, 1975, Anderson and Moore, 1979] to get the corresponding filter derivations. Interestingly, the square-root form can be adapted to previously mentioned extensions of the Kalman filter as the Square-Root Unscented Kalman Filter (SR-UKF) [Van der Merwe and Wan, 2001] or the Square-Root Information Filter (SR-IF) [Bierman et al., 1990]. Computational burden and accuracy comparisons of these methods can be found in [Kaminski et al., 1971, Verhaegen and Van Dooren, 1986].

Chapter 3

Observability properties and their roles in the convergence of Kalman filters

Propriétés d'observabilité et leurs rôles pour la convergence du filtre de Kalman

Ce chapitre rappelle dans un premier temps les propriétés usuellement utilisées pour démontrer la convergence du filtre de Kalman. La propriété d'observabilité complète et uniforme (UCO) étant souvent difficile à démontrer, une définition d'observabilité différentielle est proposée comme condition suffisante à la précédente UCO. Sur cette base, l'existence du gain de Kalman et la convergence exponentielle du filtre sont prouvés et une borne de convergence est proposée.

The convergence of the Kalman filter can be guaranteed by some observability properties of the system (2.1). Generally (see e.g. [Gadre, 2007]), it is considered that observability over a finite time interval could be considered but in fact, Uniform and Complete Observability (UCO) has to be established (Section 3.1) to guarantee the convergence of the Kalman filter for all times (Section 3.3). The UCO can be difficult to proof, therefore, we study point-wise observability and more precisely Differential Observability (DO) as sufficient condition for UCO (Section 3.2).

3.1 Uniform and Complete Observability

This property follows from the Complete Observability (CO) and the Uniform Observability (UO) recalled below for convenience.

Note $\Phi(s, t)$ the transition matrix associated to the LTV dynamics (2.1)

$$\frac{\partial \Phi}{\partial t}(t, s) = A(t)\Phi(t, s), \quad \Phi(t, t) = I \quad (3.1)$$

Definition 1. [Bucy and Joseph, 1968] *The system (2.1) is CO if and only if every present state $x(t)$ can be determined when $A(s)$ and $C(s)$ and $y(s)$ for $s \in (t_0, t)$ are known for some $t_0(t) < t$.*

Theorem 3. [Bucy and Joseph, 1968] The system (2.1) is CO if and only if for every t there exists a $t_0(t) < t$ such that

$$W^*(t_0, t) = \int_{t_0}^t \Phi^T(s, t) C^T(s) C(s) \Phi(s, t) ds$$

is positive definite. The application $W^*(t_0, t)$ is the reconstructibility Grammian.

Definition 2. [Bucy and Joseph, 1968] The system (2.1) is UO if and only if there exists γ, δ, σ so that for every t , $W^*(t - \sigma, t)$ is positive definite and

$$0 < \gamma I \leq W^*(t - \sigma, t) \leq \delta I$$

The discussed UCO property is defined below.

Definition 3. [Kalman, 1960a, Bucy and Joseph, 1968] The system (2.1) is UCO if the following relations hold for all t :

$$\begin{aligned} (i) \quad & 0 < \alpha_0(\sigma) I \leq W^*(t - \sigma, t) \leq \alpha_1(\sigma) I \\ (ii) \quad & 0 < \beta_0(\sigma) I \leq \Phi^T(t - \sigma, t) W^*(t - \sigma, t) \Phi(t - \sigma, t) \leq \beta_1(\sigma) I \end{aligned}$$

where σ is a fixed constant .

In the case of bounded matrices, the following theorem provides a simpler necessary and sufficient condition.

Theorem 4. [Silverman and Anderson, 1968, Tsakalis and Ioannou, 1993] A bounded system $[A(t), B(t), C(t)]$ is UCO if and only if there exists $\sigma > 0$ such that for all t ,

$$W^*(t - \sigma, t) \geq \alpha_0(\sigma) I > 0$$

Determining whether the uniform lower boundedness of $W^*(t - \sigma, t)$ holds is usually considered as a very difficult task. In general, computing the transition matrix is involved and computing $W^*(t - \sigma, t)$ is hardly tractable. Much more conveniently, a point-wise investigation of the observability of the analytic system (2.1) can yield interesting conclusions. This is the subject we now address.

3.2 Differential Observability

In [Silverman and Meadows, 1967], the possibility of establishing observability from the study of the observability matrix defined below has been investigated. A theorem exposing a rank condition to prove the CO on an interval (see also [Kailath, 1980]) is as follows.

Definition 4. [Silverman and Meadows, 1967] The observability matrix $Q_o(t)$ is defined below, where n is the dimension of x :

$$\begin{cases} Q_o(t) = [Q_0(t) & Q_1(t) & \cdots & Q_{n-1}(t)] \\ Q_0(t) = C^T(t) \\ Q_{i+1}(t) = \dot{Q}_i(t) + A^T(t)Q_i(t) \end{cases}$$

Theorem 5. [Silverman and Meadows, 1967] The system (2.1) is CO on the interval (t_0, t_1) if $Q_o(t)$ has rank n for some $t \in (t_0, t_1)$.

Interestingly, in the same paper [Silverman and Meadows, 1967], the notion of UO on an interval is also considered: the difficulty to find an uniform (independent of the time) bound for the observability Grammian is alleviated by the knowledge of bounds on the time.

Definition 5. [Silverman and Meadows, 1967] The system (2.1) is said to be UO on the interval (t_0, t_1) if $Q_o(t)$ has rank n for all $t \in (t_0, t_1)$.

We generalize this approach by considering the following sufficient condition for UCO (in the sense of Definition 3) which we simply refer to as Differential Observability (DO).

Definition 6. The system (2.1) is said to be DO if there exists $\mu > 0$, $m \in \mathbb{N}$ such that for all t :

$$\mathbb{O}(t) = (Q_0(t) \quad \cdots \quad Q_m(t)) \begin{pmatrix} Q_0^T(t) \\ \vdots \\ Q_m^T(t) \end{pmatrix} \geq \mu I > 0 \quad (3.2)$$

Theorem 6. [Bristeau et al., 2010b] The bounded system (2.1) is UCO if it is DO.

Proof. To a pair (x, s) , we associate $x_s(t)$ the solution of

$$\dot{x}_s(t) = A(t)x_s(t), \quad x_s(s) = x$$

So, we have $x_s(t) = \Phi(t, s)x$ and $y_s(t) = C(t)x_s(t)$.

The function $t \mapsto y_s(t)$ verifies $y_s^{(i)}(t) = Q_i^T(t)x_s(t)$ where the subscript $^{(i)}$ stands for the i -th derivative.

Since the system (2.1) is bounded, there exist $(a, c) \in \mathbb{R}$ such that

$$|A(t)| \leq a \quad , \quad |Q_i(t)| \leq c \quad \forall t, \forall i \in \{0, m\}$$

It means that, for all (s, t) ,

$$\exp(-a|t-s|) \leq |\Phi(t, s)| \leq \exp(a|t-s|)$$

and then

$$|y_s(t)| \leq c \exp(a|t-s|)|x| \quad (3.3)$$

First, consider the Taylor approximation with integral form of the remainder term applied to $y_s(t)$

$$y_s(t) = \mathcal{P}_s(t-s) + \mathcal{R}_s(t,s)$$

$$\text{with } \mathcal{P}_s(t-s) = \sum_{i=0}^m \frac{(t-s)^i}{i!} y_s^{(i)}(s) \text{ and } \mathcal{R}_s(t,s) = \int_s^t \frac{(t-r)^m}{m!} y_s^{(m+1)}(r) dr$$

One has

$$\int_{-\infty}^s \exp(-\lambda[s-t]) |y_s(t)|^2 dt \geq T_{\mathcal{P}} - T_{\mathcal{R}}$$

$$\text{where } T_{\mathcal{P}} = \frac{1}{2} \int_{-\infty}^s \exp(-\lambda[s-t]) |\mathcal{P}_s(t-s)|^2 dt \text{ and } T_{\mathcal{R}} = \int_{-\infty}^s \exp(-\lambda[s-t]) |\mathcal{R}_s(t,s)|^2 dt$$

It is desired to find a lower bound for $T_{\mathcal{P}}$

$$T_{\mathcal{P}} = \int_{-\infty}^s \exp(-\lambda[s-t]) \left| \sum_{i=0}^m \frac{(t-s)^i}{i!} y_s^{(i)}(s) \right|^2 dt = \frac{1}{\lambda} \int_{-\infty}^0 \exp(\tau) \left| \sum_{i=0}^m \frac{\tau^i}{i!} \frac{y_s^{(i)}(s)}{\lambda^i} \right|^2 d\tau$$

One can see that $T_{\mathcal{P}}$ is a non negative quadratic form in $y_s(s), \dots, y_s^{(m)}(s)$

$$T_{\mathcal{P}} = \frac{1}{\lambda} \begin{pmatrix} y_s^T(s) & \frac{y_s^{(1)T}(s)}{\lambda} & \dots & \frac{y_s^{(m)T}(s)}{\lambda^m} \end{pmatrix} \Xi \begin{pmatrix} \frac{y_s(s)}{\lambda} \\ \frac{y_s^{(1)}(s)}{\lambda} \\ \vdots \\ \frac{y_s^{(m)}(s)}{\lambda^m} \end{pmatrix}$$

$$\text{with } \Xi_{(i,j)} = (-1)^{i+j} C_{i+j-2}^{i-1}$$

Moreover, the integral $T_{\mathcal{P}}$ is null if and only if all the coefficients of the polynomial in τ under the integral are null, that is to say, if and only if all the components of all the derivatives $y_s^{(i)}(s)$ are null. So, the matrix Ξ is positive definite and there exists $\alpha > 0$ such that

$$T_{\mathcal{P}} \geq \frac{\alpha}{\lambda^{2m+1}} \sum_{i=0}^m |y_s^{(i)}(s)|^2$$

Otherwise, one has

$$x^T \mathbb{O}(s) x = \begin{pmatrix} y_s(s) & \dots & \dot{y}_s^{(m)}(s) \end{pmatrix} \begin{pmatrix} y_s^T(s) \\ \vdots \\ \dot{y}_s^{(m)T}(s) \end{pmatrix} = \sum_{i=0}^m |y_s^{(i)}(s)|^2$$

So, with Eq. (3.2), one can conclude

$$T_{\mathcal{P}} \geq \frac{\alpha\mu}{\lambda^{2m+1}} |x|^2 \quad (3.4)$$

Concerning the term $T_{\mathcal{R}}$,

$$T_{\mathcal{R}} = \frac{1}{\lambda} \int_{-\infty}^0 \exp(\tau) \left| \mathcal{R}_s \left(\frac{\tau}{\lambda} + s, s \right) \right|^2 d\tau$$

$$\text{with } \mathcal{R}_s \left(\frac{\tau}{\lambda} + s, s \right) = \int_s^{\frac{\tau}{\lambda} + s} \frac{\left(\frac{\tau}{\lambda} + s - r \right)^m}{m!} y_s^{(m+1)}(r) dr = \frac{1}{\lambda^{m+1}} \int_0^{\tau} \frac{\rho^m}{m!} y_s^{(m+1)} \left(s + \frac{\tau - \rho}{\lambda} \right) d\rho$$

From Eq. (3.3), one deduces that

$$\left| \mathcal{R}_s \left(\frac{\tau}{\lambda} + s, s \right) \right| \leq \frac{1}{\lambda^{m+1}} \frac{c}{m!} |x| \int_0^{|\tau|} \rho^m \exp \left(a \frac{|\tau - \rho|}{\lambda} \right) d\rho \leq \frac{1}{\lambda^{m+1}} \frac{c}{(m+1)!} |\tau|^{m+1} \exp \left(a \frac{|\tau|}{\lambda} \right) |x|$$

So, one can find an upper bound to $T_{\mathcal{R}}$

$$T_{\mathcal{R}} \leq \frac{1}{\lambda^{2m+3}} \frac{c^2}{[(m+1)!]^2} |x|^2 \int_{-\infty}^0 \exp(\tau) \tau^{2(m+1)} \exp \left(2a \frac{|\tau|}{\lambda} \right) d\tau$$

For any $\lambda \in [2a + \varepsilon, \infty)$ with $\varepsilon > 0$, the integral is bounded independently of λ , so there exists $\beta > 0$ such that

$$T_{\mathcal{R}} \leq \frac{\beta}{\lambda^{2m+3}} |x|^2 \quad (3.5)$$

Combining the equations (3.4) and (3.5), one obtains

$$\int_{-\infty}^s \exp(-\lambda[s-t]) |y_s(t)|^2 dt \geq \frac{\alpha\mu}{2\lambda^{2m+1}} |x|^2 - \frac{\beta}{\lambda^{2m+3}} |x|^2 \geq \frac{\alpha\mu\lambda^2 - 2\beta}{\lambda^{2m+3}} |x|^2$$

where $\eta = \frac{\alpha\mu\lambda^2 - 2\beta}{\lambda^{2m+3}}$ is strictly positive for all λ sufficiently large in $[2a + \varepsilon, \infty)$.

For all $S \geq 0$, we have

$$\int_{-\infty}^s \exp(-\lambda[s-t]) |y_s(t)|^2 dt \leq \int_{s-S}^s |y_s(t)|^2 dt + \frac{c^2}{\lambda - 2a} \exp(-(\lambda - 2a)S) |x|^2$$

We can choose $S = \frac{\log \left(\frac{2c^2}{[\lambda - 2a]\eta} \right)}{\lambda - 2a}$, thus $\forall (x, s)$

$$\int_{s-S}^s |y_s(t)|^2 dt \geq \frac{\eta}{2} |x|^2$$

Now,

$$\int_{s-S}^s |y_s(t)|^2 dt = x^T W^*(s - S, s) x$$

In summary, we have constructed S such that for all (x, s) , $W^*(s - S, s) \geq \alpha_0(S) I > 0$. We apply Theorem 4 and conclude that the system is UCO. This concludes the proof. \square

3.3 Existence and convergence of the Kalman filter

In this section, we wish to establish the well-posedness of the Kalman filter for the LTV dynamics (2.1) in Theorem 1. In details, we wish to establish that $\hat{\mathbf{X}}$ and P satisfying Eq. (2.6) exist for all times. This is the result announced in Section 2.1. To establish these facts, we consider the corresponding noise-free dynamics below

$$\begin{cases} \dot{\mathbf{X}}(t) = A(t)\mathbf{X}(t) + B(t)U(t) \\ \mathbf{Y}(t) = C(t)\mathbf{X}(t) \end{cases} \quad (3.6)$$

$$\begin{cases} \dot{\hat{\mathbf{X}}}(t) = A(t)\hat{\mathbf{X}}(t) + B(t)U(t) + K(t)(\mathbf{Y}(t) - C(t)\hat{\mathbf{X}}(t)) \end{cases} \quad (3.7)$$

$$\begin{cases} \dot{\tilde{\mathbf{X}}}(t) = (A(t) - K(t)C(t))\tilde{\mathbf{X}}(t) \end{cases} \quad (3.8)$$

Let Φ (resp. Φ_K) be defined as the transition matrix for the system (3.6)(resp. (3.8))¹

$$\begin{aligned} \frac{\partial \Phi}{\partial t}(t, s) &= A(t)\Phi(t, s), & \Phi(t, t) &= I \\ \frac{\partial \Phi_K}{\partial t}(t, s) &= (A(t) - K(t)C(t))\Phi_K(t, s), & \Phi_K(t, t) &= I \end{aligned} \quad (3.9)$$

This noise-free system can be studied at the light of the following definition

Definition 7. [Ikeda et al., 1975] *The system (3.6) is said to be Uniform and Complete Estimatability (UCE) if, for any pair of real numbers m and M such that $m \leq M$, there are positive numbers δ, η and an estimator gain $K(\cdot)$ such that any solution of the system (3.8) satisfies for all $t \geq s$*

$$\delta \|\tilde{\mathbf{X}}(s)\| e^{m(t-s)} \leq \|\tilde{\mathbf{X}}(t)\| \leq \eta \|\tilde{\mathbf{X}}(s)\| e^{M(t-s)}$$

A particular case of interest is when the system (2.1) is bounded and UCO, i.e. when there exist a, c, α_0 and T strictly positive such that

$$\|A(t)\| \leq a, \quad \|C(t)\| \leq c, \quad W^*(t-T, t) \geq \alpha_0 I > 0 \quad (3.10)$$

Then, the following result holds.

Theorem 7. [Ikeda et al., 1975] *A bounded system (3.6) is UCE by a bounded estimator if and only if it is UCO.*

On the other hand, classically, the UCO property serves to guarantee the convergence of Kalman filters.

Theorem 8. [Kalman and Bucy, 1961, Bucy and Joseph, 1968, Besançon, 2007] *If system (2.1) is UCO, then there exists an observer of the form:*

$$\dot{\hat{\mathbf{X}}}(t) = A(t)\hat{\mathbf{X}}(t) + B(t)U(t) - K(t)(C(t)\hat{\mathbf{X}}(t) - \mathbf{Y}(t))$$

1. It is the same as previously considered for system (2.1) (resp. (2.9)) in Eq. (3.1) (resp. Eq. (2.10))

with $K(t)$ given by:

$$\begin{aligned}\dot{P}(t) &= A(t)P(t) + P(t)A^T(t) - P(t)C^T(t)R^{-1}C(t)P(t) + Q + \delta P(t) \\ P(0) &= P_0 = P_0^T > 0, \quad R = R^T > 0, \\ K(t) &= P(t)C^T(t)R^{-1}\end{aligned}$$

with either $\delta > 2\|A(t)\|$ for all t , or $Q = Q^T > 0$.

Theorem 9. Consider system (2.1). Assume (A, C) are bounded matrices and (Q, R) are constant matrices. If this system is UCO, then the Kalman filter (2.6) exists for all times. There exist (Λ, κ) positive such that this Kalman filter applied to the corresponding noise-free system (3.6), leads to exponential convergence of the estimation error noted $\tilde{\mathbf{X}}_K$

$$\|\tilde{\mathbf{X}}_K(t)\|^2 \leq \kappa \|\tilde{\mathbf{X}}_K(s)\|^2 e^{-\Lambda(t-s)}$$

The following Section 3.3.1, Section 3.3.2, Section 3.3.3 and Section 3.3.4 constitute a proof, from beginning to end, of the existence of Kalman filter, starting from the definition of the solution of the variance equation to finish with an evaluation of the convergence of Kalman filter.

The existence of a solution $P(t)$ is guaranteed. It is defined on $[0, +\infty)$ if it is bounded. We now establish this fact.

3.3.1 Lower bound on the solution of the covariance equation from boundedness of the system

Let

$$p = \min \left\{ \frac{\lambda_{\min}(Q)}{\sqrt{a^2 + 2c^2\lambda_{\max}(R^{-1})\lambda_{\min}(Q)} + a}, \frac{1}{2}\lambda_{\min}(P_0) \right\} \quad (3.11)$$

To establish the lower bound by contradiction, assume the existence of t such that $\lambda_{\min}(P(t)) \leq p$.

Then, let t_0 be defined as

$$t_0 = \min\{ t \mid \lambda_{\min}(P(t)) \leq p \}$$

From the inequality $p < \lambda_{\min}(P(0))$, the inequality $t_0 > 0$ is guaranteed. Also, by continuity, the following equations hold

$$\lambda_{\min}(P(t)) > p \quad \forall t \in [0, t_0) \quad (3.12)$$

$$\lambda_{\min}(P(t_0)) = p \quad (3.13)$$

Let \mathbf{x} be any unit vector so that

$$P(t_0)\mathbf{x} = p\mathbf{x} \quad (3.14)$$

From Eq. (3.12,3.13),

$$\mathbf{x}^T P(t) \mathbf{x} > \mathbf{x}^T P(t_0) \mathbf{x} \quad t \in [0, t_0)$$

and therefore

$$\left. \overline{\mathbf{x}^T P \mathbf{x}} \right|_{t=t_0} \leq 0 \quad (3.15)$$

But, by a direct computation, using Eq. (2.6,3.14),

$$\left. \overline{\mathbf{x}^T P \mathbf{x}} \right|_{t=t_0} = \mathbf{x}^T \dot{P} \Big|_{t=t_0} \mathbf{x} = \mathbf{x}^T (pA^T(t_0) + pA(t_0) - p^2 C^T(t_0) R^{-1} C(t_0) + Q) \mathbf{x}$$

Finally, from Eq. (3.10,3.11),

$$\begin{aligned} \left. \overline{\mathbf{x}^T P \mathbf{x}} \right|_{t=t_0} &\geq -2ap - c^2 p^2 \lambda_{\max}(R^{-1}) + \lambda_{\min}(Q) \\ &\geq c^2 p^2 \lambda_{\max}(R^{-1}) > 0 \end{aligned}$$

This contradicts Eq. (3.15) and establishes

$$P(t) \geq p I > 0 \quad \forall t \geq 0 .$$

3.3.2 Upper bound stemming from the Uniform and Complete Observability property

Consider a pair of positive numbers μ and λ such that $\mu \geq \lambda > 0$. Thanks to Theorem 7, there exist positive numbers δ , η and a bounded estimator gain $K(\cdot)$ such that any solution of the system (3.8) satisfies for all $t \geq s$

$$\delta \|\tilde{\mathbf{X}}(s)\| e^{-\mu(t-s)} \leq \|\tilde{\mathbf{X}}(t)\| \leq \eta \|\tilde{\mathbf{X}}(s)\| e^{-\lambda(t-s)} \quad (3.16)$$

From Eq. (3.16), for all $t \geq s$

$$\delta e^{-\mu(t-s)} \leq \|\Phi_K(t, s)\| \leq \eta e^{-\lambda(t-s)} \quad (3.17)$$

Consider the matrix $S(t)$

$$S(t) = 2\Phi_K(t, 0)P_0\Phi_K^T(t, 0) + \int_0^t \Phi_K(t, s) [K(s)RK^T(s) + 2Q] \Phi_K^T(t, s) ds$$

By construction, this matrix S is symmetric positive definite and bounded. Its inverse is also symmetric positive definite. In particular, it satisfies $S(0) = 2P_0$ and a constant bound S_M can be found

$$S(t) \leq S_M I = \left(2\eta^2 \lambda_{\max}(P_0) + \frac{\eta^2}{2\lambda} (k^2 \lambda_{\max}(R) + 2\lambda_{\max}(Q)) \right) I$$

where k stands for the bound of $\|K(t)\|$.

Consider Ω such that $R^{-1} = \Omega\Omega$. By construction, $\Omega R\Omega = I$. From Eq. (3.9), the derivative of $S(t)$ is, omitting t for sake of simplicity,

$$\begin{aligned}\dot{S} &= (A - KC)S + S(A - KC)^T + KRK^T + 2Q \\ &= AS - KCS + SA^T - SC^TK^T + K\Omega^{-1}\Omega^{-1}K^T + 2Q \\ &= AS + SA^T - SC^TR^{-1}CS + 2Q + (K\Omega^{-1} - SC^T\Omega)(K\Omega^{-1} - SC^T\Omega)^T\end{aligned}\quad (3.18)$$

To establish that P is upper bounded, we prove by contradiction that it is smaller than S . So assume the existence of t such that $\lambda_{\min}(P(t) - S(t)) \geq 0$

Then let t_0 be defined as

$$t_0 = \min\{t \mid \lambda_{\min}(P(t) - S(t)) \geq 0\}$$

From the inequality $\lambda_{\max}(P(0) - S(0)) = -\lambda_{\min}(P_0) < 0$, strict positiveness of t_0 can be deduced. Also by continuity,

$$\begin{aligned}\lambda_{\min}(P(t) - S(t)) &< 0 \quad \forall t \in [0, t_0) \\ \lambda_{\min}(P(t_0) - S(t_0)) &= 0\end{aligned}\quad (3.19)$$

Let \mathbf{x} be a unit vector such that

$$P(t_0)\mathbf{x} = S(t_0)\mathbf{x}\quad (3.20)$$

From Eq. (3.19), the following equation is verified for all $t \in [0, t_0)$

$$\mathbf{x}^T(P(t) - S(t))\mathbf{x} < \mathbf{x}^T(P(t_0) - S(t_0))\mathbf{x} = 0$$

and therefore

$$\overbrace{\mathbf{x}^T(P(t) - S(t))\mathbf{x}}^{\cdot}\bigg|_{t=t_0} \geq 0\quad (3.21)$$

But by a direct computation, using Eq. (2.6,3.18), omitting t for sake of simplicity, one gets

$$\overbrace{P - S}^{\cdot} = \begin{vmatrix} (P - S)A^T + A(P - S) - PC^TR^{-1}CP + SC^TR^{-1}CS - Q \\ -(K\Omega^{-1} - SC^T\Omega)(K\Omega^{-1} - SC^T\Omega)^T \end{vmatrix}$$

So, at time $t = t_0$, substituting Eq. (3.20), one has

$$\overbrace{\mathbf{x}^T[P(t) - S(t)]\mathbf{x}}^{\cdot} = -\mathbf{x}^T\left(Q + (K\Omega^{-1} - SC^T\Omega)(K\Omega^{-1} - SC^T\Omega)^T\right)\mathbf{x}$$

which is strictly negative. This contradicts Eq. (3.21) and, in turn, establishes

$$P(t) \leq S(t) \quad \forall t \geq 0$$

Since $P(t)$ is lower and upper bounded, it is defined on $[0, +\infty)$.

Hence, one can consider the Kalman gain K_K for all t

$$K_K(t) = P(t)C^T(t)R^{-1}$$

3.3.3 Convergence of the Kalman filter

Further, P is symmetric positive definite

$$0 < p I \leq P(t) \leq S_M I, \quad \forall t \geq 0$$

so its inverse is also symmetric positive definite and satisfies

$$0 < \frac{1}{S_M} I \leq P^{-1}(t) \leq \frac{1}{p} I, \quad \forall t \geq 0 \quad (3.22)$$

Therefore, one can consider the candidate Lyapunov function V

$$V(t) = \tilde{\mathbf{X}}_K^T(t) P^{-1}(t) \tilde{\mathbf{X}}_K(t)$$

The error equation is now as follows

$$\dot{\tilde{\mathbf{X}}}_K(t) = (A(t) - P(t)C^T(t)R^{-1}C(t))\tilde{\mathbf{X}}_K(t) \quad (3.23)$$

The derivative of the matrix P^{-1} is obtained from the variance equation (2.6)

$$\begin{aligned} \dot{P}^{-1}(t) &= -P^{-1}(t)\dot{P}(t)P^{-1}(t) \\ &= -P^{-1}(t)A(t) - A^T(t)P^{-1}(t) + C^T(t)R^{-1}C(t) - P^{-1}(t)QP^{-1}(t) \end{aligned} \quad (3.24)$$

The derivative of the candidate Lyapunov function is obtained combining Eq. (3.23,3.24)

$$\begin{aligned} \dot{V}(t) &= -\tilde{\mathbf{X}}_K^T(t) (C^T(t)R^{-1}C(t) + P^{-1}(t)Q P^{-1}(t)) \tilde{\mathbf{X}}_K(t) \\ &\leq -\tilde{\mathbf{X}}_K^T(t) (P^{-1}(t)Q P^{-1}(t)) \tilde{\mathbf{X}}_K(t) \\ &\leq -\frac{\lambda_{\min}(Q)}{S_M} V(t) \end{aligned} \quad (3.25)$$

From Eq. (3.22,3.25), V is a Lyapunov function for the system (3.8) and exponential stability of the Kalman observer is established.

In details,

$$V(t) \leq V(s) e^{-\frac{\lambda_{\min}(Q)}{S_M}(t-s)}$$

Then,

$$\begin{aligned} \frac{1}{S_M} \|\tilde{\mathbf{X}}_K(t)\|^2 &\leq \tilde{\mathbf{X}}_K^T(t) P^{-1}(t) \tilde{\mathbf{X}}_K(t) \\ &\leq \tilde{\mathbf{X}}_K^T(s) P^{-1}(s) \tilde{\mathbf{X}}_K(s) e^{-\frac{\lambda_{\min}(Q)}{S_M}(t-s)} \end{aligned}$$

Finally,

$$\|\tilde{\mathbf{X}}_K(t)\|^2 \leq \kappa \|\tilde{\mathbf{X}}_K(s)\|^2 e^{-\Lambda(t-s)}$$

with

$$\Lambda = \frac{\lambda_{\min}(Q)}{S_M} = \frac{\lambda_{\min}(Q)}{2\eta^2\lambda_{\max}(P_0) + \frac{\eta^2}{2\lambda}(k^2\lambda_{\max}(R) + 2\lambda_{\max}(Q))} \quad (3.26)$$

$$\kappa = \frac{S_M}{p} = \frac{1}{\Lambda} \max\left(\sqrt{a^2 + 2c^2\lambda_{\min}(Q)/\lambda_{\min}(R)} + a, 2\frac{\lambda_{\min}(Q)}{\lambda_{\min}(P_0)}\right) \quad (3.27)$$

3.3.4 Estimation of the convergence rate

In establishing the upper bound of $P(t)$ in Section 3.3.2, Theorem 7 of estimatability has been used to find a bounded estimator gain. In this part, a bounded estimator is proposed in order to get a computable triplet (k, η, λ) .

From the boundedness of the system, the transition matrix of the LTV dynamics (2.1) can be bounded, for $t \geq s$,

$$e^{-a(t-s)} \leq \|\Phi(t, s)\| \leq e^{a(t-s)}$$

Let the matrix $\Sigma(t)$ be defined as follows, with ζ a real positive number

$$\Sigma(t) = \int_{t-T}^t \Phi^T(s, t) C^T(s) C(s) \Phi(s, t) e^{-\zeta(t-s)} ds$$

Definite positiveness of $\Sigma(t)$ results from boundedness and UCO,

$$0 < \bar{\alpha}_0 c^2 e^{-\zeta T} I \leq \Sigma(t) \leq c^2 \frac{1 - e^{-(\zeta-2a)T}}{\zeta - 2a} I$$

From the expression of $\Sigma(t)$,

$$\dot{\Sigma}(t) = \begin{cases} C^T(t) C(t) - A^T(t)\Sigma(t) - \Sigma(t)A(t) - \zeta\Sigma(t) \\ -\Phi^T(t-T, t)C^T(t-T) C(t-T)\Phi(t-T, t)e^{-\zeta T} \end{cases} \quad (3.28)$$

Since $\Sigma(t)$ is definite positive, the following gain $K(t)$ exists

$$K(t) = \frac{1}{2}\Sigma^{-1}(t)C^T(t) \quad (3.29)$$

Let $W(t) = \tilde{\mathbf{X}}^T(t)\Sigma(t)\tilde{\mathbf{X}}(t)$ The derivative of $W(t)$ can be calculated from Eq. (3.8,3.28,3.29)

$$\begin{aligned} \dot{W}(t) &= -\zeta W(t) - \tilde{\mathbf{X}}^T(t)\Phi^T(t-T, t)C^T(t-T) C(t-T)\Phi(t-T, t)e^{-\zeta T} \tilde{\mathbf{X}}(t) \\ &\leq -\zeta W(t) \end{aligned} \quad (3.30)$$

Thus, exponential stability of the system (3.8) can be established thanks to Eq. (3.3.4,3.30)

$$W(t) \leq W(t_0)e^{-\zeta(t-t_0)}$$

$$\|\tilde{\mathbf{X}}(t)\|^2 \leq \frac{1}{\bar{\alpha}_0} \frac{e^{\zeta T} - e^{2aT}}{\zeta - 2a} \|\tilde{\mathbf{X}}(t_0)\|^2 e^{-\zeta(t-t_0)}$$

This observer can be introduced in the preceding Eq. (3.26,3.27)

$$\|\tilde{\mathbf{X}}_{\mathbf{K}}(t)\|^2 \leq \kappa \|\tilde{\mathbf{X}}_{\mathbf{K}}(s)\|^2 e^{-\Lambda(t-s)}$$

with

$$\Lambda = \frac{\bar{\alpha}_0^2 \lambda_{\min}(Q)}{2\lambda_{\max}(P_0) + \frac{\lambda_{\max}(R) e^{2\zeta T}}{4\bar{\alpha}_0^2 c^2} + \frac{\lambda_{\max}(Q)}{\zeta}} \left(\frac{\zeta - 2a}{e^{\zeta T} - e^{2aT}} \right)^2$$

$$\kappa = \frac{S_M}{p} = \frac{1}{\Lambda} \max \left(\sqrt{a^2 + 2c^2 \lambda_{\min}(Q) / \lambda_{\min}(R)} + a, 2 \frac{\lambda_{\min}(Q)}{\lambda_{\min}(P_0)} \right)$$

3.4 Conclusion and main result

We now gather the main results of this Chapter to formulate a handy statement guaranteeing convergence of Kalman filters for LTV systems under an assumption that is relatively easy to check.

Theorem 10. *Consider a LTV system under the form (2.1) with bounded matrices (A, C) and stationary matrices (Q, R) . The Kalman filter (2.6) generates an exponentially stable error dynamics driven by noises (2.9) if the system (2.1) is DO.*

Proof. By Theorem 6, if the system is DO then it is UCO. Then, under the assumptions above, by Theorem 9, the Kalman filter defined by Eq. (2.6) is well-defined and exponentially convergent. It generates the exponentially stable dynamics of Eq. (2.9). \square

Part II

GPS-free automotive relative navigation system

*Système de navigation relative sans GPS
pour véhicule automobile*

Introduction

This part presents the navigation filter designed in this thesis for an automotive vehicle. The task of this filter is to provide relative position information over a relatively long period of time (tens of minutes to days) from data obtained with low-cost inertial sensors (MEMS) and a magnetic velocimeter.

The employed trajectory reconstruction method is to integrate measurements as is done in inertial navigation. Inertial navigation is a well-established technique which has taken key roles in the aerospace industries [Faurre, 1971][Grewal et al., 2001], as well in other areas such as undersea navigation or dynamic positioning systems [Bray, 2003]. It has also recently emerged as an enabling technology under the forms of MEMS sensors in numerous low-cost applications (small UAVs [Castillo et al., 2004, Hamel and Mahony, 2007, Bristeau et al., 2010a, Bristeau et al., 2011], ground robotics, cell-phones, among others). Yet, its main limitation is the unavoidable drift of the estimates [Faurre, 1971]. The culprits are the biases of the sensors, mostly accelerometers and gyroscopes, which result in drift in velocity and, consequently, in diverging position estimates [Dissanayake et al., 2001]. With MEMS sensors, those drift appear over short time periods (tens of seconds [Vissière et al., 2008]). This usually discards them for most critical applications if they are not complemented by some other source of information.

The contribution here is the design of a navigation filter which cancels these drifts in the sense that the sources are identified and estimated on-board. A key feature of the setup we consider in this thesis is the availability of a velocimeter which provides a relatively dependable estimate of the vehicle body velocity. This sensor is usually available in most vehicles today although it is not easy to directly connect to it. We have developed our own system which is not connected to the vehicle electronic system and uses magnetometers signals. Velocity information can be obtained through various sensor technologies application (e.g. Doppler radar [Uliana et al., 1997], camera [Kim et al., 2004], Pitot tube). Each technology has its own flaws and advantages [Skog and Handel, 2009]. Yet, this scalar information is not sufficient to estimate the motion of the vehicle as rotations come into play. Gyroscopes can be used to determine rate-of-turn information but they also have (non-constant) biases which are causes of substantial drifts.

In the case under study, the trajectory involves various dynamics and measurement equations depending whether straight-line motion or curve motion is under consideration. As will be demonstrated, the global problem of full-state estimation can be handled by sequentially estimating subsets of the full state, each one being estimated during an appropriate part of the trajectory.

We consider the vehicle as a 6-DOF rigid body moving without sideslip. The vehicle is characterized by a three-dimensional position, a curvilinear velocity and three attitude angles. We exploit the mentioned magnetic velocimeter, a trihedron of accelerometers, a trihedron of gyroscopes, and an altimeter.

The work presented here is inspired by the observers interconnection theory (see [Besançon and Hammouri, 1998]). Separately but simultaneously, we estimate the velocity, the angular dynamics (angles, rates and biases), and finally, the accelerations (and the biases

associated to the sensors). The main difficulty is to estimate the angular dynamics. For this task, we propose Temporally Interconnected Observers (TIO) arguing that during straight-line motion, one can estimate the pitch dynamics, while, during curve motion, it is possible to catch the roll dynamics. Yaw bias can be estimated at rest. From these angles, one can estimate the accelerometers biases, so that accelerometers can be used to compute speed prediction and attitudes estimates to discard unusable measurements for the magnetic compass.

The TIO formalism [Bristeau et al., 2010b] represents a handy tool to represent similar common practices in the field of observer design of vehicular systems. A typical example of such practices is found in the navigation systems of cruise and guided missiles as is thoroughly detailed in [Hicks, 1993, Ekütekin, 2007, Bezick et al., 2010]. In such applications, several distinct phases of the system trajectory are considered to reconstruct, sequentially through distinct algorithms, subsets of the whole state vector of the system. Practically, an initialization using attitude measurements from an Inertial Measurement Unit (IMU) is performed (at rest) on the launch platform, then, after the boost phase and during mid-course (high speed) flight, measurements made by the IMU and additional knowledge of the corresponding motions from terrain navigation radars is used to determine in-flight alignment of inertial sensors, and, finally, the (maneuvering) transition to terminal target is performed through data fusion from other additional sources of information such as optical devices. Decomposing the trajectory in distinct phases during which the system has well recognizable dynamics eases the design of data fusion algorithms as it suggests relatively easy and dependable means to reconstruct certain variables during certain phases. The various components of the state of the system are not estimated all at once, but, instead, well defined subsets are reconstructed during each particular phase of the vehicle trajectory.

A natural question is the convergence of this TIO scheme [Bristeau and Petit, 2011]. Indeed, having separate subsets of the state variables estimate errors decay during distinct (non overlapping) periods does not automatically guarantee the convergence of the full state to actual values. The culprit is that the remaining variables must be propagated without any possibility of corrections when they are not observed. Careful investigations reveal that, in our case, the TIO can provide convergence under certain simple assumptions on the switching policy.

This part of the thesis is organized as follows. In Chapter 4, we expose the functioning of the magnetic velocimeter and the magnetic compass employed aboard the vehicle. In Chapter 5, we detail the vehicle navigation problem under consideration. In Chapter 6, we expose the general TIO structure, and state a problem of convergence involving a succession of straight-line and curve motions. We establish the DO and therefore the UCO property of the system (focusing on curve motion) and draw some conclusions on the estimatability of the system. The main argument of proof is the study of a time-varying pulsation oscillator appearing in the attitude dynamics. Then, we establish the convergence of the proposed TIO. Here, the estimates established earlier serve to guarantee the convergence of a discrete-time dynamics governing the system according to the switching policy. This TIO strategy is finally implemented on-board a prototype navigation system. In Chapter 7, we present results of an actual implementation and stress the obtained performance.

Chapter 4

Exploitation of magnetic measurements onboard a vehicle

Exploitation des mesures magnétiques à bord d'un véhicule

Ce chapitre explique comment le champ magnétique mesuré à l'intérieur d'un véhicule peut être exploité de façon à en tirer une information sur la vitesse et le cap de ce véhicule. Cela se traduit par une analyse du spectre (transformée de Fourier) et une identification d'ellipse. Les difficultés de ces deux méthodes sont détaillées et on met en évidence la nécessité de coupler ce capteur magnétique à des capteurs inertiels classiques.

The three-dimensional representation of the magnetic field that can be sensed inside a vehicle reveals a structure which is very specific. Depending on the orientation of the vehicle (heading) and its ground velocity, the sensed field lies somewhere on an elliptic toroid (Fig. 4.1). The

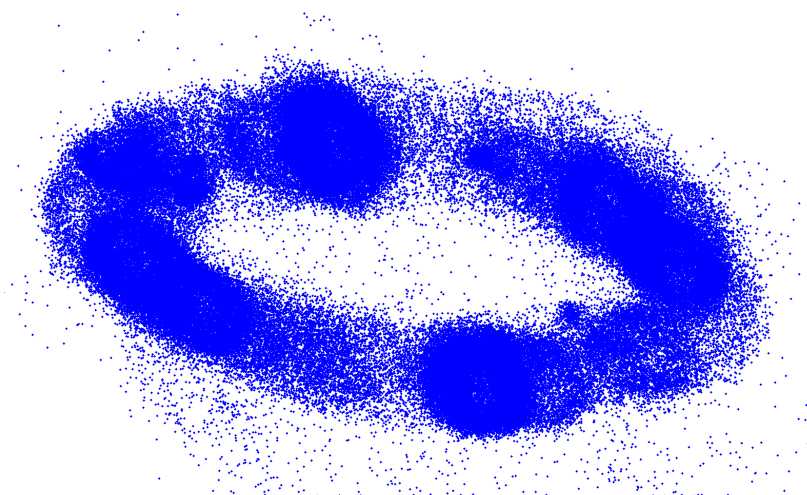


Figure 4.1: Three-dimensional representation of the magnetic field sensed inside a vehicle.

elliptic shape is the consequence of the yaw motion of the vehicle and the toroidal form stems from the rotation of the wheel closest to the sensor. This chapter is dedicated to the exploitation of this geometry to determine a heading estimate (as already studied in the literature), and the speed, which is a novelty of the GPS-free automotive navigation technique presented in this thesis.

4.1 Magnetic velocimeter

The magnetic velocimeter that we propose, under the form of an algorithm, uses a spectral analysis of the magnetometer signal obtained aboard the vehicle. Experimentally, it can be observed that the magnetic field (Earth magnetic field) surrounding a vehicle is disturbed by the presence of rotating parts, particularly the wheels. Figure 4.2 reports magnetic field measurements performed aboard a vehicle initially at rest then starting to move and finally accelerating: an oscillation appears on all three components of the measurements with an increasing frequency.

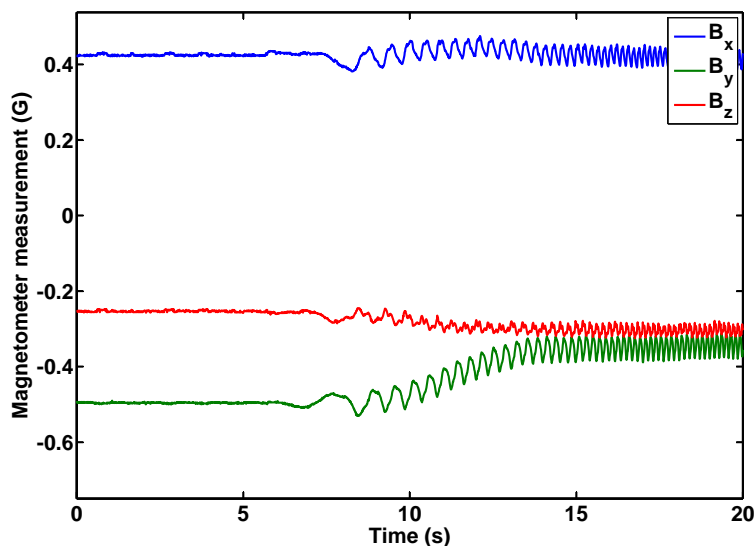


Figure 4.2: Magnetometer measurement during a vehicle start.

From this observation, a spectral analysis, e.g. by means of a Fast Fourier Transform (FFT), can be performed to extract the frequency corresponding to the wheel rotation speed. Knowing the external radius of the tire, the vehicle ground speed can be determined assuming roll-without-slip motion. These principles allow us to constitute a magnetic velocimeter which is relatively accurate and reliable. Comparison against GPS data are reported in Fig. 4.3. The magnetic velocimeter permits to obtain a good estimate of the vehicle velocity without need of GPS coverage or odometer connection. The principle of this velocimeter is protected by the international patent WO 2010/066742 *Device and Method for Determining the Speed of a Wheeled Terrestrial Vehicle from Measurements of a Magnetic Field*.

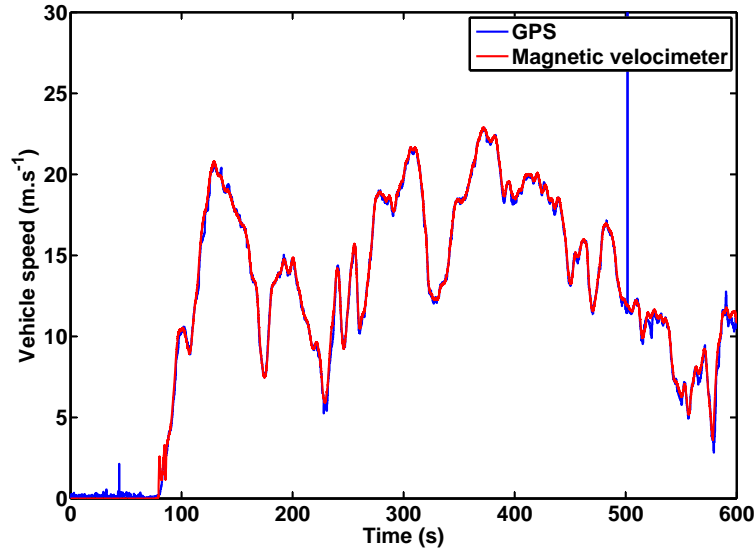


Figure 4.3: Comparison of the magnetic velocimeter (red) with the GPS speed (blue).

One difficulty in the velocity determination stems from the Pitch Determination Algorithm (PDA) employed to separate the wheels rotation frequency from other present periodic signals (see Fig. 4.4). Another difficult point is to distinguish stops, and forward motion from reverse motion (phase detection). We now briefly detail some of the employed techniques.

4.1.1 Frequency detection

Consider data such as represented in Fig. 4.2. The FFT is realized on a moving Hamming window [Tan, 2008] (the result is reported in Fig. 4.4) and its peaks (local maxima) are isolated to obtain a reduced spectrum which contains the rotation frequency, possible mechanical vibration frequencies, possible sensors frequencies and body oscillation frequencies, each being represented by a fundamental frequency and several harmonics. The useful signal being the rotation frequency, the closer the embedded system is to a wheel, the more favorable the signal-to-noise ratio is.

As is illustrated in Figure 4.5 where the reduced spectrum is reported, the main difficulty the PDA has to deal with is the existence of several frequencies in the spectrum of the measurements among which the fundamental rotation frequency has to be isolated. In our system, the PDA is based on two criteria : the existence of a powerful (in the sense of magnitude of the peak in the FFT) frequency with several harmonics and the continuity relative to previously detected frequency. Each criterion is physically sound but has a practical drawback. The first criterion relies on the harmonic decomposition of the rotation speed frequency in the measured signal but, similarly, the car engine frequencies which are present when the engine is running are also organized in harmonics. Above all, this criterion can generate misleading information due to the harmonics. For example, if the fundamental frequency f and the harmonics $2f$, $4f$ and

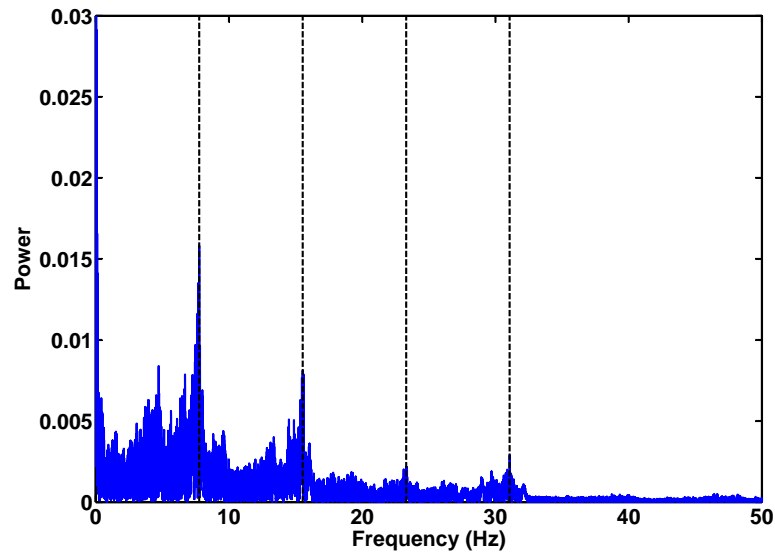


Figure 4.4: Spectrum (FFT) of a 1-axis magnetic sensor data during 150 seconds of motion at almost constant velocity: vehicle body oscillations and vibrations are present in the 0 – 10 Hz part, while the fundamental frequency associated to the wheels rotation and its harmonics are distinguishable in the higher frequencies.

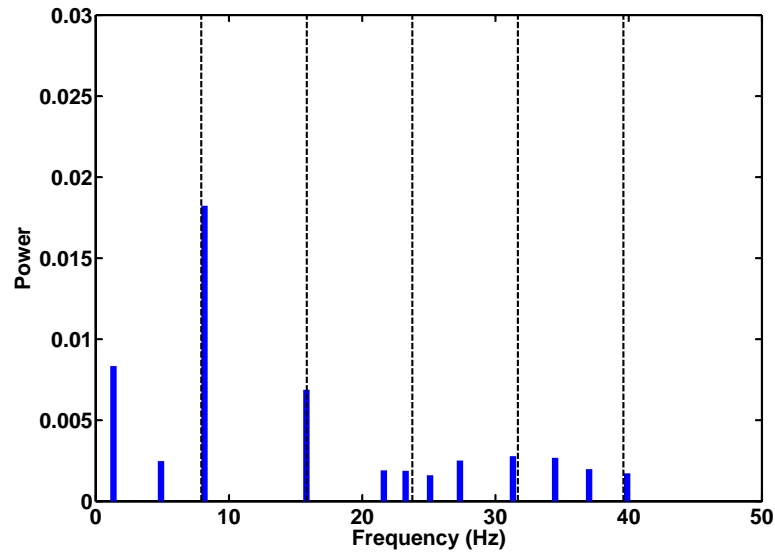


Figure 4.5: Simplified spectrum of a 1-axis magnetic sensor on a half-second Hamming window: fundamental and harmonics in the middle of perturbations frequencies.

$6f$ are present, the algorithm has to distinguish this sequence from another sequence where the fundamental $f' = 2f$ and the harmonics $2f'$ and $3f'$ would be also present, the frequency f being considered as an undesired disturbance. The second criterion uses the continuity of the vehicle speed but unfortunately, engine harmonics are also continuous and this second criterion is of little help.

The first criterion is very efficient at medium to high vehicle speed (> 30 km/h) since rotation frequencies get more powerful than other mechanical frequencies and are higher than the body oscillation frequencies. The second criterion is used to prevent switches from the fundamental to an harmonic. A last difficulty of the frequency detection occurs at low vehicle speed (< 10 km/h) when the rotation frequency of the wheel and its harmonics got very close to each other and lie near noise frequencies. During this phase, the previous criteria are not sufficient to distinguish the fundamental from an harmonic or other disturbing frequencies. The PDA need to be combined with a speed prediction from the inertial sensors to obtain a good estimate of the vehicle speed, the efficiency of this combination is shown in Fig. 4.6. This solution constitutes a *navigation system aided PDA*. However, direct accelerometer prediction is not relevant and the attitudes of the vehicle and the biases of the sensors need to be known. This is why a complete observer is derived and presented in Chapter 6.

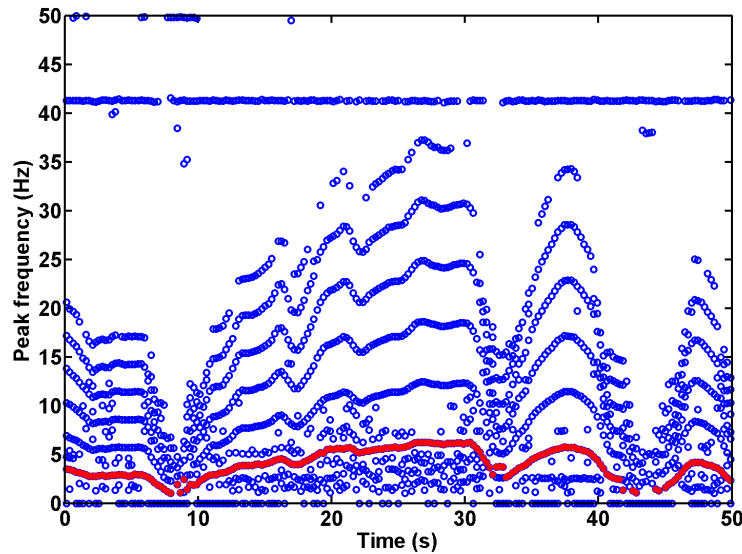


Figure 4.6: Frequency detection: the isolated fundamental frequency (red) among all the detected peaks frequencies (blue).

4.1.2 Stops detection

During stops, the PDA does not provide any information. To handle such cases, a specific algorithm has been developed to detect stops which are crucial to realize Zero velocity Update (ZUPT) [Grejner-Brzezinska et al., 2001, Ojeda and Borenstein, 2007] and to estimate

gyrometers biases. It relies on a moving recursive standard deviation (MSTD) evaluation of the signal produced by the embedded sensors (see Fig. 4.7). Depending on the actual position of the sensors inside the vehicle, the noise level from the running engine can be negligible or overwhelming. The detection threshold is adapted on the fly after identification of the low level and the high level of the standard deviation.

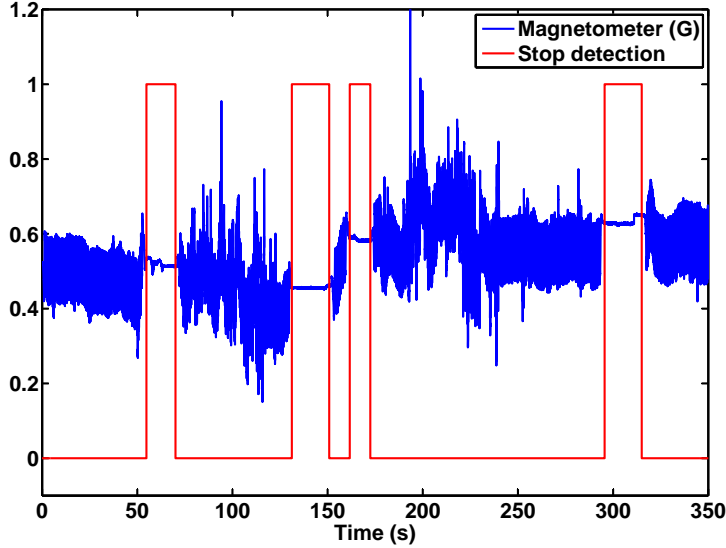


Figure 4.7: Stops detection (red) from the moving recursive standard deviation (MSTD) of the magnetometer measurements (blue).

4.1.3 Phase detection

The previously discussed pitch detection algorithm, which uses the peaks of magnitude in the FFT of the sensed signal, can only estimate the absolute value of the vehicle speed. Using a phase analysis of the signal can serve to determine if the vehicle is in forward or reverse motion. Once frequency and stops have been detected and identified, from the Cauchy's theorem in complex analysis, the motion direction can be detected. We now explain how. Preliminarily, the rotation component of the sensed signal is isolated with a moving narrow bandpass filter centered on the detected rotation frequency. This filter permits to obtain relatively regular circular paths centered on the origin, deleting the harmonics and the yaw effect (see Fig. 4.8). Then, the signal projected onto the rotation plane is integrated between two stops to obtain a winding number. The sign of this winding number indicates the direction of the vehicle (forward or backward). This algorithm is very robust to noise but highly dependent of the quality of the frequency detection since the signal is filtered through a bandpass filter function of the frequency estimate.

Consider the complex number $Z = B_{x_m}^f + iB_{z_m}^f$ where the superscript f indicates the debiased bandpass filtering. The winding number ϖ is given by

$$\varpi = \frac{1}{2\pi} \oint \frac{dZ}{Z}$$

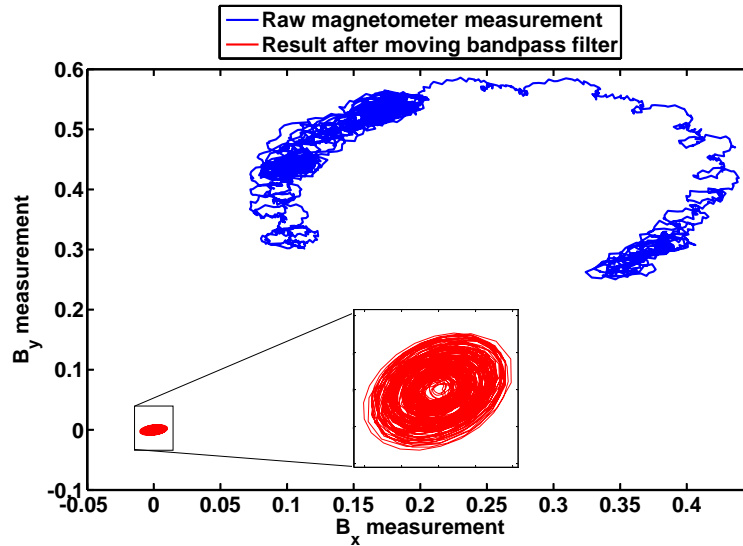


Figure 4.8: X-Y graph of the raw measurement (blue) and the result after filtering (red).

4.2 Magnetic heading determination

Considering that the Earth magnetic field \mathbf{B}_E is constant, estimating the heading seems a relatively easy task: at every possible position on the Earth, the magnetic field is directed towards the North¹. According to this assumption, the magnetometers inside a vehicle which realizes a flat 360° turn should measure a circle (blue plot in Fig. 4.9). From this point, getting the heading should be a simple arctangent calculus as follows

$$\mathbf{B}_E = \begin{bmatrix} B_N \\ 0 \\ B_D \end{bmatrix}_{|R_i} = \begin{bmatrix} c_\psi B_N \\ -s_\psi B_N \\ B_D \end{bmatrix}_{|R_b}$$

$$\psi = \arctan(-B_y/B_x)$$

We now model the measurement equation which shows the impact of the three-dimension rotation of the vehicle. Consider the magnetometer measurement \mathbf{B}_m , it is given by the three-dimension rotation of the Earth magnetic field²

$$\mathbf{B}_m = R_\phi R_\theta R_\psi \mathbf{B}_E$$

As a consequence, the locus which was a circle now lies on a sphere, near a parallel plane as long as pitch and roll angles remain small.

1. This is untrue when large displacement at the surface of the Earth are considered, magnetic field mapping may be used as the International Geomagnetic Reference Field (IGRF) [International Association of Geomagnetism and Aeronomy, 2010]

2. For sake of readability, the notation \mathbf{B}_E (respectively \mathbf{B}_m) is used to represent its components in the inertial frame (resp. body frame) which should have been noted $(\mathbf{B}_E)_{|R_i}$ (resp. $(\mathbf{B}_m)_{|R_b}$)

On top of that, it is necessary to add the magnetic pattern created by the vehicle speed, denoted by $\mathbf{B}_s(u)$ ³. The locus is now a toroid distributed on a spherical zone.

$$\mathbf{B}_m = R_\phi R_\theta R_\psi \mathbf{B}_E + \mathbf{B}_s(u) \quad (4.1)$$

Further, several well known problems discard this simple model (4.1): the East component of the field, the presence of natural metallic masses found under the roads, the magnetic declination, the diurnal variation, ... These problems exist but are not the most concerning when a magnetic compass is put inside a vehicle. They will be neglected in the following. The magnetometers measure the phenomenon discussed in Section 4.1 which allows to compute the speed of the vehicle but, further, they are also disturbed by the metallic parts of the vehicle. The metallic parts near the embedded system exert disturbances on the magnetic field which can be of two types: hard iron effect and soft iron effect [Ripka, 2001]. They are detailed in Part 4.2.1. These disturbances turn the expected circle into an ellipse which can be rotated from the North-East axes. The detection of this ellipse is explained in Part 4.2.2.

4.2.1 Hard iron / soft iron distortions

In a vehicle, some materials can be ferromagnetic, that is to say have strong magnetic susceptibility. These interact with the Earth magnetic field and deform the induced magnetic field lines. Among ferromagnetic materials, are permanent magnets (materials which can be magnetized by an external magnetic field and keep their magnetization) also referred to as *hard iron* and material which do not get permanently magnetized, i.e. *soft irons*. Majority of iron alloys can be considered as ferromagnetic. The interested reader will find more details in works about magnetometer calibration [Gebre-Egziabher et al., 2006, Renaudin et al., 2010, Vasconcelos et al., 2011]. Historically, these effects, which have been identified early [Poisson, 1838, Evans and Smith, 1863], are compensated onboard vehicles (ships in particular) by placing other magnets in the vicinity of compasses at well chosen locations.

Hard iron effects are the easiest to compensate for since they induce constant magnetic fields, which can be considered as offsets on the magnetometer measurements (green plot in Fig. 4.9). They are noted in the vector Δ .

Soft iron effects are more difficult to identify because they amplify or reduce the magnetic field in the principal directions of the material which are most often different from the sensors axes. This effect can be considered as scale factors in a particular frame. As a result, the previous circle becomes an ellipse whose axes are rotated with respect to the sensors axes (red plot in Fig. 4.9). To represent it, the rotation matrix which allows one to map the frame composed by the principal directions of the soft iron material to the sensors axes is noted R_{SI} and the diagonal matrix of the scale factors is Λ .

The magnetometer measurements can now be written as follows. Their locus when the vehicle is rolling on a road belong to toroid surface distributed about an ellipse.

$$\mathbf{B}_m = R_{SI} \Lambda R_{SI}^T (R_\phi R_\theta R_\psi \mathbf{B}_E + \mathbf{B}_s(u) + \Delta)$$

3. Similarly, the notation $\mathbf{B}_s(u)$ is used to represent its components in the body frame $(\mathbf{B}_s(u))_{|R_b}$

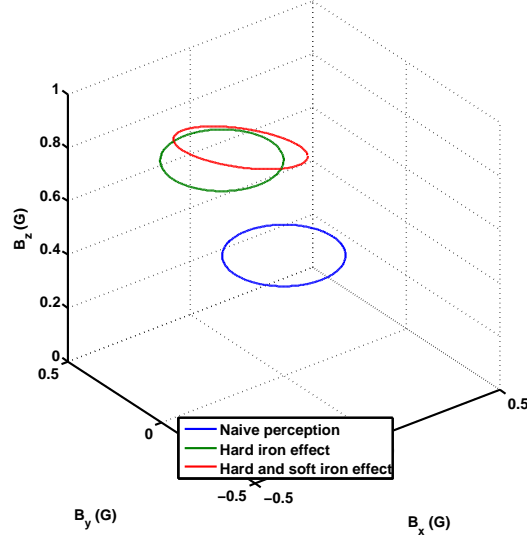


Figure 4.9: Measured magnetic field for a flat 360° turn.

Moreover, local temporary disturbances can occur due to closeness with a passing truck, a bridge or a power line, they are noted \mathbf{B}_{loc} . Gathering all these factors, one obtains a relevant model of the magnetic measurements

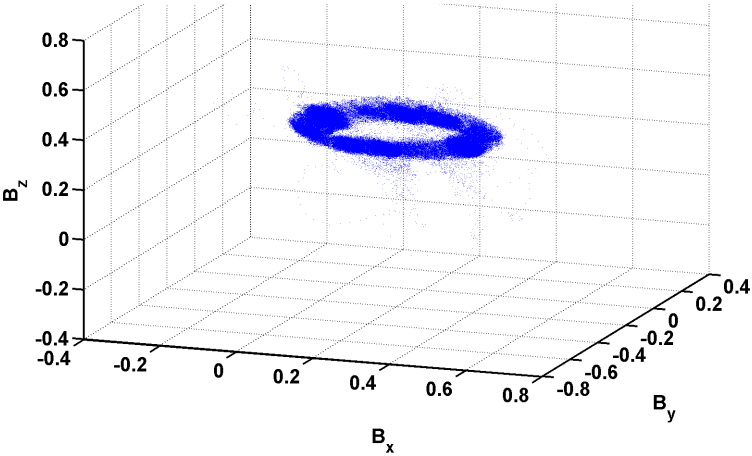
$$\mathbf{B}_m = R_{SI} \Delta R_{SI}^T (R_\phi R_\theta R_\psi \mathbf{B}_E + \mathbf{B}_s(u) + \Delta + \mathbf{B}_{loc}) \quad (4.2)$$

Depending on the position of the sensors inside the vehicle and on the trajectory, the locus of actually sensed data can be more or less “dense” and may cover more or less the ellipse based toroid. They can also be more or less disturbed, and with a toroidal structure more or less visible. In Fig. 4.10, three examples of experimental data are given to show the diversity of the possible scenarios. Effects of roll and pitch angles, even if they are not clearly visible, are present and can not be neglected.

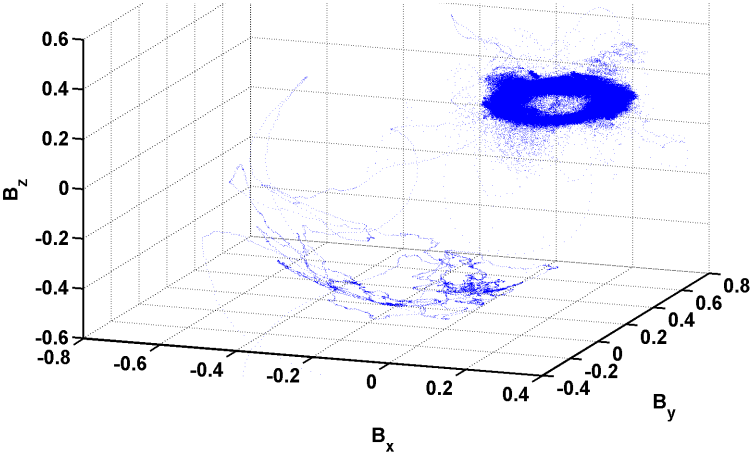
4.2.2 Ellipse detection

To obtain the heading, the most important point is to identify the parameters of the hard iron / soft iron effects which have turned the theoretical circular locus into an ellipse as discussed previously. This allows to eventually use the simple arctangent method discussed in Section 4.2. To achieve this, one can identify and then remove all the disturbances which have been discussed in the previous parts.

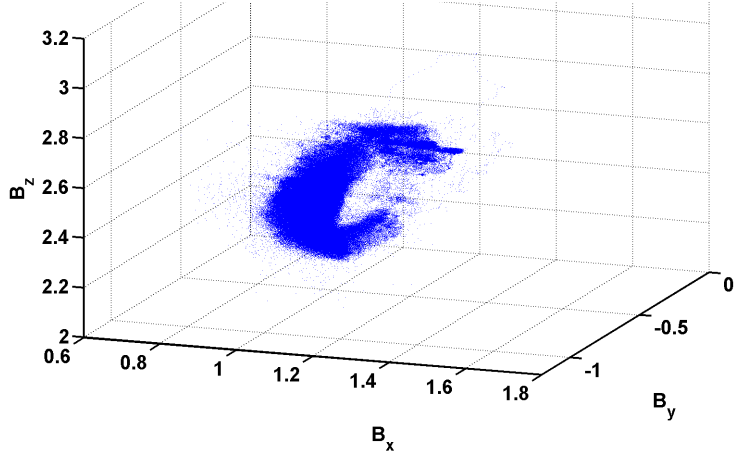
The speed pattern can be easily filtered when its frequency is not confusing with the yaw effect. For example, consider a maximum yaw rate of $120 \text{ }^\circ \cdot \text{s}^{-1}$, which corresponds to a frequency of 0.3 Hz, when the vehicle is moving with a speed higher than 20 km/h. For filtering purposes, a lowpass filter is sufficient. But, measurements performed at lower speeds can not be used to



(a) Easy case of the elliptic toroid.



(b) Elliptic toroid corrupted by erroneous data.



(c) Truncated elliptic toroid.

Figure 4.10: Examples of loci measured aboard various vehicles, along various trajectories.

estimate the heading of the vehicle. During these phases, the heading estimate is temporarily achieved using gyrometers.

Similarly, the measurements altered by roll and pitch must be discarded. Diagnosis can be based on using the attitudes observer presented in Chapter 6. The local disturbances are eliminated, using the norm of the measured magnetic field to control the consistency of the measurements with the data set.

After these operations, the processed measurements satisfy the following equation and are, theoretically, distributed along an ellipse in the three-dimensional space, for $\psi \in [0, 2\pi]$

$$\mathbf{B}_m = R_{SI} \Lambda R_{SI}^T (R_\psi \mathbf{B}_E + \Delta)$$

This ellipse can be described with others parameters, without modifying its locus. The rotation matrix $R_{\psi+\psi_0}$ describes a circle centered on the origin, the parameters a and b are the semi-axes of the ellipse, the components of Δ_0 give the center of the ellipse and finally, the rotation matrix R_{EP} defines the plane where the ellipse lies.

$$\mathbf{B}_m = R_{EP} \left(\begin{pmatrix} a & 0 & 0 \\ 0 & b & 0 \\ 0 & 0 & 1 \end{pmatrix} R_{\psi+\psi_0} \mathbf{B}_E + \Delta_0 \right)$$

All these parameters are identified with a least squares algorithm on the previously selected data set of measurements. There is one parameter which is not observable, the phase of the ellipse ψ_0 since the algorithm operates on the locus which is invariant in regard to the phase. Example of ellipse detection results is presented in Fig. 4.11.

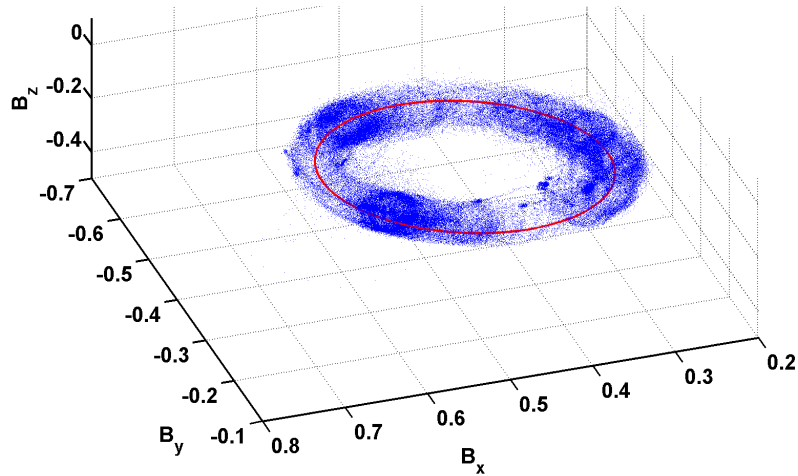


Figure 4.11: Detected ellipse (red) compared to the data set of magnetometer measurements.

4.2.3 Complementary filter

After having detected and identified the parameters of the ellipse, the heading angle can be computed with a complementary filter based on the value given by the exploitation of the magnetometer measurement, completed with informations from the gyrometer. This operation smoothes potential errors on the magnetic heading due to a bad rejection of measurements corrupted by disturbances or roll/pitch angles. Its main interest is to keep on providing an estimate when the speed is low (the speed pattern lies in the same frequency range as the yaw signal). Because of unobservability of the ellipse phase, the estimated heading angle is equal to the true heading, with a constant offset ψ_0 (in addition to the magnetic declination).

This estimation technique applied on the magnetometer measurements constitutes the equivalent of a non drifting gyrocompass. With the information on the initial heading, obtained e.g. using a reference compass when the vehicle is at rest, the value of the phase ψ_0 can be deduced and the true heading ψ can be obtained. Fig. 4.12 reports the comparison of the results obtained by the magnetic compass against the GPS data. The error is below 5° .

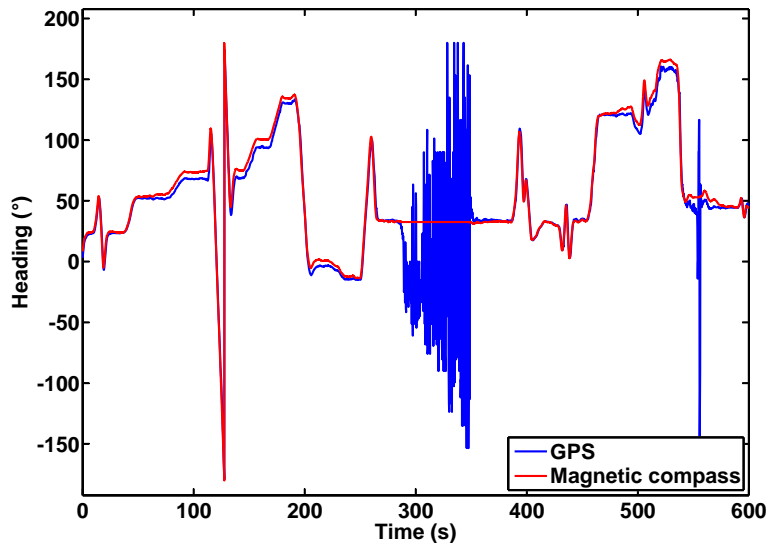


Figure 4.12: Comparison of the magnetic compass (red) with the GPS heading (blue, obtained with an arctangent on the speeds). GPS heading information gets really poor when the vector velocity is small and its orientation is ill-defined.

Chapter 5

Description of the relative navigation problem

Description du problème de navigation relative

Ce chapitre présente le problème associé à la navigation d'un véhicule automobile en rappelant le modèle dynamique associé et les capteurs embarqués à bord. L'idée directrice de la conception de l'observateur est le résultat d'une analyse des complémentarités qui peuvent être exploitées afin de compenser simultanément ou séquentiellement les différents défauts des capteurs.

We now expose the navigation problem under consideration.

5.1 Vehicle model under consideration

Consider a vehicle where inputs of the driver are unknown, rolling on a road without sideslip, in continuous contact with the road (the effects of suspension on the vehicle height are neglected as regards vehicle height). Consistently with notations of Chapter 1, the variable u denotes the longitudinal velocity of the vehicle, a_x, a_y, a_z the specific accelerations along the body axis, p, q, r the rotation speeds, ϕ, θ, ψ the roll, pitch and yaw angles and z the altitude (Fig. 5.1).

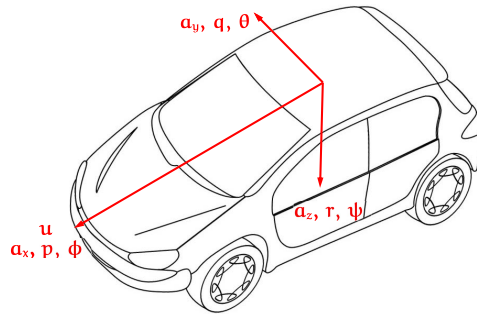


Figure 5.1: Notations in the body frame. Main directions of attitude angles are represented neglecting coupling introduced by Euler parametrization.

The dynamics and measurement equations of the 6-DOF rigid body are derived under the further assumption of small angles of roll and pitch. The dynamics of the accelerations and of the rotation speeds are unknown. The only dependable differential equations [Popp and Schiehlen, 2010] that can be written are

$$\begin{cases} \dot{z}(t) = -u(t)\theta(t) \\ \dot{u}(t) = a_x(t) - g\theta(t) \\ \dot{\phi}(t) = p(t) + r(t)\theta(t) \\ \dot{\theta}(t) = q(t) - r(t)\phi(t) \\ \dot{\psi}(t) = r(t) + q(t)\phi(t) \end{cases} \quad (5.1)$$

From the assumptions of zero sideslip and constant height relative to ground, the following equalities hold

$$\begin{cases} a_y(t) + g\phi(t) = u(t)r(t) \\ a_z(t) + g = -u(t)q(t) \end{cases} \quad (5.2)$$

The modeling proposed below corresponds to the rigid body constituted by the four wheels in contact with the road. Since the system is embedded on the vehicle shell, it can experiment small angles of roll and pitch due to the suspension system. Considering the inertial sensors on a moving frame inside the vehicle introduces second order terms in the equations (5.1-5.2) and are thus neglected. Then, we consider that the variables in these equations apply to the embedded system too (even if the assumption of no sideslip and constant height concern the vehicle). As a result, the estimated attitude angles include inclination and banking of the road as well as angles due to suspension system.

Finally, the $x - y$ trajectory is reconstructed with dead reckoning from initial conditions, as illustrated in Eq. (5.3) and Fig. 5.2, where, consistently with Chapter 1, x and y represent the coordinates of the center of gravity of the vehicle in the inertial frame of reference R_i .

$$\begin{cases} \dot{x}(t) = u(t) \cos \psi(t) \\ \dot{y}(t) = u(t) \sin \psi(t) \end{cases} \quad (5.3)$$

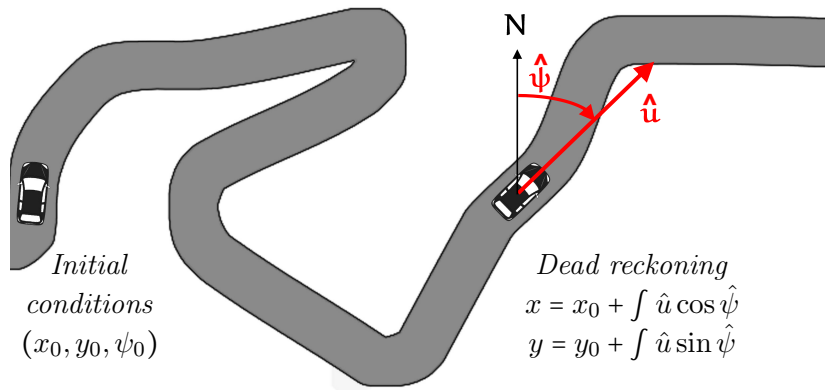


Figure 5.2: Trajectory computation based on dead reckoning.

5.2 Embedded sensors

The vehicle under consideration is equipped with

- a 3-axis magnetometer,
- a 3-axis accelerometer,
- a 3-axis gyrometer,
- a barometer.

These sensors are located on the vehicle shell. The accelerometers and the gyroscopes are biased. The altitude is derived from the barometer using the International Standard Atmosphere (ISA) model [International Organization for Standardization, 1975]. As explained in Chapter 4, the 3-axis magnetometer is used to provide a measurement of the yaw angle and of the velocity. As is detailed below in Section 5.3, it requires the knowledge of pitch and roll angles to obtain a good performance. The sensors are assumed to be aligned with the body frame, see Section 7.2 for details on the employed on-line alignment procedure.

For cinematic variables, the subscript m indicates measurements. The values $b_{a_x}, b_{a_y}, b_{a_z}$ (resp. b_p, b_q, b_r) are the bias of the accelerometers (resp. gyroscopes) which are varying over time with unknown dynamics.

Finally, the measurement equations are

$$\begin{cases} z_m(t) = z(t) \\ a_{x_m}(t) = a_x(t) - b_{a_x}(t) \\ a_{y_m}(t) = a_y(t) - b_{a_y}(t) \\ a_{z_m}(t) = a_z(t) - b_{a_z}(t) \\ p_m(t) = p(t) - b_p(t) \\ q_m(t) = q(t) - b_q(t) \\ r_m(t) = r(t) - b_r(t) \end{cases}$$

From the magnetometers, the speed can be estimated during medium to high speed phases. For low speed phases, help from inertial prediction is needed.

$$u_m(t) = u(t)$$

Subject to availability of estimates of roll and pitch angles, a heading measure can be obtained from the magnetometer (as explained in Chapter 4)

$$\psi_m(t) = \psi(t)$$

Each embedded sensor has its own pros and cons:

- The barometer has a long characteristic time and is very noisy, it is useful to detect altitude and long-term road inclination but can not be used for humps (which generate a quickly vanishing signal).
- The accelerometers are noisy and biased, they can not be directly used to get neither speed nor attitudes.

- The gyrometers are noisy and biased, they may be used at short-term to get the yaw rate during a curve or to get the pitch rate on a hump but they can not be used over long-time horizons to estimate the attitude.
- The magnetic velocimeter of Section 4.1 provides one with a speed estimate which can be improved when the accelerations of the vehicles are known.
- The magnetometer can not be used as a compass (see Section 4.2). An identification phase is necessary, in facts the (inertial) attitude estimates are usually better.

5.3 A view of practical issues

The ultimate objective is to compute the trajectory of the vehicle. Yet, the position is not observable by inertial techniques. We focus on the estimation of the speed and the heading of the vehicle, the trajectory being recreated by integration over time following Eq. (5.3). In other words, we solve a relative navigation problem. Given the restrictions on the behavior of the magnetic velocimeter and of the magnetic compass of Chapter 4, to have an accurate estimate of speed and heading, we need pitch and roll angles, debiased accelerometers. Therefore the complete state to be estimated is

$$\mathbf{X} = \begin{pmatrix} u & z & b_{a_x} & b_{a_y} & b_{a_z} & a_x & a_y & a_z & \dots \\ \phi & \theta & \psi & b_p & b_q & b_r & p & q & r \end{pmatrix}^T \quad (5.4)$$

Accelerometers and gyrometers, because of their biases, will be essentially exploited for their bandwidth and the high-frequency part of their signal. The magnetometer, as velocimeter or compass, is rather a low-frequency sensor because of the numerical treatment that is required.

Speed and heading can be delivered by the magnetometer but must be verified and/or completed with informations contained in the inertial measurements. As mentioned in Section 4.1, the magnetic velocimeter requires indication from inertial sensors during low speed phases. In practice, at high speed, the velocity information from the magnetometers measurements is used to estimate the accelerometers bias. At low speed, if the magnetic velocity estimate is not consistent with the inertial prediction, the velocimeter is deactivated (see Section 7.4) and the speed is propagated based on the last bias estimate as illustrated in Fig. 5.3. Similarly, the magnetic compass of Section 4.2 must not be used when magnetic disturbances or vehicle shell inclinations occur since the heading estimate is corrupted. During these phases, the heading estimate is computed through a complementary filter¹ with the vertical gyrometer (previously debiased outside these phases), as suggested in Section 4.2.3. This relay between the magnetic compass and the inertial sensor is pictured in Fig. 5.4.

The main difficulty concerns the attitudes angles which do not have any (direct) corresponding sensors. Knowing the speed, the low-frequency part of the pitch angle can be determined by the barometer. A complementary filter with the corresponding gyrometer would provide an estimate which neglects the roll-pitch coupling. But in this case, no information is available on the roll angle.

1. In case of a posteriori trajectory estimation, this result can be improved with optimal smoothing as presented in Section 7.5.

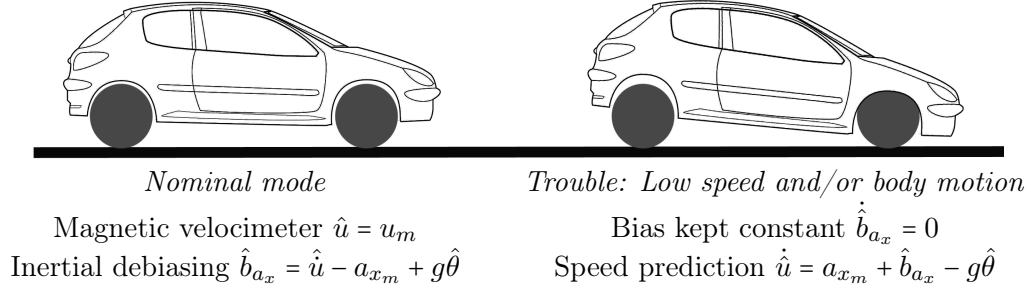


Figure 5.3: The magnetic velocimeter is used to estimate the bias of the accelerometer which takes over during low speed phases for prediction purposes.

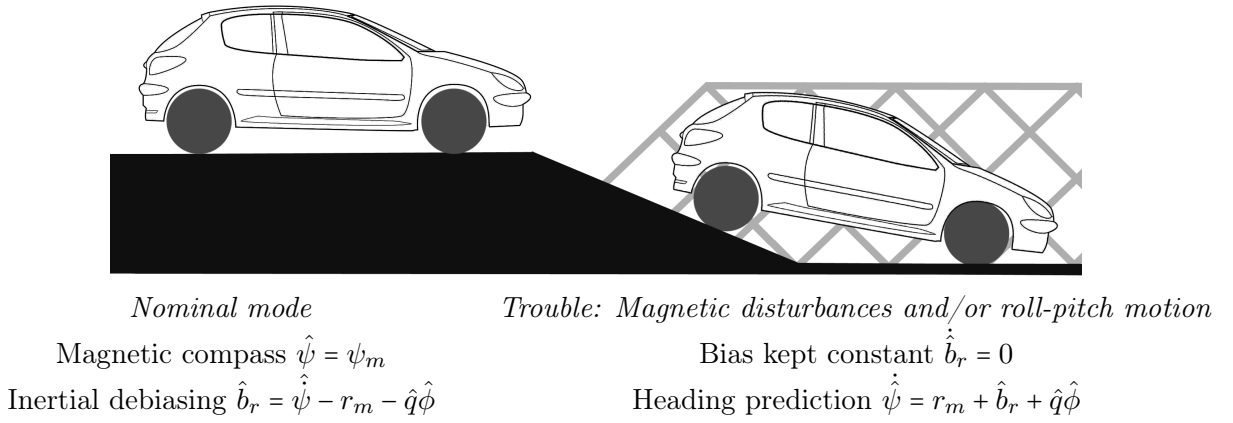


Figure 5.4: The magnetic compass is used to estimate the bias of the gyrometer which takes over when magnetic disturbances occur for prediction purposes.

The debiasing method presented in this thesis is a complex combination of algorithms based on observability properties of the vehicle dynamics: since the whole state is not observable with these sensors, we propose *Temporally Interconnected Observers (TIO)* arguing that during straight-line motion, one can estimate the pitch dynamics, while, during curve motion, it is possible to catch the roll dynamics. Permanent observability on pitch dynamics is transferred during curves on the roll dynamics by losing observability on the pitch bias. A trajectory being constituted of straight-lines and curves (Fig. 5.2), roll and pitch dynamics can be estimated whereas they are not observable simultaneously.

As a result, indirect low-frequency measurements from the barometer and the magnetometer are complementary with direct high-frequency measurements from the accelerometers and the gyrometers, and allow to design an observer which ensures the estimation of the complete state (5.4) with guaranty of convergence.

Chapter 6

Design of the navigation system

Conception du système de navigation

Sur la base du chapitre précédent, ce chapitre présente la méthode d'interconnection temporelle d'observateurs qui est mise en place pour apporter une solution au problème de navigation. Un premier niveau d'interconnection divise l'état afin d'isoler le point dur qu'est l'estimation d'attitude du véhicule. Pour cela, un second niveau d'interconnection est proposé, il s'agit justement d'observateurs temporellement interconnectés. Après avoir établi l'observabilité des différents sous-systèmes, une preuve de convergence du schéma global d'observation est apportée.

We now expose the design of the observers at the heart of the navigation system.

6.1 Observer design

According to the observability analysis presented in this chapter for the vehicle model of , the observer is designed using two levels of interconnections. The first level consists in (classically) splitting the state to estimate in subsets. In details, four sub-problems are distinguished. They can be treated simultaneously in the implementation. The second level of interconnection is precisely introduced to address the lack of observability encountered in one of the four sub-problems. The lack is due to the fact that the variables can not be simultaneously observed, but the observability deficiency corresponds to a different variable depending on the nature of the trajectory currently followed by the vehicle. then, three TIO are proposed and convergence of the scheme is proved.

6.1.1 Interconnected subsystems

The method we propose to estimate the state is inspired by the theory of observers for interconnected systems widely detailed in [Besançon and Hammouri, 1998]. The problem is split into four sub-problems. First, we assume that the magnetic velocimeter is functioning thanks to

the pitch detection algorithm. A velocity observer is directly derived from it. With an observer on the barometer to estimate the altitude, it constitutes the *first problem* Σ_I .

$$\Sigma_I : \begin{cases} \hat{u} = f(u_m) \\ \hat{z} = f(z_m) \end{cases}$$

The *second problem* Σ_{II} concerns the heading and yaw rate estimation. Only the yaw rate is interesting from the point of view of the interconnections: in a first approximation, it is estimated from the corresponding gyrometer, with ZUPTs during which the sensor bias is perfectly determined.

$$\Sigma_{II} : \{ (\hat{\psi}, \hat{r}, \hat{b}_r) = f(r_m, \psi_m) \}$$

Considering the velocity and the altitude as known parameters, from the “horizontal” gyrometers, the *third problem* Σ_{III} is to estimate the biases of the gyrometers, the pitch and roll angles.

$$\Sigma_{III} : \{ (\hat{\phi}, \hat{\theta}, \hat{p}, \hat{q}, \hat{b}_p, \hat{b}_q) = f(\hat{u}, \hat{z}, p_m, q_m, \hat{r}) \}$$

Finally, we assume that all the preceding variables are known parameters, and from the accelerometers, we reconstruct their biases and the acceleration in the *fourth problem* Σ_{IV} .

$$\Sigma_{IV} : \{ (\hat{a}_x, \hat{a}_y, \hat{a}_z, \hat{b}_{a_x}, \hat{b}_{a_y}, \hat{b}_{a_z}) = f(\hat{u}, \hat{\phi}, \hat{\theta}, \hat{q}, \hat{r}, a_{xm}, a_{ym}, a_{zm}) \}$$

Eventually, estimates are used to close the interconnection loop as is exposed in Fig. 6.1. The magnetic compass takes advantage of the roll and pitch angles estimation to reject faulty measurements and improve the heading estimate, the yaw rate estimate generated by the complementary filter is improved (which means that, in fine, the roll and pitch estimation benefits from the loop closing)¹. The acceleration estimates are used to achieve speed prediction, detect potentially erroneous information from the velocimeter and, if need be, integrated to estimate the correct velocity. The proposed observer design corresponds to the interconnection pictured in Fig. 6.1, presenting the four problems detailed above, Σ_I , Σ_{II} , Σ_{III} and Σ_{IV} , describing respectively the velocity dynamics, the vertical angular dynamics, the horizontal angular dynamics, and the acceleration measurement equations. The green arrows represent the “nominal mode”: the magnetic velocimeter and the magnetic compass are considered functioning on their own. The blue dashed arrows indicate how these magnetic informations are used to estimate the biases of the inertial sensors. Red dashed arrows show how the inertial sensors exert a backup check on the consistency of the magnetic informations and can take over if necessary. From Fig. 6.1, we can extract two functioning modes. Fig. 6.2 shows the “nominal mode” where the magnetic velocimeter and the magnetic compass are used to estimate the trajectory and the biases of the inertial sensors. In Fig. 6.3, the magnetic informations are unavailable, the biases are kept constant and the trajectory is estimated in facts with a classical inertial navigation technique.

1. Convergence of the loop will be mentioned in Part 6.1.2

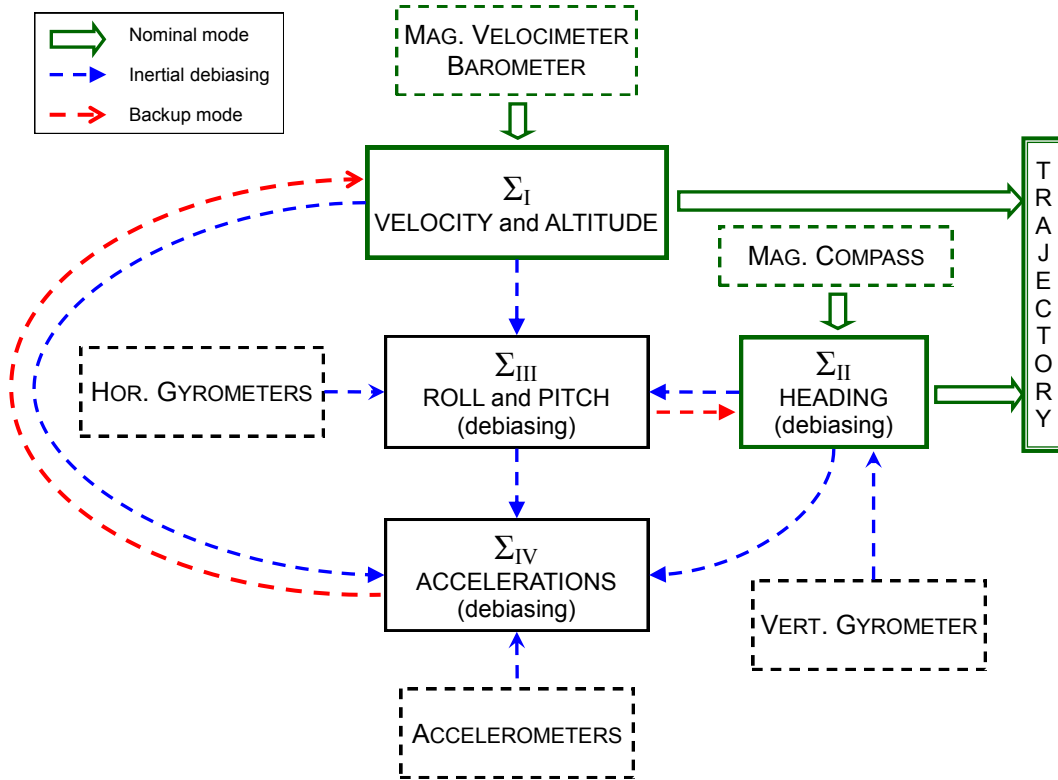


Figure 6.1: Subsystems interconnection. The nominal mode corresponds to the green path which is sufficient to reconstruct the trajectory. Meanwhile, biases are determined (blue dashed paths). They are useful when data corruption discard the nominal mode. This backup allows to continuously provide the trajectory estimate. The two modes are illustrated in Fig. 6.2 and Fig. 6.3.

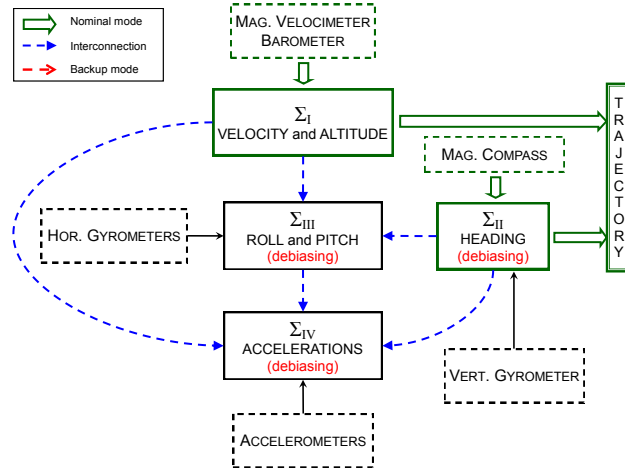


Figure 6.2: Nominal mode: trajectory reconstruction based on magnetometers measurements.

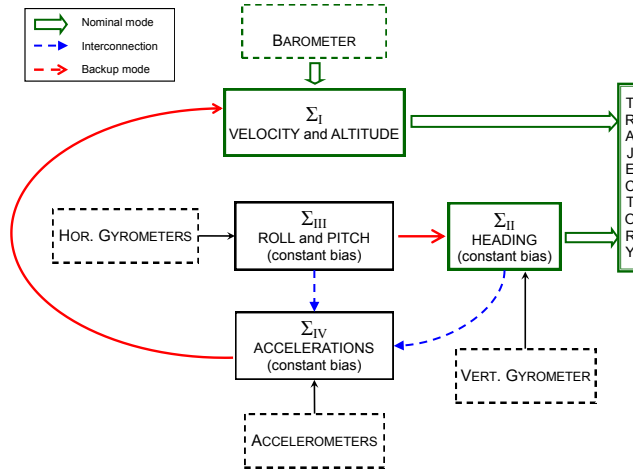


Figure 6.3: Backup mode: classic inertial navigation.

The observability of subproblem Σ_I is obvious. Any observer can be used to obtain speed and altitude estimates. Low-speed errors of the velocimeter are smoothed out using the feedback from the others subproblems.

Exploiting the vertical gyrometer with ZUPT techniques, an estimate of the yaw rate can be obtained with an accuracy sufficient to feed Σ_{III} . Observability on heading angle arises from the magnetic compass. The feedback from Σ_{III} improves the magnetic compass information and allows a fusion with the vertical gyrometer to eventually provide an improved estimate of the yaw rate.

Considering the previous interconnected subproblems, all the parameters of the fourth subproblem are known, and therefore, the observability is trivial.

The remaining third subproblem Σ_{III} is not directly observable, another level of interconnection is proposed to address it. To simplify the following discussion, rather than considering the velocity u and the altitude z in the state and in the measurement, we consider θ_m a virtual measurement of θ which can be obtained by $\theta_m = -\hat{z}/\hat{u}$. The roll and pitch rates are also discarded since they can be formed from the corresponding measurements and the biases estimates, the subset to be estimated is reduced to $X_{III} = [\phi \ \theta \ b_p \ b_r]$. With this aim in view, three main types of trajectory for the vehicle are studied. These are defined as follows. If the velocity is null, the vehicle is at rest. Otherwise, if the yaw rate is null, the vehicle is going in straight line, else the vehicle is in a curve. As will appear, for each trajectory, a subset of X_{III} is observable. This temporal interconnection is illustrated in Fig. 6.4.

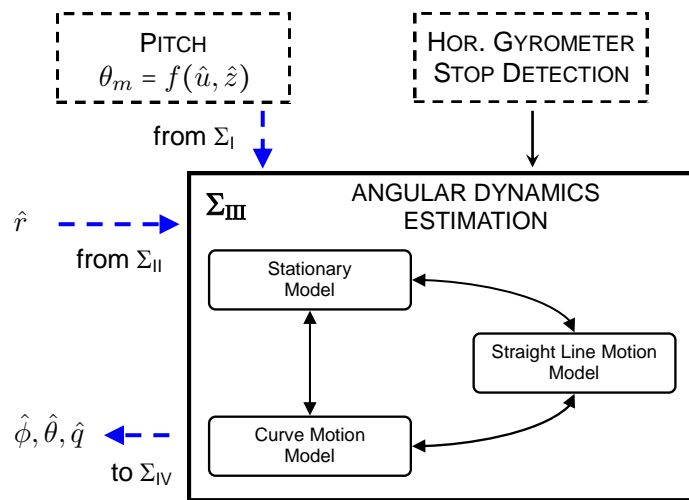


Figure 6.4: Two levels of interconnected observers.

6.1.2 Decomposition into Temporally Interconnected Observers

We now wish to write the dynamics of X_{III} . We first consider the vehicle at rest, the angular rates are null and the angles are unobservable but remain unchanged. The following relations

hold, with t_0 the initial stop-time.

$$\begin{cases} p(t) = 0 & q(t) = 0 \\ \phi(t) = \phi(t_0) & \theta(t) = \theta(t_0) \end{cases} \quad (6.1)$$

The gyrometers directly provide the values of the biases (measurements are in fact filtered to remove noise)

$$\begin{aligned} \hat{b}_p(t) &= -p_m(t) \\ \hat{b}_q(t) &= -q_m(t) \end{aligned}$$

If the angles were already known before the stop of the vehicle, \mathbf{X}_{III} could be estimated at rest. Now, we assume that the vehicle is moving. After leaving the rest phase, the vehicle switches between straight-line and curve, and this is apparent on the yaw rate. Along the trajectories, the dynamics are as follows

$$\begin{array}{cc} \text{Straight-line motion} & \text{Curve motion} \\ \left\{ \begin{array}{l} \dot{\phi} = p = p_m + b_p \\ \dot{\theta} = q = q_m + b_q \\ \dot{b}_p = 0, \quad \dot{b}_q = 0 \end{array} \right. & \left\{ \begin{array}{l} \dot{\phi} = (p_m + b_p) + r\theta \\ \dot{\theta} = (q_m + b_q) - r\phi \\ \dot{b}_p = 0, \quad \dot{b}_q = 0 \end{array} \right. \end{array} \quad (6.2)$$

For sake of simplicity, biases, which are in fact slowly varying, are considered constant in the equations. It shall be noted that having variable biases does not interfere in the observability analysis which does not take into account dynamics noise, but complexifies the convergence study, e.g. by requiring extra states to be modeled. The term of observability is kept rather than the term of identification since only the deterministic part of the bias model is null and, later, we show that variable biases are estimated and that the proof of convergence can be modified to take in account bias variability.

To study the dynamics in straight line and curve motion, we define matrices (A_1, B_1, C_1) and (A_2, B_2, C_2, D_2) such that, with $\mathbf{X}_1 = [\theta \quad b_q]^T$, $\mathbf{X}_2 = [\phi \quad \theta \quad b_p]^T$ and $\mathbf{U} = [p_m \quad q_m]^T$, the previous equations (6.2) yield

$$\begin{cases} \dot{\mathbf{X}}_1 &= A_1 \mathbf{X}_1 + B_1 \mathbf{U} \\ &= \begin{pmatrix} 0 & 1 \\ 0 & 0 \end{pmatrix} \mathbf{X}_1 + \begin{bmatrix} 0 & 1 \\ 0 & 0 \end{bmatrix} \mathbf{U} \\ \mathbf{Y}_1 &= C_1 \mathbf{X}_1 = \begin{pmatrix} 1 & 0 \end{pmatrix} \mathbf{X}_1 \end{cases} \quad (6.3)$$

$$\begin{cases} \dot{\mathbf{X}}_2 &= A_2(t) \mathbf{X}_2 + B_2 \mathbf{U} + D_2 b_q \\ &= \begin{pmatrix} 0 & r & 1 \\ -r & 0 & 0 \\ 0 & 0 & 0 \end{pmatrix} \mathbf{X}_2 + \begin{bmatrix} 1 & 0 \\ 0 & 1 \\ 0 & 0 \end{bmatrix} \mathbf{U} + \begin{bmatrix} 0 \\ 1 \\ 0 \end{bmatrix} b_q \\ \mathbf{Y}_2 &= C_2 \mathbf{X}_2 = \begin{pmatrix} 0 & 1 & 0 \end{pmatrix} \mathbf{X}_2 \end{cases} \quad (6.4)$$

Leaving out the cases when the vehicle is at rest, we consider a sequence of straight lines and curve motions. Let us note T_1 the straight-line motion duration, T_2 the curve motion duration. It

is assumed that all the straight-lines have the same duration and that the same holds for straight lines. This simplification is only made for ease of notations and can be easily relaxed. Recursively, with $i \geq 0$ and $t_0 = 0$, define t_i the straight-line motion starting time ($t_{i+1} = t_i + T_1 + T_2$), $\chi(2i)$ the variable χ at time t_i , $\chi(2i+1)$ the variable χ at time $t_i + T_1$. The times t_i are known and defined by the switching policy. The switching policy is, when the estimated yaw rate is null, to use the straight-line model, and otherwise, to use the curve model. The value of \hat{r} depends on the estimation of the yaw gyrometer bias, but potential error on \hat{b}_r does not undermine the TIO algorithm due to the small value of the bias. The yaw rate being continuous, there is consequently continuity between the two considered models and estimate error on b_r intervenes as second order in the dynamics. On the contrary, the switching policy to/from rest is more critical and, therefore, the stop detection needs to be very accurate because at rest, biases are directly updated from the gyrometers which can be detrimental. In particular, a vehicle during a parking maneuver at low-speed can generate interpretation errors and result in wrong estimates for biases.

The TIO algorithm we propose involves two observers $\hat{\mathbf{X}}_1$ and $\hat{\mathbf{X}}_2$, which each provides an asymptotically converging estimate of \mathbf{X}_1 and \mathbf{X}_2 , respectively, which are subsets of \mathbf{X}_{III} . The two observers are used alternatively according to the switching policy. The continuity between the observers is achieved by a propagator P_i of the unestimated states along with the observer $\hat{\mathbf{X}}_i$. This structure is illustrated in Fig. 6.5 where the block INIT represents the initialization which occurs at every switching time. The newly switched-on observer-propagator is initialized using the estimates obtained from the other one. The whole TIO structure can be considered as an observer which provides an estimate $\hat{\mathbf{X}}_{III}$ from the measurements.

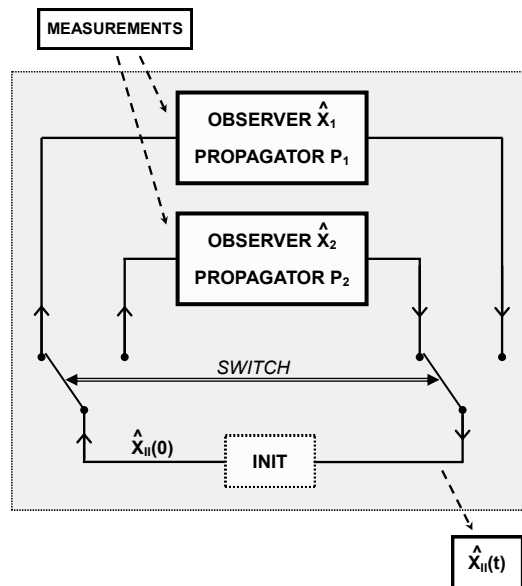


Figure 6.5: Temporally Interconnected Observers (TIO) structure for estimating the vehicle angular dynamics.

Between the times t_i and $t_i + T_1$ (straight-line motion), the following observer-propagator is considered.

$$\left| \begin{array}{l} \text{Observer: } \hat{\mathbf{X}}_1 \text{ is used to estimate } \mathbf{X}_1 = [\theta \quad b_q]^T \\ \text{Propagator: } P_1 \{ \dot{\phi} = p_m + b_p, \quad \dot{b}_p = 0 \} \end{array} \right. \quad (6.5)$$

Respectively, between the times $t_i + T_1$ and $t_i + T_1 + T_2$ (curve motion), the other observer-propagator is used.

$$\left| \begin{array}{l} \text{Observer: } \hat{\mathbf{X}}_2 \text{ is used to estimate } \mathbf{X}_2 = [\phi \quad \theta \quad b_p]^T \\ \text{Propagator: } P_2 \{ \dot{b}_q = 0 \} \end{array} \right. \quad (6.6)$$

The question we now wish to address is the asymptotic behavior of the estimate $\hat{\mathbf{X}}_{III}$ as the vehicle travels along a succession of straight-lines and curves.

6.2 Observability for the models used in the Temporally Inter-connected Observers

To address the previously formulated question, we study the observability of the various models involved.

6.2.1 Uniform and Complete Observability of the straight-line motion model

System (6.3) is trivially UCO because the reconstructibility Grammian can be readily computed as follows

$$\Phi(t, s) = \begin{pmatrix} 1 & t-s \\ 0 & 1 \end{pmatrix}, \quad W^*(t-\sigma, t) = \begin{pmatrix} \sigma & -\sigma^2/2 \\ -\sigma^2/2 & \sigma^3/3 \end{pmatrix}$$

Hence, by inspecting the eigenvalues of W^* , one obtains $W^*(t-\sigma, t) \geq \sigma/4$, for all $\sigma > 0$.

6.2.2 Differential Observability of the curve motion model

The local observability matrix is calculated below:

$$\mathbb{O}(t) = (Q_0(t) \quad Q_1(t) \quad Q_2(t)) \begin{pmatrix} Q_0^T(t) \\ Q_1^T(t) \\ Q_2^T(t) \end{pmatrix} = \begin{pmatrix} r^2(t) + \dot{r}^2(t) & \dot{r}(t)r^2(t) & \dot{r}(t)r(t) \\ \dot{r}(t)r^2(t) & 1 + r^4(t) & r^3(t) \\ \dot{r}(t)r(t) & r^3(t) & r^2(t) \end{pmatrix}$$

We wish to prove that there exists $\mu > 0$ such that $\mathbb{O}(t) \geq \mu I$ for all t . The matrix $(\mathbb{O}(t) - \mu I)$ is symmetric real, therefore it is positive semi-definite if and only if its eigenvalues are positive. Equivalently, we wish to prove that there exists $\mu > 0$ such that the eigenvalues of $\mathbb{O}(t)$ are greater than μ for all t . By construction of $\mathbb{O}(t) = Q_o(t)Q_o^T(t)$, these eigenvalues are real and positive. They are the roots of the characteristic polynomial $P(s, t) = |\mathbb{O}(t) - sI|$ which can be lower-bounded, uniformly in t , for s positive, by the polynomial $P_0(s)$ where r is the switching

policy threshold and R (respectively \mathring{R}) the dynamics upper-bound on the yaw rate (resp. yaw rate derivative)

$$P_0(s) = -s^3 + (r^2 + 1)^2 s^2 - (R^6 + R^4 + 2R^2 + \mathring{R}^2)s + r^4$$

Yet, $P_0(0) = r^4 > 0$. Therefore, there exists $\mu > 0$ such that $P_0(s) > 0$ for $s \in [0, \mu]$. In turn, the roots of $P(s, t)$ are uniformly bounded by μ .

According to Definition 6, DO of the curve motion model is proved. Further, an estimate of the reconstructibility Grammian can be established, for sake of quantitatively estimate the decay rate of the error.

Consider the following input-less system which is equivalent to the system (6.4) from the view-point of observability (b_q being known)

$$\begin{cases} \dot{\phi}(t) = r(t)\theta(t) + b_p \\ \dot{\theta}(t) = -r(t)\phi(t) \\ \dot{b}_p(t) = 0 \end{cases}$$

with $0 < r \leq |r(t)| \leq R, \quad \forall t \geq 0$.

Without loss of generality, $r(t)$ is assumed to be (strictly) positive. Consider the following bijective mapping (time-change)

$$h_{t_0}(t) = \int_t^{t_0} r(u) du$$

Lemma 11. *For any t_0 , consider $T_0 = t_0 - h_{t_0}^{-1}(2\pi)$, if $r(t)$ is sufficiently close to its first order (affine) Taylor expansion for $t \in [t_0 - T_0, t_0]$, then the reconstructibility Grammian satisfies*

$$W^*(t_0 - T_0, t_0) \geq \alpha T_0 I \tag{6.7}$$

where $\alpha = \min\left(1, \frac{1}{R^2}\right) \frac{r}{R} \frac{2-\sqrt{2}}{4}$.

Proof. For r sufficiently close to its affine Taylor expansion, there exist (r_0, r_1) which satisfy, for $t \in [t_0 - T_0, t_0]$,

$$r(t) = r_0(1 + r_1(t_0 - t) + o(r_1 T_0)) \tag{6.8}$$

Consider the following new coordinates (y, z)

$$y(h_{t_0}(t)) = -\phi(t), \quad z(h_{t_0}(t)) = \theta(t), \quad b = b_p$$

From the derivative of h_{t_0} , the derivative of the new coordinates can be obtained

$$\dot{h}_{t_0}(t) = -r(t), \quad \dot{\phi}(t) = r(t)\dot{y}(h_{t_0}(t)), \quad \dot{\theta}(t) = -r(t)\dot{z}(h_{t_0}(t))$$

Consider the new differential system (where we note $\tau = h_{t_0}(t)$)

$$\dot{y}(\tau) = z(\tau) + \frac{b}{r(h_{t_0}^{-1}(\tau))}, \quad \dot{z}(\tau) = -y(\tau), \quad \dot{b}(\tau) = 0 \tag{6.9}$$

For any $\mathbf{X}_2(t_0) = [\phi(t_0) \quad \theta(t_0) \quad b_p]_0^T$, equivalent initial conditions can be easily found

$$\phi(t_0) = -y_0, \quad \theta(t_0) = z_0, \quad b_p = b_0$$

System (6.9) is a forced linear time invariant oscillator of the form

$$\ddot{z}(\tau) = -z(\tau) + f(\tau)$$

Its solution is as follows

$$z(\tau) = z_0 \cos(\tau) - y_0 \sin(\tau) + \int_0^\tau \sin(\tau - \sigma) f(\sigma) d\sigma \quad (6.10)$$

Then, one can estimate the Grammian

$$\begin{aligned} X_2^T(t_0)W^*(t_0 - T_0, t_0)X_2(t_0) &= X_2^T(t_0) \int_{t_0-T_0}^{t_0} \Phi_2^T(t, t_0)C_2^T(t)C_2(t)\Phi_2(t, t_0)dtX_2(t_0) \\ &= \int_{t_0-T_0}^{t_0} X_2^T(s)C_2^T C_2 X_2(s)ds = \int_{t_0-T_0}^{t_0} \theta^2(s)ds \end{aligned} \quad (6.11)$$

To lower-bound (6.11), from the Taylor expansion of $r(t)$ (Eq.(6.8)) which assumes that r is close to its affine Taylor expansion, one can compute

$$f(\tau) = -\frac{b}{r(h_{t_0}^{-1}(\tau))} = f_0(1 + f_1\tau + o(f_1T_0')) \quad (6.12)$$

$$\text{with } \begin{cases} f_0 = -\frac{b}{r_0} & f_1 = \frac{r_1}{r_0} \\ T_0' = h_{t_0}(t_0 - T_0) = 2\pi & f_1T_0' \approx r_1T_0 \end{cases}$$

Introducing the Taylor expansion of (6.12) in the solution (6.10), one obtains

$$z(\tau) = z_0 \cos(\tau) - y_0 \sin(\tau) + f_0(1 - \cos(\tau) + f_1(\tau - \sin(\tau)) + o(f_1T_0'))$$

Now, consider the following decomposition of the integral

$$\int_0^{T_0'} z^2(\tau) d\tau = I_1 + I_2 + I_3 + I_4 + I_5 + I_6$$

Each term can be computed separately

$$I_1 = \int_0^{T_0'} (z_0 \cos(\tau))^2 d\tau = \frac{z_0^2}{2} T_0'$$

$$I_2 = \int_0^{T_0'} (y_0 \sin(\tau))^2 d\tau = \frac{y_0^2}{2} T_0'$$

$$I_3 = \int_0^{T_0'} f_0^2 (1 - \cos(\tau) + f_1(\tau - \sin(\tau)) + o(f_1T_0'))^2 d\tau = \frac{3}{2} f_0^2 T_0' \left(1 + \frac{2}{3} f_1 T_0' + o(f_1T_0') \right)$$

$$I_4 = -2 \int_0^{T_0'} z_0 \cos(\tau) y_0 \sin(\tau) d\tau = 0$$

$$I_5 = 2 \int_0^{T_0'} z_0 \cos(\tau) f_0 (1 - \cos(\tau) + f_1(\tau - \sin(\tau)) + o(f_1T_0')) d\tau = -z_0 f_0 T_0' (1 + o(f_1T_0'))$$

$$I_6 = -2 \int_0^{T_0'} y_0 \sin(\tau) f_0 (1 - \cos(\tau) + f_1(\tau - \sin(\tau)) + o(f_1T_0')) d\tau = 3y_0 f_0 (f_1 T_0' + o(f_1T_0'))$$

Gathering the expressions above, a symmetric matrix Π can be constructed such that

$$\int_0^{T'_0} z^2(\tau) d\tau = \frac{T'_0}{2} [y_0 \quad z_0 \quad f_0] \Pi \begin{bmatrix} y_0 \\ z_0 \\ f_0 \end{bmatrix}$$

with $\Pi = \begin{pmatrix} 1 & 0 & 3(f_1 + o(f_1)) \\ 0 & 1 & -(1 + o(f_1 T'_0)) \\ \text{sym} & \text{sym} & 3 + 2f_1 T'_0 + o(f_1 T'_0) \end{pmatrix}$.

The minimum eigenvalue can be bounded thanks to the positiveness of f_1

$$\lambda_{\min}(\Pi) = \left(2 + f_1 T'_0 - \sqrt{2 + 2f_1 T'_0 + o(f_1 T'_0)} \right) \geq 1/2$$

Thus, the Grammian (6.11) can be lower-bounded

$$\begin{aligned} \int_{t_0-T_0}^{t_0} \theta^2(t) dt &= \int_{t_0-T_0}^{t_0} z^2(h_{t_0}(t)) dt \\ &= \int_0^{T'_0} z^2(\tau) \frac{d\tau}{r(h_{t_0}^{-1}(\tau))} \geq \frac{1}{R} \int_0^{T'_0} z^2(\tau) d\tau \\ &\geq \frac{r}{R} \frac{T_0}{4} (y_0^2 + z_0^2 + f_0^2) \\ &\geq \min\left(1, \frac{1}{r_0^2}\right) \frac{r}{R} \frac{T_0}{4} \|\mathbf{X}_2(t_0)\|^2 \end{aligned}$$

Then, with $\alpha = \min\left(1, \frac{1}{R^2}\right) \frac{r}{4R}$, we have proven

$$W^*(t_0 - T_0, t_0) \geq \alpha T_0 I$$

which gives the conclusion. □

Further, one can establish the following result.

Proposition 1. *For all t_0 , for all $T \geq \frac{2\pi}{r}$, if there exist (r_0, r_1) such that, for $t \in [t_0 - \frac{2\pi}{r} \dots t_0]$,*

$$r(t) = r_0 \left(1 + r_1 (t_0 - t) + o\left(\frac{2\pi r_1}{r}\right) \right) \tag{6.13}$$

then the reconstructibility Grammian W^ satisfies*

$$W^*(t_0 - T, t_0) \geq \alpha \frac{2\pi}{R} \eta I \tag{6.14}$$

where $\alpha = \min\left(1, \frac{1}{R^2}\right) \frac{r}{4R}$ and η is the integer part of $\frac{rT}{2\pi}$.

Proof.

With Chasles' theorem,

$$\begin{aligned} W^*(t_0 - T, t_0) &\geq W^*\left(t_0 - \frac{2\pi}{r}\eta, t_0\right) \\ &\geq \sum_{i=0.. \eta-1} W^*\left(t_0 - \frac{2\pi}{r}(i+1), t_0 - \frac{2\pi}{r}i\right) \\ &\geq \sum_{i=0.. \eta-1} W^*\left(\left(t_0 - \frac{2\pi}{r}i\right) - \frac{2\pi}{r}, \left(t_0 - \frac{2\pi}{r}i\right)\right) \end{aligned}$$

By assumption, Lemma 11 holds for all $t_0^{(i)} = t_0 - \frac{2\pi}{r}i$, $i = 0.. \eta - 1$.

$$W^*\left(t_0^{(i)} - T_0^{(i)}, t_0^{(i)}\right) \geq \alpha T_0^{(i)} I$$

Yet,

$$\frac{2\pi}{R} < T_0^{(i)} < \frac{2\pi}{r}$$

Hence, since the application $T \mapsto W^*(t_0 - T, t_0)$ is increasing for all t_0

$$W^*\left(t_0^{(i)} - \frac{2\pi}{r}, t_0^{(i)}\right) \geq \alpha \frac{2\pi}{R} I$$

Finally,

$$W^*(t_0 - T, t_0) \geq \alpha \eta \frac{2\pi}{R} I$$

which gives the conclusion. □

The constants T and $\alpha\eta$ of the system are depending, on one hand, on the lower bound of the reconstructibility Grammian, and on the other hand, on the length of the integration interval. To establish the proof above, the whole curve motion has been considered and the constants arise from a worst case analysis: the lower-bound is proportional to the minimum of the yaw rate divided by its maximum, and the integration length is lower-bounded by the inverse of the minimum of the yaw rate (at small values of the yaw rate, the system is poorly observable).

Yet, an extra decomposition of the curve motion can be considered as well for sake of obtaining tighter estimates. This point is illustrated in Fig. 6.6. The switching policy defines the curve motion as the portion between the blue lines, considering short parts of curve between each couple of green lines. First, the assumption of linear variation of the yaw rate is more easily fulfilled, and second, the central parts with high rate present a larger minimum yaw rate, yielding, in turn, an increase level of observability for a shorter integration length of the Grammian.

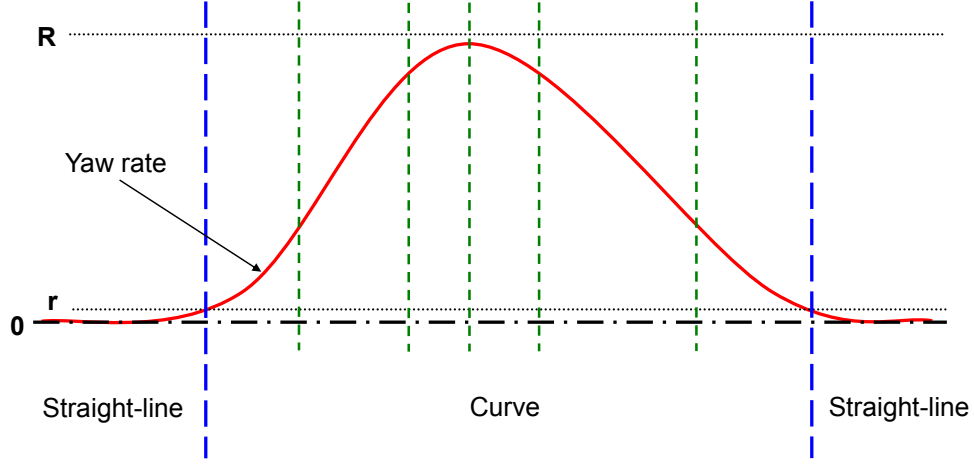


Figure 6.6: Extra decomposition of the curve motion.

6.3 Convergence of the Temporally Interconnected Observers structure

As discussed in Section 6.2.1, System (6.3) is UCO. With Theorem 10, let $K_1(t)$ be the Kalman gain corresponding to the Kalman filter with tuning matrices Q_1 and R_1 . The observer is as follows,

$$\dot{\hat{\mathbf{X}}}_1 = A_1 \hat{\mathbf{X}}_1 + B_1 \mathbf{U} + K_1(t)(\mathbf{Y}_1 - C_1 \hat{\mathbf{X}}_1) \quad (6.15)$$

At time $t_i + T_1$, estimates $\hat{\theta}(2i+1)$ and $\hat{b}_q(2i+1)$ are available. In particular, the value $\hat{b}_q(2i+1)$ can be used to drive System (6.4). Since the bias b_q is constant, considering it as a given parameter, the System (6.4) is DO (see Section 6.2.2). Let $K_2(t)$ be the Kalman gain corresponding to the Kalman filter with tuning matrices Q_2 and R_2 , given by Theorem 10. The observer is computed as follows

$$\dot{\hat{\mathbf{X}}}_2 = A_2(t) \hat{\mathbf{X}}_2 + B_2 \mathbf{U} + D_2 \hat{b}_q(2i+1) + K_2(t)(\mathbf{Y}_2 - C_2 \hat{\mathbf{X}}_2) \quad (6.16)$$

Combining System (6.3) with Eq. (6.15) and System (6.4) with Eq. (6.16), one obtains the error dynamics

$$\dot{\tilde{\mathbf{X}}}_1 = (A_1 - K_1(t)C_1) \tilde{\mathbf{X}}_1 \quad (6.17)$$

$$\dot{\tilde{\mathbf{X}}}_2 = (A_2(t) - K_2(t)C_2) \tilde{\mathbf{X}}_2 + D_2 \tilde{b}_q(2i+1) \quad (6.18)$$

Let Φ_1 and Φ_2 the transition matrices for the unforced systems corresponding to Eq. (6.17) and Eq. (6.18), respectively, one has

$$\begin{aligned} \frac{\partial \Phi_1}{\partial t}(t, s) &= (A_1 - K_1(t)C_1) \Phi_1(t, s), & \Phi_1(t, t) &= I \\ \frac{\partial \Phi_2}{\partial t}(t, s) &= (A_2(t) - K_2(t)C_2) \Phi_2(t, s), & \Phi_2(t, t) &= I \end{aligned}$$

From Theorem 10, there exist $(k_1, \lambda_1, k_2, \lambda_2)$ such that

$$\|\Phi_1(t, s)\| \leq k_1 e^{-\lambda_1(t-s)}, \quad \|\Phi_2(t, s)\| \leq k_2 e^{-\lambda_2(t-s)} \quad (6.19)$$

Our goal is to study the convergence of $\hat{\mathbf{X}}_{III}$, in particular from t_i to t_{i+1} . We now use the estimates established above to study the convergence of the TIO structure introduced in Section 6.1.2. The solutions of System (6.17) and System (6.18) are

$$\tilde{\mathbf{X}}_1(2i+1) = \Phi_1(t_i + T_1, t_i) \tilde{\mathbf{X}}_1(2i) \quad (6.20)$$

$$\tilde{\mathbf{X}}_2(2(i+1)) = \Phi_2(t_i + T_1 + T_2, t_i + T_1) \tilde{\mathbf{X}}_2(2i+1) + \int_0^{T_2} \Phi_2(t_i + T_1 + T_2, t_i + T_1 + \tau) D_2 \tilde{b}_q(2i+1) d\tau \quad (6.21)$$

Combining Eq. (6.20) and Eq. (6.21) with Eq. (6.19), one obtains

$$\|\tilde{\mathbf{X}}_1(2i+1)\| \leq \alpha \|\tilde{\mathbf{X}}_1(2i)\| \quad (6.22)$$

$$\|\tilde{\mathbf{X}}_2(2(i+1))\| \leq \beta \|\tilde{\mathbf{X}}_2(2i+1)\| + \gamma \|\tilde{b}_q(2i+1)\| \quad (6.23)$$

with $\alpha = k_1 e^{-\lambda_1 T_1}$, $\beta = k_2 e^{-\lambda_2 T_2}$ and $\gamma = \frac{k_2}{\lambda_2} (1 - e^{-\lambda_2 T_2})$.

From Eq. (6.5-6.6), the following inequalities can be obtained

$$\|\tilde{\phi}(2i+1)\| = \|\tilde{\phi}(2i) + T_1 \tilde{b}_p(2i)\| \leq \|\tilde{\phi}(2i)\| + T_1 \|\tilde{b}_p(2i)\| \quad (6.24)$$

$$\|\tilde{b}_p(2i+1)\| = \|\tilde{b}_p(2i)\|, \quad \|\tilde{b}_q(2(i+1))\| = \|\tilde{b}_q(2i+1)\| \quad (6.25)$$

To establish further estimates on $\tilde{\mathbf{X}}_1$ and $\tilde{\mathbf{X}}_2$, we consider new variables. Let vectors \mathbf{Z}_i , $i = 0..5$ be defined as follows

$$\begin{cases} \mathbf{Z}_0 = \tilde{\mathbf{X}}_{III} = [\tilde{\phi} & \tilde{\theta} & \tilde{b}_p & \tilde{b}_q]^T, & \mathbf{Z}_1 = [0 & \tilde{\theta} & 0 & \tilde{b}_q]^T, \\ \mathbf{Z}_2 = [\tilde{\phi} & \tilde{\theta} & \tilde{b}_p & 0]^T, & \mathbf{Z}_3 = [\tilde{\phi} & 0 & 0 & 0]^T, \\ \mathbf{Z}_4 = [0 & 0 & \tilde{b}_p & 0]^T, & \mathbf{Z}_5 = [0 & 0 & 0 & \tilde{b}_q]^T \end{cases}$$

With these notations, the following equations hold

$$\|\mathbf{Z}_0\|^2 = \|\mathbf{Z}_1\|^2 + \|\mathbf{Z}_3\|^2 + \|\mathbf{Z}_4\|^2 = \|\mathbf{Z}_2\|^2 + \|\mathbf{Z}_5\|^2 \quad (6.26)$$

$$\|\mathbf{Z}_i\| \leq \|\mathbf{Z}_0\|, \quad i = 0..5 \quad (6.27)$$

Equivalence with $\tilde{\mathbf{X}}_1$ and $\tilde{\mathbf{X}}_2$ are also available

$$\|\mathbf{Z}_1\| = \|\tilde{\mathbf{X}}_1\|, \quad \|\mathbf{Z}_2\| = \|\tilde{\mathbf{X}}_2\|,$$

$$\|\mathbf{Z}_3\| = \|\tilde{\phi}\|, \quad \|\mathbf{Z}_4\| = \|\tilde{b}_p\|, \quad \|\mathbf{Z}_5\| = \|\tilde{b}_q\| \quad (6.28)$$

Eq. (6.22,6.23,6.24,6.25) are re-written as follows

$$\|\mathbf{Z}_1(2i+1)\|^2 \leq \alpha^2 \|\mathbf{Z}_1(2i)\|^2 \quad (6.29)$$

$$\|\mathbf{Z}_2(2(i+1))\|^2 \leq (\beta \|\mathbf{Z}_2(2i+1)\| + \gamma \|\mathbf{Z}_5(2i+1)\|)^2 \quad (6.30)$$

$$\|\mathbf{Z}_3(2i+1)\|^2 \leq (\|\mathbf{Z}_3(2i)\| + T_1 \|\mathbf{Z}_4(2i)\|)^2 \quad (6.31)$$

$$\|\mathbf{Z}_4(2i+1)\|^2 = \|\mathbf{Z}_4(2i)\|^2 \quad (6.32)$$

$$\|\mathbf{Z}_5(2(i+1))\|^2 = \|\mathbf{Z}_5(2i+1)\|^2 \quad (6.33)$$

From Eq. (6.26,6.29,6.31,6.32),

$$\begin{aligned} \|\mathbf{Z}_0(2i+1)\|^2 &\leq \alpha^2 \|\mathbf{Z}_1(2i)\|^2 + \|\mathbf{Z}_4(2i)\|^2 + (\|\mathbf{Z}_3(2i)\| + T_1 \|\mathbf{Z}_4(2i)\|)^2 \\ &\leq \alpha^2 \|\mathbf{Z}_1(2i)\|^2 + (1 + T_1^2) \|\mathbf{Z}_4(2i)\|^2 + \|\mathbf{Z}_3(2i)\|^2 + 2T_1 \|\mathbf{Z}_3(2i)\| \|\mathbf{Z}_4(2i)\| \end{aligned}$$

With Eq. (6.26,6.27),

$$\begin{aligned} \|\mathbf{Z}_0(2i+1)\|^2 &\leq \max(\alpha^2, 1 + T_1^2) \|\mathbf{Z}_0(2i)\|^2 + 2T_1 \|\mathbf{Z}_0(2i)\|^2 \\ &\leq \max(\alpha^2 + 2T_1, (1 + T_1)^2) \|\mathbf{Z}_0(2i)\|^2 \end{aligned} \quad (6.34)$$

From Eq. (6.26,6.30,6.33),

$$\begin{aligned} \|\mathbf{Z}_0(2(i+1))\|^2 &\leq (\beta \|\mathbf{Z}_2(2i+1)\| + \gamma \|\mathbf{Z}_5(2i+1)\|)^2 + \|\mathbf{Z}_5(2i+1)\|^2 \\ &\leq \beta^2 \|\mathbf{Z}_0(2i+1)\|^2 + (1 + \gamma^2 - \beta^2) \|\mathbf{Z}_5(2i+1)\|^2 + 2\beta\gamma \|\mathbf{Z}_2(2i+1)\| \|\mathbf{Z}_5(2i+1)\| \end{aligned}$$

Knowing that $\|\mathbf{Z}_5(2i+1)\| \leq \|\mathbf{Z}_1(2i+1)\|$, with Eq. (6.29,6.27),

$$\begin{aligned} \|\mathbf{Z}_0(2(i+1))\|^2 &\leq (\beta^2 + 2\beta\gamma) \|\mathbf{Z}_0(2i+1)\|^2 + \max(0, 1 + \gamma^2 - \beta^2) \|\mathbf{Z}_1(2i+1)\|^2 \\ &\leq (\beta^2 + 2\beta\gamma) \|\mathbf{Z}_0(2i+1)\|^2 + \alpha^2 \max(0, 1 + \gamma^2 - \beta^2) \|\mathbf{Z}_1(2i)\|^2 \end{aligned}$$

Combining these with Eq. (6.34,6.27), one obtains

$$\frac{\|\mathbf{Z}_0(2(i+1))\|^2}{\|\mathbf{Z}_0(2i)\|^2} \leq (\beta^2 + 2\beta\gamma) \max(\alpha^2 + 2T_1, (1 + T_1)^2) + \alpha^2 \max(0, 1 + \gamma^2 - \beta^2)$$

Note $\Gamma = (\beta^2 + 2\beta\gamma) \max(\alpha^2 + 2T_1, (1 + T_1)^2) + \alpha^2 \max(0, 1 + \gamma^2 - \beta^2)$. From the construction of α , β and γ ,

$$\lim_{T_1 \rightarrow +\infty} \alpha = 0, \quad \lim_{T_2 \rightarrow +\infty} \beta = 0, \quad \lim_{T_2 \rightarrow +\infty} \gamma = \frac{k_2}{\lambda_2}$$

$$\lim_{\substack{T_1 \rightarrow +\infty \\ T_2 \rightarrow +\infty}} \Gamma = \lim_{\substack{T_1 \rightarrow +\infty \\ T_2 \rightarrow +\infty}} 2 \frac{k_2^2}{\lambda_2} T_1^2 e^{-\lambda_2 T_2}$$

If $T_1 = o\left(e^{\frac{\lambda_2}{2} T_2}\right)$, then

$$\lim_{\substack{T_1 \rightarrow +\infty \\ T_2 \rightarrow +\infty}} \Gamma = 0 \quad (6.35)$$

We can now state the following result.

Proposition 2. Consider Temporally Interconnected Observers (TIO), given by Eq. (6.5-6.6), taking the form of Eq. (6.15-6.16) and illustrated in Fig. 6.5, used on an alternate sequence of straight-lines and curves motions of respective durations T_1 and T_2 . Assume that the observers satisfy inequalities (6.19). Asymptotic convergence of the estimates of the TIO is guaranteed for sufficiently large values of T_1 and T_2 chosen according to $T_1 = o\left(e^{\frac{\lambda_2}{2}T_2}\right)$ where λ_2 is the decay rate of the curve motion observer introduced in Eq. (6.19).

Proof. Eq. (6.35) guarantees super-linear convergence (as defined in [Nocedal and Wright, 1999]) of the sequence $\|\mathbf{Z}_0(2i)\|$ for sufficiently large times between switching. From the definition of \mathbf{Z}_0 , the estimation error on \mathbf{X}_{III} , taken at the discrete times t_i , converges towards zero. Since the continuous dynamics of Systems (6.2) is bounded, the estimation error $\|\tilde{\mathbf{X}}_{III}(t)\|$ is asymptotically stable. From the measurements (p_m, q_m) and the estimated biases, the rates (p, q) can be evaluated with an error which also tends to zero. Therefore, the proposed TIO structure achieves asymptotic reconstruction of the state $(\phi \ \theta \ b_p \ b_q \ p \ q)^T$. \square

For sake of illustration of the statement in Proposition 2, we consider a parametrization of (T_1, T_2) that satisfy the required assumption. Consider a vector of parameter $(v_1, v_2) > 1$, for any (T_1, T_2) such that

$$T_1 > \frac{1}{\lambda_1} \log \left(k_1 \sqrt{v_1 \left(1 + \frac{k_2^2}{\lambda_2^2} \right)} \right) \quad (6.36)$$

$$T_2 > \frac{1}{\lambda_2} \log \left(\frac{\lambda_2}{\sqrt{1 + \frac{\lambda_2^2}{v_2 k_2^2 (1+T_1)^2} - 1}} \right) \quad (6.37)$$

Then, the rate of convergence Γ is bounded as follows

$$\Gamma < \frac{1}{v_1} + \frac{1}{v_2} < 1$$

In practice, the preceding discussion must be considered in another order. The magnitudes of the measurements noises and of the dynamics uncertainties implicitly define the best possible constants $\lambda_1, k_1, \lambda_2, k_2$ in Eq. (6.19). Proposition 2 states, e.g. through Eq. (6.36-6.37), that *under the assumption of constant biases* b_p, b_q , the TIO scheme is asymptotically converging for sufficiently large and well chosen values of T_1, T_2 . What can discard the application of this result to cases of practical interest is the fact that the bounds on T_1 and T_2 can be inconsistent with the assumption that the biases are constant.

In view of applications, it can be of interest to account for (slowly) varying biases. Consider varying biases modifies Eq. (6.25), because additive divergence has to be taken into account in the upper bound of the ratio of the sequence. It is not a real problem since the (polynomial in t) divergence during straight-line motion (respectively curve motion) will be followed by the (exponential) convergence of the observer during curve motion (respectively straight-line motion):

6.3. CONVERGENCE OF THE TEMPORALLY INTERCONNECTED OBSERVERS STRUCTURE

exponential decrease easily compensates polynomial increase. In a pinch, the only divergence which is not compensated for is the last of the sequence. Being the last, it is followed by a stop of the vehicle during which biases are both observable and estimated.

Chapter 7

Practical implementation and experimental results

Implémentation pratique et résultats expérimentaux

Ce chapitre présente l'implémentation pratique du système de navigation précédemment présenté. La procédure d'alignement à la volée du système embarqué est détaillée. Une estimation numérique des temps de convergence est réalisée à partir des caractéristiques des capteurs utilisés afin de valider la convergence théorique. La mise en oeuvre de stratégies de détection d'erreurs et de lissage a posteriori illustre la complémentarité des capteurs utilisés. Enfin, des résultats de simulation puis expérimentaux valident le fonctionnement et la performance du système de navigation proposé.

We now present implementation of the previously presented observer of Chapter 6 constituting the heart of the navigation system. Its functioning is illustrated with simulation results and, finally experimental results are presented. Consistently with the observability analysis, the navigation system embeds a 3-axis accelerometer, a 3-axis gyrometer and a 3-axis magnetometer which are gathered inside the IMU ADIS16405 from *Analog Devices*© and a barometer MS5534C from *Measurement Specialties*™. The embedded system is a robust two processors design such as in [Bristeau et al., 2010a]. It can transmit data in real time while storing them onboard for later analysis. Based on the sensors capabilities, we now explain how Kalman filters are tuned.

7.1 Implementation of Kalman filtering

The first (and classic) level of interconnection does not appear in the implementation of the Kalman filter as the observers are all coded up together. This is not the case of the TIO. The estimate of the state (5.4) is the result of the three temporally interconnected global Kalman filters, which are triggered depending of the stop detection and of the yaw rate estimate.

The Kalman filters obey the following tables. The aggressiveness of the considered dynamics is bounded by the values presented in Table 7.1. Table 7.2 shows the uncertainties on dynamics

Roll angle	$ \phi < 0.2 \text{ rad}$
Roll rate	$ p < 0.2 \text{ rad.s}^{-1}$
Pitch angle	$ \theta < 0.2 \text{ rad}$
Pitch rate	$ q < 0.5 \text{ rad.s}^{-1}$
Yaw rate	$ r < 1 \text{ rad.s}^{-1}$

Table 7.1: Practical bounds on the dynamics under consideration.

Roll angle	$5 \cdot 10^{-7} (\text{rad.s}^{-1})^2 \cdot \text{s}$
Pitch angle	$10^{-7} (\text{rad.s}^{-1})^2 \cdot \text{s}$
Gyrometer bias	$10^{-6} (\text{rad.s}^{-1} \cdot \text{s}^{-1})^2 \cdot \text{s}$
Accelerometer bias	$3 \cdot 10^{-4} (\text{m.s}^{-2} \cdot \text{s}^{-1})^2 \cdot \text{s}$

Table 7.2: Dynamics PSD.

equations used in the dynamics noise matrix Q , stemming from modeling approximation or representing sensors errors. Angle dynamics uncertainty is estimated from the assumption of small angles. Sensor bias dynamics is a first-order approximation of the pink noise specified in the manufacturer data sheet [IEEE, 1998, Analog Devices, 2009].

Measurements from the IMU are sampled at 102 Hz and experimental standard deviations, given in Table 7.3, are consistent with random walk specified in the manufacturer data sheet [Analog Devices, 2009]. The barometer is sampled at 28 Hz. Standard deviation values are used in the measurement noise matrix V . By extension, in Table 7.4, equivalence of noise can be found for the created virtual sensors. Standard deviations should be taken for reference only since the noise is not Gaussian.

The Kalman filters are implemented in a discrete multi-rates form of Section 2.3, with Joseph form and sequential processing, as presented in Section 2.4. Propagation and IMU update are realized at 102 Hz whereas barometer update occurs at 28 Hz and the magnetic velocimeter is computed at 2 Hz. The algorithms are running in real time on an embedded processor such as the Renesas© SH7216, running at 200 MHz. A Microchip© PIC24 microcontroller is used to gather at 102 Hz the measurements in a fixed message which is sent to the computation processor through a serial port.

According to the previous discussions, a 19-states Kalman filter is run at 102 Hz. The 19 states cover 3 positions (x, y, z), 1 velocity (u), 3 angles (ϕ, θ, ψ), 3 (specific) accelerations (a_x, a_y, a_z),

Accelerometers	0.1 m.s^{-2}
Gyrometers	0.01 rad.s^{-1}
Magnetometers	0.002 G
Barometer	1 m

Table 7.3: Measurement noise standard deviation.

Pitch-meter	0.1 rad
Velocimeter	0.1 m.s ⁻¹
Compass	0.1 rad

Table 7.4: Virtual measurement noise standard deviation.

3 angular rates (p, q, r) , 3 accelerometers biases $(b_{a_x}, b_{a_y}, b_{a_z})$ and 3 gyrometers biases (b_p, b_q, b_r) . The position (x, y) is in the state to allow a posteriori smoothing and obtain a estimation error variance concerning the relative positioning of the vehicle. The accelerometers and gyrometers measurements are taken as measured outputs.

7.2 On-line alignment procedure

For practical reasons, the sensors employed by the navigation system can not be perfectly aligned with the body frame of reference of the vehicle. Yet, the alignment of the embedded system is of prime importance for the performance of the navigation. The procedure which is used to calculate this orientation relies on three observations : a vehicle is on average at null acceleration, the yaw motion is the strongest angular dynamics for a vehicle, centrifugal acceleration is exerted during curve motions.

The proposed procedure of alignment is the following. The first step is to detect a stop, then from the reading of the accelerometers, a first rotation matrix can be obtained to put the system in the horizontal plane. This rotation is only approximatively estimated since accelerometers are biased and the vehicle could be parked on an inclined place (in this case, the gravity horizontal plane is not coinciding with the vehicle horizontal plane). This first approximative rotation matrix is corrected by the reading of the mean values of accelerometers during motion, leaving out curve motions detected by the newly aligned almost vertical gyrometer. This allows to remove potential inclination of the vehicle during stops.

From now, the system can be assumed to be almost parallel to the horizontal plane of the vehicle. A yaw rotation is achieved using the values of the accelerometers during strong curve motions. When the yaw rate is strong, there is centrifugal acceleration and the yaw alignment is computed such that the measured acceleration belongs to the lateral axis of the vehicle.

Using these two alignment steps, the system is almost aligned with the vehicle. A correction of pitch and roll is executed using information from the gyrometers (already debiased thanks to detection of a stop). This corrective matrix rotation has to cancel any projection of yaw rate on other gyrometer axes, its value is calculated especially during gentle curve motions, where roll angle is very small.

Finally, an ultimate correction is brought with another yaw alignment on the newly rotated centrifugal acceleration. These successive steps are represented in Fig. 7.1.

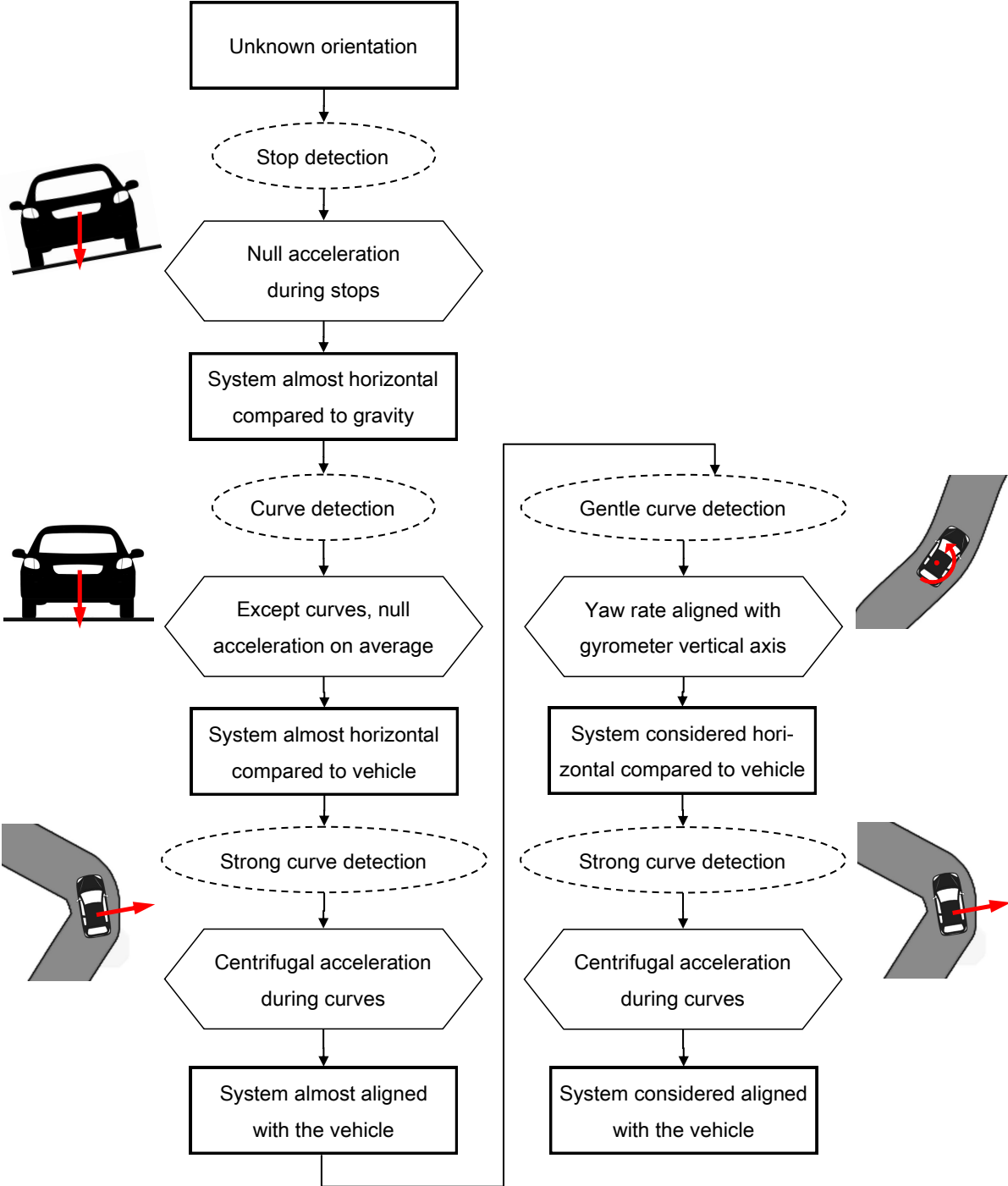


Figure 7.1: Alignment procedure from an unknown orientation of the embedded system. The current status is represented in square boxes, the detected events are in dashed ellipses and the modeling assumptions are in hexagonal boxes. Iteratively, the orientation of the embedded system is reconstructed from the sensors measurements.

7.3 Numerical rate of convergence estimates

The proof of TIO convergence is based on the existence of sufficiently large times between switching to ensure the ratio of the sequence to be upper-bounded by 1. However, in practice, durations are set by the switching policy, i.e. by the driver and can not be chosen. Convergence is guaranteed if the bounds of Eq. (6.36-6.37) are sufficiently small to be satisfied by the actual values of durations of straight-lines and curve motions. Numerical values of the bounds can be evaluated from the UCO characteristics of the separate systems and the convergence rates of the separate observers.

But the established convergence estimates are very conservative due to the following:

1. The UCO parameters are the result of a succession of lower bounds (Section 6.2.2)
2. The observer proposed to estimate Kalman filter convergence is not optimal (Section 3.3.4)
3. The proof of existence of Kalman gain is based on worst case analysis and thus, the convergence estimates of Kalman filter are very poorly dimensioned (Section 3.3.3)
4. The proof of TIO convergence is also a sequence of inequalities (Section 6.3)

The main merit of these very conservative boundaries is to guarantee the convergence of the TIO structure from a strict theoretical point of view.

If the calculus are led with the values used for the implementation of the Kalman filtering, the following orders of magnitude may be found:

- Estimates for first observer during straight-line motion: $\lambda_1 \approx 1$, $\eta_1 \approx 20$
- Estimates for Kalman filtering of straight-line motion: $\Lambda_1 \approx 10^{-5}$, $k_1 \approx 10^5$
- Estimates for first observer during curve motion: $\lambda_2 \approx 10^{-1}$, $\eta_2 \approx 10^{10}$
- Estimates for Kalman filtering of curve motion: $\Lambda_2 \approx 10^{-22}$, $\kappa_2 \approx 10^{22}$
- Necessary durations of straight-line and curve: $T_1 \approx 10^8$ s, $T_2 \approx 10^{24}$ s

These values can not be used to assess the validity of the proposed TIO. To evaluate more precisely, we consider, for curve motion, a curve with constant rate of 0.5 rad.s^{-1} . In these conditions, as for the straight-line motion, the Grammian can be computed and better UCO parameters found than with the time-varying proof. Skipping the Kalman filter estimates, values of the observer proposed in Eq. (3.29) are directly used in the calculus of the characteristic durations.

- Estimates for first observer during straight-line motion: $\lambda_1 \approx 1$, $\eta_1 \approx 20$
- Estimates for first observer during curve motion: $\lambda_2 \approx 1$, $\eta_2 \approx 10^4$
- Minimal necessary durations of straight-line and curve: $T_1 \approx 10$ s, $T_2 \approx 10$ s

These orders of magnitude are much better suited to real trajectories (even if 10 seconds remains relatively long for curves) and do not challenge the assumption of constant bias during these durations.

7.4 Fault detection strategy

As presented in Chapter 4, the error of the indirect measurements of speed and heading from the magnetometer can not be considered as white, zero-mean Gaussian noise. In practice, the

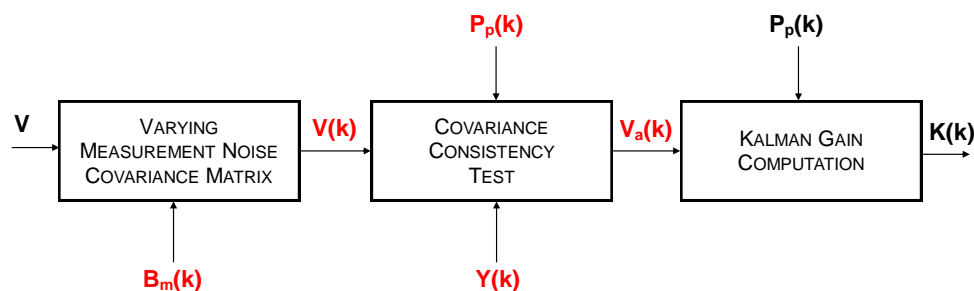


Figure 7.2: Two supplementary steps in the adaption of the Kalman gain to improve fault detection.

measurement noise covariance matrix, which is a tuning parameter, is not taken constant but is continuously tuned for the estimated confidence on velocimeter and compass outputs. The speed error is related to the cost of the two criteria of harmonics and continuity and the heading error is quantified by the distance of the measurements to the identified ellipse. Moreover, a fault detection is realized during the data fusion with the inertial sensors with a simple test of covariance consistency.

This fault detection process magnifies the behavior of the Kalman filter which naturally adapts the gain to the estimation error covariance matrix: the input of the gain computation is now a varying measurement noise covariance matrix, and this input is moderated by a $3 - \sigma$ consistency test (Fig. 7.2).

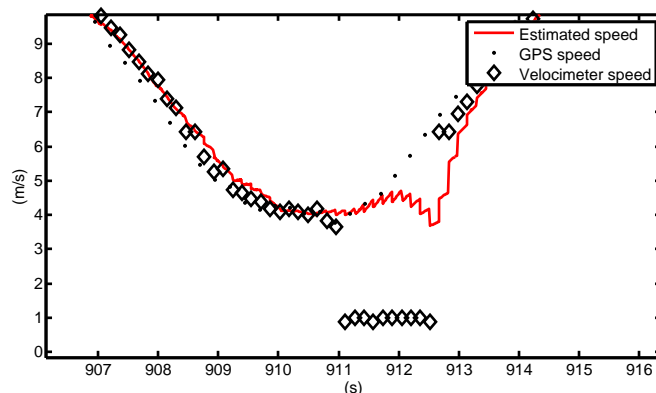


Figure 7.3: Estimation of the velocity using complementary information from continuously debiased accelerometers in case of malfunction of the velocimeter.

Figure 7.3 illustrates the non-Gaussian characteristic of the velocimeter error and the necessary fault detection. First, it appears that the propagation is efficient and erroneous speed measurements are rejected. Subsequently, as the propagation covariance increases, the velocimeter gets more and more difficult to reject. Finally, the velocimeter being consistent with the propagation, the speed estimate error can be quickly set back to zero, as is suggested by

the GPS given here only to serve as a reference. This underlines the interest of removing the biases from the accelerometers to be able to provide a performing propagation. The same process can be realized on the heading estimation to reduce or reject erroneous measurements from the magnetic compass.

7.5 Optimal smoothing for multi-rates filtering and a posteriori trajectory smoothing

In case of a posteriori treatment of the data gathered during a trajectory, improvements can be realized with smoothing. The real-time state estimate $\hat{\mathbf{X}}(t)$ is $\hat{\mathbf{X}}(t|\tau \in [0, t])$, the estimate at time t , given all the previous measurements from the beginning until the time t . For off-line (a posteriori) processing, smoothing provides an estimate using all the measurements available, $\hat{\mathbf{X}}(t|\tau \in [0, T])$ for $t \in [0, T]$. For simplicity, filtering estimate is noted $\hat{\mathbf{X}}(t)$ whereas $\hat{\mathbf{X}}(t|T)$ corresponds to the smoothing estimate.

Complete theory about smoothing may be found in [Gelb, 1974, Anderson and Moore, 1979], main ideas of which are reminded here for convenience. Consider the state estimate $\hat{\mathbf{X}}(t)$ being the result of a classical (forward) filtering, associated to a corresponding error estimation covariance $P(t)$. Consider now another estimate $\hat{\mathbf{X}}_b(t) = \hat{\mathbf{X}}(t|\tau \in [t, T])$ using the future measurements and starting from the end of the time interval, which is actually a filtering in reverse time, or backward filtering. Let note $P_b(t)$ the corresponding error estimation covariance. Both estimates are computed with Kalman filters: they tend to be debiased, with minimum error estimation covariance, furthermore, considering white noises, they are uncorrelated.

In the same way of finding the Kalman filter as the optimal observer, the optimal smoother is built to extract the best information of these two estimates: consider it as a combination with two weighting matrices $S(t)$ and $S_b(t)$ such that estimate is unbiased and estimation error covariance is minimum.

$$\hat{\mathbf{X}}(t|T) = S(t)\hat{\mathbf{X}}(t) + S_b(t)\hat{\mathbf{X}}_b(t)$$

Generalizing the error notation $\tilde{\mathbf{X}} = \mathbf{X} - \hat{\mathbf{X}}$,

$$\tilde{\mathbf{X}}(t|T) = (I - S(t) - S_b(t))\mathbf{X}(t) + S(t)\tilde{\mathbf{X}}(t) + S_b(t)\tilde{\mathbf{X}}_b(t)$$

If the forward and backward estimates are unbiased, to keep the smoothing estimate unbiased, the weighting matrices must verify

$$S(t) + S_b(t) = I$$

Looking at the smoothing error covariance, with $E[\tilde{\mathbf{X}}(t)\tilde{\mathbf{X}}_b(t)] = 0$,

$$\begin{aligned} P(t|T) &= E[\tilde{\mathbf{X}}(t|T)\tilde{\mathbf{X}}^T(t|T)] \\ &= E[(S(t)\tilde{\mathbf{X}}(t) + (I - S(t))\tilde{\mathbf{X}}_b(t))(S(t)\tilde{\mathbf{X}}(t) + (I - S(t))\tilde{\mathbf{X}}_b(t))^T] \\ &= S(t)E[\tilde{\mathbf{X}}(t)\tilde{\mathbf{X}}^T(t)]S^T(t) + (I - S(t))E[\tilde{\mathbf{X}}_b(t)\tilde{\mathbf{X}}_b^T(t)](I - S(t))^T \\ &= S(t)P(t)S^T(t) + (I - S(t))P_b(t)(I - S(t))^T \end{aligned}$$

The minimum of $P(t|T)$ is obtained for

$$2S(t)P(t) - 2(I - S(t))P_b(t) = 0 \Leftrightarrow S(t) = P_b(t) (P(t) + P_b(t))^{-1}$$

Reintroducing these results in the formulations of $\hat{\mathbf{X}}(t|T)$ and $P(t|T)$,

$$P(t|T) = (P^{-1}(t) + P_b^{-1}(t))^{-1}$$

$$\hat{\mathbf{X}}(t|T) = P(t|T) (P^{-1}(t)\hat{\mathbf{X}}(t) + P_b^{-1}(t)\hat{\mathbf{X}}_b(t))$$

Of course, at time T , the smoothing estimate must coincide with final values of the forward filtering, $\hat{\mathbf{X}}(T|T) = \hat{\mathbf{X}}(T)$ and $P(T|T) = P(T)$, which means that $P_b^{-1}(T) = 0$.

Figure 7.4 illustrates how the optimal smoother takes benefits of the available measurements to improve the estimation for any time t . Practical implementation of smoothing can be realized with the Rauch-Tung-Striebel form which does not require the computation of the backward estimate (see [Gelb, 1974]).

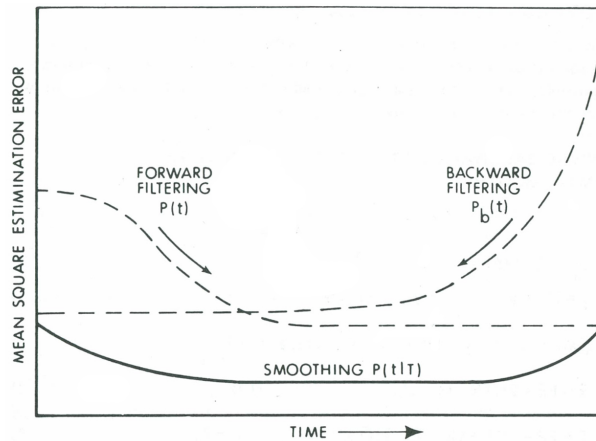


Figure 7.4: Benefits of optimal smoothing relative to the estimation error covariance [Gelb, 1974].

Concerning our application, smoothing can be useful at three time scales. The shortest one is just the consequence of the multi-rates filtering: the velocity being estimated at 2 Hz, the propagation at 102 Hz based on inertial sensors should be smoothed knowing future values of the speed. The longest scale comes into play when the position of the end-point of the trajectory is known. In this case, the whole trajectory estimate can be improved, knowing where to arrive. Between these two time scales, the intermediate scale concerns the magnetic compass. In practice, in case of magnetic disturbances, the magnetic heading is not available and heading estimate is propagated based only on the gyrometer with the last estimated value of the bias. When magnetic disturbances disappear, the inertial heading may have drifted and smoothing is particularly interesting to compensate for with newly available magnetic heading. This smoothing implementation gets relevant when crossing a long bridge (see Fig.7.5) or going through tunnels.

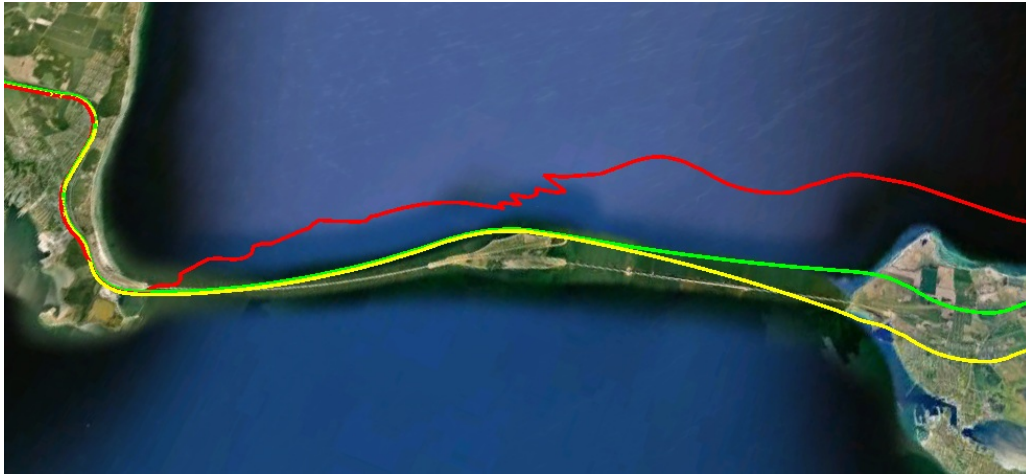


Figure 7.5: Crossing of the Great Belt Fixed Link, Denmark (17km): navigation filter with raw magnetic heading (red), or complementary filter with gyrometer (yellow), or optimal smoothing (green).

7.6 Results

7.6.1 Simulation illustrating biases estimation properties

To illustrate the merits of our proposed navigation system, we first report some simulation results. A synthesis model of a 6-DOF rigid body with longitudinal velocity and angular rates as inputs is considered. A representative succession of curves and straight lines is simulated. Measurements are polluted with Gaussian white noises, and pink noises are added to simulate the biases of the gyroscopes. Modeled errors and biases are representative of typical considered low-cost MEMS sensors for automotive applications. In the figures, we refer to debiased values with ZUPT which is a reference solution for this problem.

In Fig. 7.6, one can see the estimated pitch bias (blue), the real pitch bias (green) and the debiased pitch bias (red). Debiasing is obtained by a simple technique consisting in removing the mean value of the bias during the stationary phase. At the beginning of the simulation is a stationary phase: the estimated bias converges towards the real bias. After this first phase, one can observe a succession of varying values and constant parts. The parts when the bias estimation varies are straight-line motions during which the pitch bias is observable. It is kept constant in curve motion. The TIO bias is centered around the real bias but remains updated continuously.¹ The mean error on the value of the bias is divided by 4 between the ZUPT pitch bias and the TIO pitch bias. This is a substantial improvement.

Figure 7.7 reports comparisons of the TIO pitch angle (blue) and the ZUPT pitch angle (red) to the real pitch angle (green). The mean error is divided by 50. This vast improvement is

1. A simple second order model for the bias would suppress the high frequencies in the estimated bias dynamics without modifying the observability. This would have yielded some additional low-pass filtering property.

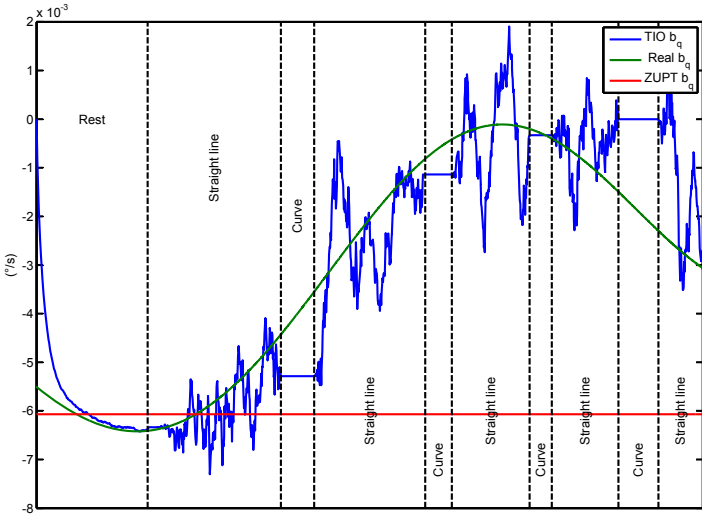


Figure 7.6: Estimation of the pitch bias.

essentially due to the barometer which provides observability on the low-frequency part of the pitch angle variations. One clearly sees that TIO does not disturb this estimation in spite of a coupling between roll and pitch angles during curve motion.

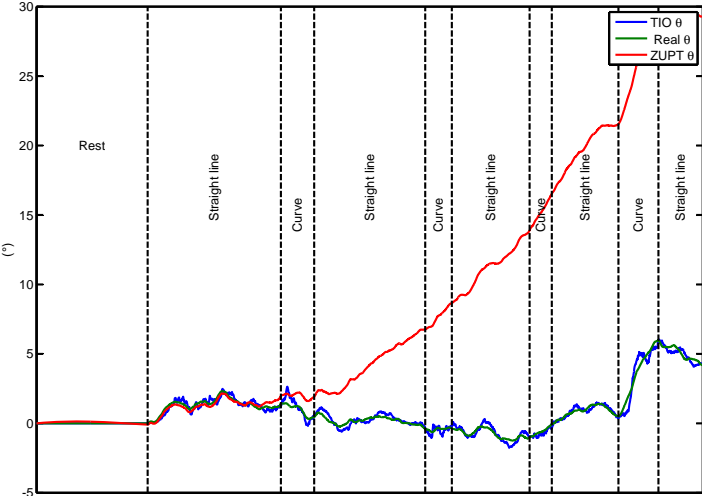


Figure 7.7: Estimation of the pitch angle.

In Fig. 7.8, one can see the TIO roll bias (blue), the real roll bias (green) and the ZUPT roll bias (red). During straight-line motion, TIO roll bias is kept constant and its estimate is updated only during curve motion. Each correction step is relatively effective and the estimate of the roll bias is improved after each curve motion. The mean error is divided by 2.

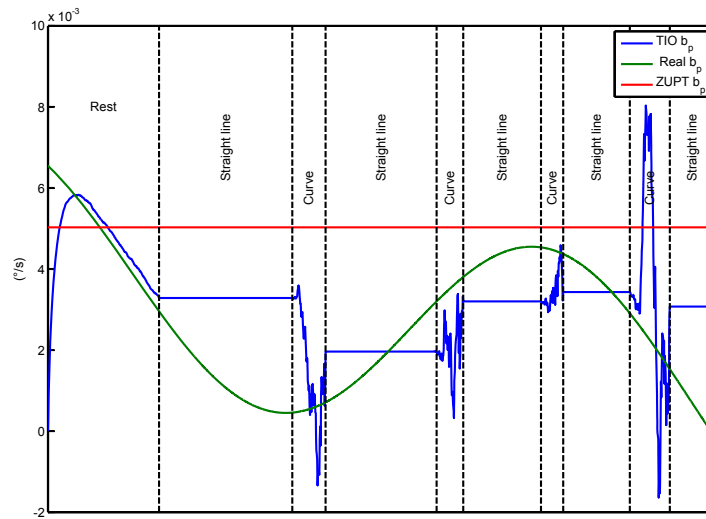


Figure 7.8: Estimation of the roll bias.

The benefits of the use of TIO are also emphasized in Fig. 7.9 where the TIO roll angle (blue), the real roll angle (green) and the ZUPT roll angle (red) are reported. For each straight-line motion, one can see the TIO roll angle becomes erroneous because of the natural variations of the bias. Each curve motion allows to estimate the angle (correction of the value) and the bias (correction of the drift). On overall, with the proposed TIO, the mean error on roll angle is divided by 10, compared to the ZUPT technique.

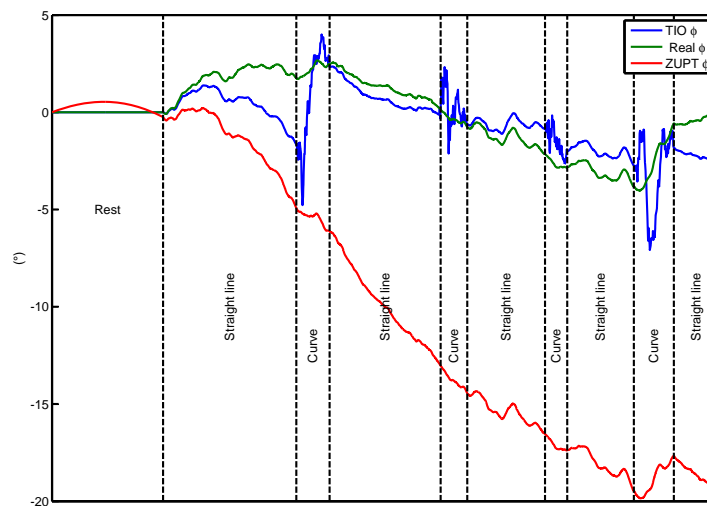


Figure 7.9: Estimation of the roll angle.

7.6.2 Short range experimental real-time reconstruction

We now present some results obtained on-board an actual passenger car.

In Figure 7.10, the estimated yaw rate is presented (in green) and compared to the threshold of the switching policy. In the second plot representing the roll bias estimate, a long straight line is visible with a large constant part between 500 s and 1500 s, corresponding to a value of yaw rate lower than the threshold.

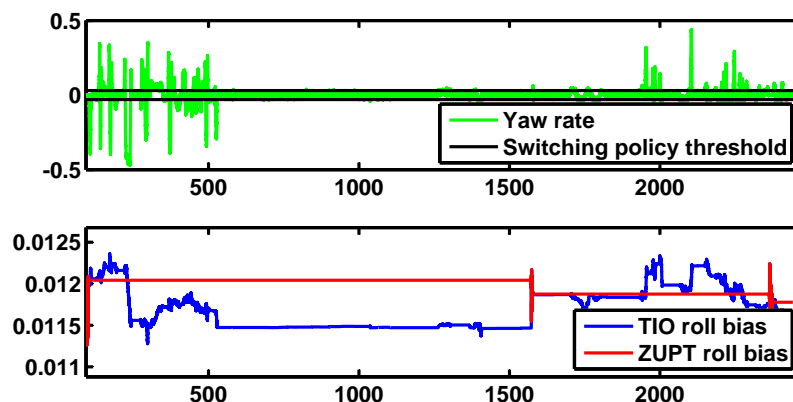


Figure 7.10: Switching policy and roll bias estimation.

Figure 7.11 shows the pitch bias estimation which reveals the performance of the algorithm since the TIO bias is almost continuous and kindly interpolates the values estimated during ZUPTs without showing any steps like the bias estimated only during ZUPTs. Further, the TIO estimates provides continuous time estimate of the bias, while the ZUPT can only operate at discrete times (from time to time). In Figure 7.11, the succession of varying values and constant parts are not easily detectable because constant parts appear only during curves which are in-between straight lines.

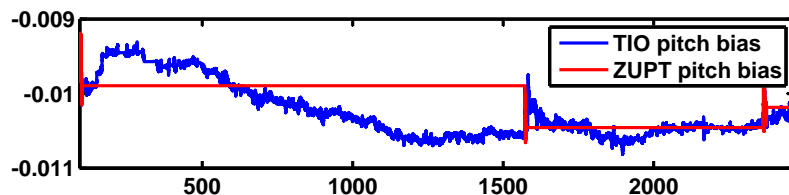


Figure 7.11: Pitch bias estimation showing the continuity of the estimation.

Figure 7.12 shows the efficiency of the algorithm of phase detection proposed in Part 4.1.3 to detect reverse motion during park maneuvers.



Figure 7.12: Reverse motion detection during maneuvers.

7.6.3 Long range trajectory real-time reconstruction

Figure 7.13 shows the reconstruction of a 90 km long trajectory in the urban network of Paris with numerous tunnels, the final position error is below 1.5 km. Figure 7.14 gives an example of less accurate reconstruction of 45 km long trajectory with final error of 3.5 km, nevertheless the trajectory estimate remains easily identifiable. Figure 7.15 presents a 600 km long trajectory estimation, the final position error is below 4 km. Figure 7.16 illustrates an European trip of 2250 km with an arrival at Stockholm, the final position error is below 80 km. These results are representative of the estimation accuracy: whatever the final position error (always below 10% of the traveled distance), the trajectory shape is preserved.

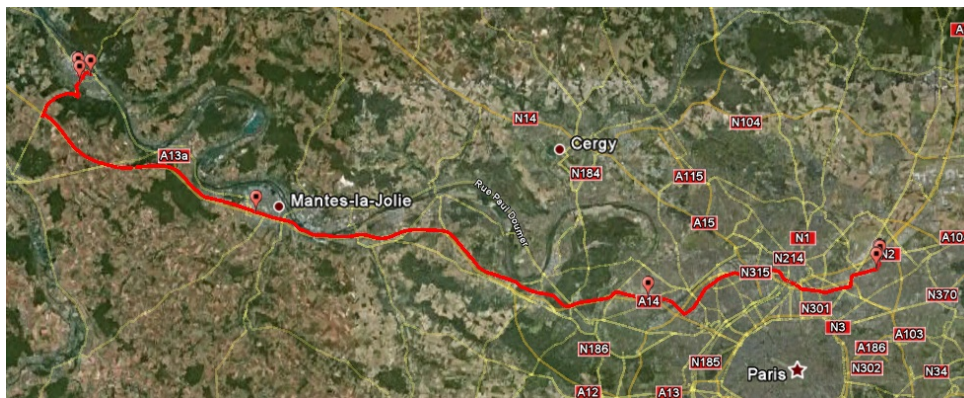


Figure 7.13: Trajectory estimation (90 km long, dense network, several tunnels).



Figure 7.14: Trajectory estimation (45 km long, dense network, several tunnels).



Figure 7.15: Trajectory estimation (600 km long).

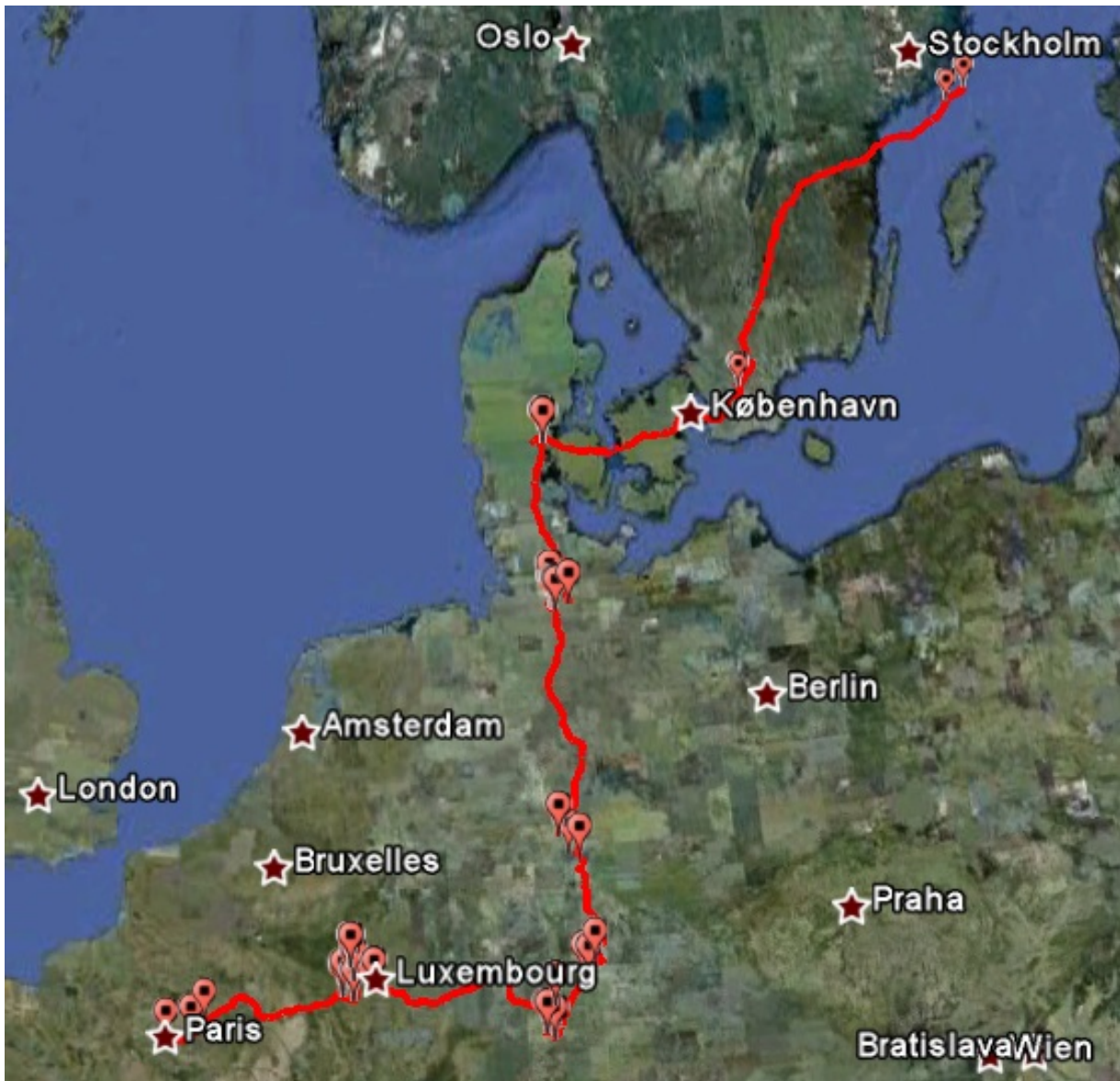


Figure 7.16: Trajectory estimation (2250 km long).

Part III

Other examples of navigation system design

*Autres exemples de conception
de système de navigation*

Chapter 8

The navigation problem aboard the AR.Drone

Le problème de navigation à bord de l'AR.Drone

Ce chapitre présente comment le problème de navigation de l'AR.Drone de Parrot a été résolu afin de garantir une stabilisation robuste du quadrirotor. L'estimation est réalisée par une fusion de données provenant d'une caméra, de capteurs inertiels classiques et d'un magnétomètre triaxe. Les capteurs sont exploités au sein d'un modèle aérodynamique prenant en compte la flexibilité des hélices et soulignant l'existence d'un terme linéaire de traînée aérodynamique.

Introduction

Lately, the quadrotor has emerged as a popular aerial platform for control design experiments among small rotary-wing vehicles [Young et al., 2002]. The UAV platform is a quadrotor which is a very popular and has attracted much attention from academia ([Hamel et al., 2002, Castillo et al., 2004, Pounds et al., 2004, Pounds et al., 2006, Tayebi and McGilvray, 2006, Romero et al., 2007, Guénard, 2007, Hoffmann et al., 2007, Efe, 2007, Cunha et al., 2009, Martin and Salaün, 2010a, Martin and Salaün, 2010b, Lupashin et al., 2010]).

In 2004, the Parrot company started a project named AR.Drone (Fig. 8.1) aiming at producing a micro-UAV for the mass market of videos games and home entertainment. The project was publicly presented at the 2010 Consumer Electronics Show, and, starting on August, 18th, 2010, the AR.Drone has been released on the market. This project has involved from 5 to 12 engineers from Parrot with the technical support of SYSNAV and his academic partner MINES ParisTech for navigation and control design. One of its unique features is that it is a stabilized aerial platform, remotely controlled through a user-friendly graphical interface running on an Apple iPhone, iPad or iTouch. It is available from numerous retail stores in various countries and the on-line Apple store at a price below 300 euros.



Figure 8.1: Parrot AR.Drone, with its outdoor hull.

While numerous teams have reported successful automatic flights, this aerial platform, which is light, affordable and capable of hover and fast forward flight in narrow spaces, is still a subject of a collection of theoretical questions. Yet, in open-loop, the quadrotor is an unstable vehicle. In turn, this raises the issue of state estimation. To provide the customer with an easy to pilot platform, the embedded control systems have to be very effective and plays the role of an enabling technology for the whole project.

To address the problem of state estimation, UAVs are usually equipped with embedded inertial sensors (gyrometers and accelerometers, see [Titterton and Weston, 2004]), a sonar altitude sensor (or a barometer), and, often, an absolute position or velocity sensor such as a GPS or a camera feeding vision algorithms (see e.g. [Hamel and Mahony, 2007, Rondon et al., 2009]). Combined into data fusion algorithms, these devices have allowed to obtain relatively good results of state estimation and stabilization on rotary wing (ducted fan, see [Marconi and Naldi, 2007, Hua et al., 2008, Naldi et al., 2010, Pfimlin et al., 2010, Marconi et al., 2011], small-scale helicopters, see [Vissière et al., 2008, Hua, 2009, Bristeau et al., 2010a, de Plinval et al., 2011]) and fixed wing UAVs, thus guaranteeing stabilized flights with residuals errors of the order of magnitude of the sensors.

The constraints under consideration for the applications envisioned by Parrot in the AR.Drone project are much more restrictive than the ones usually bearing on micro-UAVs applications. Here, it is required to handle both indoor and outdoor autonomous flights, irrespective of the potential unavailability of the GPS or the camera. This point is of importance since these sensors can fail in numerous cases such as GPS signal unavailability, low-light flight,

or weakly textured visual environments.

In summary, the AR.Drone project has consisted in designing a micro rotary wing UAV which cost is lower by several orders of magnitude than its competitors, while providing the end-user with unprecedented motion control accuracy, robustness and ease of handling. To obtain the presented results, the algorithms embedded in the AR.Drone contains state-of-the-art low-cost navigation methods, video processing algorithms [Bristeau et al., 2011]. In this thesis, the contribution is focused on the modeling and the use of usual sensors to provide a robust estimate of the air speed and of the heading of the vehicle. Indeed, to compensate for the poor accuracy of the embedded sensors, we focus on the observed aerodynamics drag induced by the rotors during a translational motion. Its analytic expression plays key roles in the quadrotor stability and observability [Bristeau et al., 2009]. While the mechanical structure of a quadrotor is simple (four rotors with simple propellers and rigid frame), the dynamic behavior is surprisingly involved.

In Section 8.1, we detail the observation problem corresponding to the AR.Drone project. Section 8.2 is the study of the aerodynamics modeling of a quadrotor, based on the aerodynamics of a propeller moving with the vehicle body. In Section 8.3, we propose an observer design, depending of the informations available onboard (from the modeling and from the sensors). Complementary discussions on the role of the center of gravity and the propellers flexibility are given in Appendix B.

8.1 Navigation problem

Designed for mass-market, the quadrotor must be easy to fly and safe. Ease of flying means that the end-user shall only provide high level orders which must be handled by an automatic controller dealing with the complexity of low-level sub-systems. Because the system is unstable, feedback is needed. In turn, this raises the issue of state estimation. Safety means that the vehicle control system must be robust to the numerous disturbances that can be met in practice as the UAV is used in various and unknown environments. Redundancy in the state estimation is the solution in this case.

For these reasons, the critical points are the accuracy and the robustness of the vehicle state estimation. While absolute position estimation is not a strict requirement (at the exception of the altitude for safety reasons), it is of paramount importance to know the translational velocity during all the flight phases, so that it is possible to stop the vehicle and to prevent it from drifting. The capability of stopping the vehicle is a security requirement, while cancellation of the drift of the vehicle –which is particularly annoying– has a large added value in terms of end-user experience. Other key questions are stabilization and robustness. Finally, one shall realize that the UAV under consideration must be plug-and-play, in the sense, that it is not a laboratory experiment, and must fly autonomously once it is handed out of its package by the end-user and its the battery is loaded. No sophisticated calibration or tuning procedure can be performed by the end-user who is usually totally unfamiliar with control technology.

This Chapter focuses on state estimation, stabilization algorithms being developed by Parrot (see [Bristeau et al., 2011]). The problem addressed in this chapter is similar to the automotive

navigation: on top the angular rates estimation mandatory for angular stabilization, an accurate estimate of velocity and heading is required to ensure non-drifting trajectories of the quadrotor. To solve this problem, MEMS sensors are used in conjunction with a model of the quadrotor, based on the dynamics of 6-DOF rigid body and extended by the aerodynamics modeling as presented in Section 8.2.

The navigation system is realized on board the quadrotor with a Parrot P6 processor (32bits ARM9-core, running at 468 MHz) which is coupled with a 16bits PIC micro-controller running at 40 MHz, in the role of interface with the sensors. These sensors are a 3-axis accelerometer, a 2-axis gyroscope, a 1-axis vertical gyroscope, and 2 ultrasonic sensors. The ultrasonic sensors are 2 Prowave ultrasonics sensors which are used for altitude estimation. The PIC micro-controller handles the ultrasonic transmitter, and digitalizes the signal from the ultrasonic receiver. Ultrasonic sensors are used to estimate the altitude and the vertical displacements of the UAV. They can also be used to determine the depth of the scene observed by the vertical camera. The ultrasonic sensors have a 40 kHz resonance frequency and can measure distances as large as 6 m at a 25 Hz rate. The accelerometers and gyroscopes constitute a low-cost IMU. The cost of this IMU is less than 10 USD. A Bosch BMA150 3-axis accelerometer using a 10 bits A/D converter is used. It has a +/- 2g range. The two axis gyro is an Invensense IDG500. It is an analog sensor. It is digitalized by the PIC 12 bits A/D converter, and can measure rotation rates up to 500 degrees/s. On the vertical axis, a more accurate gyroscope is considered. It is an Epson XV3700. It has an auto-zero function to minimize heading drift. The IMU is running at a 200Hz rate. Lately, a 3-axis magnetometer AKM AK8975 has been added to obtain a heading estimate.

This set of sensors is completed by a vertical camera to measure the vehicle speed. It is a 64 degrees diagonal lens camera producing data at a framerate of 60 frames per second. A vision-based velocity estimation algorithm (see [Bristeau et al., 2011]), jointly developed by Parrot and SYSNAV, provides velocity estimate when the ground is sufficiently textured.

8.2 Aerodynamics modeling

This section aims to determine in general the aerodynamics effects on the quadrotor, and in particular, to prove the existence of a linear velocity term in the drag force. To do that, we consider a quadrotor UAV as a 6-DOF rigid body, with notations presented in Chapter 1, depicted in Fig. 8.2.

Considering a general wind speed which coordinates in the body frame are u_w , v_w , w_w , and the induced velocity v_i being a consequence of the rotation of the rotor blades, we use the following notations : $\bar{u} = u_w - u$, $\bar{v} = v_w - v$, $\bar{w} = v_i + w_w - w$. Each motor acts on the body depending on its rotation speed and the lever-arm L which is the length between the rotation axis and the center of gravity (Fig. 8.2). The mass of the quadrotor is around 1 kilogram.

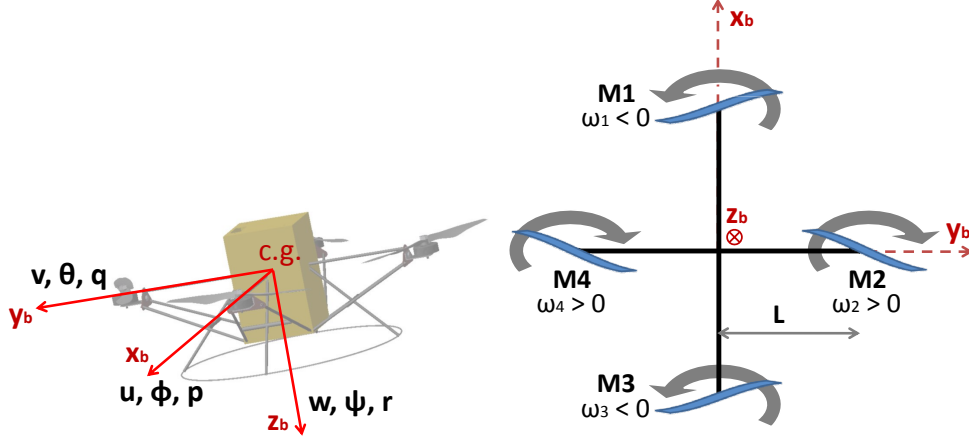


Figure 8.2: Notations in the body frame.

8.2.1 Method to calculate aerodynamics effects

Our modeling is widely inspired by works on large-size helicopter rotors [Johnson, 1980, Leishman, 2002, Prouty, 1990], and models proposed specifically for quadrotors [Romero et al., 2007, Guénard, 2007]. We transpose the large-size rotors modeling techniques to small-size rotors, taking into account angular rates, which are negligible at larger scales. By contrast with [Mettler, 2003, Vissière et al., 2008], we do not neglect the forward flight speed (u, v) . The aerodynamic effects applied to the rotor are evaluated by integrating, along each rotor blade, the aerodynamic resultant force per surface increment. We assume that, at a current point y along the rotor blade, the resultant force decomposes into a lift force $d\mathbf{L}$ and a drag force $d\mathbf{D}$

$$\begin{aligned} d\mathbf{L} &= \frac{1}{2} \rho U(y)^2 C_{L\alpha} \alpha(y) c dy \mathbf{z}_b, \\ d\mathbf{D} &= \frac{1}{2} \rho U(y)^2 (C_{D0} + C_{Di} \alpha(y)^2) c dy \mathbf{e}_\theta \end{aligned}$$

where ρ is the air density, U is the airspeed, c is the chord, $c dy$ is the surface increment, $C_{L\alpha}$ is the lift coefficient, C_{D0} is the parasitic drag coefficient, and C_{Di} is the lift-induced drag coefficient.

For each point y , we decompose the airspeed (Fig. 8.3) to calculate the local angle of attack $\alpha(y)$ as a function of the position y along the rotor blade, and of the rotation speed ω of the rotor. Importantly, we also consider the motion of the rigid body of the quadrotor in those variables.

After integrating the aerodynamic resultant force with respect to the space variable y , the result is averaged over a period of rotation while assuming the overall motion of the quadrotor is smooth and slow during a period of rotation of the rotor (this is a quasi-stationarity hypothesis). Then, the obtained formulas are simplified considering the following orders of magnitude for

the various variables: $\omega \approx 4200 \text{ tr/min} \approx 440 \text{ rad.s}^{-1}$, $|p|_{max} \approx |q|_{max} \approx |r|_{max} \approx 1 \text{ rad.s}^{-1}$, $|\bar{u}|_{max} \approx |\bar{v}|_{max} \approx 10 \text{ m.s}^{-1}$. In summary, using blade element theory, we obtain formulas for the aerodynamic forces and moments applied at the center of the rotor disc. We now present the results.

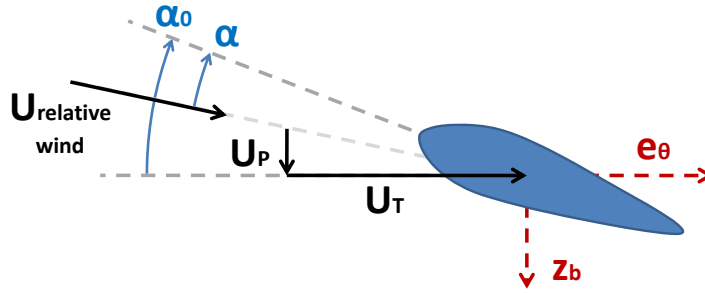


Figure 8.3: Decomposition of the airspeed to calculate the angle of attack.

Lift Force and Drag Moment

By integrating the lift per surface increment, we obtain the lift force \mathbf{LF} (or thrust)

$$\mathbf{LF} = \rho c R^3 \omega^2 C_{L\alpha} \left(\frac{\alpha_0}{3} - \frac{\bar{w} + L(\epsilon_1 q - \epsilon_2 p)}{2R|\omega|} \right) \mathbf{z}_b$$

where R is the radius of the rotor blade, α_0 its pitch angle at rest. The coefficients ϵ_1 and ϵ_2 depend on the rotor under consideration (Mi stands for the i^{th} rotor). In details, $\epsilon_1 = \{ 1 \text{ for M1, } 0 \text{ for M2, } -1 \text{ for M3, } 0 \text{ for M4} \}$, $\epsilon_2 = \{ 0 \text{ for M1, } 1 \text{ for M2, } 0 \text{ for M3, } -1 \text{ for M4} \}$.

By integrating the drag per surface increment relative to the rotation axis and considering the drag due to lift, we find the drag moment \mathbf{DM}

$$\mathbf{DM} = -sgn(\omega) \rho c R^4 \omega^2 \left(\begin{array}{c} \frac{C_{D0}}{4} + C_{Di} \alpha_0^2 \left(\frac{\alpha_0}{4} - \frac{2\bar{w}}{3R|\omega|} \right) \\ -C_{L\alpha} \frac{\bar{w}}{R|\omega|} \left(\frac{\alpha_0}{3} - \frac{\bar{w}}{2R|\omega|} \right) \end{array} \right) \mathbf{z}_b$$

We have found two expressions. Both feature a quadratic term in the rotation speed, and a linear term with respect to this same variable. Actually, the distribution of the pitch angle α_0 along the rotorblade is an hyperbolic function of the space variable y . In consequence, *the angle of attack* α (considering the induced velocity) *is assumed constant along the rotorblade*. We call α_t this constant for all y .

$$\alpha(y) = \alpha_0(y) - \frac{v_i}{y|\omega|} = \alpha_t$$

From now on, we consider a modeling around stationary flight, and we make the assumption that the induced velocity is uniform and does not vary more than $\pm 1 \text{ m.s}^{-1}$ around its hover value of 4.5 m.s^{-1} . This is a reasonable assumption as suggested in [Leishman, 2002,

Hoffmann et al., 2007]. Under this hypothesis, we admit that the parameter α_t is also independent of the rotation speed since v_i is proportional to $|\omega|$ around stationary flight.

With this twisted rotor blade, the following expressions of the lift force and the drag moment hold

$$\mathbf{LF} = \rho c R^3 \omega^2 C_{L\alpha} \left(\frac{\alpha_t}{3} - \frac{L}{2R|\omega|} (\epsilon_1 q - \epsilon_2 p) \right) \mathbf{z}_b, \quad (8.1)$$

$$\mathbf{DM} = -\text{sgn}(\omega) \rho c R^4 \omega^2 \left(\frac{C_{D0} + C_{Di} \alpha_t^2}{4} - \frac{C_{L\alpha} \alpha_t \bar{w}}{3R|\omega|} \right) \mathbf{z}_b \quad (8.2)$$

Drag Force

By integrating the drag per surface increment, the drag force \mathbf{DF} can be decomposed into two parts. On the one hand, there is the parasitical drag \mathbf{DF}_0

$$\mathbf{DF}_0 = \frac{1}{2} \rho c R^2 C_{D0} (|\omega| (\bar{u} \mathbf{x}_b + \bar{v} \mathbf{y}_b) - \text{sgn}(\omega) \bar{w} (p \mathbf{x}_b + q \mathbf{y}_b)) \quad (8.3)$$

On the other hand, there is a term coming from induced drag \mathbf{DF}_i

$$\mathbf{DF}_i = \rho c R^3 C_{Di} \alpha_t \left(\frac{\bar{w}}{R^2} (\bar{u} \mathbf{x}_b + \bar{v} \mathbf{y}_b) + \frac{\omega}{3} (p \mathbf{x}_b + q \mathbf{y}_b) \right) \quad (8.4)$$

And finally, we have to consider the component of lift in the rotation plane. We call it "drag due to lift" and note it \mathbf{DF}_L

$$\mathbf{DF}_L = -\frac{1}{2} \rho c C_{L\alpha} \left(\begin{array}{c} R \alpha_t \bar{w} (\bar{u} \mathbf{x}_b + \bar{v} \mathbf{y}_b) \\ + \left(\text{sgn}(\omega) R^2 \bar{w} - \frac{R^3 \alpha_t \omega}{3} \right) (p \mathbf{x}_b + q \mathbf{y}_b) \end{array} \right) \quad (8.5)$$

One can notice the existence of a term proportional to the speed u, v . Interestingly, unlike the usual quadratic drag of a body, this linear dependence can be used to estimate the translational speed using accelerometers measurements during slow forward flight. Conversely, if the interactions of the vehicle dynamics onto the aerodynamic effects are neglected, the drag force caused by the rotors is zero.

Lift Moment

Lastly, by integrating the lift per surface increment relative to the rotation axis, we obtain the lift moment

$$\mathbf{LM} = \rho c R^4 C_{L\alpha} \left(\frac{|\omega|}{8} (p \mathbf{x}_b + q \mathbf{y}_b) + \frac{\bar{w} \text{sgn}(\omega)}{4R^2} (\bar{u} \mathbf{x}_b + \bar{v} \mathbf{y}_b) \right) \quad (8.6)$$

In this expression, a side effect on the vehicle can be observed (last term in (8.6)). In particular, a rotor facing a non-zero airspeed along \mathbf{x}_b is subjected to flip and roll.

Consideration of flapping dynamics

In fact, these expressions can be rendered more precise by adding a degree of freedom to the rotor dynamics. We take into account the flexibility of the rotor blade, and, implicitly, we allow it to rotate out of the plane normal to the rotation axis. The angle between the blade and this plane is called flapping angle β . The flapping dynamics of the rotor blade can be approximately determined using the Fourier expansion of β , and the conservation of angular momentum around the flapping axis. The flapping angle is determined by the equilibrium between aerodynamic moment, centrifugal moment and stiffness moment. Additionally, the flapping dynamics can be considered (see [Bristeau et al., 2010a]), here, we simply use the expressions of stabilized flapping angles (this is another quasi-stationarity assumption). In details, one has:

$$a = (K_r q + K_{rq} p + K_v \bar{u} + K_{vq} \bar{v}) / K_d \quad (8.7)$$

$$b = (-K_r p + K_{rq} q + K_v \bar{v} - K_{vq} \bar{u}) / K_d \quad (8.8)$$

$$\text{with } K_d = \gamma \omega^2 + k_\beta^2 / (\gamma I_\beta^2 \omega^2), \gamma = \rho c |C_{L\alpha}| R^4 / (8 I_\beta), \quad (8.9)$$

$$K_r = 2|\omega| + k_\beta / (I_\beta |\omega|), \quad (8.10)$$

$$K_{rq} = \text{sgn}(\omega) (\gamma |\omega| - 2k_\beta / (\gamma I_\beta |\omega|)), \quad (8.11)$$

$$K_v = 2\gamma \bar{\omega} / R^2, \quad K_{vq} = \text{sgn}(\omega) 2k_\beta \bar{\omega} / (I_\beta R^2 \omega^2), \quad (8.12)$$

where a (respectively b) is the flapping angle along the \mathbf{x}_b axis (respectively the \mathbf{y}_b axis), γ is the Lock number of the blade (ratio between aerodynamics effects and inertial effects), k_β its stiffness and I_β a moment of inertia on the flapping axis. Thus, we find new expressions of the lift effects on a rotor

$$\mathbf{LF} = \rho c R^3 \omega^2 C_{L\alpha} \left(\frac{\alpha_t}{3} - \frac{L}{2R|\omega|} (\epsilon_{1q} - \epsilon_{2p}) \right) \begin{bmatrix} -a \\ -b \\ 1 \end{bmatrix}, \quad (8.13)$$

$$\mathbf{LM} = k_\beta [b \quad -a \quad 0]^T \quad (8.14)$$

Naturally, the expressions (8.1,8.6) for the rigid rotor are the limit of the expressions (8.13,8.14) when the stiffness k_β approaches ∞ .

8.2.2 Dynamic coupling between the vehicle and the rotors

In this section, we consider the whole vehicle with its four rotors. The UAV is assumed to fly out of ground effects. Applying Newton's second law, the efforts created by the four rotors are incorporated into the rigid body dynamics. To easily observe the impact of each modeling assumption, the equation will be linearized around stationary flight, i.e. $|\omega_i| = \omega_0$ (nominal speed). The linearized state model writes under the form $\dot{X} = AX + BU$ with $X = [u \ v \ w \ p \ q \ r \ \phi \ \theta \ \psi]^T$ and $U = [\delta_1 \ \delta_2 \ \delta_3 \ \delta_4]^T$ where δ_i is a small variation of rotation speed of the motor M_i around ω_0 (we could discuss the transfer between motor current and rotation speed). By convention, a positive value for δ_i means that the motor M_i thrusts more.

Modeling without interactions

First, we examine a model without interactions of the motion onto the aerodynamics effects. The linearization around stationary flight makes the aerodynamic effort on the body vanish. To help the interested reader, we put stars to show where these terms would appear. In details, one has

$$A = \begin{bmatrix} * & 0 & 0 & 0 & * & 0 & 0 & -g & 0 \\ 0 & * & 0 & * & 0 & 0 & g & 0 & 0 \\ 0 & 0 & * & 0 & 0 & 0 & 0 & 0 & 0 \\ 0 & * & 0 & * & 0 & 0 & 0 & 0 & 0 \\ * & 0 & 0 & 0 & * & 0 & 0 & 0 & 0 \\ 0 & 0 & 0 & 0 & 0 & * & 0 & 0 & 0 \\ 0 & 0 & 0 & 1 & 0 & 0 & 0 & 0 & 0 \\ 0 & 0 & 0 & 0 & 1 & 0 & 0 & 0 & 0 \\ 0 & 0 & 0 & 0 & 0 & 1 & 0 & 0 & 0 \end{bmatrix}$$

$$B = \begin{bmatrix} 0 & 0 & 0 & 0 \\ 0 & 0 & 0 & 0 \\ -K_{thr} & -K_{thr} & -K_{thr} & -K_{thr} \\ 0 & -K_{cmd} & 0 & K_{cmd} \\ K_{cmd} & 0 & -K_{cmd} & 0 \\ K_{yaw} & -K_{yaw} & K_{yaw} & -K_{yaw} \\ 0 & 0 & 0 & 0 \\ 0 & 0 & 0 & 0 \\ 0 & 0 & 0 & 0 \end{bmatrix}$$

where K_{thr} , K_{cmd} , K_{yaw} are positive coefficients. This model emphasizes a general lack of observability of the motion of the UAV, since aerodynamic effects are quadratic and the matrix A is quite sparse. As we have assumed the inertia matrix to be diagonal, the dynamics of the three axis are decoupled. Therefore, one can study the dynamics on each axis separately. Precisely, we now focus on the pitch dynamics. The roll dynamics is similar to it up to a rotation, whereas the yaw and vertical dynamics are less critical. We use a reduced state vector $X = [u \ q \ \theta]^T$ and the control vector U is reduced to the pitch torque $U = [\delta_1 - \delta_3]$.

Rigid modeling

Now, we take in account the coupling between the rigid body motion and the aerodynamic effects. Here, rigid rotor blades are considered. Consequently, we find new terms in the (reduced) matrix A and the (reduced) vector B appear.

$$A = \begin{bmatrix} -K_{df} & 0 & -g \\ -K_{dm} & -K_{lf} & 0 \\ 0 & 1 & 0 \end{bmatrix} \quad B = \begin{bmatrix} 0 \\ K_{cmd} \\ 0 \end{bmatrix}$$

The coefficient K_{df} is positive and stems from the drag force (8.3-8.5) which is summed over the four motors. Velocity terms sum up, but angular rates terms cancel out at first order. The coefficient K_{lf} is positive. It represents the fact that each rotor counteract the vehicle rotation. This phenomenon also appears in the lift effects (8.1,8.6). Finally, the coefficient K_{dm} has the same sign as h , which is the height of the center of gravity relative to the rotors plane (h being positive means that the center of gravity is above the rotors). It stems from the moment exerted at the center of gravity by the drag force (8.3-8.5). Typical numerical values for these parameters are $K_{df} \approx 0.049$, $K_{lf} \approx 4.1$, $K_{dm} \approx 3.8h$. Compared to the modeling without interactions, one can notice that some coefficients of the diagonal of the matrix A have been enlarged. Interestingly, these negative terms have a stabilizing effect. The coefficient K_{dm} will be discussed later on, in Section B. It can also be noticed that the advantage of the quadrotor, compared to the helicopter, is to cancel the side effect visible in Eq. (8.6) by associating contrarotative rotors.

Flexible modeling

At last, we incorporate the flexibility of the rotor blades about stationary flight. Consequently, the matrix A is updated as follows while the vector B remains identical

$$A = \begin{bmatrix} -K_1 & K_3 & -g \\ K_4 & -K_2 & 0 \\ 0 & 1 & 0 \end{bmatrix} \quad (8.15)$$

We have obtained four new positive coefficients. First, K_1 reinforces K_{df} with a more important term coming from the tilt phenomenon of the rotor discs (8.13). This phenomenon takes place as follows. During a forward flight, the advancing blade experiments stronger lift than the retreating one. Under the rigid modeling assumption, one would obtain roll moments on each rotor which would cancel on the whole vehicle. By contrast, by considering the flexibility, stronger lifts do not cause any moment but induces flapping speeds. The flapping angle has the same extrema for all the rotation direction (Fig. 8.4).

In fact, one has to notice that, as well as in the rigid model, on a quadrotor, axial effects are added while side effects cancel (8.7-8.12). In the same manner, K_2 contributes to incrementing K_{lf} thanks to the same phenomenon (8.14), stemming this time from the angular rates. The coefficient K_3 represents the inertia of rotor discs which leads to tilt the lift (8.13). Finally, the coefficient K_4 comes from the stiffness of the blades which tends to keep rotor discs orthogonal to the rotation axis of the motors (8.14).

Experimental measurements of the blade stiffness yield

$$K_1 \approx 0.072, \quad K_2 \approx 5.6, \quad K_3 \approx 0.079, \quad K_4 \approx 0.41 - 3.8h.$$

In summary, the flexibility of the propellers results into larger coefficients into the matrix A and stresses a stronger coupling phenomenon between speed and angular rates.

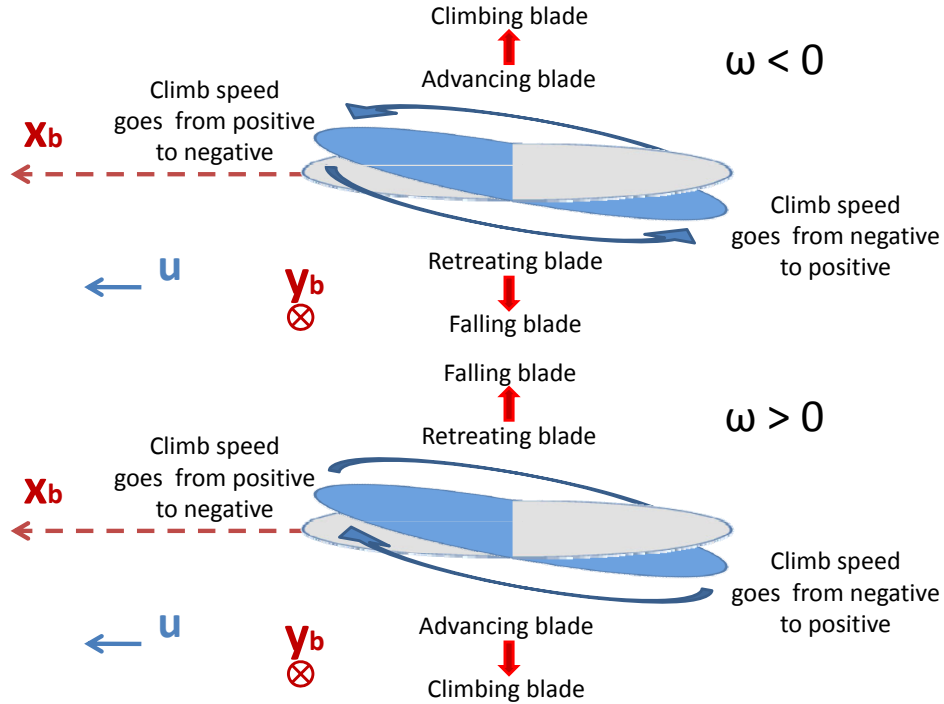


Figure 8.4: Tilt phenomenon in case of forward flight: counter-clockwise rotation (top) and clockwise rotation (bottom).

8.3 Observer design and presentation of results

In summary, the previous section proves that linear drag term exists from the interaction between the rigid body and the rotors and this term is reinforced by tilt phenomenon which changes a lift force component in drag. These induced-drag effects are non negligible and they yield interesting information on the velocity of the system. The induced forces are directly measured by the accelerometers, and through the model, can be used to reliably estimate the velocities of the UAV. With this information, we are able to design an observer which relies on the exploitation of the different sensors time-horizons to provide a mutual drift-compensation. The inertial sensors, which are noisy and biased, are essentially exploited for the high-frequency part of their signal. The vision-based algorithm and the magnetic sensors (disturbed by the motors) are used at low-frequency.

Without going into details (see [Bristeau et al., 2011]), the images provided to the vision-based algorithm need to be preprocessed to cancel micro-rotations and allow the estimation of the velocity. These micro-rotations are compensated for with the knowledge of the angular rates of the quadrotor. Similarly, vertical motion must be compensated for in the images before estimating the horizontal velocity. Vision velocity may be unavailable depending of the scene textures.

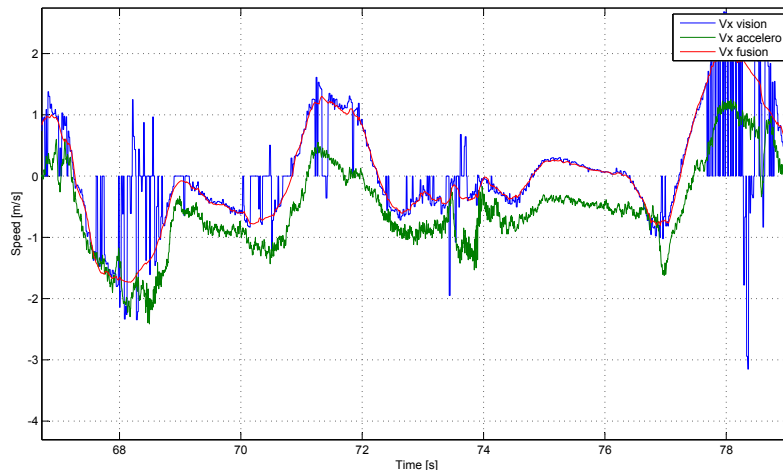


Figure 8.5: Velocity estimates: computer vision velocity estimate (blue), aerodynamics model velocity estimate from direct accelerometer reading (green), fused velocity estimate (red).

From the modeling proposed in Section 8.2, it appears that the accelerometers can be used to measure directly the quadrotor velocity, if their biases are known. At rest (null ground speed), the measurements are constituted from the biases of the sensors and the attitudes of the quadrotor.

As in Section 6.1, we distinguish interconnected systems to visualize the complex combination of inertial sensors and vision which is realized onboard the AR Drone. Vision-based algorithm provides velocity estimate but its accuracy is improved by the knowledge of the angular rates and the vertical motion. A complementary filter between the velocity from the computer vision algorithm and the accelerometers measurements permits to smooth the partial information from the camera, remove biases from the accelerometers. This fusion is illustrated in Fig. 8.5.

With the previously debiased accelerometers and the gyrometers, one can build an attitude estimation algorithm based on another complementary filter (see [Mahony et al., 2005, Metni et al., 2006, Jung and Tsiotras, 2007, Martin and Salaün, 2008]). Thus, gyrometers biases and attitudes estimates are available to compensate for micro-rotations in the camera images¹.

Independently, an altitude (height) observer is realized with the ultrasonic sensors in order to be able to realize vertical stabilization of the quadrotor and also to compensate for vertical motion in the camera images.

This interconnection is illustrated in Fig. 8.6 where one can find four estimation blocks : the velocity, the roll and pitch attitudes, the altitude and the heading. The last block deserves a particular attention since phenomena similar to those encountered in the automotive vehicle occurs. The expression of the measured magnetic field is the same as in Eq. (4.2)

1. The attitude estimates are not necessarily the exact attitudes of the quadrotor as defined in Section 1: in case of constant wind, the rest position of the quadrotor corresponds to non-zero attitudes which means that from the complementary filter between the vision-based ground speed estimate and the accelerometers measurements, the biases estimates take in account these non-zero attitudes. Attitudes estimates are always computed relative to the rest attitudes of the quadrotor.

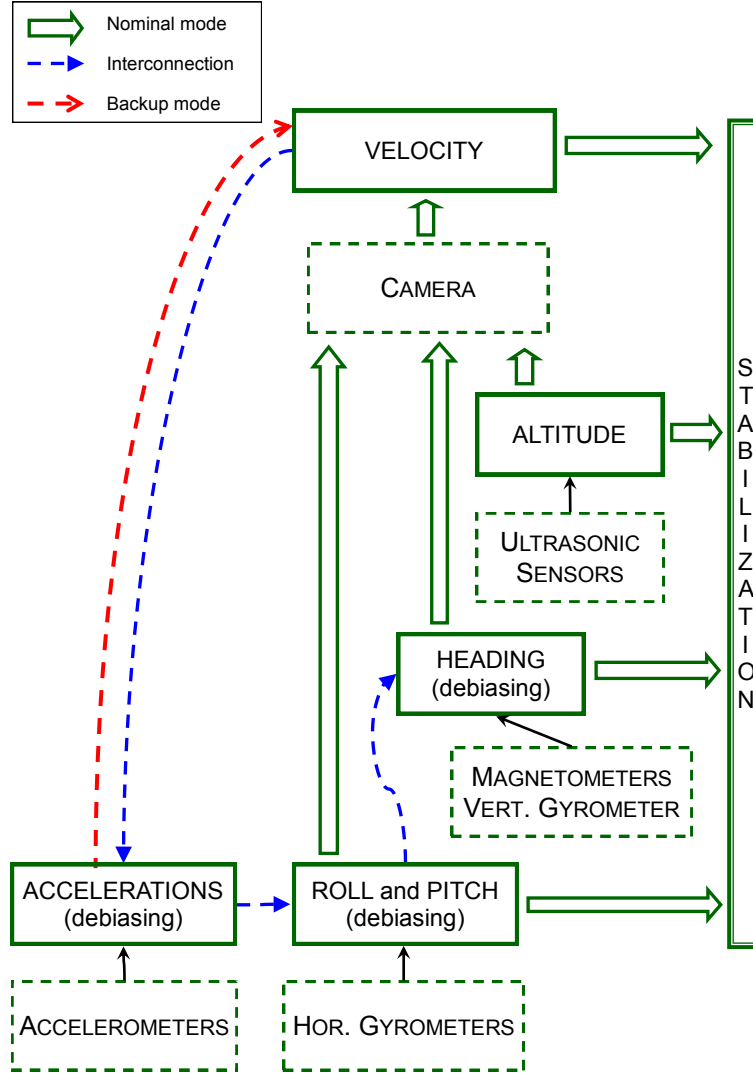


Figure 8.6: Observer structure as a combination of inertial sensors and vision. The green path constitutes a nominal mode, sufficient to provide estimates fed back to stabilizing controllers. Meanwhile, biases are estimated and serve as backup when the video processing algorithms fail.

$$\mathbf{B}_m = R_{SI} \Lambda R_{SI}^T (R_\phi R_\theta R_\psi \mathbf{B}_E + \mathbf{B}_s(u) + \Delta + \mathbf{B}_{loc})$$

The vector Δ and the matrices R_{SI} and Λ still stand for the hard/soft iron effects. The vector $\mathbf{B}_s(u)$ represents the magnetic field created by the four running motors². The vector \mathbf{B}_{loc} is constituted by the magnetic disturbances, ubiquitous during indoor flights. Furthermore,

2. The contribution of the stopped motors is in the hard iron effects vector.

the magnetic field \mathbf{B}_E expressed in the inertial frame is subject to non negligible variations as the quadrotor moves inside a building.

The solution to find heading estimate is different since in the case of the quadrotor, a calibration of the system (sensors + quadrotor) can be realized. Using calibration algorithms ([Dorveaux et al., 2009]), the hard/soft iron effects can be identified. The remaining unknowns are the variations of the magnetic field expressed in the body frame (essentially due to the motors) and the variations of the magnetic field expressed in the inertial frame (due to close metallic parts during flight).

To prove the observability of these variations, we now consider the calibrated sensor B_c neglecting the hard/soft iron effects

$$\mathbf{B}_c = R_{SI}^T \Lambda^{-1} R_{SI} \mathbf{B}_m - \Delta = R_\phi R_\theta R_\psi \mathbf{B}_E + \mathbf{B}_s(u) + \mathbf{B}_{loc}$$

With the roll and pitch estimates, one can constitute a virtual sensor

$$\mathbf{Y}_m = R_\theta^{-1} R_\phi^{-1} \mathbf{B}_c = R_\psi \mathbf{B}_E + R_\theta^{-1} R_\phi^{-1} (\mathbf{B}_s(u) + \mathbf{B}_{loc}) \quad (8.16)$$

Note $B_E = [B_x \ B_y \ B_z]^T$ the components of the indoor magnetic field and $[\delta_x \ \delta_y \ \delta_z]^T$ the disturbances generated by the motors (compensated for roll and pitch angles).

$$\mathbf{Y}_m = R_\psi \begin{bmatrix} B_x \\ B_y \\ B_z \end{bmatrix} + \begin{bmatrix} \delta_x \\ \delta_y \\ \delta_z \end{bmatrix} = \begin{bmatrix} c_\psi B_x + s_\psi B_y + \delta_x \\ -s_\psi B_x + c_\psi B_y + \delta_y \\ B_z + \delta_z \end{bmatrix}$$

Focusing on the objective of heading estimate, we leave out the (inertial) vertical axis. It appears that the absolute heading can not be obtained without knowledge of the local magnetic field. As in Section 4.2.2, it is necessary to introduce a phase ψ_0 .

$$\mathbf{Y}_m = \begin{bmatrix} c_{(\psi+\psi_0)} B_x + \delta_x \\ -s_{(\psi+\psi_0)} B_x + \delta_y \end{bmatrix} \quad (8.17)$$

In the same way, from the vertical gyrometer and the roll and pitch estimates, one can build a virtual sensor of the yaw rate

$$\Psi_m = \frac{r_m + \hat{\theta} s_{\hat{\phi}}}{c_{\hat{\phi}} c_{\hat{\theta}}} \approx r_m + \hat{\theta} \hat{\phi} \quad (8.18)$$

Consider the following state with $\psi^* = \psi + \psi_0$

$$\mathbf{X} = [\psi^* \ b_r \ B_x \ \delta_x \ \delta_y]^T \quad (8.19)$$

The deterministic part of the state dynamics concerns only the heading

$$\dot{\mathbf{X}} = \begin{pmatrix} 0 & -1 & 0 & 0 & 0 \\ 0 & * & 0 & 0 & 0 \\ 0 & 0 & * & 0 & 0 \\ 0 & 0 & 0 & * & 0 \\ 0 & 0 & 0 & 0 & * \end{pmatrix} \mathbf{X} + \begin{bmatrix} 1 \\ 0 \\ 0 \\ 0 \\ 0 \end{bmatrix} \Psi_m$$

For simplicity of observability analysis, the stars will be taken as zeros but in practice, the biases and the magnetic field component dynamics can be represented by first-order dynamics driven by a Gaussian noise, depending on the motors rotation speed and the quadrotor velocity. Thus, the different characteristic times of the first-order dynamics introduce frequency separation, and so on, more observability.

Assuming the non-linearity of the measurement equation (8.17) negligible compared to the measurement frequency, and dropping out non necessary terms in $\dot{\psi}$, we derive the observability matrix as presented in Definition 4

$$\begin{aligned} Q_0(t) &= \begin{pmatrix} -s_{\psi^*} B_x & c_{\psi^*} & 1 & 0 & 0 \\ -c_{\psi^*} B_x & -s_{\psi^*} & 0 & 1 & 0 \end{pmatrix}^T \\ Q_1(t) &= \begin{pmatrix} -\dot{\psi} c_{\psi^*} B_x & -\dot{\psi} s_{\psi^*} & 0 & 0 & s_{\psi} B_x \\ \dot{\psi} s_{\psi^*} B_x & -\dot{\psi} c_{\psi^*} & 0 & 0 & c_{\psi} \end{pmatrix}^T \\ Q_2(t) &= \begin{pmatrix} \dot{\psi}^2 s_{\psi^*} B_x & -\dot{\psi}^2 c_{\psi^*} & 0 & 0 & \dot{\psi} c_{\psi^*} B_x - s_{\psi^*} B_x \\ \dot{\psi}^2 c_{\psi^*} B_x & \dot{\psi}^2 s_{\psi^*} & 0 & 0 & -\dot{\psi} s_{\psi^*} B_x - c_{\psi^*} B_x \end{pmatrix}^T \end{aligned}$$

The local observability matrix is calculated below

$$\begin{aligned} \mathbb{O}(t) &= (Q_0(t) \quad Q_1(t) \quad Q_2(t)) \begin{pmatrix} Q_0^T(t) \\ Q_1^T(t) \\ Q_2^T(t) \end{pmatrix} \\ &= \begin{pmatrix} B_x^2(\dot{\psi}^4 + \dot{\psi}^2 + 1) & 0 & -B_x s_{\psi^*} & -B_x c_{\psi^*} & -B_x^2 \dot{\psi}^2 \\ 0 & \dot{\psi}^4 + \dot{\psi}^2 + 1 & c_{\psi^*} & -s_{\psi^*} & -B_x \dot{\psi}(\dot{\psi}^2 + 1) \\ -B_x s_{\psi^*} & c_{\psi^*} & 1 & 0 & 0 \\ -B_x c_{\psi^*} & -s_{\psi^*} & 0 & 1 & 0 \\ -B_x^2 \dot{\psi}^2 & -B_x \dot{\psi}(\dot{\psi}^2 + 1) & 0 & 0 & B_x^2(\dot{\psi}^2 + 2) \end{pmatrix} \end{aligned}$$

The characteristic polynomial $P(s, t)$ of the matrix $\mathbb{O}(t)$ can be lower-bounded, uniformly in t , for s positive by a polynomial $P_0(s)$ whose coefficients are depending on the state boundaries. In particular, $P_0(0) = \min_t (B_x^4 \dot{\psi}^4 (1 + \dot{\psi}^2))$.

Quite naturally, it appears that if the magnetic field is not null and if there are heading changes, then there exists $\mu > 0$ such that $P_0(s) > 0$ for $s \in [0, \mu]$. In turn, the roots of $P(s, t)$ are uniformly bounded by μ . Therefore, the heading estimation problem is DO and according to Theorem 10, a Kalman Filter allows to estimate the state in Eq. (8.19): in spite of unknown variations of the sensed magnetic field, the magnetometer can be exploited to remove the bias from the vertical gyrometer and estimate ψ^* . Thus, one obtains a non-drifting compass (the phase ψ_0 remaining unobservable).

Simulation results are presented below to assess the observability of the biases and the magnetic field variations. These results take in account that the roll and pitch angles used in Eq. (8.16,8.18) are the output of the attitudes observer which induces errors on the measurements.

Figure 8.7 shows how well the magnetic field variations are estimated after tens of second despite a bad initialization.

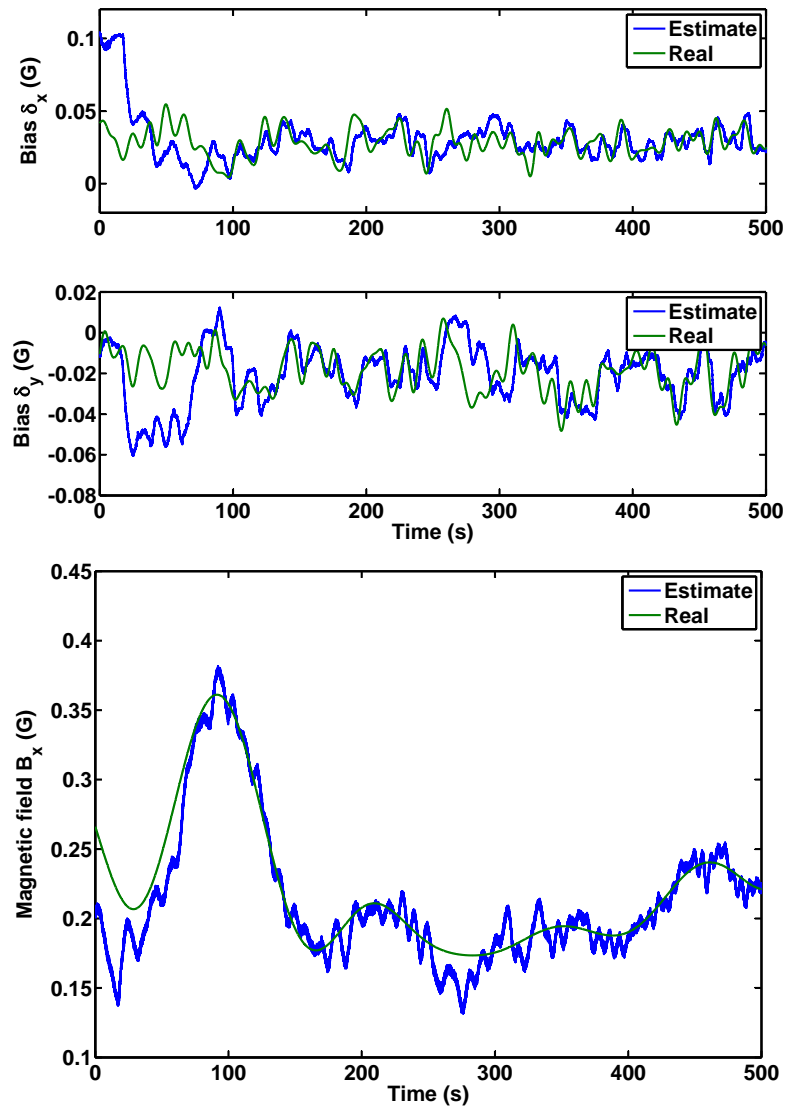


Figure 8.7: Estimate of the magnetic field variations.

Figure 8.8 illustrates the merits of the magneto-inertial fusion. The gyrometer bias is estimated and the heading error is reduced and no more diverging.

This observer completes the interconnection scheme presented in Fig. 8.6. The resulting estimation architecture is a complex combination of several principles, used to determine, over distinct time-horizons, the biases and other defects of each sensor. The Parrot AR.Drone project illustrates how observability analysis permits to realize an embedded system which takes the most of the available sensors and compensate for their defects by mutual compensation. The outcome is a sophisticated system but this complexity is not apparent to the user who can enjoy flights easily and with full safety.

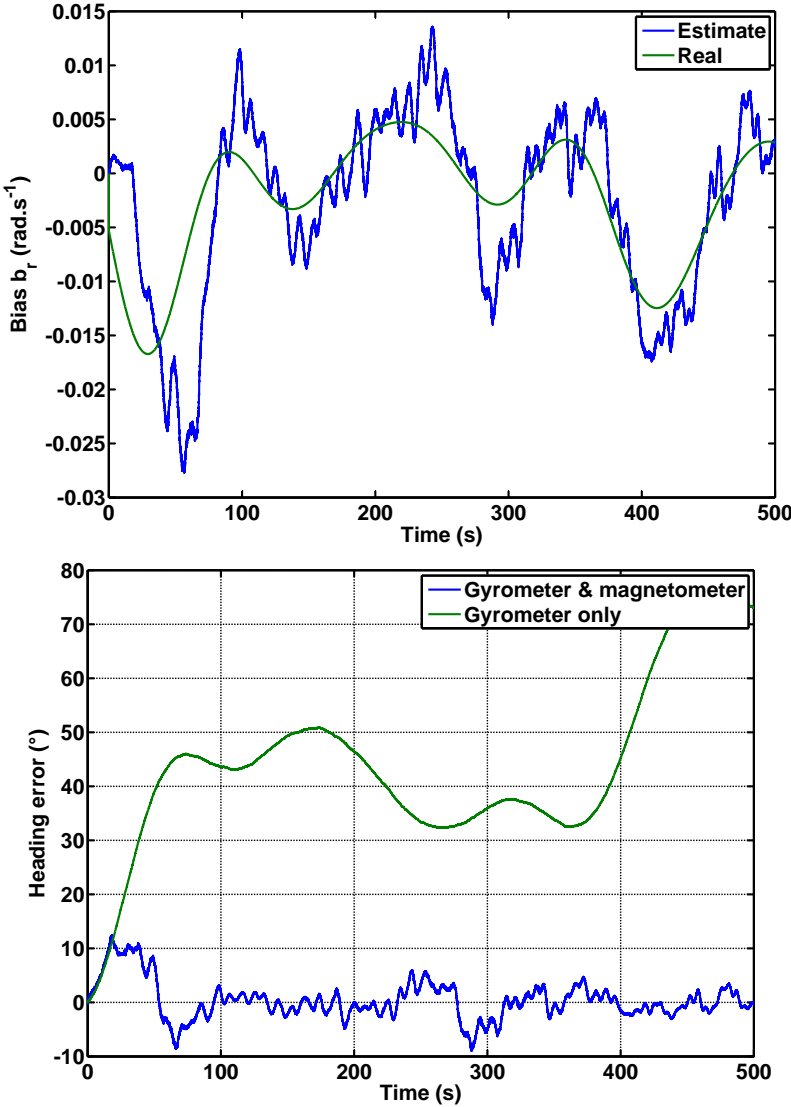


Figure 8.8: Estimate of the gyrometer bias and heading error reduction.

Chapter 9

A navigation problem for an experimental mini-rocket

Le problème de navigation associé à une mini-fusée expérimentale

Dans le cadre du projet PERSEUS mené par le CNES, ce chapitre présente comment des capteurs MEMS peuvent fournir une solution bas-coût à l'estimation de trajectoire pour mini-fusées. La reconstitution de trajectoire est assurée par la technique classique de navigation inertielle, couplée à l'usage de magnétomètres calibrés a priori. En outre, les capteurs embarqués sont également utilisés pour quantifier le fonctionnement du système de propulsion et ainsi faire de ces mini-fusées un banc d'essai volant.

Introduction

Space launcher navigation systems usually incorporate high quality inertial sensors [Titterton and Weston, 2004]. This requirement is due to the lack of possible reconciliation of data with extraneous information (GPS, or pilot instructions), the total flight time which can be as large as 40 minutes to 2 hours, and the quality requirements on navigation signal for the stabilizing closed-loop controllers.

Nano launchers, i.e. launcher capable of putting a typical payload of 10 kg at an altitude of 250 km, have been the subject of a substantial research effort over the last decades. In this field, hybrid rockets have attracted much attention [Mukunda et al., 1979] because of their low cost, good performance and safety record. A main reason is the emergence of an interest of end-users for short terms space missions where tiny satellites are to be used for a short period (a few days) in a specific geographic region. Prime examples are United Nations Organization related missions (to monitor sudden disasters such as flooding or earthquakes), or military operations requiring specific observation and/or communication capabilities. Another interest of such systems is their relatively low cost, due to the possibility of small series mass production, to attract new potential users such as metrological and microgravity researchers [Nagata et al., 2006].

Due to their costs and weights, the high quality sensors usually embedded in aerospace systems must be discarded for nano/micro rockets. Fortunately, the specifications of these rockets are also different. In particular, the flight time is much lower, which enables to use possibly biased and noisy signals.

In this context, several projects have been under development. In particular, we present here a study being part of the *Projet Etudiant de Recherche Spatiale Européen Universitaire et Scientifique*, European Student Project on Academic and Scientific Space Research (PERSEUS project) conducted by CNES. These systems must rely on low-cost technologies. This is also true for all the included subsystems ranging from the propulsion system, the mechanical structure, and very importantly the navigation system which is studied here.

Therefore, it seems reasonable to use MEMS inertial sensors on-board such a rocket and to integrate the equations of motion to obtain an estimate of the trajectory. In practice, only a real experiment can support this fact.

We consider a very small rocket (2.5 m high) equipped with MEMS inertial sensors. This rocket is propelled either by a classical solid motor or an hybrid engine especially developed for this project. The ascent trajectory lasts a few tens of seconds with a culmination less than 2 km high. This rocket belongs to the smallest class of rockets considered in the PERSEUS project. Soon, further developments will include a second class of rockets capable of reaching an altitude of 15 km, which will be followed by a third class targeting the altitude of 100 km.

The rockets from PERSEUS project are designed to be in-flight test-benches. We prove here the feasibility of trajectory estimation for rockets, based on MEMS sensors, and the calibration of propulsion system compared to values obtained on ground test-bench [Bristeau and Petit, 2009].

9.1 The rocket under consideration

The structure of the rocket is almost constant on a rocket (Fig. 9.1). It consists of three main parts: the engine in the lower part of the body, the parachute box in the middle zone, and the electronic devices in the higher part. Parachute box and electronic devices can be swapped, but the motor which is the main mass contribution remains in the lower part. Thus, the mass distribution and the induced location of the center of gravity above the center of aerodynamics forces guarantee aerodynamic stability.

9.1.1 Model

We now detail a model for the rocket under consideration here. It is considered as a 6-DOF rigid body subjected to a thrust generated by the engine. The mass of the rocket (resp. the moment of inertia tensor) is noted M (resp. J).

Variable mass rigid body equations

Based on Kane's formalism and volume integrals [Eke, 1998], under the assumption of axisymmetric and/or negligible displacements of matter inside the rocket, the dynamics of a variable mass rigid body is given by the following equations, where \mathbf{V} is the speed relative to

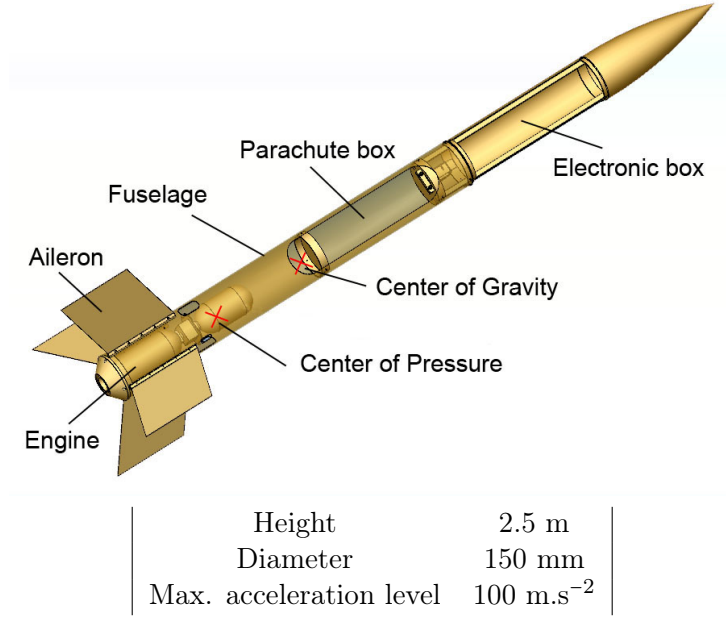


Figure 9.1: Rocket components and main characteristics.

an inertial frame of a fixed point of the rocket and CG is the vector distance of this point with respect to the center of gravity

$$M \left(\frac{d\mathbf{V}}{dt} \Big|_{R_i} + \frac{d\boldsymbol{\Omega}}{dt} \Big|_{R_i} \wedge CG + \boldsymbol{\Omega} \wedge (\boldsymbol{\Omega} \wedge CG) \right) = \sum \mathbf{F} + \mathbf{F}_t + \mathbf{F}_c$$

$$J \frac{d\boldsymbol{\Omega}}{dt} \Big|_{R_i} + \frac{dJ}{dt} \boldsymbol{\Omega} = \sum \mathbf{M} + \mathbf{M}_d$$

The mass loss induces the force \mathbf{F}_t which is the thrust, the force \mathbf{F}_c which is the Coriolis acceleration and the moment \mathbf{M}_d which is a damping moment. The external forces (resp. external moments) are gathered in $\sum \mathbf{F}$ (resp. $\sum \mathbf{M}$).

In the case considered here (compared to expendable launchers), the maximum loss of mass is relatively small compared to the total mass of the rocket. Therefore, the displacement of the center of gravity is small and slow, and one can neglect some terms compared to the thrust. Under this assumption, the dynamics write

$$M \left(\frac{d\mathbf{V}}{dt} \Big|_{R_b} + \boldsymbol{\Omega} \wedge \mathbf{V} \right) = \sum \mathbf{F} + \mathbf{F}_t + \mathbf{F}_c \quad (9.1)$$

$$J \frac{d\boldsymbol{\Omega}}{dt} \Big|_{R_b} + \boldsymbol{\Omega} \wedge J\boldsymbol{\Omega} + \frac{dJ}{dt} \boldsymbol{\Omega} = \sum \mathbf{M} + \mathbf{M}_d$$

Among the external forces are the gravity, the pressure force which is applied at the nozzle exit, the aerodynamic forces which are applied at the center of pressure, and the force exerted

by the parachute when it is deployed. The various lever arms generate external torques. To determine the moment \mathbf{M}_d and the effect due to the inertia variation requires the knowledge of the mass distribution during the combustion.

Aerodynamics

For this kind of small experimental rockets, the aerodynamic modeling is not essential. On one hand, drag effects are negligible compared to the thrust force since the airspeed does not reach important values in a so short acceleration time (less than 2 sec). On the other hand, transverse effects like incidence oscillations (short period mode) are difficult to identify because of large uncertainties on aerodynamic parameters (like the lift coefficient) and mechanical parameters (principally the inertia tensor). Fortunately, they are well visible on the gyrometers measurements.

9.1.2 Onboard instrumentation

To reconstruct the ascent trajectory of the rocket, except heading and inclination of the ramp measured with reference system, only onboard measurements are available. Certainly, it would be possible and beneficial to consider ground instrumentations too, but so far this has been out of the scope of the experimentations.

The rocket is equipped with the sensors previously presented in the automotive embedded system: an IMU providing digital measurements of a three-axis accelerometer, a three-axis gyrometer and a three-axis magnetometer, and a barometer. A GPS receiver LEA5H from ublox® is added essentially to provide the position of the rocket on the ramp and after parachute opening: during the propelled phase, the GPS signal is lost due to too high level of acceleration. The barometer and the GPS solution navigation are stored at low frequency, respectively 28 Hz and 4 Hz but the IMU data rate is 819 Hz. The time-stamping and the logging on a micro-SD card are realized with a standard deviation of 3 μ s on the sampling period and a frame loss rate less than $10^{-4}\%$.

For practical reasons, the IMU is aligned with the body frame but is in the electronic box, which is not located at the center of gravity (Fig. 9.1). This complexifies the analysis as one must take into account lever arms which disturb the measurement of the accelerations by introducing angular velocities when they are not zero. The magnetic field measurements are heavily disturbed by the various metallic components of the rocket (hard/soft iron effects).

9.2 Trajectory estimation

9.2.1 A typical trajectory

The trajectory of the rocket can be divided into four stages. The first one lasts until ignition. During this time period, the rocket is standing still on the launch-pad. It is possible to take advantage of this to calibrate the IMU sensors.

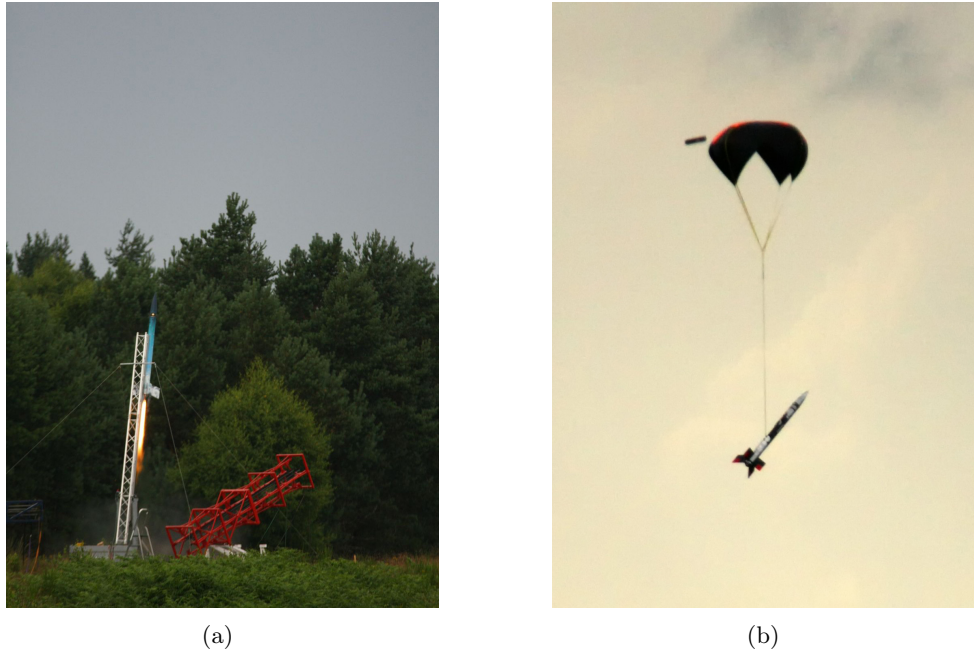


Figure 9.2: Rocket after ignition on the launching ramp (a) and descent flight under parachute (b).

During the second stage of the trajectory (Fig. 9.2a), the engine is on and the rocket is propelled and moving but remains on the launch ramp. The modeling of this period is quite uncertain due to unmodeled interactions with the ramp. Fortunately, the time spent moving on the ramp is very short.

Then, the third and main stage is the ascent flight of the rocket which is propelled. During this stage, the rocket accelerates before reaching its maximum velocity. Then, it slows down and reaches its peak altitude. Finally, the parachute is deployed at a time controlled by an onboard timer. The predominant effect during this ascent stage is the thrust.

Finally, the fourth stage (Fig. 9.2b) is the descent flight when the rocket hangs under the parachute until landing. During this period, the rocket and its parachute constitute a non-rigid flying object submitted to drag aerodynamics effects whose coefficients are badly known [Dobrokhodov et al., 2003]. Further, the system is quite sensitive to wind disturbances.

9.2.2 Estimation technique

The estimation problem for mini-rocket has very particular characteristics. The dynamics environment is very severe: during propelled phase, the acceleration level is around 6 to 10 g depending on the engine, during descent phase, the angular rates are very high due to oscillations under the parachute. The rocket undergoes spin during ascent phase and its inclination varies from almost vertical on the launchpad to almost horizontal at the culmination before being

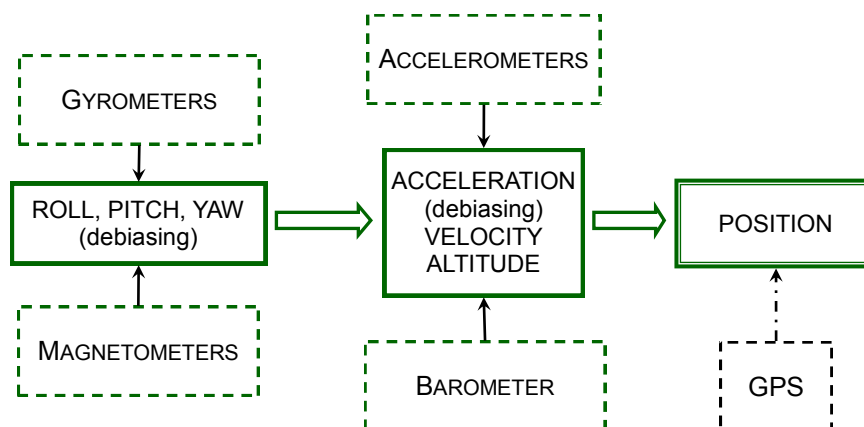


Figure 9.3: Observer design adapted to mini-rocket estimation problem. The green path constitutes a real time mode sufficient to provide trajectory estimate. Available GPS information can be used for a posteriori smoothing.

chaotic under the parachute. The flight duration is very short : tens of second for the ascent time, minutes for the descent. The magnetic environment does not change during the flight.

These observations suggest the following observer design (Fig. 9.3). Due to high level of acceleration, the accelerometers must be discarded to obtain the attitude of the rocket. Fortunately, the magnetometers can be calibrated in situ [Dorveaux et al., 2009] and offer a measurement of the rotation matrix. On the same model as in [Mahony et al., 2005, Metni et al., 2006, Jung and Tsiotras, 2007, Martin and Salaün, 2008] (the magnetometer playing the role of accelerometer), an attitude observer can be realized.

Given the attitudes, the accelerometers, associated to the barometer, are used to estimate inertial velocity. It appears that the barometer measurement suffers from first-order dynamics, negligible before now, but relevant considering the vertical speed of the rocket.

Finally, the trajectory is estimated by integration of the velocity since GPS is not available during the flight. Nevertheless, the knowledge of the landing point allows us to realize smoothing on the whole trajectory to improve in first place the velocity estimate, then the attitudes estimate.

In practice, the observers are not distinct, we use a discrete multi-rates EKF to reconcile data from all the sensors, completed by a smoother if GPS is available at the end of the flight (according to the algorithm presented in Section 7.5).

9.2.3 Results exploiting in-flight measurements

During the descent under parachute, the severe angular dynamics magnifies the residual error in the angular rates estimation. After calibration of the magnetometers inside the rocket, hard/soft iron effects are identified. They can be used to compensate for the biases of the gyrometers. Figure 9.4 shows the improvements brought by the magnetometers on the attitude estimation, and, therefore, on the trajectory. GPS information is not used here.

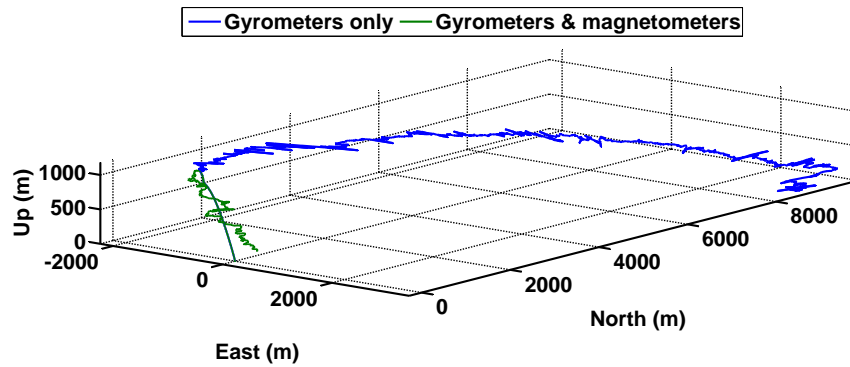


Figure 9.4: Trajectory estimation: benefits of usage of calibrated magnetometers (green), compared against diverging estimation with gyrometers only (blue).

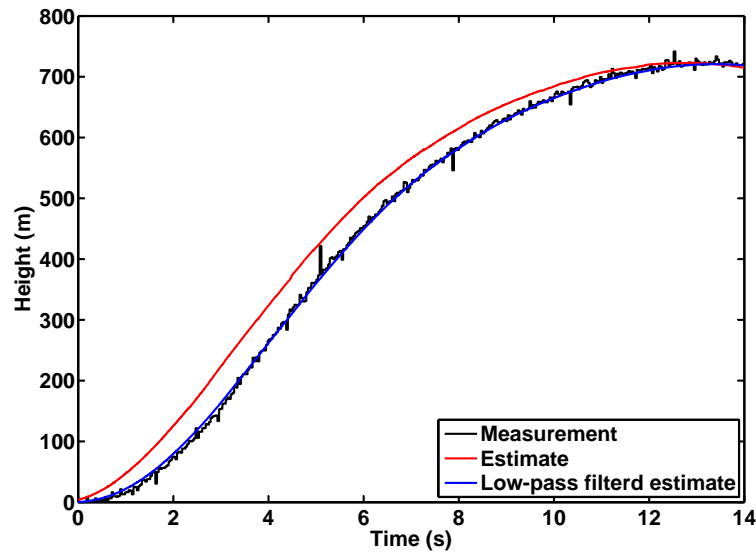


Figure 9.5: Vertical motion estimation: mutual compensation of accelerometer bias and barometer low-pass filtering.

The association of accelerometers to the barometer to estimate vertical motion highlights a complementarity between the two sensors: the accelerometers suffer from biases but have an excellent bandwidth, on the contrary, the barometer gives a direct reading of the height but its measurement is compromised by the rocket structure which acts as an acoustic filter for the pressure equilibrium inside the rocket where is the sensor. Figure 9.5 illustrates how the stabilized measurements of the barometer (launch and culmination) allows to estimate accelerometer bias whereas the vertical dynamics permits to identify the characteristic time of the barometer measurement. GPS information is not used here.

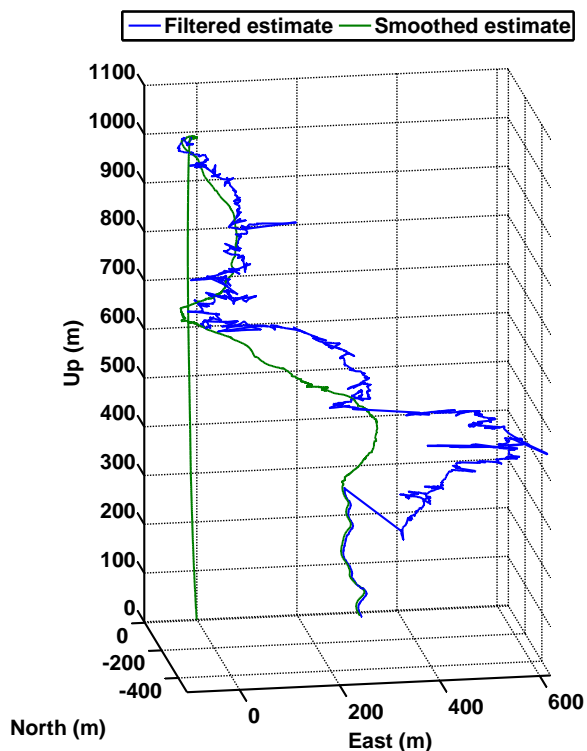


Figure 9.6: Smoothing of trajectory estimation after GPS recovery.

The unavailability of the GPS signal during the ascent phase is not prejudicial since this phase is relatively short and the drift of the inertial navigation is negligible. Nevertheless, the GPS position, which is recovered during the descent under parachute, allows to smooth all this part of the trajectory estimate. Figure 9.6 presents the filtered trajectory estimate (blue) with a discontinuity when the GPS signal is back and the smoothed trajectory estimate (green) where the GPS information is propagated backward. Magnetometer information is not used here.

9.3 Estimation of propulsion parameters

Independently of the trajectory estimation, one of the objectives of the PERSEUS project is to estimate the efficiency of a hybrid engine prototype¹ provided by the *Office National d'Etudes et de Recherches Aérospatiales*, French Aerospace Lab (ONERA) [Prévot and Jézéquel, 2008], compared against experiments on ground test benches because hybrid rockets offer control perspectives due to the possibility of throttling and restarting their engines [Humble et al., 1995, Chiaverini and Kuo, 2007].

1. Interestingly, the same procedure can be applied to solid engine propulsion in order to evaluate the deviation of the performances relative to manufacturer data sheet.

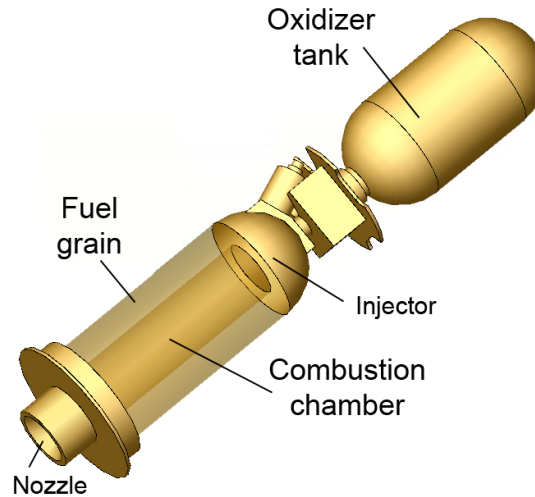


Figure 9.7: Hybrid engine.

9.3.1 Combustion system measurements

The hybrid engine is equipped with a thermocouple along with a pressure transducer in the oxidizer tank and a pressure transducer in the combustion chamber. Each analog signal is sampled at 1 kHz. Interestingly, the high frequency of combustion measurements permits to take in account the phenomenon of combustion oscillations (200 Hz). Finally, the initial amount of liquid oxidizer is evaluated from the weight of the whole system before and after filling of the tank. The burned mass of solid fuel is determined from the weight of the fuel grain at the beginning and at the end of the flight.

9.3.2 Thrust model of hybrid engine

The considered rocket has a classic multi-port hybrid engine. It uses an oxidizer N_2O which is stored in liquid form in a tank and solid fuel (PE). The combustion is self-pressurized: when the compressed oxidizer tank is opened, the N_2O flows to the combustion chamber through the injector. In gaseous phase, it reacts with the fuel which constitutes the chamber envelope. Then, the thermo-chemical reaction generates mass ejection at high speed.

For navigation purposes, the thrust model is important to predict the thrust level but also to determine the mass-flow rate and thus the mass distribution, i.e. the position of the center of gravity and the inertia tensor. To monitor the thrust generation, the hybrid engine is equipped with three particular sensors: the tank temperature T_r , the pressure P_r inside the oxidizer tank, and the pressure P_{ch} in the combustion chamber are measured at high frequency. In details, two phases can be distinguished during the combustion: the first phase when the oxidizer gets out the reservoir in the liquid phase, and the second phase, called “tail of combustion”, during which the pressure in the oxidizer tank is so low that the N_2O is already under gaseous phase in the

tank before it goes to the combustion chamber without any phase change. During the first phase of combustion, pressure oscillations around 200 Hz can be observed.

Under the hypothesis of steady operations, in the oxidizer tank, one can formulate an equation of the oxidizer mass-flow rate \dot{m}_o which represents the oxidizer mass loss and the engine regime change. In details, a liquid and a gaseous phase are modeled in the tank. The density ρ_o depends on the phase under which the oxidizer comes out the tank.

$$\dot{m}_o = k\sqrt{2\rho_o(P_r - P_{ch})} \quad (9.2)$$

Knowing the oxidizer mass-flow rate, one can compute the oxidizer mass flux G_o and, then, the regression rate \dot{r} of the fuel grain (with r the radius of each port of the fuel block)

$$\begin{aligned} G_o &= \frac{\dot{m}_o}{N\pi r^2} \\ \dot{r} &= aG_o^n \end{aligned} \quad (9.3)$$

The model parameters a and n can be determined so that the regression rate verifies the initial and final conditions. This is how the fuel mass flux and the oxidizer-to-fuel ratio can be computed. Further, a thermo-chemical model, taking the form of look-up tables, gives the characteristic exhaust velocity c^* and the specific impulse I_{sp} as functions of the oxidizer-to-fuel ratio and of the chamber pressure.

It can be checked that the ejected mass-flow rate is consistent with the total mass loss

$$\dot{m}_e = A_t g / c^*$$

where A_t is the throat cross-sectional area and g is the gravity.

Finally, the theoretical thrust force is expressed as an indirect function of the measurements available on the engine. This takes the following form

$$F_T = \dot{m}_e I_{sp} g \triangleq f(T_r, P_r, P_{ch})$$

9.3.3 Results exploiting in-flight measurements

We now expose how the previously discussed model, associated to the dynamics equation (9.1), can be used to estimate the efficiency of the rocket engine from available measurements. The previous part of trajectory estimation has been based on inertial navigation without extensive modeling, the accelerometers and gyrometers measurements being taken as measured inputs. We now introduce the rocket dynamics equation and the engine modeling and the sensors are all considered measured outputs, with their previously identified flaws.

Figure 9.8 shows the fitting of the mass flow rate equation (9.2) such that the combustion oscillations end (dash line) coincides with the transition between liquid combustion and gaseous combustion. The mass flow rate verifies that the combustion end corresponds to an empty oxidizer tank.

The parameters of the regression rate equation (9.3) are determined to satisfy initial and final conditions on the port radius (measured before and after flight).

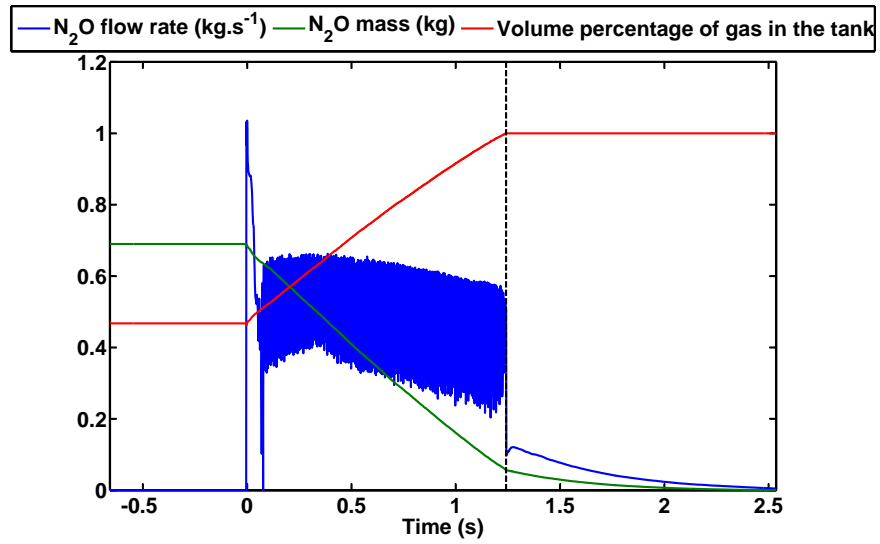


Figure 9.8: Mass flow rate equation fitting.

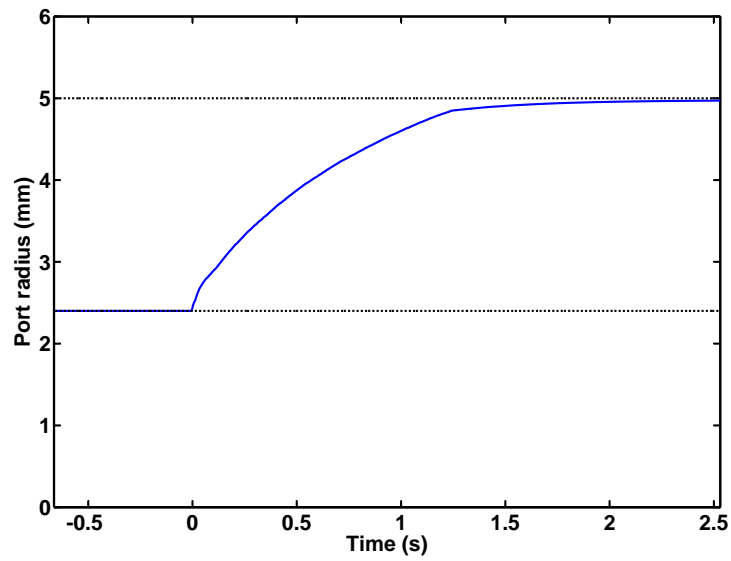


Figure 9.9: Port radius evolution along the combustion.

Finally, the Kalman filtering with the introduced dynamics equation (9.1) permits to isolate in the accelerometers measurements the part corresponding to the thrust force. Thus, a mean (fit) coefficient α can be computed between the theoretical thrust force F_T obtained from the model and the effective thrust force F_t exerted during the flight. It appears that the in-flight performance corresponds approximatively to 80% of the performance evaluated on ground test-bench.

$$F_t = \alpha F_T$$

In Fig. 9.10, the mean coefficient α shows the superposition of the thrust force (blue) computed with the engine model and the engine measurements with the accelerometer measurement (red). The difference of level in negative time corresponds to the measurement of the ramp reaction. During the first tenths of second of combustion, the ramp frictional resistance reduces the measured acceleration. During the “tail of combustion”, the aerodynamics drag force interferes in the accelerometer measurement.

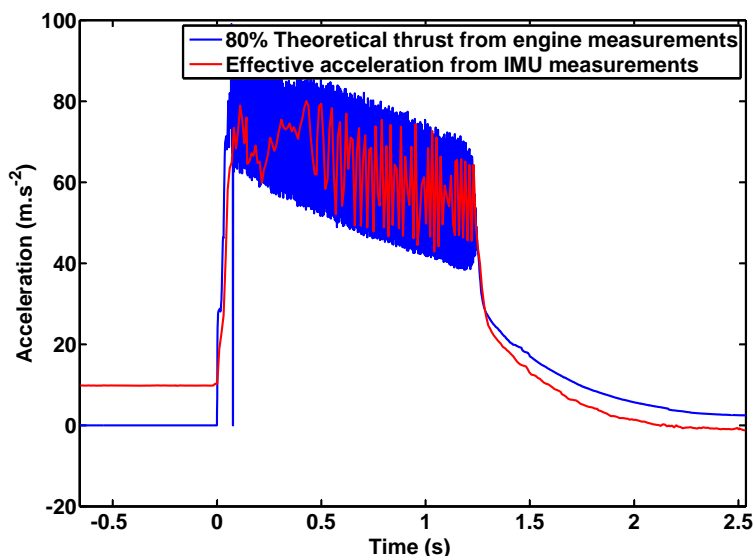


Figure 9.10: Comparison of thrust deduced from engine measurements against accelerometers measurements.

9.4 Conclusion

As has been demonstrated on the case-study presented in this chapter, trajectory estimation for a (hybrid) rocket based on low-cost sensors from the MEMS category can be achieved (Fig. 9.11). This proves the relevance of the concept of data fusion of IMU measurements, engine combustion models, and measurements in this context. Certainly, the accuracy of the estimation can be improved by using additional sensors. Generally, these could be ground-based

(e.g. theodolites, cameras) or located on-board (altimeter, or GPS for longer missions). The work presented here represents only a first step toward a more general goal: trajectory estimation for (relatively) low-cost rockets using low-cost sensors. As a side product, the combustion model has been fitted using in-flight data. This is an interesting result since, despite its moderate accuracy compared to ground test-bench model identification [Lohner et al., 2006][Stamatov et al., 2005], this approach is representative of in-flight engine behavior (which accounts for numerous disturbances such as aerodynamics effects, various oscillations, etc...).

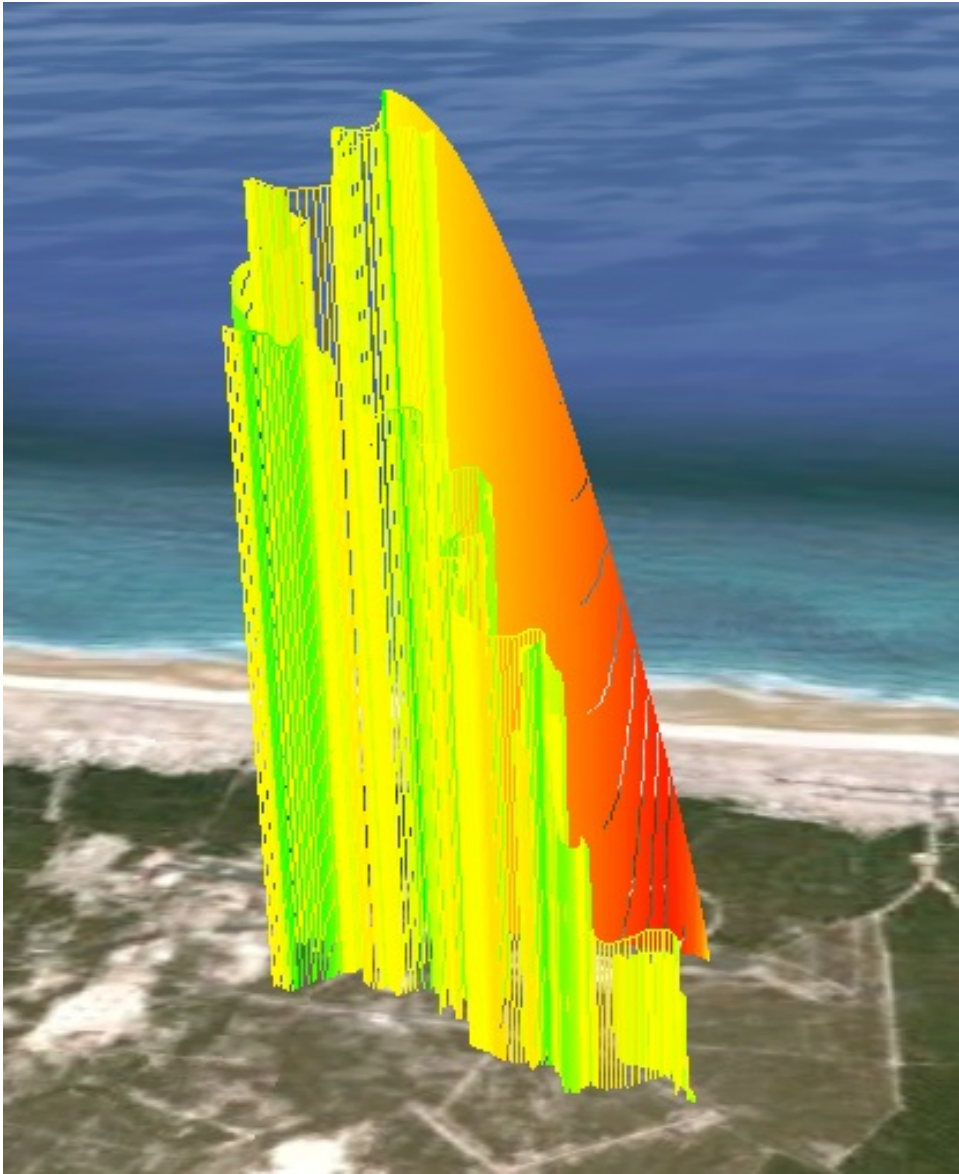


Figure 9.11: Estimated 3D trajectory with color gradation depending on the rocket speed.

Conclusion

In this thesis, we have presented an embedded GPS-free relative navigation system based on low-cost MEMS sensors, which is totally autonomous (i.e. it does not require any external sources of information), and requires neither alignment nor calibration procedures. The capabilities of trajectory reconstruction stem from the exploitation of magnetometers measurements to estimate the vehicle velocity and its heading. The obtained performance allows one to consider applications of long-term navigation with a final error below 10% of the traveled distance (Fig. 7.16). This navigation system (Fig. 6.1) design is grounded on a structure of Temporally Interconnected Observers (TIO), which is explicit for the attitudes estimation (Fig. 6.4), and implicit for the compensation of the magnetic velocimeter and compass defects (Fig. 5.3, 5.4). The observability analysis has yielded a proof of convergence of this TIO scheme. In details, the implemented observer is a Kalman filter whose convergence is proved in Theorem 10 under the assumption of Differential Observability (DO) defined in Definition 6, which relates the point-wise observability to the difficult-to-prove Uniform and Complete Observability (UCO) property generally invoked in the literature.

The resulting navigation system optimizes the exploitation of the sensors drifts over different time-horizons and realizes a mutual drift-compensation and fault-detection. In the same spirit, navigation systems for the Parrot AR.Drone quadrotor and CNES experimental mini-rockets are presented. Quadrotor stabilization requirements are fulfilled by an embedded navigation system which tightly combines vision-based algorithms, aerodynamics modeling and inertial MEMS sensors (Fig. 8.6). Similarly, we have presented results of rocket trajectory reconstruction and propulsion estimation from data fusion of MEMS sensors (Fig. 9.3) in spite of the severe dynamics these rockets are subjected to.

Interestingly, it appears that, for every application presented in this thesis, there is always a sensor which considerably improves the performance. For the automotive navigation, obviously, the magnetic velocimeter fully exploits the structure of the magnetic field sensed inside a vehicle but the barometer should not be neglected as critical source of observability for the TIO. Concerning the quadrotor, the velocity provided by vision-based algorithms is made robust enough only thanks to the velocity information contained in the accelerometers measurements analyzed through the aerodynamics model. Finally, inertial navigation with MEMS sensors succeed to handle the rocket severe dynamics only thanks to calibrated magnetometers.

More prospectively, another sensor could be a solution in a completely different domain, the indoor positioning. The wide-spread of flat panels screens inside buildings provides an

unsuspected source of orientation information. Indeed, the light emitted by the Light Crystal Display (LCD) screens is polarized along a constant direction. We show here briefly how this information can be exploited to provide orientation measurements.

Let us start with a 1-dimension problem. Given a rigid body in front of a LCD screen with only one free rotation, how can we use the light polarization to obtain an estimate of the angular position of the body relative to the screen? Consider an ordinary camera placed behind a polarizing filter called analyzer, both fixed in the body frame. According to the Malus law [Born and Wolf, 1980], for normal incidence of the light, the transmitted intensity I_t is as follows

$$I_t = I_0 \cos^2 \alpha \quad (\text{i})$$

where I_0 is the incident intensity and α the angle between the polarization direction of the incident light and the analyzer direction

Without knowledge of the incident intensity, from one measurement, it is impossible to determine the angle α . One solution could be to rotate the analyzer as suggested in [Atsumi and Sano, 2010] but in order to avoid mechanics related issues, we choose to keep a fixed structure. We realize a virtual rotation of the analyzer thanks to the Faraday effect [Abeles, 1972]. The Faraday effect is a magneto-optical phenomenon: submitted to a magnetic field, some mediums, e.g. Flint glass, induce rotations of the light polarization according to the following equation, where $\Delta\alpha$ is the induced rotation, ν the Verdet constant of the medium, l the length of traversed medium, B the magnetic field

$$\Delta\alpha = \nu l B$$

In practice, we add, before the analyzer, a cylinder of a SF6 Flint glass surrounded by a coil. Rather than putting high current level in the coil to rotate the polarization direction and map Eq. (i), we supply the coil with a low level alternative current which induce an sinusoidal magnetic field, and in turn reduces the power consumption. The frequency can be chosen high enough to consider quasi-stationarity of the angle α compared to the oscillation period of the magnetic field. Thus, the transmitted intensity is given by

$$I_t = I_0 \cos^2 (\alpha + \nu l B_0 \cos \omega t)$$

For low current level (relative to the angle α), the following approximation holds

$$I_t = I_0 \cos^2 \alpha - 2I_0 \nu l B_0 \cos \omega t \cos \alpha \sin \alpha \quad (\text{ii})$$

It appears that the comparison of the high frequency amplitude $I_\omega = 2I_0 \cos \alpha \sin \alpha \nu l B_0$ against the mean value $I_m = I_0 \cos^2 \alpha$ gives the searched angle (as illustrated in Fig. I)

$$\frac{I_\omega}{I_m} = 2\nu l B_0 \tan \alpha \quad (\text{iii})$$

The result of Eq. (iii) is exploited in [Tan and Arndt, 1997] as a dual mean to identify the Verdet constant of a medium when the orientation is known. Here we propose to use it to determine the orientation knowing the Verdet constant.

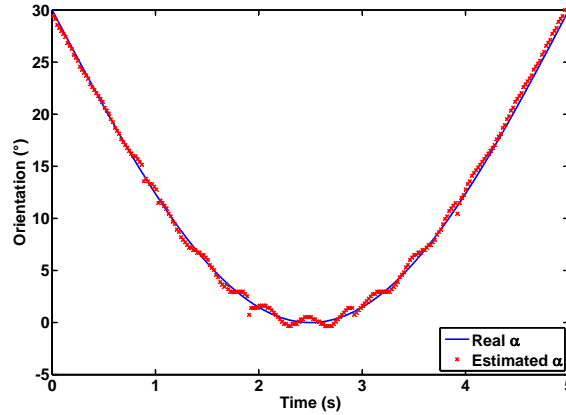


Figure I: Simulation result for the one-dimension angle estimation problem. The approximation in Eq. (ii) is not justified for low angle values and explain the disturbances.

This result can be extended to an orientation with two angles. Considering an incidence angle β , an equivalent angle of polarization α^* can be defined by $\tan \alpha^* = \tan \alpha / \cos \beta$ as presented in Fig. II. With Eq. (iii), one now obtains the following measurement

$$I_\omega / I_m = 2\nu l B_0 \tan \alpha / \cos \beta$$

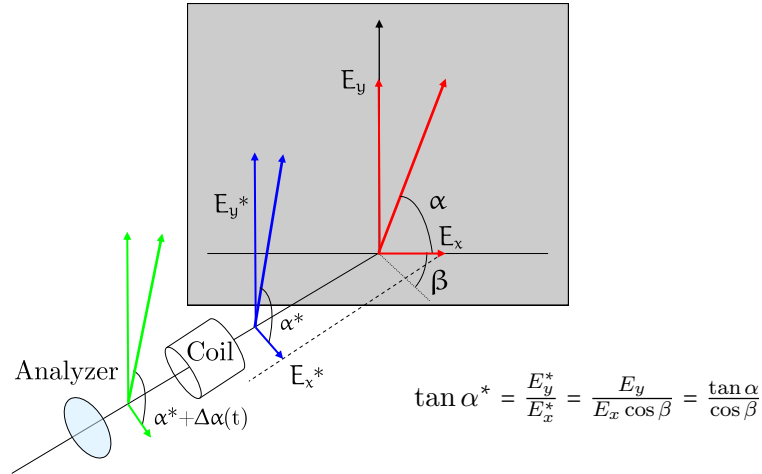


Figure II: Angle of polarization in the analyzer plane depending on the incidence angle.

The previous equation is not sufficient to determine the two angles but can be used to estimate the bias of gyrometers. The experimental apparatus is pictured in Fig.II and we plan to integrate it in a forth-coming navigation system. Thus, once again, the drift compensation of inertial sensors can be realized by an indirect but non-drifting sensor on the same model than the combinations previously presented in this thesis: accelerometer / magnetic velocimeter, accelerometer / camera, gyrometer / magnetic compass, gyrometer / barometer, gyrometer / magnetometer and here, gyrometer / Faraday analyzer.

Appendix

Appendix A

Discussion on the smoothing technique: a comparison with back-and-forth filtering on simple examples

In Chapter 2, we have introduced the Kalman filter as an optimal observer. In Section 7.5, we have proposed to exploit the information a posteriori with an optimal smoother. A natural question concerns the limit of this process : the Kalman filter is optimal relative to forward filtering, the smoother is optimal relative to forward and backward treatment of the information. What about the multiplication of forward and backward filtering on the same set of measurements?

In [Auroux and Blum, 2008, Donovan et al., 2010, Auroux and Nodet, 2011], an original filtering technique has been proposed, called Back-and-Forth Nudging (BFN). It deals with large dimension state estimation problem [Vidard et al., 2003]. To reduce the computational burden, the authors prefer use a simple constant observer and realize a large number of forward and backward filtering rather than using one carefully tailored gain, e.g. such as the one produced by the Kalman filter. To minimize the estimation error variance, a low gain is chosen.

In this chapter, we focus our attention on two simple problems: the identification of a constant and the identification of a first-order dynamics. We compare the proposed BFN technique against Kalman filtering. Further, we introduce Back-and-Forth Kalman Filtering on the same model to investigate potential benefits. Computational burden is not the object of the comparison, we focus on the optimality (in sense of minimum variance) of the estimation. The Cramér-Rao bound is used as reference to assess the performance of the different methods. The Cramér-Rao bound is computed relative to the information contained in the measurements and it defines a lower bound for unbiased estimators variance. In Section A.1, we derive the Cramér-Rao bound for a biased estimator of a first-order dynamics. Further details can be found in [Van Trees, 1968, Frieden, 2004].

We want to address the problem of identification of a constant

$$\begin{cases} \dot{x}(t) = 0 \\ y(t) = x + v(t) \end{cases}, \quad t \in [0..T] \quad (\text{A.1})$$

and the problem of estimation of a first-order dynamics

$$\begin{cases} \dot{x}(t) = ax(t) \\ y(t) = x(t) + v(t) \end{cases}, \quad t \in [0, T] \quad (\text{A.2})$$

with $v(t)$ a zero-mean Gaussian white noise of PSD R

$$\begin{cases} E(v(t)) = 0 \\ E(v(t)v(\tau)) = R\delta(t - \tau) \end{cases}$$

Given a finite measurements interval T , we wish to estimate the variance of the BFN technique compared to Kalman filtering and Cramér-Rao bound.

A.1 Cramér-Rao bound for a biased estimator

For $t \in [0, T]$, consider the constant value x_0 , the state $x(t) = x_0 e^{at}$ with $a > 0$. Consider the following discretization of the interval $[0, T]$ with step size Δt which gives $t_k = k\Delta t$ and $v_k = v(k\Delta t)$. Note V_k the random variable associated to the realization v_k ¹.

$$\begin{cases} E(V_k) = 0 \\ E(V_k V_l) = R\Delta t \delta_{k,l} \end{cases}$$

From the nature of the noise, the probability density function can be expressed as follows

$$f(v(t), 0) = \frac{1}{\sqrt{2\pi R}} e^{-\frac{v(t)^2}{2R}}$$

To this noise, are associated measurements $y_k = x(t_k) + v_k$ whose probability density functions are

$$f(y_k, 0) = \frac{1}{\sqrt{2\pi R}} e^{-\frac{(y_k - x_0 e^{at_k})^2}{2R}}$$

Note V_k the score associated to each random variable Y_k (y_k being a realization of Y_k)

$$V_k = \frac{\partial \log f(Y_k, x_0)}{\partial x_0} = \frac{1}{f(Y_k, x_0)} \frac{\partial f(Y_k, x_0)}{\partial x_0} = \frac{1}{R} (Y_k - x_0 e^{at_k}) e^{at_k} = \frac{V_k e^{at_k}}{R}$$

1. The notations in Chapter 2 are sloppy in regard to distinction between realizations and random variables but widespread.

Consider the estimator \hat{x}_k of the value $x(t_k)$ using the measurement y_l , $l \in [0..k]$. Note \hat{X}_k the random variable associated. The expected value of the estimator is given by

$$E(\hat{X}_k) = \int \cdots \int_{l \in [0..k]} \hat{x}_k \prod_{l=0}^k f(y_l, x_0) \prod_{l=0}^k dy_l$$

One can derive the derivative of the expected value relative to x_0 where $v_k = \frac{1}{f(y_k, x_0)} \frac{\partial f(y_k, x_0)}{\partial x_0}$

$$\begin{aligned} \frac{\partial E(\hat{X}_k)}{\partial x_0} &= \int \cdots \int_{l \in [0..k]} \hat{x}_k \frac{\partial}{\partial x_0} \left(\prod_{l=0}^k f(y_l, x_0) \right) \prod_{l=0}^k dy_l \\ &= \int \cdots \int_{l \in [0..k]} \hat{x}_k \sum_{m=0}^k \left(\frac{\partial f(y_m, x_0)}{\partial x_0} \prod_{\substack{l=0 \\ l \neq m}}^k f(y_l, x_0) \right) \prod_{l=0}^k dy_l \\ &= \int \cdots \int_{l \in [0..k]} \hat{x}_k \sum_{m=0}^k \left(v_m \prod_{l=0}^k f(y_l, x_0) \right) \prod_{l=0}^k dy_l \\ &= \int \cdots \int_{l \in [0..k]} \hat{x}_k \left(\sum_{m=0}^k v_m \right) \prod_{l=0}^k f(y_l, x_0) \prod_{l=0}^k dy_l \\ &= E \left(\hat{X}_k \sum_{m=0}^k V_m \right) = E(\hat{X}_k S_k) \text{ with } S_k = \sum_{m=0}^k V_m \end{aligned}$$

The random variable S_k is the score of the measurements exploited to produce the estimate \hat{x}_k

$$E(S_k) = \sum_{m=0}^k E(V_m) = \sum_{m=0}^k \frac{E(V_k) e^{at_k}}{R} = 0$$

Then, we can compute the Fisher information $\text{Var}(S_k)$

$$\begin{aligned} \text{Var}(S_k) &= E(S_k^2) = E \left(\sum_{m=0}^k \frac{V_m}{R} e^{am\Delta t} \sum_{l=0}^k \frac{V_l}{R} e^{al\Delta t} \right) = \sum_{m=0}^k \sum_{l=0}^k \frac{E(V_m V_l)}{R^2} e^{a(m+l)\Delta t} \\ &= \sum_{m=0}^k \frac{\Delta t}{R} e^{2am\Delta t} = \frac{\Delta t}{R} \frac{1 - e^{2at_{k+1}}}{1 - e^{2a\Delta t}} \xrightarrow{\Delta t \rightarrow 0} \frac{e^{2at_k} - 1}{2aR} \end{aligned}$$

Yet, from the Cauchy-Schwarz inequality,

$$\begin{aligned} \text{Var}(\hat{X}_k) \text{Var}(S_k) &= E((\hat{X}_k - E(\hat{X}_k))^2) E(S_k^2) \\ &\geq (E((\hat{X}_k - E(\hat{X}_k)) S_k))^2 \\ &\geq (E(\hat{X}_k S_k))^2 \end{aligned}$$

Finally, coming back in the continuous domain,

$$\text{Var}(\hat{X}(t)) \geq \frac{2aR}{e^{2at} - 1} \left(\frac{\partial E(\hat{X}(t))}{\partial x_0} \right)^2$$

Let E (respectively P) be the expected value (resp. the variance) of \tilde{x}_0^2 at filtering time t

$$E(\hat{X}(t)) = x_0 e^{at} + E(t) e^{at}, \quad \text{Var}(\hat{X}(t)) = P(t) e^{2at}$$

Then, one has for $t \in [0, T]$

$$P(t) \geq \frac{2aR}{e^{2at} - 1} \left(1 + \frac{\partial E(t)}{\partial x_0} \right)^2 \quad (\text{A.3})$$

By extension, the Fisher information saturates for time T since there is no new measurements. Therefore, for $t > T$,

$$P(t) \geq \frac{2aR}{e^{2aT} - 1} \left(1 + \frac{\partial E(t)}{\partial x_0} \right)^2 \quad (\text{A.4})$$

The classical result of Cramér-Rao bound for the problem of identification of a constant (A.1) can be found with a tending to 0

$$P(t) \geq \frac{R}{t} \left(1 + \frac{\partial E(t)}{\partial x_0} \right)^2, \quad \forall t \in [0, T] \quad (\text{A.5})$$

$$P(t) \geq \frac{R}{T} \left(1 + \frac{\partial E(t)}{\partial x_0} \right)^2 \quad \forall t > T \quad (\text{A.6})$$

A.2 Identification of a constant

Consider $k(t)$ as the gain of the observer \hat{x} for the system A.1

$$\dot{\hat{x}}(t) = k(t) (y(t) - \hat{x}(t))$$

The observer error $\tilde{x} = \hat{x} - x$ satisfies

$$\dot{\tilde{x}} = -k(t)\tilde{x}(t) + k(t)v(t)$$

The following back-and-forth observer is for $t \in [0, T]$ with $T_i = iT$

$$\begin{cases} \tilde{x}(0) = \tilde{x}_0 \\ \dot{\tilde{x}}(T_{2i} + t) = -k(T_{2i} + t)\tilde{x}(T_{2i} + t) + k(T_{2i} + t)v(t) \\ \dot{\tilde{x}}(T_{2i+1} + t) = -k(T_{2i+1} + t)\tilde{x}(T_{2i+1} + t) + k(T_{2i+1} + t)v(T - t) \end{cases}$$

2. We focus on the estimation error on \tilde{x}_0 to discard the dynamics from disturbing the variance comparison.

A.2.1 Back-and-Forth Nudging

Consider $k(s) = r$ for all $s \in [0, T_{2N}]$

The recursive form of the solution \tilde{x} above is as follows

$$\begin{cases} \tilde{x}(0) = \tilde{x}_0 \\ \tilde{x}(T_{2i} + t) = \tilde{x}(T_{2i})e^{-rt} + e^{-rt} \int_0^t e^{rs} r v(s) ds \\ \tilde{x}(T_{2i+1} + t) = \tilde{x}(T_{2i+1})e^{-rt} + e^{-rt} \int_{T-t}^T e^{r(T-s)} r v(s) ds \end{cases}$$

Introduce the following notations

$$\alpha_t = \int_0^t e^{rs} r v(s) ds, \quad \beta_t = \int_{T-t}^T e^{r(T-s)} r v(s) ds, \quad \gamma_i = \frac{1 - e^{-2irT}}{1 - e^{-2rT}}$$

The solution \tilde{x} can be written under explicit form

$$\begin{cases} \tilde{x}(0) = \tilde{x}_0 \\ \tilde{x}(T_{2i} + t) = e^{-rt} (\tilde{x}_0 e^{-2irT} + \gamma_i e^{-rT} (\alpha_T e^{-rT} + \beta_T) + \alpha_t) \\ \tilde{x}(T_{2i+1} + t) = e^{-rt} (\tilde{x}_0 e^{-(2i+1)rT} + \alpha_T e^{-rT} + \gamma_i e^{-2rT} (\alpha_T e^{-rT} + \beta_T) + \beta_t) \end{cases}$$

Let the expected value E and the variance Var of the estimation error for back-and-forth nudging at gain r be noted as follows

$$\begin{cases} E_r(s) \triangleq E(\tilde{x}(s)) & \begin{cases} P_r(s) \triangleq \text{Var } \tilde{x}(s) \\ P_r(0) \triangleq P_0 = \text{Var } \tilde{x}_0 \end{cases} \\ E_r(0) \triangleq E_0 = E(\tilde{x}_0) \end{cases}$$

The expected value features the expected exponential decrease

$$E_r(T_i + t) = E_0 e^{-r(iT+t)} \tag{A.7}$$

The variance is slightly more complicated because of correlation between measurements used by the back-and-forth nudging since they are from the same sample of measurements $v(t), t \in [0, T]$

$$\begin{aligned} P_r(T_{2i} + t) &= \begin{cases} P_0 e^{-2r(2iT+t)} + r R e^{-rt} \sinh rt + r R \gamma_i^2 e^{-2r(T+t)} (2rT + \sinh 2rT) \\ + 2r R \gamma_i e^{-2rt} (rt + e^{r(t-2T)} \sinh rt) \end{cases} \\ P_r(T_{2i+1} + t) &= \begin{cases} P_0 e^{-2r((2i+1)T+t)} + r R e^{-2rt} (2rt + e^{r(t-T)} \sinh r(t+T)) \\ + r R \gamma_i^2 e^{-2r(2T+t)} (2rT + \sinh 2rT) + 2r R \gamma_i e^{-2r(t+T)} r(t+T) \\ + 2r R \gamma_i e^{-2r(t+T)} e^{r(t-T)} \sinh r(t+T) \end{cases} \end{aligned}$$

In particular,

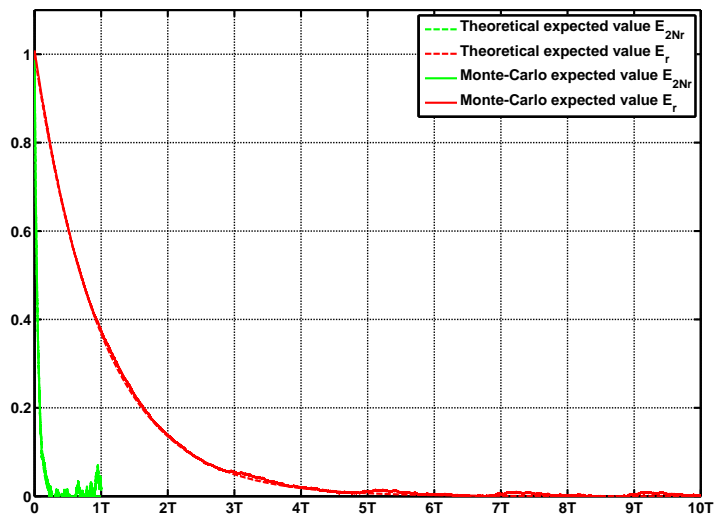
$$P_{2Nr}(T) = P_0 e^{-4NrT} + 2Nr R e^{-2NrT} \sinh 2NrT \tag{A.8}$$

$$P_r(T_{2N}) = P_0 e^{-4NrT} + r R \gamma_N^2 e^{-2rT} (2rT + \sinh 2rT) \tag{A.9}$$

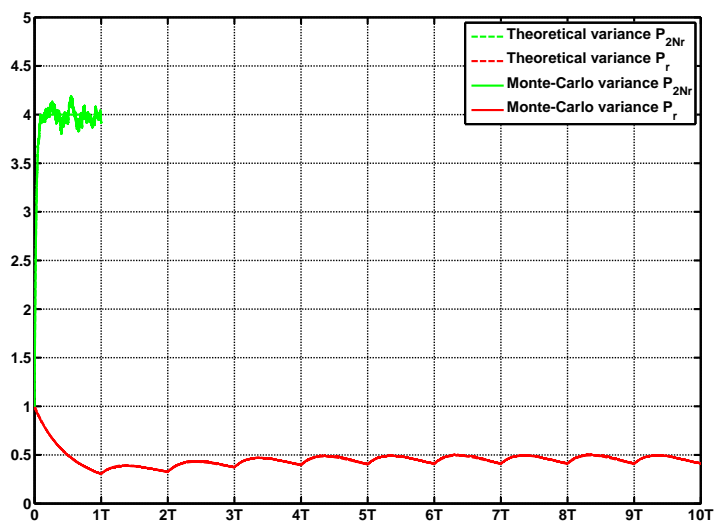
From Eq. (A.7-A.9), the following equation can be verified

$$\forall(T, r, P_0, N), \quad E_r(T_{2N}) = E_{2Nr}(T), \quad P_r(T_{2N}) \leq P_{2Nr}(T)$$

Claim 1. *For identification of a constant from the same set of noisy measurements, back-and-forth nudging (i.e. N back-and-forth processing with gain r) provides a smaller variance than classical Luenberger filtering (i.e. one processing with gain $2Nr$) as illustrated in Fig. A.1.*



(a) Expected value



(b) Variance

Figure A.1: Comparison of expected value and variance for $2Nr$ gain (green) and r gain (red).

A.2.2 Back-and-Forth Kalman filtering

From the Riccati equation, with a null dynamics, the variance \bar{P}_K of a classical Kalman filter and the associated Kalman gain K can be computed.

$$\begin{cases} \dot{\bar{P}}_K(t) = -\frac{\bar{P}_K(t)^2}{R} \\ K(t) = \frac{\bar{P}_K(t)}{R} \end{cases}, \quad K(t) = \frac{1}{R/\bar{P}_K(s) + t - s}$$

The evolution of the solution $\tilde{x}(t)$ during forward and backward filtering is as follows

$$\begin{cases} \tilde{x}(0) = \tilde{x}_0 \\ \tilde{x}(T_{2i} + t) = \frac{\tilde{x}(T_{2i})R/\bar{P}_K(T_{2i}) + \int_0^t v(s)ds}{R/\bar{P}_K(T_{2i}) + t} \\ \tilde{x}(T_{2i+1} + t) = \frac{\tilde{x}(T_{2i+1})R/\bar{P}_K(T_{2i+1}) + \int_0^t v(T-s)ds}{R/\bar{P}_K(T_{2i+1}) + t} \end{cases}$$

Introduce the following notations

$$\lambda_t = \int_0^t v(s)ds, \quad \mu_t = \int_0^t v(T-s)ds$$

The solution for each pass of back-and-forth Kalman filtering can be determined

$$\begin{cases} \tilde{x}(0) = \tilde{x}_0, \quad \bar{P}_K(0) = P_0 \\ \tilde{x}(T_{2i} + t) = \frac{\tilde{x}_0 R/P_0 + 2i\lambda_T + \mu_t}{R/P_0 + 2iT + t} \\ \tilde{x}(T_{2i+1} + t) = \frac{\tilde{x}_0 R/P_0 + (2i+1)\beta_T + \mu_t}{R/P_0 + (2i+1)T + t} \end{cases}$$

Let the expected value E and the variance Var of the estimation error for back-and-forth Kalman filtering be noted as follows

$$\begin{cases} E_K(s) \triangleq E(\tilde{x}(s)) \\ E_K(0) \triangleq E_0 \end{cases} \quad \begin{cases} P_K(s) \triangleq \text{Var } \tilde{x}(s) \\ P_K(0) \triangleq P_0 \end{cases}$$

Back-and-forth Kalman filtering has the same behavior during forward and backward filtering

$$E_K(T_i + t) = E_0 \frac{R/P_0}{R/P_0 + t + iT} \tag{A.10}$$

$$P_K(T_i + t) = R \frac{R/P_0 + (i+1)^2 t + i^2(T-t)}{(R/P_0 + t + iT)^2} \tag{A.11}$$

From Eq. (A.11),

$$\min_t P_K(T_i + t) = \begin{cases} P_K(T_i + T) & \text{if } i = 0 \\ P_K(T_i) & \text{otherwise} \end{cases}$$

$$\min_i P_K(T_i) = P_K(T) = \frac{R}{R/P_0 + T}$$

Claim 2. *Back-and-forth Kalman filtering does not improve the variance of the error produced by a single pass of Kalman filter. Minimum variance is reached after one pass.*

Interpretation By construction, Kalman filtering is optimized to provide the minimum variance. Add back-and-forth filtering with the same set of measurements can not improve the variance.

Further, from Eq. (A.10-A.11),

$$\lim_{N \rightarrow +\infty} E_K(T_N) = 0, \quad \lim_{N \rightarrow +\infty} P_K(T_N) = \frac{R}{T} > \frac{R}{R/P_0 + T}$$

Claim 3. *Back-and-forth Kalman filtering provides an unbiased error estimation at the expense of a loss of variance performance.*

Interpretation Back-and-forth Kalman filtering increases virtually the time of filtering and allows the filter to reach its asymptotic behavior of unbiased observer but since the measurements are correlated, the variance increases.

Further,

$$\lim_{P_0 \rightarrow +\infty} E_K(T) = 0, \quad \lim_{P_0 \rightarrow +\infty} P_K(T) = \frac{R}{T}$$

Claim 4. *Same results are obtained with infinite uncertainty and one forward Kalman filtering.*

Interpretation Back-and-forth Kalman filtering allows the filter to reach its asymptotic behavior, that is to say to forget its variance initialization.

A.2.3 Mean estimator

Consider the following estimator and its mirror extension

$$\begin{aligned} \hat{x}(t) &= \frac{1}{t} \int_0^t y(s) ds \\ \hat{x}(T+t) &= \frac{1}{T+t} \left(\int_0^T y(s) ds + \int_0^t y(T-s) ds \right) \end{aligned}$$

The form of the error estimation can be computed explicitly for back-and-forth mean

$$\begin{aligned} \tilde{x}(T_{2i} + t) &= \frac{i(\lambda_T + \mu_T) + \lambda_t}{2iT + t} \\ \tilde{x}(T_{2i+1} + t) &= \frac{(i+1)\lambda_T + i\mu_T + \mu_t}{(2i+1)T + t} \end{aligned}$$

Let the expected value E and the variance Var of the estimation error for back-and-forth mean estimation be noted as follows

$$E_M(s) = E(\tilde{x}(s)), \quad P_M(s) = \text{Var} \tilde{x}(s)$$

Since the measurement noise has zero mean, this observer is always unbiased

$$E_M(T_i + t) = 0 \tag{A.12}$$

$$P_M(T_i + t) = R \frac{(i+1)^2 t + i^2 (T-t)}{(iT+t)^2} \tag{A.13}$$

From Eq. (A.13),

$$\min_t P_M(T_i + t) = \begin{cases} P_M(T_i + T) & \text{if } i = 0 \\ P_M(T_i) = P_M(T_i + T) & \text{otherwise} \end{cases}$$

$$\min_i P_M(T_i) = \frac{R}{T} = P_M(T_i), i \neq 0$$

Claim 5. *During the first forward filtering ($t < T$), the variance of the mean estimator is the Cramér-Rao bound (A.5), that is to say the minimum possible variance for an unbiased estimator.*

$$E_M(t) = 0, \quad P_M(t) = \frac{R}{t}$$

Interpretation For constant identification, the mean estimator is the simplest and best estimator in term of estimation bias. The Kalman filtering provides a smaller variance of the error estimation but is biased.

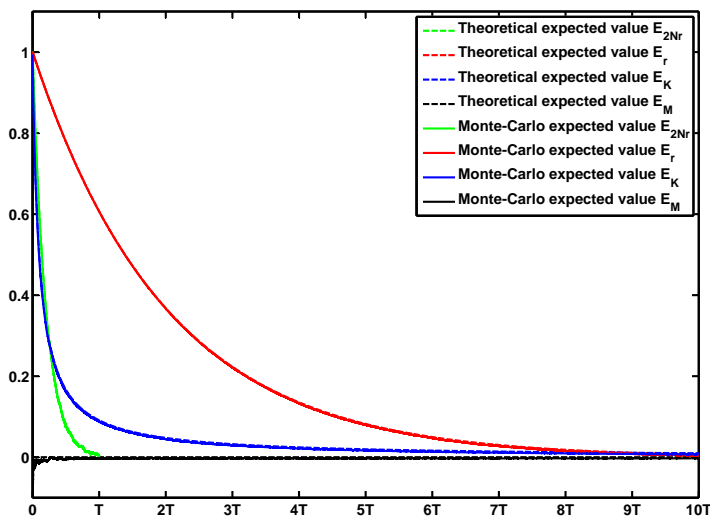
$$E_K(t) = E_0 \frac{R/P_0}{R/P_0 + t}, \quad P_K(t) = \frac{R}{R/P_0 + t}$$

Finally, from Eq. (A.7,A.9-A.13)

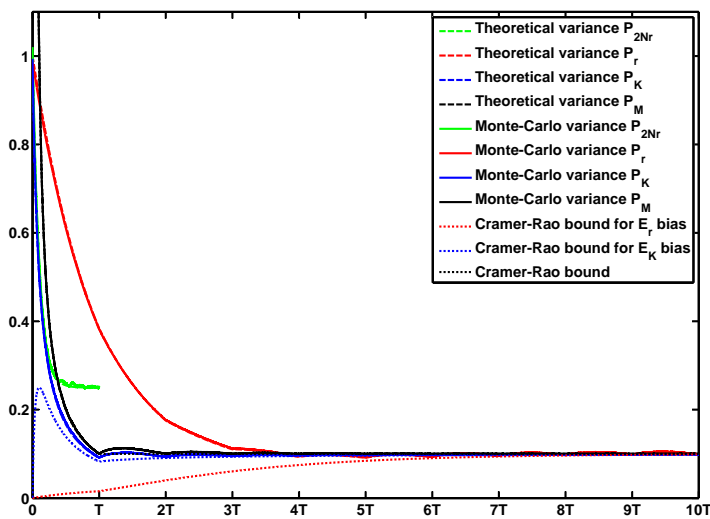
$$\begin{aligned} \lim_{N \rightarrow +\infty} E_r(T_N) &= 0, & \lim_{N \rightarrow +\infty} P_r(T_N) &\xrightarrow{r \rightarrow 0} \frac{R}{T} \\ \lim_{N \rightarrow +\infty} E_K(T_N) &= 0, & \lim_{N \rightarrow +\infty} P_K(T_N) &= \frac{R}{T} \\ E_M(T) &= 0, & P_M(T) &= \frac{R}{T} \end{aligned}$$

Claim 6. *Back-and-forth nudging and back-and-forth Kalman filtering converge towards the Cramér-Rao bound (A.6) as the number of back-and-forth goes to infinity (Fig. A.2)*

Interpretation Back-and-forth nudging and back-and-forth Kalman filtering can give a better error estimation variance than the Cramér-Rao bound as long as they are biased. Since the estimation bias decreases as the number of back-and-forth goes to infinity, the variance approaches the Cramér-Rao bound. An unbiased estimator can not get more information from a given set of data than that it contains, even treating the data set an infinity of times.



(a) Expected value



(b) Variance

Figure A.2: Comparison of expected value and variance for $2Nr$ gain (green), r gain (red), Kalman filtering (blue) and mean (black). Theoretical calculus is confirmed with Monte-Carlo simulations.

A.3 Estimation of a first-order dynamics

Consider $k(t)$ as the gain of the observer \hat{x} for the problem of estimation of a first-order dynamics (A.2)

$$\dot{\hat{x}}(t) = a\hat{x}(t) + k(t)(y(t) - \hat{x}(t))$$

The observer error $\tilde{x} = \hat{x} - x$ satisfies

$$\dot{\tilde{x}} = (a - k(t))\tilde{x}(t) + k(t)v(t)$$

Let $\tilde{x}(s)$ be defined for $s \in [0, T_{2N}]$, $N \in \mathbb{N}$

$$\begin{cases} \tilde{x}(0) = \tilde{x}_0 \\ \dot{\tilde{x}}(T_{2i} + t) = (a - k(T_{2i} + t))\tilde{x}(T_{2i} + t) + k(T_{2i} + t)v(t) \\ \dot{\tilde{x}}(T_{2i+1} + t) = (-a - k(T_{2i+1} + t))\tilde{x}(T_{2i+1} + t) + k(T_{2i+1} + t)v(T - t) \end{cases}$$

A.3.1 Back-and-Forth Nudging

Consider $k(T_{2i} + t) = k_0 = a + r_0$ and $k(T_{2i+1} + t) = k_1 = -a + r_1$ with $r_0 + r_1 > 0$

The solution \tilde{x} is as follows

$$\begin{cases} \tilde{x}(0) = \tilde{x}_0 \\ \tilde{x}(T_{2i} + t) = \tilde{x}(T_{2i})e^{-r_0 t} + e^{-r_0 t} \int_0^t e^{r_0 s} (r_0 + a)v(s) ds \\ \tilde{x}(T_{2i+1} + t) = \tilde{x}(T_{2i+1})e^{-r_1 t} + e^{-r_1 t} \int_{T-t}^T e^{r_1 (T-s)} (r_1 - a)v(s) ds \end{cases}$$

Introduce the following notations

$$\alpha_t = \int_0^t e^{r_0 s} (r_0 + a)v(s) ds, \quad \beta_t = \int_{T-t}^T e^{r_1 (T-s)} (r_1 - a)v(s) ds, \quad \gamma_i = \frac{1 - e^{-i(r_0+r_1)T}}{1 - e^{-(r_0+r_1)T}}$$

The solution \tilde{x} can be written under explicit form

$$\begin{cases} \tilde{x}(0) = \tilde{x}_0 \\ \tilde{x}(T_{2i} + t) = e^{-r_0 t} (\tilde{x}_0 e^{-i(r_0+r_1)T} + \gamma_i (\alpha_T e^{-(r_0+r_1)T} + \beta_T e^{-r_1 T}) + \alpha_t) \\ \tilde{x}(T_{2i+1} + t) = e^{-r_1 t} (\tilde{x}_0 e^{-i(r_0+r_1)T} e^{-r_0 T} + \gamma_i e^{-(r_0+r_1)T} (\alpha_T e^{-r_0 T} + \beta_T) + \alpha_T e^{-r_0 T} + \beta_t) \end{cases}$$

Let $E_{r_0, r_1}(s)$ be the expected value of \tilde{x}_0 at filtering time s , that it to say the expected value of $\tilde{x}(s)$ extrapolated backward according to the dynamics until time 0

$$\begin{aligned} E_{r_0, r_1}(T_{2i} + t) &= E_0 e^{-i(r_0+r_1)T} e^{-r_0 t} e^{-at} \\ E_{r_0, r_1}(T_{2i+1} + t) &= E_0 e^{-i(r_0+r_1)T} e^{-r_0 T} e^{-r_1 t} e^{-a(T-t)} \end{aligned}$$

Introduce the following notations

$$\begin{aligned} f_t &= E(\alpha_t^2) = \frac{(r_0 + a)^2}{r_0} R e^{r_0 t} \sinh r_0 t, \quad g_t = E(\beta_t^2) = \frac{(r_1 - a)^2}{r_1} R e^{r_1 t} \sinh r_1 t \\ h_t &= E(\alpha_t \beta_T) e^{-r_1 T} = E(\alpha_T \beta_t) e^{-r_1 T} e^{(r_0 - r_1)(t - T)} = (r_0 + a)(r_1 - a) R \frac{e^{(r_0 - r_1)t} - 1}{r_0 - r_1} \end{aligned}$$

In the same manner, let $P_{r_0, r_1}(s)$ be the variance of \tilde{x}_0 at filtering time s

$$P_{r_0, r_1}(T_{2i} + t) = \left(\begin{array}{c} P_0 e^{-2i(r_0+r_1)T} + f_t + 2\gamma_i (f_t e^{-(r_0+r_1)T} + h_t) \\ + \gamma_i^2 (f_T e^{-2(r_0+r_1)T} + g_T e^{-2r_1T} + 2h_T e^{-(r_0+r_1)T}) \end{array} \right) e^{-2r_0 t} e^{-2at}$$

$$P_{r_0, r_1}(T_{2i+1} + t) = \left(\begin{array}{c} P_0 e^{-2i(r_0+r_1)T} + f_T + g_t e^{2r_0T} \\ + 2h_t e^{2r_0T} e^{(r_1-r_0)t} + 2\gamma_i (f_T e^{-(r_0+r_1)T} \\ + g_t e^{(r_0-r_1)T} + h_T + h_t e^{(r_0-r_1)(T-t)}) \\ + \gamma_i^2 (f_T e^{-2(r_0+r_1)T} + g_T e^{-2r_1T} + 2h_T e^{-(r_0+r_1)T}) \end{array} \right) e^{-2r_0 T} e^{-2r_1 t} e^{-2a(T-t)}$$

Consider the case $k_0 = k_1 = k > 0$ which gives $r_0 + r_1 = 2k$

$$P_k(T_{2i}) = P_0 e^{-4ikT} + Rk^2 \gamma_i^2 e^{-2kT} \left(\frac{1-e^{-2aT}}{a} + \frac{e^{-(k+a)T}}{k-a} \sinh(k-a)T + \frac{e^{(k-a)T}}{k+a} \sinh(k+a)T \right)$$

$$P_k(T_{2i+1}) = \left[\begin{array}{c} P_k(T_{2i}) e^{-2kT} + \frac{k^2}{k-a} R e^{-(k+a)T} \sinh(k-a)T \\ + 2k^2 R \gamma_i e^{-2kT} \left(\frac{1-e^{-2aT}}{2a} + \frac{e^{-(k+a)T} \sinh(k-a)T}{k-a} \right) \end{array} \right]$$

Considering large number of back-and-forth procedures, one has

$$\lim_{\substack{2NkT \gg 1 \\ 2Nk \gg a}} P_{Nk}(T) \cong NkR/2, \quad \lim_{\substack{NkT \gg 1 \\ k \ll |a| \\ kT \ll 1}} P_k(NT) \cong \frac{R}{T} \frac{1 - e^{-2aT}}{2aT}$$

Claim 7. For the estimation of a first-order dynamics (A.2) from the same set of measurements, back-and-forth nudging (i.e. N back-and-forth processing with gain r) provides a smaller variance than classical Luenberger filtering (i.e. one processing with gain $2Nr$) for a sufficiently large number of back-and-forth procedures.

$$\forall (a, T, P_0) \quad \exists (k, N) \quad |E_k(NT) = E_{Nk}(T), \quad P_k(NT) < P_{Nk}(T)$$

Interpretation To get the same mean of estimation than N back-and-forth filtering with gain r , classical filtering has to use a $2Nr$ gain which amplifies the measurement noise. In back-and-forth nudging at small gain, even if measurement noise is proportional to the dynamics of the system, exponential decrease due to the small gain tends to reduce the variance.

A.3.2 Back-and-Forth Kalman Filtering

During forward filtering, from the Riccati equation, the variance \bar{P} of a classical Kalman filter and the associated Kalman gain K can be computed.

$$\begin{cases} \dot{\bar{P}}(t) = 2a\bar{P}(t) - \frac{\bar{P}(t)^2}{R} \\ K(t) = \frac{\bar{P}(t)}{R} \end{cases}$$

which gives $P(T_{2i} + t) = \frac{2aR}{1 - (1 - 2aR/\bar{P}(T_{2i}))e^{-2at}}$

During backward filtering, the dynamics is inverted

$$P(T_{2i+1} + t) = \frac{-2aR}{1 - (1 + 2aR/P(T_{2i+1}))e^{2at}}$$

By induction, noting $\delta_i = 2aR/P_0 + i(e^{2aT} - 1)$,

$$P(T_{2i}) = \frac{2aR}{\delta_{2i}}, \quad P(T_{2i+1}) = \frac{2aRe^{2aT}}{\delta_{2i+1}}$$

The Kalman gain can be written explicitly

$$K(T_{2i} + t) = \frac{2a}{1 - (1 - \delta_{2i})e^{-2at}}$$

$$K(T_{2i+1} + t) = \frac{-2a}{1 - (1 + \delta_{2i+1}e^{-2aT})e^{2at}}$$

Using the following notations,

$$\lambda_t = \int_0^t e^{as} v(s) ds, \quad \mu_t = \int_0^t e^{-as} v(T-s) ds$$

the differential equation on \tilde{x} can be solved

$$\begin{cases} \tilde{x}(T_{2i} + t) = \left(\frac{\tilde{x}(T_{2i})}{K(T_{2i})} + \lambda_t \right) K(T_{2i} + t) e^{-at} \\ \tilde{x}(T_{2i+1} + t) = \left(\frac{\tilde{x}(T_{2i+1})}{K(T_{2i+1})} + \mu_t \right) K(T_{2i+1} + t) e^{at} \end{cases}$$

and by induction,

$$\tilde{x}(T_{2i} + t) = (\tilde{x}_0 R/P_0 + 2i\lambda_T + \lambda_t) K(T_{2i} + t) e^{-at}$$

$$\tilde{x}(T_{2i+1} + t) = (\tilde{x}_0 R/P_0 e^{-aT} + (2i+1)\mu_T + \mu_t) K(T_{2i+1} + t) e^{at}$$

Let $E_K(s)$ be the expected value of \tilde{x}_0 at filtering time s , that is to say the expected value of $\tilde{x}(s)$ extrapolated backward according to the dynamics until time 0

$$E_K(T_{2i} + t) = E_0 R/P_0 K(T_{2i} + t) e^{-2at}$$

$$E_K(T_{2i+1} + t) = E_0 R/P_0 K(T_{2i+1} + t) e^{2a(t-T)}$$

In the same manner, let $P_K(s)$ be the variance of \tilde{x}_0 at filtering time s

$$P_K(T_{2i} + t) = \frac{R}{a} \left(\begin{array}{c} aR/P_0 + 4i^2 e^{aT} \sinh aT \\ + (4i+1)e^{at} \sinh at \end{array} \right) K^2(T_{2i} + t) e^{-4at}$$

$$P_K(T_{2i+1} + t) = \frac{R}{a} \left(\begin{array}{c} aR/P_0 + (2i+1)^2 e^{aT} \sinh aT \\ + (4i+3)e^{at} \sinh ate^{2a(T-t)} \end{array} \right) K^2(T_{2i+1} + t) e^{4a(t-T)}$$

$$\lim_{N \rightarrow +\infty} P_K(T_{2N} + t) = \lim_{N \rightarrow +\infty} P_K(T_{2N+1} + t) = \frac{2aR}{e^{2aT} - 1}$$

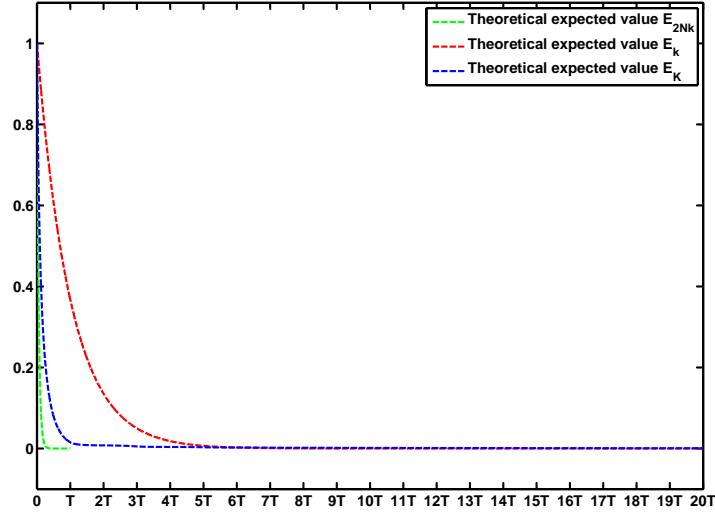
Claim 8. *Back-and-forth Kalman filtering converges towards the Cramér-Rao bound (A.4) as illustrated in Fig. A.3.*

$$\lim_{P_0 \rightarrow +\infty} P_K(T_{2i})_{(i>0)} = \lim_{P_0 \rightarrow +\infty} P_K(T_{2i+1}) = \frac{2aR}{e^{2aT} - 1}$$

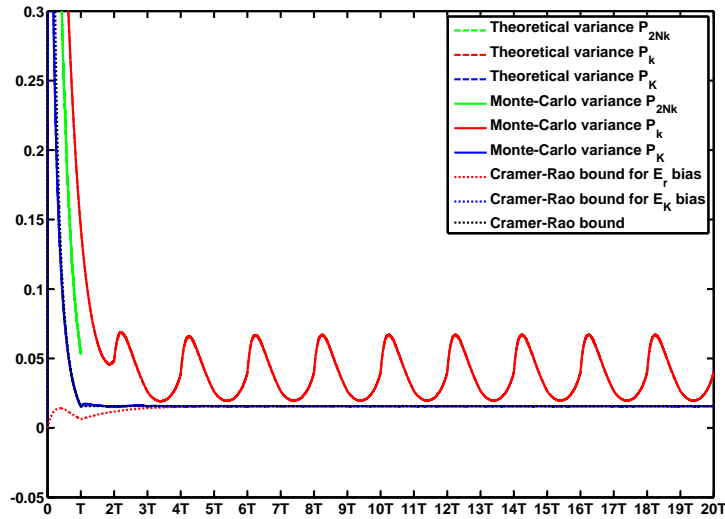
Claim 9. *The Cramér-Rao bound can also be reached by Kalman filtering with infinite initial uncertainty.*

Interpretation Back-and-forth Kalman filtering gives time to allow the filter to forget the initialization. Same phenomenon can be realized with larger initialization. The parallelism between the two mechanisms relies on the following equation

$$\text{Given } N, P_0 \rightarrow +\infty \equiv P_0 \gg \frac{2aR}{e^{2aT} - 1} \frac{1}{N}$$



(a) Expected value



(b) Variance

Figure A.3: Comparison of expected value and variance for $2Nk$ gain (green), k gain (red), Kalman filtering (blue). Theoretical computation of the variance is confirmed with Monte-Carlo simulations (concerning the expected value, the expected value of the random walk of the pseudo-random measurements is not negligible).

Appendix B

The role of the location of the center of gravity in quadrotor stability

A common thought, which refers to an analogy between a quadrotor and the celebrated inverted pendulum dynamical system, is that the location of the center of gravity must play an important role in the overall stability of the quadrotor. Due to physical limitations, actual prototypes (both commercial products and academic platforms) consider only center of gravity slightly distant from the "equatorial plane" defined by the rotors. Yet, it remains unclear whether this can improve stability. In fact, two properties must be distinguished [Guénard, 2007]. The first one is forward flight stability and the second one is wind gust rejection. In forward flight, the induced wind generates (at the center of gravity) a pitch torque and an aerodynamic force. Both can be calculated from (8.3-8.5). Depending on the vertical location of the center of gravity, the torque (which is the dominant effect) can either tend to increase, or decrease, the translational speed of the UAV. This point is pictured in Fig. B.1. In details, the torque which depends on the translational velocity u will drive the attitude dynamics θ . If the center of gravity is below the equatorial plane, the absolute value of the pitch angle will decrease and this will damp the system. Otherwise, the absolute value of the pitch angle will increase, and the system will go unstable.

Interestingly, the reasoning is symmetric for wind gust disturbances. The situation is pictured in Fig. B.2. While the generated effects are similar to the previous case, for stability, it is desired that the attitude of the vehicle counteracts the wind gust. In details, to avoid that the translational velocity follows the wind gust, the UAV should have a negative pitch angle. Having the center of gravity above the equatorial plane generates a contra rotating torque which contributes to this desired effect. It is certainly not a sufficient condition for stability, but the situation would be much worse if the torque would have the opposite sign, i.e. if the center of gravity would be below the equatorial plane.

Fig. B.1 and Fig. B.2 give insight into the "static stability" (as defined in [Johnson, 1980, Leishman, 2002, Prouty, 1990]). Further, the situation can also be seen on transfer functions. In fact, the location of the center of gravity plays a role on the poles of the transfer function between U and X and on the zeros of the transfer function between the disturbance \bar{u} and X .

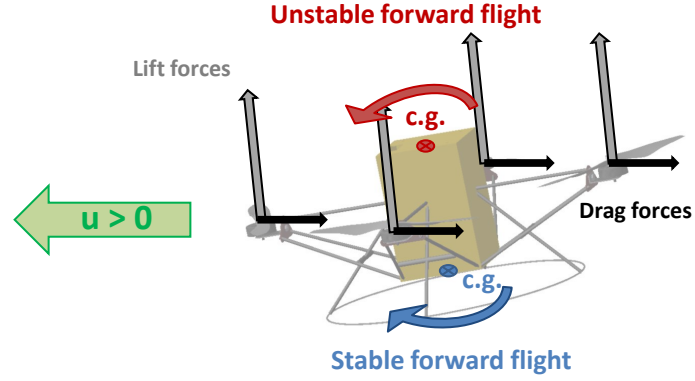


Figure B.1: Impact of the location of the center of gravity during forward flight.

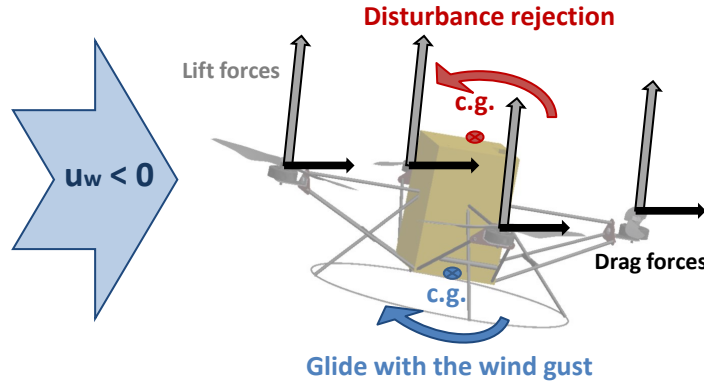


Figure B.2: Impact of the location of the center of gravity on disturbance rejection.

In particular, the sign of K_4 determines the sign of the zeros of the transfer between \bar{u} and the states. Under the rigid modeling assumption, a (large) positive value of h induces a non minimum phase transfer

$$\begin{aligned} \frac{u}{\bar{u}}(s) &= \frac{K_1 s^2 + (K_1 K_2 - K_3 K_4) s + g K_4}{s(s + K_1)(s + K_2) + K_4(g - s K_3)} \\ \frac{q}{\bar{u}}(s) &= \frac{-K_4 s^2}{s(s + K_1)(s + K_2) + K_4(g - s K_3)} \\ \frac{\theta}{\bar{u}}(s) &= \frac{-K_4 s}{s(s + K_1)(s + K_2) + K_4(g - s K_3)} \end{aligned}$$

These discussions show a necessary trade-off between stability and disturbance rejection. It is interesting to know in which configuration the quadrotor is, depending on the location of the center of gravity. We saw in Section 8.2.2 that, in the rigid model, the motion speed exerts a moment which value is proportional to the height of the center of gravity. Considering the

flexible modeling, the torque exerted by the tilt phenomenon adds an offset to this value. This implicitly appears in (8.14), and is summarized by the affine expression of the coefficient K_4 . The pole-zero map of the two models (Fig. B.3), obtained for varying locations of the center of gravity, supports these conclusions. With the rigid modeling of Section 8.2.2, the system always has a stable node, while an unstable focus becomes a pair of stable/unstable nodes as the center of gravity goes from below the rotor plane to above it. With the flexible modeling of Section 8.2.2, there is no remarkable change on the pole-zero map apart from a faster stable node.

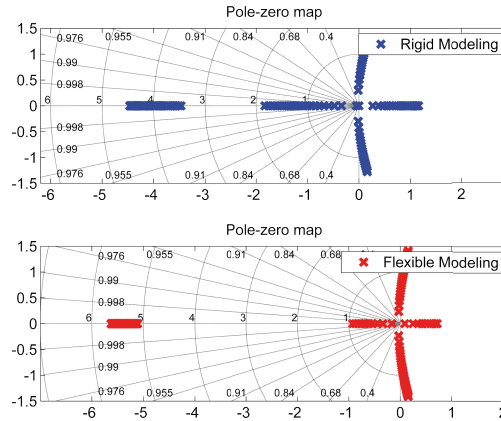


Figure B.3: Pole-zero map.

It is instructive to look at the real part of the eigenvalues, as function of the height of the center of gravity (Fig. B.4). The flexible modeling changes the switching value of the center of gravity where the focus split in two stable/unstable nodes. In other words, it impacts on the bifurcation diagram in Figure B.4 by sliding it to the right. Typically, the critical point is reached when the center of gravity is located nearly 10 centimeters above the rotor plane.

When the flexibility of the propellers is accounted for, we conclude that, when the center of gravity is close to the rotor plane ($|h| < 5$ cm), we face a slow unstable focus and the precise location of the center of gravity does not matter. The location of the center of gravity is not used to avoid an unstable node. By contrast, the rigid model features a bifurcation when h is near zero which is inconsistent with every reported experimental flights. We conclude here that, because of the flexibility of the propellers, the location of the center of gravity about the equatorial plane does not play any critical role on the dynamics of the quadrotor. The above reasoning is interestingly complemented by the following discussion. In [Pounds et al., 2004, Pounds et al., 2006], a quadrotor has been proposed where flapping dynamics is taken in account, but where the rotors have the particularity to be connected to their motors through teetering hubs. In this case, the coefficient K_4 can be neglected and only K_{dm} needs to be considered. Its sign can be determined by the location of the center of gravity. The particularity of teetering hubs is to generate stronger drag forces due to tilt phenomenon without undergoing the corresponding

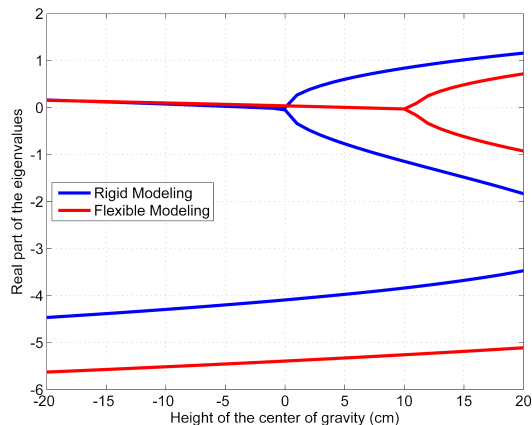


Figure B.4: Real part of the eigenvalues depending as a function of the location of the center of gravity.

torques. In this case, the dynamics are indeed qualitatively depending on the location of the center of gravity.

From a closed-loop control perspective, it is very instructive to compare the frequency domain representation of the previously considered modeling assumptions. In Fig. B.5, the Bode diagram of the model (8.15), which accounts for the rigid body and the flexibility of the propellers, is represented. The input signal is the pitch torque, $\delta_3 - \delta_1$ and the outputs are u , q and θ .

To evaluate the impact of the above mentioned hypothesis, we compare the frequency response for various modelings derived from the flexible modeling. It appears that the interactions of the angular velocities on the flexible modeling are negligible: considering $(0, K_{lf})$ or (K_3, K_2) yields relatively similar results (see Fig. B.6). Similarly, the drag force created by the rotor-disc tilt does not impact drastically the Bode diagram.

The only coefficient which significantly varies between the rigid and the flexible model is K_4 . Neglecting the flexibility moments yields an important error on the whole dynamics in the low-frequency domain. Therefore, it would be prejudicial to consider the rigid modeling for control design purposes since it induces a large error for low-frequencies (below 1 rad.s^{-1} , which includes the typical frequency of the desired closed-loop behavior) and an offset in the location of the resonance frequency (see Fig. B.5). Using the flexible model, slight displacements of the center of gravity induce only negligible modifications of the Bode diagram as can be observed in Fig. B.6. In view of closed-loop control design, the above results stress the challenges induced by the coupling effects and the flexibility.

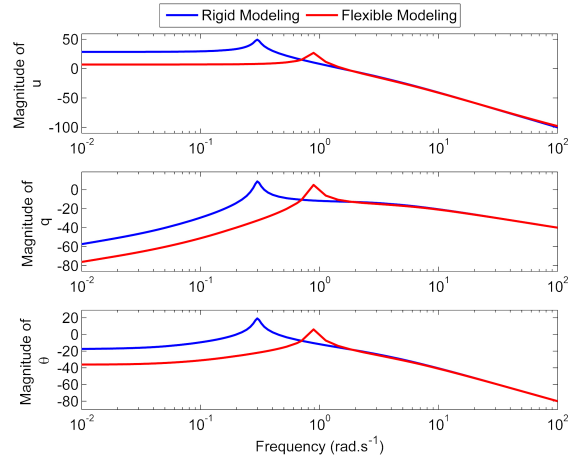


Figure B.5: Bode diagram (rigid and flexible models). Center of gravity is located 1 cm below the equatorial plane.

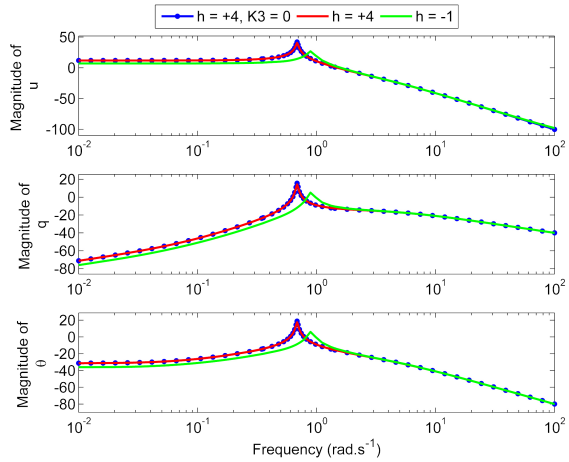


Figure B.6: Bode diagram (flexible model) for various locations of the center of gravity.

Bibliography

- [Abeles, 1972] Abeles, F., editor (1972). *Optical Properties of Solids*. North Holland.
- [Alazard, 2006] Alazard, D. (2006). Introduction au filtre de Kalman. Technical report, SUPAERO.
- [Analog Devices, 2009] Analog Devices (2009). *Triaxial Inertial Sensor with Magnetometer ADIS16400/ADIS16405*.
- [Anderson and Moore, 1979] Anderson, B. D. and Moore, J. B. (1979). *Optimal Filtering*. Prentice Hall.
- [Atsuumi and Sano, 2010] Atsuumi, K. and Sano, M. (2010). Indoor IR azimuth sensor using a linear polarizer. In *International Conf. on Indoor Positioning and Indoor Navigation*.
- [Auroux and Blum, 2008] Auroux, D. and Blum, J. (2008). A nudging-based data assimilation method: the back and forth nudging (BFN) algorithm. *Nonlinear Processes in Geophysics*, 15:305–319.
- [Auroux and Nodet, 2011] Auroux, D. and Nodet, M. (2011). The back and forth nudging algorithm for data assimilation problems: theoretical results on transport equations. *ESAIM Control, Optimisation and Calculus of Variations*, E-first.
- [Besançon, 2007] Besançon, G. (2007). *Nonlinear Observers and Applications*, volume 363, chapter An Overview on Observer Tools for Nonlinear Systems, pages 1–33. Springer.
- [Besançon and Hammouri, 1998] Besançon, G. and Hammouri, H. (1998). On observer design for interconnected systems. *J. Mathematical Systems, Estimation, and Control*, 8:1–25.
- [Bezick et al., 2010] Bezick, S. M., Pue, A. J., and Patzelt, C. M. (2010). Inertial navigation for guided missile systems. *John Hopkins APL Technical Digest*, 28(4):331–342.
- [Bierman et al., 1990] Bierman, G., Belzer, M., Vandergraft, J., and Porter, D. (1990). Maximum likelihood estimation using square root information filters. *IEEE Trans. Automatic Control*, 35:1293–1298.
- [Boizot, 2010] Boizot, N. (2010). *Adaptive High-Gain Extended Kalman Filter and Applications*. PhD thesis, Université du Luxembourg.
- [Bonnabel et al., 2008] Bonnabel, S., Martin, P., and Rouchon, P. (2008). Symmetry-preserving observers. *IEEE Trans. Automatic Control*, 53:2514–2526.
- [Born and Wolf, 1980] Born, M. and Wolf, E. (1980). *Principles of Optics*. Pergamon Press.

- [Bray, 2003] Bray, D. (2003). *Dynamic Positioning*. Oilfield Publications Ltd., 2nd edition.
- [Bristeau et al., 2011] Bristeau, P.-J., Callou, F., Vissière, D., and Petit, N. (2011). The navigation and control technology inside the AR drone micro UAV. In *Proc. 18th IFAC World Congress*.
- [Bristeau et al., 2010a] Bristeau, P.-J., Dorveaux, E., Vissière, D., and Petit, N. (2010a). Hardware and software architecture for state estimation on an experimental low-cost small-scaled helicopter. *Control Engineering Practice*, 18:733–746.
- [Bristeau et al., 2009] Bristeau, P.-J., Martin, P., Salaün, E., and Petit, N. (2009). The role of propeller aerodynamics in the model of a quadrotor UAV. In *Proc. European Control Conf.*
- [Bristeau and Petit, 2009] Bristeau, P.-J. and Petit, N. (2009). Trajectory estimation for a hybrid rocket. In *Proc. AIAA Guidance, Navigation and Control Conf.*
- [Bristeau and Petit, 2011] Bristeau, P.-J. and Petit, N. (2011). Navigation system for ground vehicles using temporally interconnected observers. In *Proc. American Control Conference*.
- [Bristeau et al., 2010b] Bristeau, P.-J., Petit, N., and Praly, L. (2010b). Design of a navigation filter by analysis of local observability. In *Proc. 49th IEEE Conf. on Decision and Control*.
- [Bucy and Joseph, 1968] Bucy, R. S. and Joseph, P. D. (1968). *Filtering for Stochastic Processes with Applications to Guidance*. AMS Chelsea Publishing.
- [Castillo et al., 2004] Castillo, P., Dzul, A., and Lozano, R. (2004). Real-time stabilization and tracking of a four rotor mini rotorcraft. *IEEE Trans. Control Systems Technology*, 12:510–516.
- [Chiaverini and Kuo, 2007] Chiaverini, M. and Kuo, K., editors (2007). *Fundamentals of Hybrid Rocket Combustion and Propulsion*. American Institute of Aeronautics and Astronautics, Inc.
- [Cunha et al., 2009] Cunha, R., Cabecinhas, D., and Silvestre, C. (2009). Nonlinear trajectory tracking control of a quadrotor vehicle. In *Proc. European Control Conference*.
- [de Plinval et al., 2011] de Plinval, H., Morin, P., Mouyon, P., and Hamel, T. (2011). Visual servoing for underactuated VTOL UAVs: A linear homography-based approach. In *IEEE International Conf. Robotics and Automation*.
- [Denham and Pines, 1966] Denham, W. F. and Pines, S. (1966). Sequential estimation when measurement function nonlinearity is comparable to measurement error. *AIAA Journal*, 4:1071–1076.
- [Deza, 1991] Deza, F. (1991). *Contribution to the synthesis of exponential observers*. PhD thesis, INSA Rouen.
- [Deza et al., 1992] Deza, F., Busvelle, E., Gauthier, J., and Rakotopara, D. (1992). High gain estimation for nonlinear systems. *Systems & Control Letters*, 18:295–299.
- [Dissanayake et al., 2001] Dissanayake, G., Sukkarieh, S., Nebot, E., and Durrant-Whyte, H. (2001). The aiding of a low-cost strapdown inertial measurement unit using vehicle model constraints for land vehicle applications. *IEEE Trans. Robotics and Automation*, 17(5):731–747.
- [Dobrokhodov et al., 2003] Dobrokhodov, V., Yakimenko, O., and Junge, C. (2003). Six-degree-of-freedom model of a controlled circular parachute. *J. Aircraft*, 40(3):482–493.

-
- [Donovan et al., 2010] Donovan, A., Mirrahimi, M., and Rouchon, P. (2010). Back and forth nudging for quantum state reconstruction. In *Proc. 4th International Symposium on Communications, Control and Signal Processing*.
- [Dorveaux et al., 2009] Dorveaux, E., Vissière, D., Martin, A. P., and Petit, N. (2009). Iterative calibration method for inertial and magnetic sensors. In *Proc. 48th IEEE Conf. on Decision and Control*.
- [Efe, 2007] Efe, M. (2007). Robust low altitude behavior control of a quadrotor rotorcraft through sliding modes. In *Mediterranean Conf. on Control Automation*.
- [Eke, 1998] Eke, F. O. (1998). Dynamics of variable mass systems. Technical report, Departement of Mechanical and Aeronautical Engineering, University of California.
- [Ekütekin, 2007] Ekütekin, V. (2007). *Navigation and control studies on cruise missiles*. PhD thesis, Middle East Technical University.
- [Evans and Smith, 1863] Evans, F. and Smith, A. (1863). *Admiralty Manual for Ascertaining and Applying the Deviations of the Compass caused by the Iron in a Ship*. Hydrographic Office.
- [Faurre, 1971] Faurre, P. (1971). *Navigation inertielle et filtrage stochastique*. Dunod.
- [Frieden, 2004] Frieden, B. R. (2004). *Science from Fisher Information*. Cambridge University Press.
- [Gadre, 2007] Gadre, A. (2007). *Observability Analysis in Navigation Systems with an Underwater Vehicle Application*. PhD thesis, Faculty of Virginia Polytechnic Institute and State University.
- [Gebre-Egziabher et al., 2006] Gebre-Egziabher, D., Elkaim, G., Powell, J., and Parkinson, B. (2006). Calibration of strapdown magnetometers in magnetic field domain. *J. Aerospace Engineering*, 19:87–102.
- [Gelb, 1974] Gelb, A., editor (1974). *Applied Optimal Estimation*. The MIT Press.
- [Grejner-Brzezinska et al., 2001] Grejner-Brzezinska, D. A., Yi, Y., and Toth, C. K. (2001). Bridging GPS gaps in urban canyons: the benefits of ZUPTs. *J. Navigation*, 48(4):217–225.
- [Grewal et al., 2001] Grewal, M. S., Weill, L. R., and Andrews, A. P. (2001). *Global Positioning Systems, Inertial Navigation, and Integration*. Wiley Inter-Science.
- [Guénard, 2007] Guénard, N. (2007). *Optimisation et implémentation de lois de commande embarquées pour la téléopération intuitive de micro drones aériens X4-flyer*. PhD thesis, Université Nice Sophia-Antipolis.
- [Hamel and Mahony, 2007] Hamel, T. and Mahony, R. (2007). Image based visual servo-control for a class of aerial robotic systems. *Automatica*, 43:1975–1983.
- [Hamel et al., 2002] Hamel, T., Mahony, R., Lozano, R., and Ostrowski, J. (2002). Dynamic modelling and configuration stabilization for an X4-flyer. In *Proc. IFAC Symposium*.
- [Hicks, 1993] Hicks, S. (1993). Advanced cruise missile guidance system description. In *Proc. IEEE National Aerospace and Electronics Conference*.

- [Hoffmann et al., 2007] Hoffmann, G. M., Huang, H., Waslander, S. L., and Tomlin, C. J. (2007). Quadrotor helicopter flight dynamics and control: Theory and experiment. In *Proc. AIAA Guidance, Navigation, and Control Conference*.
- [Hua, 2009] Hua, M.-D. (2009). *Contributions au controle automatique de véhicules aériens*. PhD thesis, Université de Nice Sophia-Antipolis.
- [Hua et al., 2008] Hua, M.-D., Hamel, T., Morin, P., and Samson, C. (2008). Control of thrust-propelled underactuated vehicles. Technical report, Institut National de Recherche en Informatique et Automatique.
- [Humble et al., 1995] Humble, R., Henry, G., and Larson, W., editors (1995). *Space Propulsion Analysis and Design*. The McGraw-Hill Companies Inc.
- [IEEE, 1998] IEEE (1998). Standard specification format guide and test procedure for single-axis interferometric fiber optic gyros.
- [Ikeda et al., 1975] Ikeda, M., Maeda, H., and Kodama, S. (1975). Estimation and feedback in linear time-varying systems: A deterministic theory. *SIAM J. Control*, 13:304–326.
- [International Association of Geomagnetism and Aeronomy, 2010] International Association of Geomagnetism and Aeronomy (2010). International geomagnetic reference field.
- [International Organization for Standardization, 1975] International Organization for Standardization (1975). Iso 2533:1975 standard atmosphere.
- [Jazwinski, 1970] Jazwinski, A. H. (1970). *Stochastic Processes and Filtering Theory*, volume 64 of *Mathematics in Science and Engineering*. Academic Press.
- [Johnson, 1980] Johnson, W. (1980). *Helicopter Theory*. Princeton University Press.
- [Julier and Uhlmann, 1997] Julier, S. and Uhlmann, J. (1997). A new extension of the kalman filter to nonlinear systems. In *Proc. Aerospace Defense Sensing Simulation and Controls Symposium*, pages 182–193.
- [Jung and Tsiotras, 2007] Jung, D. and Tsiotras, P. (2007). Inertial attitude and position reference system development for a small UAV. In *AIAA Infotech Aerospace*.
- [Kailath, 1974] Kailath, T. (1974). A view of three decades of linear filtering theory. *IEEE Trans. Information Theory*, 20:146–181.
- [Kailath, 1980] Kailath, T. (1980). *Linear Systems*. Prentice Hall.
- [Kalman, 1960a] Kalman, R. E. (1960a). Contributions to the theory of optimal control. *Boletín de la Sociedad Matemática Mexicana*, 5:102–119.
- [Kalman, 1960b] Kalman, R. E. (1960b). A new approach to linear filtering and prediction problems. *Trans. ASME - J. Basic Eng.*, 82:35–45.
- [Kalman and Bucy, 1961] Kalman, R. E. and Bucy, R. S. (1961). New results in linear filtering and prediction theory. *Trans. ASME - J. Basic Eng.*, 83:95–108.
- [Kaminski et al., 1971] Kaminski, P. G., Bryson, Arthur E., J., and Schmidt, S. F. (1971). Discrete square root filtering: a survey of current techniques. *IEEE Trans. Automatic Control*, 16:727–736.

-
- [Kim et al., 2004] Kim, S.-B., Lee, S.-Y., Hwang, T.-H., and Choi, K.-H. (2004). An advanced approach for navigation and image sensor integration for land vehicle navigation. In *Proc. IEEE 60th Vehicular Technology Conference*, volume 6, pages 4075–4078.
- [Kolmogorov, 1941] Kolmogorov, A. (1941). Interpolation and extrapolation of stationary stochastic series. *Izv. Akad. Nauk SSSR*, 5:3–14.
- [Leishman, 2002] Leishman, J. G. (2002). *Principles of Helicopter Aerodynamics*. Cambridge University Press.
- [Levinson, 1947] Levinson, N. (1947). The Wiener RMS (root mean square) error criterion in filter design and prediction. *Journal of Mathematics and Physics*, 25:261–278.
- [Lohner et al., 2006] Lohner, K., Dyer, J., Doran, E., Dunn, Z., and Ziliac, G. (2006). Fuel regression rate characterization using a laboratory scale nitrous oxide hybrid propulsion system. In *Proc. 42nd AIAA Joint Propulsion Conference and Exhibit*, Sacramento, CA.
- [Lupashin et al., 2010] Lupashin, S., Schollig, A., Sherback, M., and D’Andrea, R. (2010). A simple learning strategy for high-speed quadcopter multi-flips. In *Proc. IEEE International Conf. on Robotics and Automation*.
- [Mahony et al., 2005] Mahony, R., Hamel, T., and Pflimlin, J.-M. (2005). Complementary filter design on the special orthogonal group $SO(3)$. In *44th IEEE Conf. on Decision and Control*.
- [Marconi and Naldi, 2007] Marconi, L. and Naldi, R. (2007). Robust full degree-of-freedom tracking control of a helicopter. *Automatica*, 43:1909–1920.
- [Marconi et al., 2011] Marconi, L., Naldi, R., and Gentili, L. (2011). Modelling and control of a flying robot interacting with the environment. *Automatica*, (0).
- [Martin and Salaün, 2008] Martin, P. and Salaün, E. (2008). A general symmetry-preserving observer for aided attitude heading reference systems. In *Proc. 47th IEEE Conf. on Decision and Control*.
- [Martin and Salaün, 2010a] Martin, P. and Salaün, E. (2010a). Design and implementation of a low-cost observer-based attitude and heading reference system. *Control Engineering Practice*, 18:712–722.
- [Martin and Salaün, 2010b] Martin, P. and Salaün, E. (2010b). The true role of accelerometer feedback in quadrotor control. In *IEEE International Conf. on Robotics and Automation*.
- [Metni et al., 2006] Metni, N., Pflimlin, J.-M., Hamel, T., and Souères, P. (2006). Attitude and gyro bias estimation for a VTOL UAV. *Control Engineering Practice*, 14:1511–1520.
- [Mettler, 2003] Mettler, B. (2003). *Identification Modeling and Characteristics of Miniature Rotorcraft*. Kluwer Academic Publishers.
- [Morf and Kailath, 1975] Morf, M. and Kailath, T. (1975). Square-root algorithms for least-squares estimation. *IEEE Trans. Automatic Control*, 20:487–497.
- [Mukunda et al., 1979] Mukunda, H., Jain, V., and Paul, P. (1979). A review of hybrid rockets: Present status and future potential. *Sadhana*, 2:215–242.

- [Murray et al., 2002] Murray, R., Astrom, K., Boyd, S., Brockett, R., and Stein, G. (2002). Control in an information rich world. Technical report, Panel on Future Directions in Control, Dynamics, and Systems.
- [Nagata et al., 2006] Nagata, H., Ito, M., Maeda, T., Watanabe, M., Uematsu, T., Totani, T., and Kudo, I. (2006). Development of CAMUI hybrid rocket to create a market for small rocket experiments. *Acta Astronautica*, 59(1-5):253–258.
- [Naldi et al., 2010] Naldi, R., Gentili, L., Marconi, L., and Sala, A. (2010). Design and experimental validation of a nonlinear control law for a ducted-fan miniature aerial vehicle. *Control Engineering Practice*, 18:747–760.
- [Nocedal and Wright, 1999] Nocedal, J. and Wright, S. J. (1999). *Numerical Optimization*. Springer.
- [Ojeda and Borenstein, 2007] Ojeda, L. and Borenstein, J. (2007). Non-GPS navigation for security personnel and first responders. *J. Navigation*, 60(3):391–407.
- [Olfati-Saber, 2005] Olfati-Saber, R. (2005). Distributed kalman filter with embedded consensus filters. In *Proc. 44th IEEE Conf. on Decision and Control and European Control Conf.*
- [Pflimlin et al., 2010] Pflimlin, J.-M., Binetti, P., Souères, P., Hamel, T., and Trouchet, D. (2010). Modeling and attitude control analysis of a ducted-fan micro aerial vehicle. *Control Engineering Practice*, 18:209–218.
- [Poisson, 1838] Poisson, S. D. (1838). *Compte-rendu des séances de l’Académie des Sciences*, volume 6, chapter Mémoire sur les déviations de la boussole, produites par le fer des vaisseaux, pages 755–766. Bachelier.
- [Popp and Schiehlen, 2010] Popp, K. and Schiehlen, W. (2010). *Ground Vehicle Dynamics*. Springer.
- [Pounds et al., 2004] Pounds, P., Gresham, J., Mahony, R., Robert, J., and Corke, P. (2004). Towards dynamically favourable quad-rotor aerial robots. In *Proc. Australasian Conference on Robotics and Automation*, Canberra, Australia.
- [Pounds et al., 2006] Pounds, P., Mahony, R., and Corke, P. (2006). Modelling and control of a quad-rotor robot. In *Proc. Australasian Conf. on Robotics and Automation*.
- [Prouty, 1990] Prouty, R. W. (1990). *Helicopter Performance, Stability, and Control*. Krieger Publishing Company Inc.
- [Prévot and Jézéquel, 2008] Prévot, P. and Jézéquel, P. (2008). Programme fusex - propulsion hybride : Tirs en vol la courtine 2008 - synthèse. Technical report, ONERA.
- [Rao and Durrant-Whyte, 1991] Rao, B. and Durrant-Whyte, H. (1991). Fully decentralised algorithm for multisensor Kalman filtering. *IEE Proc. on Control Theory and Applications*, 138:413–420.
- [Renaudin et al., 2010] Renaudin, V., Afzal, M. H., and Lachapelle, G. (2010). New method for magnetometers based orientation estimation. In *IEEE/ION Position Location and Navigation Symposium*.
- [Ripka, 2001] Ripka, P., editor (2001). *Magnetic Sensors and Magnetometers*. Artech House.

-
- [Romero et al., 2007] Romero, H., Salazar, S., Sanchez, A., Castillo, P., and Lozano, R. (2007). Modelling and real-time control stabilization of a new VTOL aircraft with eight rotors. In *Proc. of IEEE International Conf. on Intelligent Robots and Systems*.
- [Rondon et al., 2009] Rondon, E., Fantoni-Coichot, I., Sanchez, A., and Sanahuja, G. (2009). Optical flow-based controller for reactive and relative navigation dedicated to a four rotor rotorcraft. In *Proc. IEEE/RSJ International Conf. on Intelligent Robots and Systems*.
- [Silverman and Anderson, 1968] Silverman, L. M. and Anderson, B. D. O. (1968). Controllability, observability and stability of linear systems. *SIAM J. Control*, 6:121–130.
- [Silverman and Meadows, 1967] Silverman, L. M. and Meadows, H. E. (1967). Controllability and observability in time-variable linear systems. *SIAM J. Control*, 5:64–73.
- [Skog and Handel, 2009] Skog, I. and Handel, P. (2009). In-car positioning and navigation technologies: a survey. *IEEE Trans. Intelligent Transportation Systems*, 10(1):4–21.
- [Stamatov et al., 2005] Stamatov, V., Honnery, D., and Soria, J. (2005). Visualization of flow development in hybrid rocket motors with high regression rates. *J. Propulsion and Power*, 21(4):613–619.
- [Stengel, 1994] Stengel, R. F. (1994). *Optimal Control and Estimation*. Dover Publications.
- [Tan and Arndt, 1997] Tan, C. and Arndt, J. (1997). Faraday effect in silica glasses. *Physica B: Condensed Matter*, 233:1–7.
- [Tan, 2008] Tan, L. (2008). *Digital Signal Processing: Fundamentals and Applications*. Academic Press.
- [Tayebi and McGilvray, 2006] Tayebi, A. and McGilvray, S. (2006). Attitude stabilization of a VTOL quadrotor aircraft. *IEEE Trans. Control Systems Technology*, 14:562–571.
- [Titterton and Weston, 2004] Titterton, D. H. and Weston, J. L. (2004). *Strapdown Inertial Navigation Technology*. The American Institute of Aeronautics and Astronautics.
- [Tsakalis and Ioannou, 1993] Tsakalis, K. S. and Ioannou, P. A. (1993). *Linear Time-Varying Systems: Control and Adaptation*. Prentice Hall.
- [Uliana et al., 1997] Uliana, M., Andreucci, F., and Papalia, B. (1997). The navigation system of an autonomous underwater vehicle for Antarctic exploration. In *Proc. IEEE Marine Technology Society Conference*, volume 1, pages 403–408.
- [Van der Merwe and Wan, 2001] Van der Merwe, R. and Wan, E. (2001). The square-root unscented Kalman filter for state and parameter-estimation. In *IEEE International Conf. Acoustics, Speech, and Signal Processing*.
- [Van Trees, 1968] Van Trees, H. L. (1968). *Detection, Estimation, and Modulation Theory, Part I*. John Wiley & Sons.
- [Vasconcelos et al., 2011] Vasconcelos, J., Elkaim, G., Silvestre, C., Oliveira, P., and Cardeira, B. (2011). Geometric approach to strapdown magnetometer calibration in sensor frame. *IEEE Trans. Aerospace and Electronic Systems*, 47:1293–1306.

- [Verhaegen and Van Dooren, 1986] Verhaegen, M. and Van Dooren, P. (1986). Numerical aspects of different kalman filter implementations. *IEEE Trans. Automatic Control*, 31:907–917.
- [Vidard et al., 2003] Vidard, P., Le Dimet, F.-X., and Piacentini, A. (2003). Determination of optimal nudging coefficients. *Tellus*, 55:1–15.
- [Vissière et al., 2008] Vissière, D., Bristeau, P.-J., Martin, A. P., and Petit, N. (2008). Experimental autonomous flight of a small-scaled helicopter using accurate dynamics model and low-cost sensors. In *Proc. 17th IFAC World Congress*.
- [Viéville and Sander, 1992] Viéville, T. and Sander, P. (1992). Using pseudo Kalman-filters in the presence of constraints application to sensing behaviors. Technical report, Institut National de Recherche en Informatique et Automatique.
- [Wan and Van Der Merwe, 2000] Wan, E. and Van Der Merwe, R. (2000). The unscented kalman filter for nonlinear estimation. In *IEEE Adaptive Systems for Signal Processing, Communications, and Control Symposium*.
- [Wiener, 1942] Wiener, N. (1942). The extrapolation, interpolation and smoothing of stationary time series. Technical report, MIT.
- [Wiener, 1949] Wiener, N. (1949). *Extrapolation, Interpolation and Smoothing of Stationary Time Series*. John Wiley & Sons.
- [Young et al., 2002] Young, L., Aiken, E., Johnson, J., Demblewski, R., Andrews, J., and Klem, J. (2002). New concepts and perspectives on micro-rotorcraft and small autonomous rotary-wing vehicles. In *Proc. AIAA Applied Aerodynamics Conference*.

Techniques d'estimation du déplacement d'un véhicule sans GPS et autres exemples de conception de systèmes de navigation MEMS

Résumé: Dans cette thèse, on explique la conception et la mise au point d'un système de navigation sans GPS pour un véhicule automobile. Ce système exploite des mesures de champs magnétiques réalisées à bord du véhicule en mouvement, combinées à des mesures inertielles réalisées à partir de capteurs MEMS bas coût. Il permet de reconstituer, à partir d'une condition initiale, la trajectoire du véhicule en temps réel. Un prototype fonctionnel complet est présenté ainsi que des résultats expérimentaux. La conception de ce système repose sur une analyse de l'observabilité d'un modèle classique du véhicule, qui permet d'établir comment les différents biais et défauts des capteurs peuvent être estimés grâce à des filtres de Kalman agencés suivant deux schémas d'interconnexion: par partition des variables d'états et par séquençement. Une analyse de convergence des schémas d'estimation est étudiée. En dernière partie du manuscrit, deux autres exemples de systèmes de navigation à base de capteurs MEMS sont décrits, celui du quadricoptère Parrot AR.Drone et celui de fusées expérimentales à propulsion hybride, pour lesquels les mêmes principes de conception sont appliqués.

Mots clés: systèmes de navigation sans GPS, capteurs MEMS, systèmes embarqués, observabilité, filtrage de Kalman, observateurs interconnectés, observateurs temporellement interconnectés, véhicule automobile, micro-drone, mini-fusée

Motion estimation techniques for GPS-free vehicle and other examples of MEMS navigation systems design

Abstract: In this thesis, we explain the design and development of a GPS-free navigation system for automotive vehicles. This system uses magnetic field measurements performed onboard the vehicle in motion, and combines them with inertial measurements from other low costs MEMS sensors. It allows one to reconstruct the path of the vehicle from the initial condition in real time. A complete prototype is presented along with experimental results. The design of this system is based on an analysis of the observability of a classical model of the vehicle. This serves to establish how the various biases and shortcomings of the sensors can be estimated through Kalman filters arranged in two interconnection schemes: a partition of the state variables and a temporal interconnection. An analysis of convergence of the estimates is performed. In the final part of the manuscript, two other examples of MEMS-based navigation systems are described, including the AR.Drone quadrotor and experimental hybrid rockets for which the same design principles are applied.

Keywords: GPS-free navigation systems, MEMS sensors, embedded systems, observability, Kalman filtering, interconnected observers, temporally interconnected observers, automotive vehicle, micro-UAV, mini-rocket

